energies

Modeling and Optimal Operation of Hydraulic, Wind and Photovoltaic Power Generation Systems

Edited by
Chaoshun Li, Yun Zeng, Beibei Xu and Dong Liu

Printed Edition of the Special Issue Published in *Energies*

www.mdpi.com/journal/energies

MDPI

Modeling and Optimal Operation of Hydraulic, Wind and Photovoltaic Power Generation Systems

Modeling and Optimal Operation of Hydraulic, Wind and Photovoltaic Power Generation Systems

Editors

Chaoshun Li
Yun Zeng
Beibei Xu
Dong Liu

MDPI • Basel • Beijing • Wuhan • Barcelona • Belgrade • Manchester • Tokyo • Cluj • Tianjin

Editors

Chaoshun Li
Huazhong University of Science and Technology
China

Yun Zeng
Kunming University of Science and Technology
China

Beibei Xu
Northwest A&F University
China

Dong Liu
North China University of Water Resources and Electric Power
China

Editorial Office
MDPI
St. Alban-Anlage 66
4052 Basel, Switzerland

This is a reprint of articles from the Special Issue published online in the open access journal *Energies* (ISSN 1996-1073) (available at: https://www.mdpi.com/journal/energies/special_issues/Hydraulic_Wind_Photovoltaic).

For citation purposes, cite each article independently as indicated on the article page online and as indicated below:

LastName, A.A.; LastName, B.B.; LastName, C.C. Article Title. *Journal Name* **Year**, *Volume Number*, Page Range.

ISBN 978-3-0365-5837-0 (Hbk)
ISBN 978-3-0365-5838-7 (PDF)

Contents

About the Editors

Chaoshun Li

Chaoshun Li is professor at Huazhong University of Science and Technology. He has been selected as a young top talent in the National "Ten Thousand Plan", a winner of the Hubei Outstanding Youth Fund, executive director of the Rotor Dynamics Committee of the Chinese Society of Vibration Engineering, director of the Hubei Hydropower Engineering Society and an editorial board member of SCI journals. He has presided over one national young talent project, four National Natural Science Foundation of China (NSFC) projects, one National Key Research and Development Program (sub-project) project, one Doctoral Point Fund project of the Ministry of Education, one Wuhan City Applied Basic Frontier Project, and participated in many major projects including 973 key projects of the National Science and Technology Support Program and National Natural Science Foundation of China (NSFC). He has authored three monographs and published 162 papers, including 102 in SCI journals, 13 in EI conferences, and 47 in Chinese journals. He received academic honors such as the 2020 MDPI Highest Influential Author and the Elsevier 2020 Highly Cited Scholar in China (with only 24 scholars working in the discipline of water resource engineering).

Yun Zeng

Yun Zeng is a professor with Kunming University of Science and Technology. He is the director of the Yunnan University Hydraulic Machinery Intelligent Test Engineering Research Center. He is also the Chairman of the Hydroelectric Power Subcommittee of IEEE PES Energy Department and Power Generation Satellite Committee—China, a member of the Hydro Turbine Committee of Chinese Society of Power Engineering, a member of the Automation Committee of the Chinese Society for Hydropower Engineering, a member of Hydropower Equipment Committee of the Chinese Society for Electrical Engineering, and a member of the Drainage and Irrigation Machinery Committee of the Chinese Society for Agricultural Machinery. His research interests include the stability and control of hydro turbine generating units, renewable energy generation, nonlinear dynamics and control. He has published more than 80 papers, including more than 60 SCI and EI papers. He has published the monograph "Modeling Theory of Hydropower Units", and a textbook entitled "Computer Monitoring of Hydropower Stations".

Beibei Xu

Beibei Xu, Ph.D., is with Northwest A&F University. He received his bachelor's, master's and doctorate degrees in hydraulic engineering from Northwest A&F University in 2014, 2017, and in 2020, respectively. In 2019, he spent three months at Universitat Politecnica de Catalunya as part of a student exchange program. Since 2020, he has been worked at Northwest A&F University as an associate professor. His research interests cover a number of R&D topics including hydropower generation integration into renewable energy, risk analysis and reliability evaluation, as well as dynamics and control theories. Now, he serves as a reviewer for more than 30 international journals.

Dong Liu

Dong Liu, Ph.D., is with College of Energy and Power Engineering, North China University of Water Resources and Electric Power. He received his B.E. degree in thermal and power engineering (hydrodynamic direction) from the North China University of Water Resources and Electric Power in 2015 and his Ph.D. in fluid mechanics and engineering from Wuhan University in 2020. Between July 2020 and August 2022, he worked as a postdoctoral researcher in the discipline of water resource engineering at Huazhong University of Science and Technology with the co-supervision of Prof. Chaoshun Li. From 2017 to the present, he has published more than 25 academic papers in journals such as *Applied Energy*, *Renewable Energy*, *Measurement*, etc. He has hosted one Chinese Postdoctoral Science Foundation and participated in two National Natural Science Foundation of China. His research interests include refined modeling, stability analysis, optimal control, and monitoring and diagnosis of renewable energy generation systems, including hydropower units.

energies

MDPI

Article

Hopf Bifurcation and Parameter Sensitivity Analysis of a Doubly-Fed Variable-Speed Pumped Storage Unit

Zhiwei Zhu, Xiaoqiang Tan, Xueding Lu, Dong Liu * and Chaoshun Li *

School of Civil and Hydraulic Engineering, Huazhong University of Science and Technology, Wuhan 430074, China; M202074043@hust.edu.cn (Z.Z.); D201981040@hust.edu.cn (X.T.); D202081166@hust.edu.cn (X.L.)

* Correspondence: liudongwhu@126.com (D.L.); csli@hust.edu.cn (C.L.); Tel.: +86-132-0718-2985 (D.L.); +86-158-7180-0142 (C.L.)

Abstract: The doubly-fed variable speed pumped storage unit is a storage system suitable for joint operation with renewable energy sources to smooth the imbalance between renewable energy supply and electricity demand. However, its working principle and operation control are more complex than those of constant speed pumped storage. In this study, a nonlinear model of doubly-fed variable speed pumped storage units (VSPSUs) considering nonlinear characteristics of the head loss is established. The study finds that a supercritical Hopf bifurcation occurs in the system, and the area enclosed by the lower side of the bifurcation line and the coordinate axis is the stability domain of the system. The active power step perturbation from −0.3 to 0.3 will gradually reduce the area of the stability domain and narrow the adjustable range of the control parameters. In addition, the sensitivity of the model full state variables and the primary and secondary relationships to the changes of subsystem parameters is analyzed systematically using the trajectory sensitivity. It is found that there is a large difference in the sensitivity of different state variables to the parameters. The state variables are much more sensitive to the transfer coefficient of hydraulic turbine torque to guide vane opening, the unit inertia time constant, and the controller proportional gain change than other parameters, which are defined as highly sensitive parameters. The receiver response time constant and the turbine flow-to-head transfer coefficient are the corresponding low-sensitivity parameters.

Keywords: doubly-fed variable-speed pumped storage; Hopf bifurcation; stability analysis; parameter sensitivity

Citation: Zhu, Z.; Tan, X.; Lu, X.; Liu, D.; Li, C. Hopf Bifurcation and Parameter Sensitivity Analysis of a Doubly-Fed Variable-Speed Pumped Storage Unit. *Energies* **2022**, *15*, 204. https://doi.org/10.3390/en15010204

Academic Editor: Dimitrios Katsaprakakis

Received: 26 November 2021
Accepted: 21 December 2021
Published: 29 December 2021

1. Introduction

As power system operators pursue low-carbon investments and long-term energy sustainability, large-scale development and a high proportion of variable renewable energy (VRE) access in the power system will become inevitable in the coming decades. In fact, renewables remained the fastest growing source of energy in buildings, increasing 4.1% annually on average between 2009 and 2019, and reached their highest recorded share in the global electricity mix in 2020—an estimated 29% [1]. The higher the share of generation from variable renewable energy sources, the more flexible the power system must be to maintain a daily or annual balance between supply and demand. To manage the long-term imbalance between VRE supply and electricity demand, scholars have investigated solutions to smooth the imbalance between VRE supply and electricity demand and evaluated their role in deep decarbonization of power generation using advanced power system investment and operation models. These systems include nuclear power plants and natural gas plants equipped with carbon capture and storage, flexible demand, battery energy storage, and long-term storage technologies [2–4]. Energy storage technologies can provide long-term and seasonal energy conversion, allow for the temporal separation of energy generation and consumption, and address the intermittency of variable renewables. Dimanchev et al. used a detailed capacity expansion and dispatch model to verify the optimal role of reservoir

hydro as an energy storage resource. Therefore, pumped storage units (PSUs), which use both upstream and downstream reservoirs for energy conversion and storage, are currently large-scale energy storage systems that are widely used around the world [5]. PSUs do not involve chemical conversion processes, which may easily generate pollution. They are highly adjustable to flexible and variable operating conditions, and have a combined operating efficiency of 70–85% [6]. Therefore, PSUs as energy storage devices are well suitable for combined operation with renewable energy in hybrid energy power systems [7].

There are two common types of PSU, namely constant speed pumped storage units (CSPSUs) and variable speed pumped storage units (VSPSUs) [8]. Currently, most of the PSUs are of constant speed. However, for CSPSUs, the speed regulation of the units is slow in the generation condition, and the input power of the unit is not adjustable in the pumping condition. Compared with the CSPSU, recent studies have demonstrated that the VSPSU not only inherits the advantages but also has the following additional advantages: (a) the active power of VSPSUs can be controlled quickly; (b) the frequency stability of the grid can be greatly improved; (c) and the efficiency of the units can be improved in both power generation and pumping conditions [9–11]. However, the working principle and operation control of VSPSUs are more complicated than those of CSPSUs. Therefore, the understanding of the dynamic behavior of VSPSUs is now in urgent need of enhancement, and the stability of VSPSUs has significant research value.

At present, the research on doubly-fed variable-speed pumped storage units (VSPSUs) is focused on the following aspects: mathematical modeling and simulation, dynamic characteristics and operational stability and reliability, and optimal control. Their contributions are mainly as follows. Gao et al. developed a fast and high-precision model of a VSPSU, which can better characterize VSPSUs [12]. Mohanpurkar et al. achieved real-time co-simulation of hydrodynamics and electrical events for adjustable-speed pumped storage hydro [13]. Zhao et al. established a model for the power generation and pumping conditions of VSPSUs and verified the model and the proposed control strategy using the MATLAB/Simulink simulation platform [14]. Xie et al. studied an electromechanical transient model of the VSPSU, preserving the dynamic process of the motor flux linkage and the dynamic characteristics of the controller inner loop [15]. Zhao et al. established the output power model of VSPSUs, and found that the VSPSU has good compensation ability for the power fluctuation of a power system [16]. Yang et al. evaluated the performance of the VSPSU in mitigating the power regulation of wind power variations and found that it excels in promoting power system stability [17]. Joseph et al. investigated the dynamic performance of VSPSUs in the event of power and control circuit failures as well as converter and sensor failures, providing ideas for the stable operation of VSPSUs [18,19]. Damdoum et al. proposed new simple fault ride-through strategies to reduce the negative impacts of grid fault occurrence on the doubly-fed induction machine pumped storage system [20]. Madeira et al. investigated the effect of sudden changes in excitation capacitances, resistive loads, or recovered head on the operation of a pump working as a turbine-self-excited induction generator model (PAT-SEIG) system using a constructed PAT-SEIG model [21]. Pagaimo et al. studied the transient characteristics of series-connected pumps working as turbines in an off-grid system and found that one change in the first pump of a turbine group will significantly affect the other group dynamics [22]. Gao et al. studied the stability of a VSPSU regulation system and found that the stability domain of the pumping condition is larger than that of the generation mode when the parameters of the power controller are fixed [23]. The above literature provides a basis for studying the stability of VSPSUs but does not investigate the effect of the intrinsic nonlinear characteristics of the system components on the stability of the whole unit.

Meanwhile, Cruz et al. showed that stability robustness has a close relationship with sensitivity robustness in nonlinear feedback systems [24]. Therefore, parameter sensitivity analysis is also an important part of system stability analysis. Some of the current studies focus on the influence of individual subsystem parameters (e.g., turbine system parameters [25]) on individual system characteristics (e.g., unit vibration [26]), and

some scholars have also studied the influence of unit parameters on control characteristics using the zero-pole variation of the closed-loop transfer function and have used it to design the unit parameters [27]. Liu et al. analyzed the sensitivity of the hydropower unit damping to the system parameters and revealed the influence mechanism of the parameters on ultra-low-frequency oscillations [28]. These studies lack a systematic study of the primary and secondary relationships between the effects of parameters on the system, and there are few examples of their application to VSPSUs.

Therefore, this paper focuses on the nonlinear bifurcation and parameter sensitivity characteristics of the VSPSU. In Section 2, the process of deriving the models of each subsystem is described, and a fifth-order nonlinear model of the VSPSU considering pressure head loss is established. A parameter sensitivity analysis method is also introduced in this section. In Section 3, nonlinear bifurcation analysis of the VSPSU under PI control strategy is performed to find its stability domain and analyze the bifurcation types of the system. The dynamic response of the system under active power perturbation is simulated numerically, and the conclusions obtained from the theoretical analysis are verified by the simulation. In Section 4, the effects of different active power steps on the stability domain of the system and the sensitivity of the system to the changes of key parameters of each subsystem are analyzed. Conclusions are drawn in the final section.

2. Mathematical Modeling and Parameter Sensitivity Analysis Method of Doubly-Fed Variable Speed Pumped Storage Units

In the field of automatic control, we often use the state space method to analyze systems, where the dynamic characteristics of the system are described by a number of first-order differential equations composed of state variables. They can reflect the changes of all independent variables of the system, so that all the internal motion states of the system can be determined at the same time, and they can also handle the initial conditions easily. In addition, they can be used in nonlinear systems, time-varying systems, multiple-input-multiple-output systems, and stochastic processes because they can be analyzed and designed with computers and controlled in real time. A VSPSU is a nonlinear system with hydraulic-mechanical-electrical coupling, for which a reliable and realistic mathematical model can be developed using the state space method. The VSPSU mainly consists of a governor, electro-hydraulic servo system, pump turbine, water diversion system and doubly-fed induction motor (DFIM), and the structure diagram of a VSPSU is shown in Figure 1.

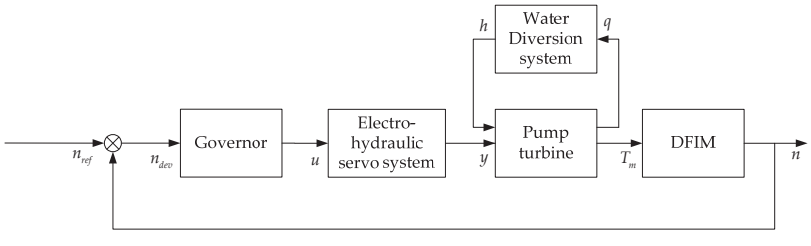

Figure 1. Structure diagram of a VSPSU.

2.1. Modeling of Hydraulic Subsystem

In building the mathematical model of a VSPSU, we need to consider a combination of hydraulic–mechanical–electrical factors. The hydraulic part of the factors is mainly represented by the pressure pipe used to transmit water, whose dynamic characteristics can be described using an ordinary differential equation. Assuming that the walls of the pressure pipe and the water in the pressure pipe are rigid, the water hammer pressure due to the variation of the guide vane opening of the pump turbine can be calculated by the

rigid water column theory. Based on Newton's second law of motion, the fluid motion in the pressure pipe can be described by the following equation:

$$\frac{L_t V_{t0}}{g H_0} \frac{\mathrm{d}(\frac{Q_t - Q_{t0}}{Q_{t0}})}{\mathrm{d}t} = -\frac{H - H_0}{H_0} - \frac{h_t - h_{t0}}{H_0} \tag{1}$$

where L_t is the length of penstock, V_{t0} is the initial value of flow velocity in penstock, H is the turbine working head, H_0 is the initial value of the turbine working head, g is acceleration of gravity, Q_t is the reference flow rate of the turbine, Q_{t0} is the initial value of the reference flow rate of the turbine. h_t is the head loss of penstock, h_{t0} is the initial value of the head loss of penstock.

Since the state variables in this paper are expressed in the form of relative values of deviation, the deviation of the above equation regarding flow rate and water pressure can be simplified by $h = \frac{H - H_0}{H_0}$ and $q = \frac{Q_t - Q_{t0}}{Q_{t0}}$. $\frac{L_t V_{t0}}{g H_0}$ represents the characteristics of the inertia of water flow in the pressure pipe. We can use a time constant of water inertia T_W to simplify the substitution. Then the simplified equation is obtained as follows:

$$h = -T_w \frac{\mathrm{d}q}{\mathrm{d}t} - \frac{h_t - h_{t0}}{H_0} \tag{2}$$

By associating with the flow rate at this moment, we can obtain the differential equation containing only h and q. For the head loss in penstock, the expression for the head loss is $h_t = \alpha Q_t^2$. At the initial moment, that is $t = 0$, when there is $h_{t0} = \alpha Q_{t0}^2$, then we find $h_t = h_{t0}(\frac{Q_t}{Q_{t0}})^2$, using the relationship between Q_t and q, and $h_t = h_{t0}(1 + 2q + q^2)$ can be obtained by substituting $Q_t = Q_{t0} + Q_{t0}q$. Therefore, we can obtain the equation at the initial moment: $h_t - h_{t0} = h_{t0}(2q + q^2)$.

The above equations can be combined to obtain the dynamic equation considering the pressure pipe head loss as follows [29]:

$$h = -T_w \frac{\mathrm{d}q}{\mathrm{d}t} - \frac{h_{t0}(2q + q^2)}{H_0} \tag{3}$$

This shows that the head loss of the penstock is nonlinear.

2.2. Modeling of Mechanical Subsystem

The mechanical part of the factors is reflected in the prime mover of hydroelectric power generation, i.e., the pump turbine, and the governor used to control the turbine speed and thus ensure the frequency stability of the power generation. In the modeling of the pump turbine, to represent the dynamic characteristics of the turbine in a relatively simple form, and considering that the variation of the turbine speed, head and guide vane opening is small in the study of this paper, we assume that the nonlinear relationship of the pump turbine is linear. The moment equation and flow equation of the pump turbine are used for further analysis and research, and the specific expressions of the equations are as follows:

$$\begin{cases} m_{\mathrm{t}} = e_h h + e_x x + e_y y \\ q = e_{qh} h + e_{qx} x + e_{qy} y \end{cases} \tag{4}$$

where $x = \frac{n - n_0}{n_0}$ and $y = \frac{a - a_0}{a_0}$; e_h, e_x, e_y are the transfer coefficients of pump turbine torque to head, speed, guide vane opening respectively, e_{qh}, e_{qx}, e_{qy} are the transfer coefficients of pump turbine flow to head, speed, guide vane opening respectively, n is the pump turbine speed, n_0 is the initial value of speed, a is the guide vane opening of pump turbine, a_0 is the initial value of guide vane opening.

The governor is the controller of the unit, and its control law commonly used in industrial applications is mainly PI control or PID control. PI control is used in this paper. In order to achieve the control goal, an electrohydraulic servo system is required to convert

the output of the PI control strategy into the action of the guide vane, i.e., the guide vane opening. This conversion is generally in the form of integration, supplemented by the conversion coefficient of the response. The equations of this control strategy and the electrohydraulic servo system are:

$$\begin{cases} \frac{\mathrm{d}u}{\mathrm{d}t} = -K_\mathrm{p}\frac{\mathrm{d}x}{\mathrm{d}t} - K_\mathrm{i}x \\ \frac{\mathrm{d}y}{\mathrm{d}t} = \frac{1}{T_\mathrm{y}}(u-y) \end{cases} \tag{5}$$

where u is the governor regulation output, K_p is the proportional gain, K_i is the integral gain, and T_y is the receiver response time constant.

2.3. Modeling of Electrical Subsystem

The electrical factors are concentrated in the DFIM of a VSPSU. The mathematical model of the DFIM consists of voltage equations, magnetic chain equations, torque equations and equations of motion. The mathematical model of the DFIM in the conventional three-phase stationary coordinate system is a very complex and strongly coupled time-varying system. To facilitate the analysis and solution of the operating characteristics, the mathematical model of the DFIM is transformed by using the coordinate transformation method, and the mathematical model in the three-phase stationary *abc* coordinate system is equated to that in two identical rotating *dq* coordinate systems.

The transformed voltage and magnetic chain equations are as follows:

$$\begin{cases} u_{ds} = R_s i_{ds} + \dot{\Psi}_{ds} - \omega_s \Psi_{qs} \\ u_{qs} = R_s i_{qs} + \dot{\Psi}_{qs} + \omega_s \Psi_{ds} \\ u_{dr} = R_r i_{dr} + \dot{\Psi}_{dr} - s_r \omega_s \Psi_{qr} \\ u_{qr} = R_r i_{qr} + \dot{\Psi}_{qr} + s_r \omega_s \Psi_{dr} \end{cases} \tag{6}$$

$$\begin{cases} \Psi_{ds} = L_{ss} i_{ds} + L_m i_{dr} \\ \Psi_{qs} = L_{ss} i_{qs} + L_m i_{qr} \\ \Psi_{dr} = L_m i_{ds} + L_{rr} i_{dr} \\ \Psi_{qr} = L_m i_{qs} + L_{rr} i_{qr} \end{cases} \tag{7}$$

where u_{ds}, u_{qs}, u_{dr}, u_{qr} are the d, q axis voltage of stator and rotor, respectively; R_s, R_r is the stator and rotor resistance, respectively; i_{ds}, i_{qs}, i_{dr}, i_{qr} are the d, q axis current of stator and rotor, respectively; Ψ_{ds}, Ψ_{qs}, Ψ_{dr}, Ψ_{qr} are the d, q axis flux linkage of stator and rotor, respectively; ω_s denotes the synchronous speed, $s_r = \frac{\omega_s - \omega_r}{\omega_s}$ denotes the relative speed deviation. L_m is the mutual inductance between stator and rotor; L_{ss}, L_{rr} are the inductance of stator and rotor respectively; subscripts s and r represent the stator and rotor components respectively; subscripts d and q represent the d-axis and q-axis components respectively.

The equation of motion and the equation of torque can be described as follows:

$$\begin{cases} T_a \frac{\mathrm{d}x}{\mathrm{d}t} = T_m - T_e \\ T_e = \frac{3}{2} p_n L_m (i_{ds} i_{qr} - i_{qs} i_{dr}) \end{cases} \tag{8}$$

where T_a is the unit inertia time constant; T_m is the active torque of the turbine; and T_e is the load torque of the generator; p_n is the number of poles.

When the model of the DFIM is converted to two identical steps in a rotation coordinate system, vector control is generally used as the control method. We can let the d-axis coincide with the stator voltage vector, while ignoring the stator resistance which is much smaller than the reactance, and finally obtain the stator magnetic chain vector in steady state with 90° phase difference from the stator voltage vector. After orientation, a series of updated

system equations can be obtained. The most important power equation and torque equation will be updated in Equation (9):

$$\begin{cases} P_s = -\frac{3}{2}U_s\frac{L_m}{L_s}i_{dr} \\ Q_s = -\frac{3}{2}U_s\left(\frac{U_s}{\omega_s}\frac{1}{L_s} - \frac{L_m}{L_s}i_{qr}\right) \\ T_e = -\frac{3}{2}p_n\frac{U_s}{\omega_s}\frac{L_m}{L_s}i_{dr} \end{cases} \tag{9}$$

where U_s is effective value of grid voltage; P_s is active power; Q_s is reactive power.

$$\begin{cases} \dot{q} = -\frac{1}{T_w}[(\frac{2h_{t0}}{H_0} + \frac{1}{e_{qh}})q - \frac{e_{qx}}{e_{qh}}x - \frac{e_{qy}}{e_{qh}}y + \frac{h_{t0}}{H_0}q^2] \\ \dot{x} = \frac{1}{T_a}[\frac{e_h}{e_{qh}}q + (e_x - \frac{e_h}{e_{qh}}e_{qx} - e_g)x + (e_y - \frac{e_h}{e_{qh}}e_{qy})y + \frac{3u_sL_m}{2L_sw_s}i_{dr}] \\ \dot{y} = \frac{1}{T_y}(u - y) \\ \dot{u} = -\frac{K_P}{T_a}[\frac{e_h}{e_{qh}}q + (e_x - \frac{e_h}{e_{qh}}e_{qx} - e_g)x + (e_y - \frac{e_h}{e_{qh}}e_{qy})y + \frac{3u_sL_m}{2L_sw_s}i_{dr}] - K_ix \\ \dot{i}_{dr} = -\frac{3K_{i2}u_sL_m}{2L_s+3K_{p2}u_sL_m}i_{dr} + \frac{2L_sK_{i2}}{2L_s+3K_{p2}u_sL_m}P_{ref} \end{cases} \tag{10}$$

By combining the above equations and selecting the independent state variables q, x, y, u, i_{dr} that represent the characteristics of the VSPSU, with appropriate variable substitutions and simplifications, we can obtain a fifth-order nonlinear model for a VSPSU as Equation (10).

2.4. Parameter Sensitivity Analysis Method

In this paper, the definition of trajectory sensitivity and average trajectory sensitivity in the literature [30] are used to analyze the parameters in the system accordingly, and the nonlinear model of a VSPSU is expressed as Equation (10). Under certain operating conditions, taking the rotational speed of VSPSU as an example, the trajectory sensitivity of the system state variables with respect to a parameter can be defined as Equation (11):

$$S_{x(t)/p}(t) = \frac{\frac{\partial x(t)}{x(t)}}{\frac{\partial p}{p}} = \frac{\frac{x(\theta_r,\theta_{i0}+\Delta\theta_i,t) - x_0(\theta_r,\theta_{i0},t)}{x_0(\theta_r,\theta_{i0},t)}}{\frac{\Delta\theta_i}{\theta_{i0}}} \tag{11}$$

where, x_0 is the rotational speed of the VSPSU when the value of the parameter θ_i is θ_{i0}, $\Delta\theta_i$ is the variation of the θ_i, and θ_r is the other parameters in the model except for the θ_i.

In order to facilitate the comparison and analysis of the parameter trajectory sensitivity, the relative trajectory sensitivity is defined, and its absolute average value is taken as the index for quantitative analysis. The specific expression is shown in Equation (12):

$$S_{AVE} = \overline{S}_{x(t)/p}(t) = \frac{1}{t_2 - t_1}\int_{t_1}^{t_2}\left|S_{x(t)/p}(t)\right|dt \tag{12}$$

where t_1, t_2 are the start and end moments of a dynamic process, respectively, which are reasonably chosen according to the response dynamic curve of the system.

3. Hopf Bifurcation Analysis

3.1. Hopf Bifurcation Theory

Power systems consist of various nonlinear parts, including synchronous generators (providing active and reactive power for the networks), load buses (representing power consumers), and distribution transmission lines. The dynamic characteristics of those systems are represented by the swing equation of synchronous generators, and derivative and algebraic equations of dynamic load (such as induction motors), thus proving the nonlinear load characteristics of the power system [31]. In actual engineering problems,

the parameters on which the dynamic system depends often undergo arbitrarily small changes (also known as perturbations). When these parameters change, the phase trajectory topology of the unstable system will undergo essential changes. This situation is called bifurcation. As the load conditions change, the system with nonlinear derivative equations undergoes a qualitative change at the bifurcation point. Hopf bifurcation and saddle node bifurcation are considered as typical bifurcations in power systems. Hopf bifurcation theory is applied in this paper to study the nonlinear bifurcation characteristics of VSPSUs.

Consider a general nonlinear system $\dot{x}$ as follows:

$$\begin{array}{l} \dot{x} = f(x, \mu), x \in R^n \\ \mu \in R^m, f : R^{n+m} \to R^n \end{array} \tag{13}$$

where x is the n dimensional state variable, and μ is the m dimensional parameter vector.

When the parameter μ passes a certain critical value μ_0, the phase trajectory topology of the system suddenly changes at $\mu = \mu_0$, and the system is called bifurcated at $\mu = \mu_0$, and μ_0 is called the bifurcation value. The totality of bifurcation values is called the bifurcation set. When the parameters change, the dynamic behavior of the nonlinear system switches between a stable equilibrium point and a stable limit cycle. This dynamic evolution process is called Hopf bifurcation.

Assume that $x = x_0$ is the equilibrium point of the system: that is, $f(x_0, \mu) = 0$ is satisfied. Suppose the Jacobian matrix of the system at the equilibrium point x_0 is $J(\mu) = DF_x(x_0, \mu)$. Expand the characteristic equation $\det(sI - J(\mu)) = 0$ of the Jacobian matrix and arrange them in descending powers to obtain Equation (14):

$$s^n + c_1(\mu)s^{n-1} + \ldots + c_{n-1}(\mu)s + c_n(\mu) = 0 \tag{14}$$

where $c_i(\mu)(i = 1, 2, \cdots, n)$ is the coefficient of the characteristic equation, and for a certain bifurcation parameter value $\mu = \mu_c$, if the following conditions are met, the n-dimensional nonlinear dynamic system has Hopf bifurcation:

1. $c_i(\mu_c) > 0 (i = 1, 2, \cdots, n)$;
2. $\Delta_j(\mu_c) > 0 (j = 2, \cdots, n-2)$, $\Delta_{n-1}(\mu_c) = 0$;
   Among them, $\Delta_k = \begin{vmatrix} c_1 & 1 & 0 & \cdots & 0 \\ c_3 & c_2 & c_1 & \cdots & 0 \\ c_5 & c_4 & c_3 & \cdots & 0 \\ \vdots & \vdots & \vdots & \ddots & \vdots \\ c_{2k-1} & c_{2k-2} & c_{2k-3} & \cdots & c_k \end{vmatrix} (k = 1, 2, \cdots, n)$. If $i > n$, then there is $c_i = 0$. At this moment, the characteristic equation has a pair of pure imaginary roots at $\mu = \mu_c$;
3. The transversal coefficient $\sigma'(\mu_c)$ satisfies $\sigma'(\mu_c) = \mathrm{Re}\left(\frac{dS}{d\mu}\Big|_{\mu=\mu_c} \right) \neq 0$. Then the system will have Hopf bifurcation at $\mu = \mu_c$, and the period of periodic motion at this time is $T = \frac{2\pi}{\omega}$.

In addition, the transversal coefficient $\sigma'(\mu_c)$ can also be used to distinguish the type of bifurcation. When $\sigma'(\mu_c) > 0$, the Hopf bifurcation that occurs is supercritical, and at $\mu < \mu_c$, the equilibrium point of the system is the stable focus, and for a sufficiently small μ which satisfies $\mu > \mu_c$, the system will bifurcate from the equilibrium position and perform periodic motion. In the phase trajectory, it will produce a stable limit cycle, and then the system will enter a continuous oscillation. When $\sigma'(\mu_c) < 0$, the Hopf bifurcation that occurs is subcritical. At this time, the system shows stable limit cycles and stable focal motion characteristics at the left and right sides of μ_c respectively.

3.2. Hopf Bifurcation Analysis of VSPSU

For the fifth-order VSPSU nonlinear model established in this paper, firstly, the equilibrium point of the nonlinear dynamic system can be described as $X_B = (q_B, x_B, y_B, u_B, i_{drB})$,

and it can be calculated based on the nonlinear state equation $f(X_B, \mu) = 0$. The result is shown in Equation (15).

$$\begin{cases} q_B = \frac{H_0}{2h_{t0}} \left[\begin{array}{c} -\left(\frac{2h_{t0}}{H_0} + \frac{1}{e_{qh}} - \frac{e_{qy}}{e_{qh}} \frac{e_h w_s q_B}{e_h w_s e_{qy} - e_{qh} e_y w_s}\right) \\ \pm\sqrt{\left(\frac{2h_{t0}}{H_0} + \frac{1}{e_{qh}} - \frac{e_{qy}}{e_{qh}} \frac{e_h w_s q_B}{e_h w_s e_{qy} - e_{qh} e_y w_s}\right)^2 + 4\frac{h_{t0}}{H_0} \frac{e_{qy} P_{ref}}{e_h w_s e_{qy} - e_{qh} e_y w_s}} \end{array} \right] \\ x_B = 0 \\ y_B = \frac{e_{qh} P_{ref} + e_h w_s q_B}{e_h w_s e_{qy} - e_{qh} e_y w_s} \\ u_B = y_B \\ i_{drB} = \frac{2L_s}{3u_s L_m} P_{ref} \end{cases} \tag{15}$$

Secondly, the Jacobian matrix of the nonlinear dynamic system is formulated at the equilibrium point to determine the existence of Hopf bifurcation. The Jacobian matrix of the system at its equilibrium point X_B is shown in Equation (16). The detailed partial derivatives in the Jacobi matrix are given in Appendix A.

$$J(\mu) = Df_x(x_B, \mu) = \begin{bmatrix} \frac{\partial \dot{q}}{\partial q} & \frac{\partial \dot{q}}{\partial x} & \frac{\partial \dot{q}}{\partial y} & \frac{\partial \dot{q}}{\partial u} & \frac{\partial \dot{q}}{\partial i_{dr}} \\ \frac{\partial \dot{x}}{\partial q} & \frac{\partial \dot{x}}{\partial x} & \frac{\partial \dot{x}}{\partial y} & \frac{\partial \dot{x}}{\partial u} & \frac{\partial \dot{x}}{\partial i_{dr}} \\ \frac{\partial \dot{y}}{\partial q} & \frac{\partial \dot{y}}{\partial x} & \frac{\partial \dot{y}}{\partial y} & \frac{\partial \dot{y}}{\partial u} & \frac{\partial \dot{y}}{\partial i_{dr}} \\ \frac{\partial \dot{u}}{\partial q} & \frac{\partial \dot{u}}{\partial x} & \frac{\partial \dot{u}}{\partial y} & \frac{\partial \dot{u}}{\partial u} & \frac{\partial \dot{u}}{\partial i_{dr}} \\ \frac{\partial \dot{i}_{dr}}{\partial q} & \frac{\partial \dot{i}_{dr}}{\partial x} & \frac{\partial \dot{i}_{dr}}{\partial y} & \frac{\partial \dot{i}_{dr}}{\partial u} & \frac{\partial \dot{i}_{dr}}{\partial i_{dr}} \end{bmatrix} \tag{16}$$

According to the Hopf bifurcation theory introduced earlier, the characteristic equation of $J(\mu)$ can be formulated from $\det(sI - J(\mu)) = 0$ and the result is shown in Equation (17):

$$s^5 + c_1 s^4 + c_2 s^3 + c_3 s^2 + c_4 s + c_5 = 0 \tag{17}$$

where s is the eigenvalue of $\det(sI - J(\mu)) = 0$, and the expressions of c_i (i = 1, 2, . . . , 5) are presented in Appendix B.

Then the existence of Hopf bifurcation can be verified according to the following criterion:

1. $c_i(\mu_c) > 0 (i = 1, 2, \cdots, 5)$
2. $$\Delta_2 = \begin{vmatrix} c_1 & 1 \\ c_3 & c_2 \end{vmatrix} > 0$$
$$\Delta_3 = \begin{vmatrix} c_1 & 1 & 0 \\ c_3 & c_2 & c_1 \\ c_5 & c_4 & c_3 \end{vmatrix} > 0$$
$$\Delta_4 = \begin{vmatrix} c_1 & 1 & 0 & 0 \\ c_3 & c_2 & c_1 & 1 \\ c_5 & c_4 & c_3 & c_2 \\ 0 & 0 & c_5 & c_4 \end{vmatrix} = 0$$

For the VSPSU nonlinear system in this paper, the bifurcation point where the Hopf bifurcation occurs is the edge point between the stability and the instability of the system. In the coordinate plane composed of several parameters (K_p, K_i), we consider the set of bifurcation points in different states will form a curve in the coordinate plane. The bifurcation line can divide the stable region and unstable region of the system. Therefore, the position of the bifurcation line can largely reflect the dynamic characteristics of the system. Assuming that the system is affected by perturbation (the aforementioned perturbation), in

the stable region, the dynamic response of the system will converge to a new steady state; on the bifurcation line, the response of the system will oscillate with the same amplitude; and in the unstable region, the response of the system will diverge, and a new steady state cannot be obtained. According to those principles, the bifurcation line of the system can be drawn.

Select K_i as the bifurcation parameter of the system, and the corresponding bifurcation point can be expressed as $\mu_c = K_i^*$; select the proportional-integral parameter plane, and K_p, K_i are the abscissa and ordinate, respectively, to determine the bifurcation line of the system. The disturbance is set to a 10% step drop of the rated value of the active power at the time $t = 0$ s; that is, $P_{ref} = -0.1$. The rest of the parameters involved in the system are shown in Table 1. Use the inequality in the aforementioned criterion to determine the feasible range of the parameter, and the equation to obtain the relationship between the parameters. The determined bifurcation line of the system is shown in Figure 2.

Table 1. Model parameters of the VSPSU.

Parameters	Values	Parameters	Values	Parameters	Values
e_x	-1	e_g	0	w_s	1
e_y	1	T_w	1.9927	L_m	2.9
e_h	1.5	h_{t0}	4	L_s	3.08
e_{qx}	0	H_0	115	T_y	0.2
e_{qy}	1	T_a	12.66	K_{p2}	1
e_{qh}	0.5	u_s	1	K_{i2}	3

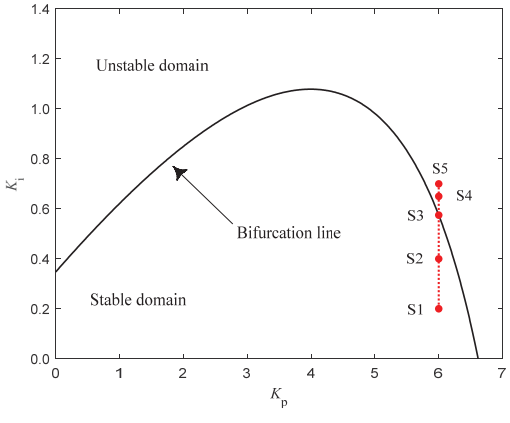

Figure 2. Stable domain of the VSPSU.

At the same time, applying the aforementioned definition of transversal coefficient to the system described in this paper, the available system's transversal coefficient expression is shown in Equation (18):

$$\sigma\prime(\mu_c) = \mathrm{Re}\left(\frac{c_1' s^4 + c_2' s^3 + c_2' s^2 + c_4' s + c_5'}{5s^4 + 4c_1 s^3 + 3c_2 s^2 + 2c_3 s + c_4}\right)\Bigg|_{\mu = K_i^*} \tag{18}$$

where $c_i' = \frac{dc_i}{d\mu}, (i = 1, \cdots, 5)$, and the pure virtual characteristic root at $\mu = \mu_c$ is $s_{1,2} = \pm i\sqrt{\frac{c_5 - c_1 c_4}{c_3 - c_1 c_2}}$, and the values of the transversal coefficient corresponding to all bifurcation points are shown in Figure 3.

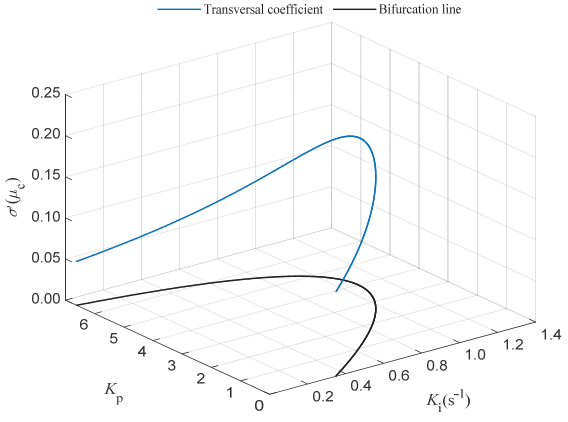

Figure 3. Transversal coefficient of the VSPSU.

It can be clearly found that all the transversal coefficients are bigger than 0, which means that the bifurcation in the fifth-order VSPSU nonlinear system is supercritical. That is, the area enclosed by the coordinate axis under the bifurcation line is the stable region of the system.

3.3. Numerical Stability Simulation

In order to verify the accuracy of the stable region drawn above, 5 points S1–S5 are selected in Figure 2 for the numerical simulation of the dynamic response, and the values of K_p, K_i of the selected five points are shown in Table 2.

Table 2. Control parameters for points S1–S5.

Parameters	**Points**				
	S1	**S2**	**S3**	**S4**	**S5**
K_p	6	6	6	6	6
K_i	0.2000	0.4000	0.5748	0.6500	0.7000
Location area	Stable domain	Stable domain	Bifurcation line	Unstable domain	Unstable domain

Using the ode45 solving function in MATLAB software to solve the nonlinear derivative equations for numerical simulation, we can calculate the dynamic response process of the characteristic state variables q, x, y corresponding to the five different points in Table 2 under the active power disturbance, and the phase trajectory of the dynamic response of these variables as well. The results are shown in Figure 4.

From the results in Figure 4, we can conclude that the dynamic responses and phase trajectories of the selected four state point variables are consistent with the results obtained from the Hopf bifurcation theory analysis. S1 and S2 are located in the stable domain of the coordinate plane formed by the parameters. After the system is disturbed by the change of active power, the dynamic response of characteristic variables (i.e., flow, frequency, opening) needs to go through several cycles of response attenuation and oscillation before reaching the final equilibrium state. Correspondingly, the three-dimensional phase composed of characteristic variables will have several trajectories before reaching the equilibrium point; S3 is located on the bifurcation line of the coordinate plane formed by the parameters, the dynamic response of the characteristic variables will enter a continuous oscillation state with constant amplitude, and the corresponding phase trajectory is a stable limit cycle. For S4 and S5, which are located in the unstable domain, the characteristic variables will first go through several cycles of divergent response state before entering a stable constant

amplitude oscillation, and the phase space trajectory is divergent first and then enters a stable limit cycle.

Comparing S1 and S2, the smaller the value of K_i and the larger the distance ($\left|K_i - K_i^*\right|$) from the bifurcation line, the shorter the time for the system to return to the equilibrium state after the disturbance. This means that the further the points in the stability domain are from the bifurcation line, the better the stability of the system. Similarly, comparing S4 and S5, the larger the value of K_i and the greater the distance ($\left|K_i - K_i^*\right|$) from the bifurcation line, the shorter the time from divergence to the equal amplitude oscillation, and the larger the amplitude of the oscillation in the constant amplitude oscillation. In other words, the system becomes less stable when the points in the unstable domain are far from the bifurcation line. It can be seen that the improper selection of the control parameters of the system will cause the CSPSU to enter a state of constant amplitude oscillation. In order to protect the safe and stable operation of the system, it is necessary to guide the selection of the PI controller parameters according to the reference stability domain.

At the same time, by substituting the pure imaginary characteristic root of the system into the calculation formula of the oscillation period and then taking the reciprocal, the oscillation frequency of the point on the bifurcation line can be obtained. The specific formula is shown in Equation (19).

$$f_{LC} = \frac{1}{T_{LC}} = \frac{\sqrt{\frac{c_5 - c_1 c_4}{c_3 - c_1 c_2}}}{2\pi} \tag{19}$$

Calculate the oscillation frequency corresponding to all the bifurcation points, and carry out the dynamic response simulation at the same time to obtain the amplitude value of the state variable x in the system during constant amplitude oscillation. The result is shown in Figure 5. The three equal-amplitude oscillation points P1, P2, P3 are selected to verify the results in Figure 5, and the control parameters are shown in Table 3, while the simulated curves are obtained as shown in Figure 6.

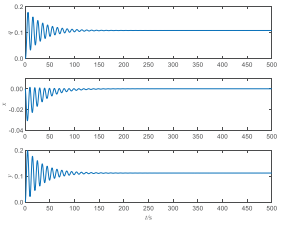

(**a**) Time response for S1

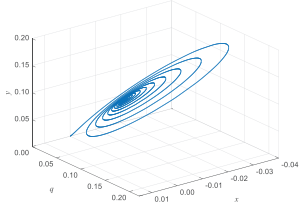

(**b**) Phase trajectory for S1

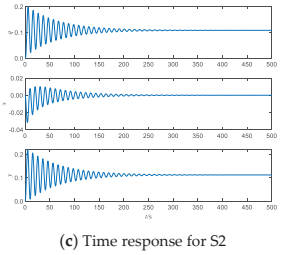

(**c**) Time response for S2

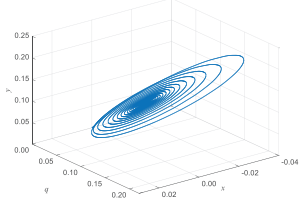

(**d**) Phase trajectory for S2

Figure 4. *Cont.*

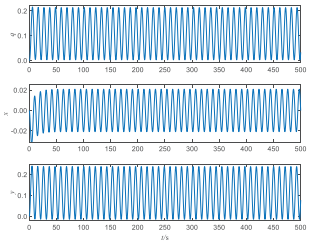

(**e**) Time response for S3

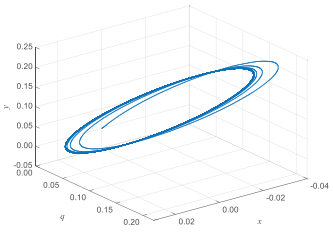

(**f**) Phase trajectory for S3

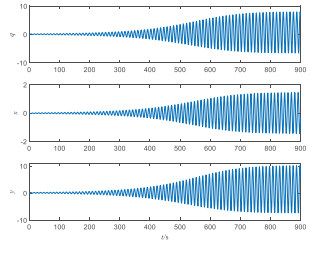

(**g**) Time response for S4

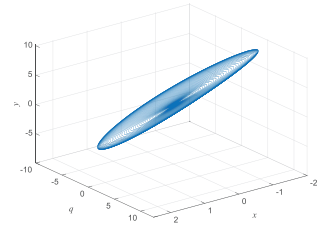

(**h**) Phase trajectory for S4

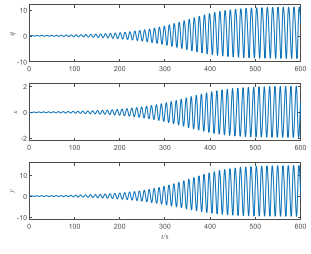

(**i**) Time response for S5

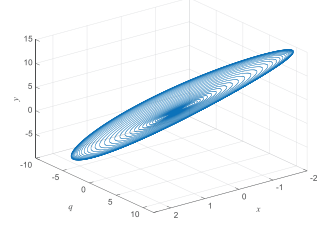

(**j**) Phase trajectory for S5

Figure 4. Dynamic response and phase trajectory of state variables at points S1–S5.

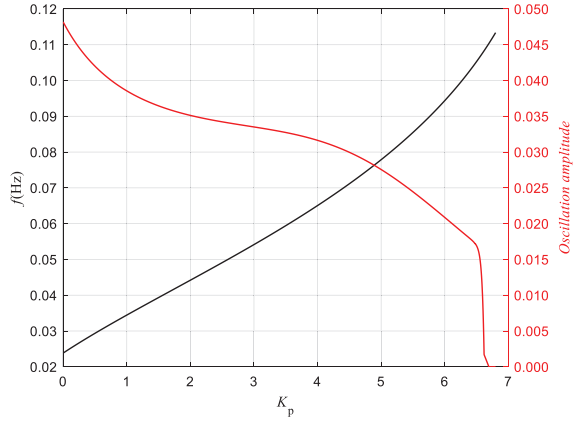

Figure 5. Oscillation frequency and amplitude of equal-amplitude oscillations at points on the bifurcation line.

Table 3. Control parameters for points P1–P3.

Parameters	Points		
	P1	**P2**	**P3**
K_p	2	4	6
K_i	0.8499	1.0789	0.5748

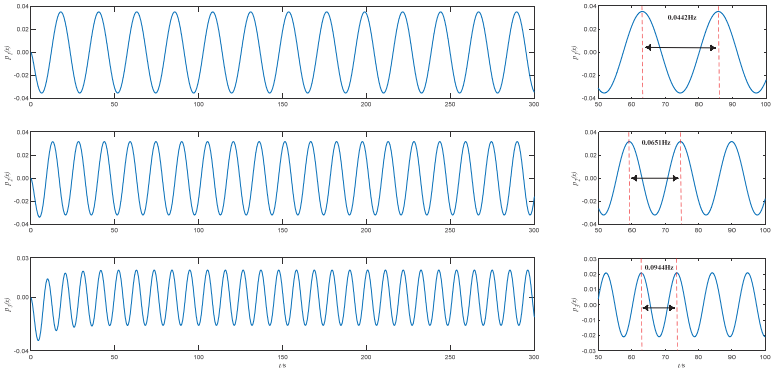

Figure 6. Dynamic response of x at points P1–P3.

From Figure 5, it can be clearly seen that with the change of K_p from small to large, the oscillation frequency presents a monotonically increasing trend, becoming larger in a nearly linear manner. The amplitude of the oscillation changes in a more tortuous manner, while the overall trend is downward. There is a sharp drop in amplitude near the intersection of the bifurcation line with the horizontal axis. On the whole, the amplitude and frequency of the system's constant-amplitude oscillation have roughly the opposite trend; that is, the greater the frequency, the smaller the amplitude, and vice versa. This may indicate from the side that the energy of the system is generally conserved. The results shown in Figure 6 are the dynamic response of state variable x at points P1–P3. These response curves and the frequency marked on the right side of the figure verify the previous frequency-amplitude diagram.

4. Parameter Sensitivity Analysis

4.1. The Effect of Active Power Step on the Stability Domain

The aforementioned stable region is drawn when the active power has a step drop of 10% of the rated value. In actual engineering, the magnitude and direction of the disturbances are unpredictable. For this reason, the influence of different disturbances on the system stable region is studied. We selected a total of six active power disturbances with different directions and magnitudes, and drew the stable region according to the same method as described above, and the results are shown in Figure 7.

It can be seen from Figure 7 that as the active power disturbance changes from -0.3 to 0.3, the intersection points between the stable domain and the horizontal axis (i.e., K_p) gradually shifts to the left, and the intersection point with the vertical axis (i.e., K_i) gradually moves downward. The area of the stable region also gradually decreases, and the specific values are shown in Table 4. This means that the adjustable range of the PI controller parameters is also reduced for the stable operation of the system. This may be manifested in actual engineering operation: when the VSPSU is operating with 70% rated load under power generation conditions, the pressure to ensure its stable operation is lower than when operating with a rated load.

Table 4. Stable domain area under different active power perturbations.

Case	$P_{ref} = -0.3$	$P_{ref} = -0.2$	$P_{ref} = -0.1$	$P_{ref} = 0.1$	$P_{ref} = 0.2$	$P_{ref} = 0.3$
Area	18.7364	18.4972	18.2579	17.7849	17.5499	17.3150

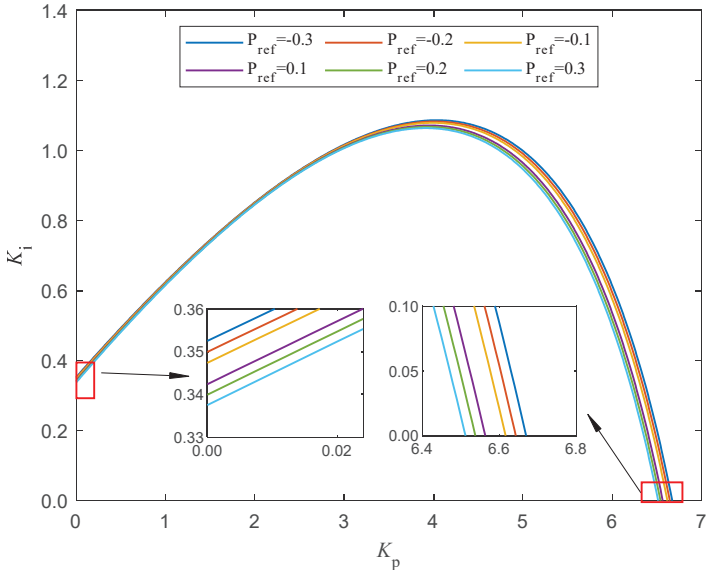

Figure 7. Stable domain of the VSPSU under different active power disturbances.

4.2. Sensitivity Analysis of Key System Parameters

4.2.1. System Parameter Trajectory Sensitivity Analysis Process

To facilitate the calculation of the above indicators, the simulation conditions are designed to subject the VSPSU to an active power disturbance, setting the active power to 10% of its rated value with a pulse width of 0.1 s. Under this disturbance, the system state will fluctuate for a short time from the initial equilibrium point and return to the original equilibrium point again under the regulation of the controller. The reason why the form of perturbation is not chosen from the aforementioned step perturbation used to calculate the stability domain is, on the one hand, to facilitate the calculation of the sensitivity index; on the other hand, the equilibrium point of the system will change after the step perturbation, which means that the parameter sensitivity will be affected by both the dynamic characteristics and the steady-state characteristics, while the study in the section is actually concerned with the effect of the parameter change on the dynamic characteristics of the system. According to the formula of trajectory sensitivity, it is only necessary to calculate the area of the dynamically changing part of the system variables. The sensitivity of the system state variables to the parameters can be obtained by comparing the difference between the areas before and after the parameter variation. The flow chart of parameter sensitivity analysis is shown in Figure 8.

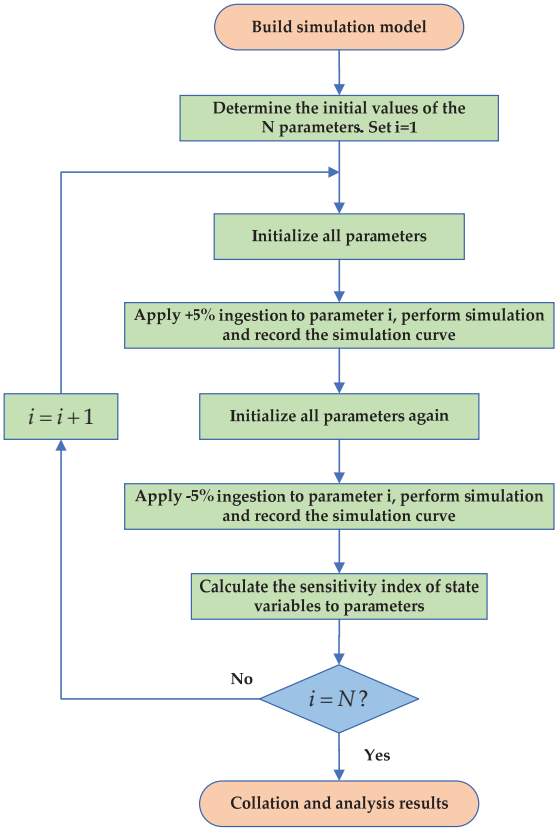

Figure 8. Parameter sensitivity calculation and analysis process.

4.2.2. System Parameter Trajectory Sensitivity Results

The parameters of the system that will vary within a reasonable range during the dynamic transients of the system are e_x, e_y, e_h, e_{qx}, e_{qy}, e_{qh}, T_w, T_a, T_y, K_p, K_i, and the system variables to be analyzed are the five state variables that are selected when the model is built.

According to Figure 7, a $\pm$ 5% perturbation is applied to each parameter on the basis of its initial value, and the simulation test of active power pulse disturbance is performed. The total duration of the simulation is 200 s, in which the disturbance occurs at $t = 1$ s. Due to the large number of parameters, only the parameter with the greatest influence on the system state (i.e., T_a) is selected to analyze the influence of the parameter perturbation on the system state variables. Taking the rotational speed of the VSPSU as an example, the simulation curve before and after the parameter ingestion is obtained, which is shown in Figure 9a, and the corresponding trajectory sensitivity calculation results are shown in Figure 9b (only the trajectory sensitivity of the first 100 s is selected to optimize the display effect).

From Figure 9a, it can be seen that the positive perturbation of the T_a slows down the decrease rate of the speed to a small extent and reduces the minimum and maximum during the dynamic process of the speed; i.e., at the same time when the speed decreases, its value subject to the positive perturbation of T_a is larger than that subject to the negative regression of T_a, and vice versa. As can be seen from Figure 9b, the sensitivity of different state variables to the T_a varies, and the sensitivity of variables q, y, u to parameter T_a is

significantly greater than that of variable x, and the sensitivity of y, u to T_a is basically the same, which can also be clearly seen from the derivative equations of the VSPSU. The sensitivity indexes of the complete system state variables to each parameter are listed in Table 5, and the depth of the color bars in the cells can visually reflect the size of the sensitivity indexes.

Table 5. Sensitivity index of different parameters of the system to state variables.

Parameters	State Variables				
	q	x	u	y	i_{dr}
e_x	6.185×10^{-4}	2.972×10^{-4}	6.447×10^{-4}	6.449×10^{-4}	1.638×10^{-2}
e_y	1.199×10^{-3}	6.453×10^{-4}	1.240×10^{-3}	1.240×10^{-3}	1.580×10^{-2}
e_h	5.124×10^{-4}	2.833×10^{-4}	5.488×10^{-4}	5.495×10^{-4}	1.645×10^{-2}
e_{qx}	9.328×10^{-4}	1.538×10^{-4}	2.831×10^{-4}	2.836×10^{-4}	1.639×10^{-2}
e_{qy}	1.330×10^{-3}	2.833×10^{-4}	5.488×10^{-4}	5.495×10^{-4}	1.645×10^{-2}
e_{qh}	4.098×10^{-4}	9.612×10^{-5}	1.883×10^{-4}	1.890×10^{-4}	1.638×10^{-2}
T_W	5.949×10^{-4}	2.842×10^{-4}	5.489×10^{-4}	5.496×10^{-4}	1.639×10^{-2}
T_a	1.294×10^{-3}	7.342×10^{-4}	1.395×10^{-3}	1.398×10^{-3}	1.644×10^{-2}
T_y	9.412×10^{-5}	2.612×10^{-5}	1.096×10^{-4}	5.043×10^{-5}	1.641×10^{-2}
k_p	1.307×10^{-3}	5.905×10^{-4}	1.404×10^{-3}	1.407×10^{-3}	1.633×10^{-2}
k_i	4.644×10^{-4}	3.334×10^{-4}	4.826×10^{-4}	4.827×10^{-4}	1.639×10^{-2}

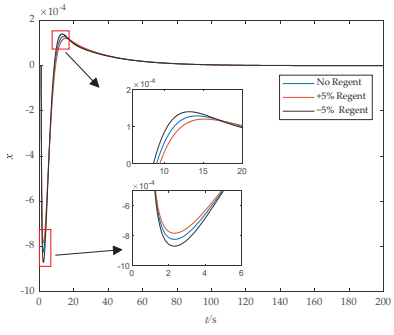

(**a**) Dynamic response comparison of x

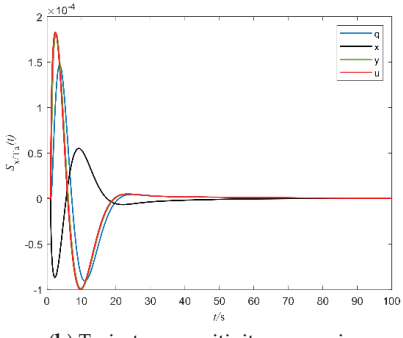

(**b**) Trajectory sensitivity comparison

Figure 9. Comparison of simulation curve and trajectory sensitivity before and after parameter T_a ingestion.

It can be seen from Table 5 that the sensitivity of each state variable to the e_y, T_a, K_p is much higher than that of the other parameters; i.e., e_y, T_a, K_p are the high sensitivity parameters, and the corresponding low sensitivity parameters are T_y, e_{qh}. In addition to the aforementioned highly sensitive parameters, the state variable q is also highly sensitive to the changes of the e_{qy}, and the sensitivity of u, y is almost the same for different parameters. Moreover, the sensitivity of the state variable i_{dr} is almost the same for different parameters.

5. Conclusions

As a long-term energy storage system, it is a very meaningful topic to study the stability and dynamic characteristics of the VSPSU at a time when the share of variable renewable energy access is continuously increasing.

The focus of this study was on the nonlinear bifurcation characteristics and parameter sensitivity of the VSPSU. Considering the nonlinear characteristics of head loss, a fifth-order nonlinear mathematical model of the VSPSU was developed. The numerical simulation verified the Hopf bifurcation theory derivation. When the system was subjected to active power step disturbance, the bifurcation in the system was supercritical. Considering the points located on the bifurcation line, the system perturbation response showed the

characteristics of equal-amplitude oscillation, and when the PI controller proportional gain varied from small to large, the oscillation frequency was between 0.02 and 0.12, and showed a monotonic increasing trend. The amplitude of oscillation was opposite to the trend of frequency. As the active power step disturbance changed from −0.3 to 0.3, the area of the stability domain gradually decreased from 18.7364 to 17.3150.

Parameter sensitivity analysis of the established model yielded the correlation between the system full-state variables and subsystem parameter variations. The system state variables were more sensitive to changes in the transfer coefficient of turbine torque to guide vane opening, the unit inertia time constant, and the controller proportional gain, while they were less sensitive to changes in the receiver response time constant and the turbine flow-to-head transfer coefficient.

The stability domain can be used to guide the selection of unit control parameters for operation of the VSPSU, and the variation of the stability domain area with disturbance can provide a basis for rational load planning during the actual operation of the VSPSU, thus helping to exploit its ability to solve the intermittent problems of renewable energy sources.

Author Contributions: Conceptualization, Z.Z.; methodology, Z.Z.; software, X.L.; validation, Z.Z.; formal analysis, Z.Z.; investigation, Z.Z.; resources, X.T.; data curation, X.L.; project administration, X.T.; writing—original draft preparation, Z.Z.; writing—review and editing, D.L.; visualization, X.T.; supervision, C.L.; funding acquisition, C.L. All authors have read and agreed to the published version of the manuscript.

Funding: This research was funded by the National Natural Science Foundation of China (Grant No. 51879111), the Fundamental Research Funds for the Central Universities, HUST (Grant No. 2021JYCXJJ043), the China Postdoctoral Science Foundation (Grant No. 2020M682416), the Applied Fundamental Frontier Project of Wuhan Science and Technology Bureau (Grant No. 2018010401011269), and the Hubei Provincial Natural Science Foundation of China (Grant No. 2019CFA068).

Conflicts of Interest: The authors declare no conflict of interest.

Appendix A

$$J(\mu) = Df_x(x_{\mathrm{B}}, \mu) = \begin{bmatrix} J_{11} & J_{12} & J_{13} & J_{14} & J_{15} \\ J_{21} & J_{22} & J_{23} & J_{24} & J_{25} \\ J_{31} & J_{32} & J_{33} & J_{34} & J_{35} \\ J_{41} & J_{42} & J_{43} & J_{44} & J_{45} \\ J_{51} & J_{52} & J_{53} & J_{54} & J_{55} \end{bmatrix} = \begin{bmatrix} \frac{\partial \dot{q}}{\partial q} & \frac{\partial \dot{q}}{\partial x} & \frac{\partial \dot{q}}{\partial y} & \frac{\partial \dot{q}}{\partial u} & \frac{\partial \dot{q}}{\partial i_{dr}} \\ \frac{\partial \dot{x}}{\partial q} & \frac{\partial \dot{x}}{\partial x} & \frac{\partial \dot{x}}{\partial y} & \frac{\partial \dot{x}}{\partial u} & \frac{\partial \dot{x}}{\partial i_{dr}} \\ \frac{\partial \dot{y}}{\partial q} & \frac{\partial \dot{y}}{\partial x} & \frac{\partial \dot{y}}{\partial y} & \frac{\partial \dot{y}}{\partial u} & \frac{\partial \dot{y}}{\partial i_{dr}} \\ \frac{\partial \dot{u}}{\partial q} & \frac{\partial \dot{u}}{\partial x} & \frac{\partial \dot{u}}{\partial y} & \frac{\partial \dot{u}}{\partial u} & \frac{\partial \dot{u}}{\partial i_{dr}} \\ \frac{\partial \dot{i}_{dr}}{\partial q} & \frac{\partial \dot{i}_{dr}}{\partial x} & \frac{\partial \dot{i}_{dr}}{\partial y} & \frac{\partial \dot{i}_{dr}}{\partial u} & \frac{\partial \dot{i}_{dr}}{\partial i_{dr}} \end{bmatrix}$$

$$\frac{\partial \dot{q}}{\partial q} = -\frac{1}{T_{\mathrm{w}}}\left(\frac{2h_{t0}}{H_0} + \frac{1}{e_{qh}} + \frac{2h_{t0}}{H_0}q\right),\ \frac{\partial \dot{q}}{\partial x} = \frac{e_{qx}}{T_{\mathrm{w}}e_{qh}},\ \frac{\partial \dot{q}}{\partial y} = \frac{e_{qy}}{T_{\mathrm{w}}e_{qh}},\ \frac{\partial \dot{q}}{\partial u} = 0,\ \frac{\partial \dot{q}}{\partial i_{dr}} = 0,$$

$$\frac{\partial \dot{x}}{\partial q} = \frac{e_h}{T_a e_{qh}},\ \frac{\partial \dot{x}}{\partial x} = \frac{1}{T_a}\left(e_x - \frac{e_h}{e_{qh}}e_{qx} - e_{\mathrm{g}}\right),\ \frac{\partial \dot{x}}{\partial y} = \frac{1}{T_{\mathrm{a}}}\left(e_y - \frac{e_h}{e_{qh}}e_{qy}\right),\ \frac{\partial \dot{x}}{\partial u} = 0,\ \frac{\partial \dot{x}}{\partial i_{dr}} = \frac{3u_s L_m}{2L_s w_s T_a}$$

$$\frac{\partial \dot{y}}{\partial q} = 0,\ \frac{\partial \dot{y}}{\partial x} = 0,\ \frac{\partial \dot{y}}{\partial y} = -\frac{1}{T_y},\ \frac{\partial \dot{y}}{\partial u} = \frac{1}{T_y},\ \frac{\partial \dot{y}}{\partial i_{dr}} = 0,\ \frac{\partial u}{\partial q} = -\frac{K_P e_h}{T_a e_{qh}},$$

$$\frac{\partial \dot{u}}{\partial x} = -\frac{K_p}{T_a}(e_x - \frac{e_h}{e_{qh}}e_{qx} - e_{\mathrm{g}}) - K_{\mathrm{i}},\ \frac{\partial \dot{u}}{\partial y} = -\frac{K_{\mathrm{P}}}{T_{\mathrm{a}}}(e_y - \frac{e_h}{e_{qh}}e_{qy}),\ \frac{\partial \dot{u}}{\partial u} = 0,\ \frac{\partial \dot{u}}{\partial i_{dr}} = -\frac{3u_s L_m K_{\mathrm{P}}}{2L_s w_s T_{\mathrm{a}}},$$

$$\frac{\partial \dot{i}_{dr}}{\partial q} = 0,\ \frac{\partial \dot{i}_{dr}}{\partial x} = 0,\ \frac{\partial \dot{i}_{dr}}{\partial y} = 0,\ \frac{\partial \dot{i}_{dr}}{\partial u} = 0,\ \frac{\partial \dot{i}_{dr}}{\partial i_{dr}} = -\frac{3K_{i2}u_s L_m}{2L_s + 3K_{p2}u_s L_m}.$$

Appendix B

$$c_1 = -(J_{11} + J_{22} + J_{33} + J_{55})$$
$$c_2 = J_{11}(J_{22} + J_{33} + J_{55}) + J_{22}(J_{33} + J_{55}) + J_{33}J_{55} - J_{12}J_{21} - J_{34}J_{43}$$
$$c_3 = J_{11}J_{34}J_{43} + J_{12}(J_{21}J_{33} + J_{21}J_{55}) + J_{22}J_{34}J_{43} + J_{34}J_{43}J_{55}$$
$$-J_{11}(J_{22}J_{33} + J_{22}J_{55} + J_{33}J_{55}) - J_{13}J_{34}J_{41} - J_{22}J_{33}J_{55} - J_{23}J_{34}J_{42}$$
$$c_4 = J_{11}(J_{22}J_{33}J_{55} + J_{23}J_{34}J_{42}) + J_{12}J_{21}J_{34}J_{43} + J_{13}(J_{22}J_{34}J_{41} + J_{34}J_{41}J_{55}) + J_{23}J_{34}J_{42}J_{55}$$
$$-J_{11}(J_{22}J_{34}J_{43} + J_{34}J_{43}J_{55}) - J_{12}(J_{21}J_{33}J_{55} + J_{23}J_{34}J_{41}) - J_{13}J_{21}J_{34}J_{42} - J_{22}J_{34}J_{43}J_{55}$$
$$c_5 = J_{11}J_{22}J_{34}J_{43}J_{55} + J_{12}J_{23}J_{34}J_{41}J_{55} + J_{13}J_{21}J_{34}J_{42}J_{55} - J_{11}J_{23}J_{34}J_{42}J_{55} - J_{12}J_{21}J_{34}J_{43}J_{55} - J_{13}J_{22}J_{23}J_{41}J_{55}$$

References

1. *Renewables 2021 Global Status Report*; REN21: Paris, France, 2021. Available online: https://www.ren21.net/wp-content/uploads/2019/05/GSR2021_Full_Report.pdf (accessed on 15 June 2021).
2. Sepulveda, N.A.; Jenkins, J.D.; de Sisternes, F.J.; Lester, R.K. The role of firm low-carbon electricity resources in deep decarbonization of power generation. *Joule* **2018**, *2*, 2403–2420. [CrossRef]
3. Brown, T.; Schlachtberger, D.; Kies, A.; Schramm, S.; Greiner, M. Synergies of sector coupling and transmission reinforcement in a cost-optimised, highly renewable European energy system. *Energy* **2018**, *160*, 720–739. [CrossRef]
4. Krey, V.; Luderer, G.; Clarke, L.; Kriegler, E. Getting from here to there–energy technology transformation pathways in the EMF27 scenarios. *Clim. Change* **2014**, *123*, 369–382. [CrossRef]
5. Dimanchev, E.G.; Hodge, J.L.; Parsons, J.E. The role of hydropower reservoirs in deep decarbonization policy. *Energy Policy* **2021**, *155*, 112369. [CrossRef]
6. Valavi, M.; Nysveen, A. Variable-speed operation of hydropower plants: Past, present, and future. In Proceedings of the 2016 XXII International Conference on Electrical Machines (ICEM), Lausanne, Switzerland, 1–4 September 2016.
7. Feng, C.; Zheng, Y.; Li, C.; Mai, Z.; Chen, H. Cost advantage of adjustable-speed pumped storage unit for daily operation in distributed hybrid system. *Renew. Energy* **2021**, *176*, 1–10. [CrossRef]
8. Guo, W.; Zhu, D. Nonlinear modeling and operation stability of variable speed pumped storage power station. *Energy Sci. Eng.* **2021**, *9*, 1703–1718. [CrossRef]
9. Zhou, J.X.; Jiang, J.G.; Wei, W.U. A Study on the Control System for the Adjustable-speed Pump Storage Group. *Electr. Autom.* **2015**, *37*, 1–3.
10. Silva, B.; Moreira, C. Contribution of variable-speed pump hydro storage for power system dynamic performance. *J. Phys. Conf. Ser.* **2017**, *813*, 012012. [CrossRef]
11. Xiong, W.; Zheng, J.; Jinshui, W.U. General situation and technical analysis of Okinawa seawater pumped-storage power station. *Hydropower Pumped Storage* **2018**, *4*, 56–66.
12. Gao, C.; Yu, X.; Nan, H.; Men, C.; Fu, J. A Fast High-Precision Model of the Doubly-Fed Pumped Storage Unit. *J. Electr. Eng. Technol.* **2021**, *16*, 797–808. [CrossRef]
13. Mohanpurkar, M.; Ouroua, A.; Hovsapian, R.; Luo, Y.; Singh, M.; Muijadi, E.; Gevorgian, V.; Donalek, P. Real-time co-simulation of adjustable-speed pumped storage hydro for transient stability analysis. *Electr. Power Syst. Res.* **2018**, *154*, 276–286. [CrossRef]
14. Guopeng, Z.; Qiang, Z.; Jiyun, R.; Xiaofang, S.; Minxiao, H. Modeling and Control of Doubly-Fed Variable-Speed Pumped Storage Units for Grid Power Regulation. *J. Eng.* **2017**, *1*, 745–750. [CrossRef]
15. Xie, H.; Liu, L.; Li, S.; Liang, H.; Tan, Q.; Song, W.; Li, M. Modeling and Simulation of Mechanical and Electrical Transient of Variable-Speed Pumped Storage Units. In Proceedings of the IOP Conference Series: Earth and Environmental Science 2021, Changsha, China, 18–20 September 2020; Volume 634, p. 012053.
16. Zhao, G.; Ren, J. Research on an Output Power Model of a Doubly-Fed Variable-Speed Pumped Storage Unit with Switching Process. *Appl. Sci.* **2019**, *9*, 3368. [CrossRef]
17. Yang, W.; Yang, J. Advantage of variable-speed pumped storage plants for mitigating wind power variations: Integrated modelling and performance assessment. *Appl. Energy* **2019**, *237*, 720–732. [CrossRef]
18. Joseph, A.; Desingu, K.; Semwal, R.R.; Chelliah, T.R.; Khare, D. Dynamic Performance of Pumping Mode of 250 MW VariableSpeed Hydro-Generating Unit Subjected to Power and Control Circuit Faults. *IEEE Trans. Energy Convers.* **2017**, *33*, 430–441. [CrossRef]
19. Joseph, A.; Selvaraj, R.; Chelliah, T.R.; Sarma, S. Starting and Braking of a Large Variable Speed Hydro-Generating Unit Subjected to Converter and Sensor Faults. *IEEE Trans. Ind. Appl.* **2018**, *54*, 3372–3382. [CrossRef]
20. Damdoum, A.; Slama-Belkhodja, I.; Pietrzak-David, M.; Debbou, M. Low voltage ride-through strategies for doubly fed induction machine pumped storage system under grid faults. *Renew. Energy* **2016**, *95*, 248–262. [CrossRef]
21. Madeira, F.C.; Fernandes, J.F.; Pérez-Sánchez, M.; López-Jiménez, P.A.; Ramos, H.M.; Costa Branco, P. Electro-hydraulic transient regimes in isolated pumps working as turbines with self-excited induction generators. *Energies* **2020**, *13*, 4521. [CrossRef]
22. Pagaimo, M.C.; Fernandes, J.F.; Pérez-Sánchez, M.; López-Jiménez, P.A.; Ramos, H.M.; Branco, P.C. Transient study of series-connected pumps working as turbines in off-grid systems. *Energy Convers. Manag.* **2021**, *245*, 114586. [CrossRef]

23. Gao, C.; Yu, X.; Nan, H.; Men, C.; Zhao, P.; Cai, Q.; Fu, J. Stability and dynamic analysis of doubly-fed variable speed pump turbine governing system based on Hopf bifurcation theory. *Renew. Energy* **2021**, *175*, 568–579. [CrossRef]
24. Cruz, J., Jr.; Looze, D.; Perkins, W. Sensitivity analysis of nonlinear feedback systems. *J. Frankl. Inst.* **1981**, *312*, 199–215. [CrossRef]
25. Xu, B.; Yan, D.; Chen, D.; Gao, X.; Wu, C. Sensitivity analysis of a Pelton hydropower station based on a novel approach of turbine torque. *Energy Convers. Manag.* **2017**, *148*, 785–800. [CrossRef]
26. Xu, B.; Chen, D.; Patelli, E.; Shen, H.; Park, J.H. Mathematical model and parametric uncertainty analysis of a hydraulic generating system. *Renew. Energy* **2019**, *136*, 1217–1230. [CrossRef]
27. Zhao, G.; Zhang, Y.; Ren, J. Analysis of Control Characteristics and Design of Control System Based on Internal Parameters in Doubly Fed Variable-Speed Pumped Storage Unit. *Complexity* **2021**, *2021*, 1–23. [CrossRef]
28. Liu, D.; Li, C.; Malik, O. Operational characteristics and parameter sensitivity analysis of hydropower unit damping under ultra-low frequency oscillations. *Int. J. Electr. Power Energy Syst.* **2022**, *136*, 107689. [CrossRef]
29. Zhu, D.; Guo, W. Setting condition of surge tank based on stability of hydro-turbine governing system considering nonlinear penstock head loss. *Int. J. Electr. Power Energy Syst.* **2019**, *113*, 372–382. [CrossRef]
30. Wang, Y.; Lu, C.; Zhu, L.; Zhang, G.; Li, X.; Chen, Y. Comprehensive modeling and parameter identification of wind farms based on wide-area measurement systems. *J. Mod. Power Syst. Clean Energy* **2016**, *4*, 383–393. [CrossRef]
31. Jazaeri, M.; Khatibi, M. A study on Hopf bifurcations for power system stability analysis. In Proceedings of the Electric Power Conference, Vancouver, BC, Canada, 6–7 October 2008.

energies

MDPI

Article

Degradation Trend Prediction of Pumped Storage Unit Based on MIC-LGBM and VMD-GRU Combined Model

Peng Chen [1], Yumin Deng [2], Xuegui Zhang [2], Li Ma [2], Yaoliang Yan [2], Yifan Wu [1] and Chaoshun Li [1,*]

[1] School of Civil and Hydraulic Engineering, Huazhong University of Science and Technology, Wuhan 430074, China; hustpengchen@163.com (P.C.); wyfan@hust.edu.cn (Y.W.)
[2] China Yangtze Three Gorges Group Co. Ltd., Wuhan 430010, China; deng_yumin@ctg.com.cn (Y.D.); zhang_xuegui@ctg.com.cn (X.Z.); ma_li2@ctg.com.cn (L.M.); yan_yaoliang@ctg.com.cn (Y.Y.)
* Correspondence: csli@hust.edu.cn; Tel.: +86-158-7180-0142

Abstract: The harsh operating environment aggravates the degradation of pumped storage units (PSUs). Degradation trend prediction (DTP) provides important support for the condition-based maintenance of PSUs. However, the complexity of the performance degradation index (PDI) sequence poses a severe challenge of the reliability of DTP. Additionally, the accuracy of healthy model is often ignored, resulting in an unconvincing PDI. To solve these problems, a combined DTP model that integrates the maximal information coefficient (MIC), light gradient boosting machine (LGBM), variational mode decomposition (VMD) and gated recurrent unit (GRU) is proposed. Firstly, MIC-LGBM is utilized to generate a high-precision healthy model. MIC is applied to select the working parameters with the most relevance, then the LGBM is utilized to construct the healthy model. Afterwards, a performance degradation index (PDI) is generated based on the LGBM healthy model and monitoring data. Finally, the VMD-GRU prediction model is designed to achieve precise DTP under the complex PDI sequence. The proposed model is verified by applying it to a PSU located in Zhejiang province, China. The results reveal that the proposed model achieves the highest precision healthy model and the best prediction performance compared with other comparative models. The absolute average ($|AVG|$) and standard deviation (STD) of fitting errors are reduced to 0.0275 and 0.9245, and the RMSE, MAE, and R^2 are 0.00395, 0.0032, and 0.9226 respectively, on average for two operating conditions.

Keywords: pumped storage unit; degradation trend prediction; maximal information coefficient; light gradient boosting machine; variational mode decomposition; gated recurrent unit

Citation: Chen, P.; Deng, Y.; Zhang, X.; Ma, L.; Yan, Y.; Wu, Y.; Li, C. Degradation Trend Prediction of Pumped Storage Unit Based on MIC-LGBM and VMD-GRU Combined Model. *Energies* **2022**, *15*, 605. https://doi.org/10.3390/en15020605

Academic Editor: Davide Astolfi

Received: 16 December 2021
Accepted: 12 January 2022
Published: 15 January 2022

1. Introduction

Pump storage units (PSUs) store excessive power during light load periods and convert hydro energy into electricity at peak load periods [1]. According to the hydropower status report [2], the installed capacity of PSUs reached 159.5 GW in 2020, accounting for 94% of the capacity of all energy storage facilities. PSUs are playing an increasingly important role in peak–valley reduction and emergency reserves [3–5]. However, the frequent condition conversion and the complex hydro-mechanical–electric coupling aggravate the wear and degradation of PSUs. Degradation trend prediction (DTP) ensures the secure operation of PSUs by evaluating the degradation and predicting the degradation trend of PSUs. Generally, DTP includes the mechanism-analysis approaches and data-driven approaches [6]. The mechanism-analysis approaches describe the degradation process by building a mathematical model based on the failure mechanism. However, complex systems are difficult to describe precisely with mathematical models, which limits their application. With the improvement of monitoring systems, data-driven approaches are attracting increased attention [7]. The data-driven based DTP always consists of two phases: (a) building a healthy model that represents the good running conditions of PSUs and then

constructing the performance degradation index (PDI); (b) establishing a precise prediction model to forecast the future degradation trend of PSUs.

Healthy model building is the process of constructing mapping relationships between working parameters and status data. Its accuracy directly affects the reliability of PDI. In relevant literature, the artificial neural network (ANN) [8], Gaussian process regression (GPR) [9], radial basis function interpolation surface [10,11], Shepard interpolation surface [12], etc. are frequently used. These methods need plenty of computational resources and time, while their performances are always not satisfactory. Recently, the gradient boosting machines (GBMs) [13] have developed rapidly due to their low computational resources, fast training speed, and high fitting accuracy. They are widely used in regression and classification tasks, such as wind speed forecasting [14,15], fault diagnosis [16,17], and anomaly detection [18,19]. The light gradient boosting machine (LGBM) [20] is a novel GBM proposed by Ke et al. in 2017. It has similar performance while requiring far less memory and training time compared with gradient boosting decision tree (GBDT) and has achieved state-of-the-art results in numerous competitions. Considering the outstanding advantages and the potential engineering demand, LGBM would be a great choice to build a healthy model to fit the mapping relationships exactly and save expensive computational resources.

Moreover, the input and the output of the healthy model should be determined. The status data, such as swing, vibration, etc., provide a wealth of information on the operating status of PSUs [21]. It is suitable to use the status data as the output of the healthy model. The working parameters, which describe the operating mode of PSU in detail, should be used as the input of the healthy model [8]. However, some working parameters have a weak correlation with the status data and bring confusion when judging the status of PSUs. To make sure the healthy model entirely learns the characteristics of a PSU under good running conditions, it is necessary to screen the working parameters by correlation. The maximal information coefficient (MIC) [22] can explore not only linear correlation but also nonlinear and nonfunctional correlations between variables, thus achieving remarkable success in data screening. Jiang et al. [23] designed a two-step feature selection method based on MIC to screen the best feature for predicting remaining useful life of the bearing. Ji et al. [24] proposed a novel selection method of software attribute by combining MIC and automatic clustering. Due to its superior performance, MIC is adopted to screen the working parameters in this paper.

The PDI is obtained after building the healthy model, after which the degradation trend of the PSU should be predicted to support decision-making. Classical machine learning methods, such as autoregressive integrated moving average (ARIMA) [25], support vector regression (SVR) [26], ANN [27], etc., are widely used in related works. With the development of machine learning, recurrent neural networks (RNNs) [28] have obtained excellent results in prediction tasks. Park et al. [29] used long short-term memory (LSTM) to predict the remaining useful life of a battery. Xia et al. [30] combined the multilayer attention and LSTM models to predict the degradation trend of mechanical systems. Wu et al. [31] predicted the remaining useful life of a cooling system by using LSTM and gated recurrent unit (GRU), respectively, finding that GRU performs better than LSTM. Compared with LSTM, GRU [32] only has two gates and fewer parameters, while it often achieves slightly better results [33–35]. However, the degradation trend of PSU is nonperiodic, with irregular fluctuation components. Even GRU cannot learn the degradation trend of PSU well. The complexity of PDI sequences brings difficulty for high-precision prediction. One way to solve this issue is to make the PDI sequence simpler. Empirical mode decomposition (EMD) [36] is a classical decomposition method which has been widely used. However, EMD lacks a theoretical foundation and suffers from problems such as mode mixing and boundary effect. To overcome these shortcomings, variational mode decomposition (VMD) [37] has been proposed. It has a sound theoretical foundation and is suitable for dealing with nonlinear and non-stationary series [38]. It decomposes the complex series into a series of approximately orthogonal simple modes and is popular in the fields of signal denoising [39], runoff forecasting [40], wind speed forecasting [41],

etc. Thus, the complex PDI sequences are decomposed into simpler modes by VMD before being fed into GRU to improve the accuracy of prediction.

To achieve precise degradation trend prediction for a PSU, a combined DTP model of a PSU is proposed based on MIC-LGBM and VMD-GRU. Firstly, the working parameters are selected by MIC. Afterwards, the LGBM healthy model is built, and the PDI is obtained by measuring the difference between the benchmark output of the healthy model and the monitoring status data. Finally, the PDI sequence is sent into the VMD-GRU prediction model to obtain a reliable future degradation trend. The main contributions of this work are listed as follows:

(a) Considering that the relationships between the working condition parameters and the state data are not linear, MIC is utilized to screen the relevant working parameters. The interference of irrelevant working parameters is reduced, and the performance of the healthy model is improved.
(b) Inspired by the superiority of LGBM, the healthy model is constructed and not only achieves a high-precision fitting result but also consumes fewer computational resources as it has a strongly competitive training speed.
(c) To address the challenges caused by the complexity of PDI sequences, the VMD-GRU prediction model is designed for reliable prediction. The complex degradation trend is decomposed into a series of simple sequences by VMD, which can be more adequately learned by GRU. An outstanding prediction result is obtained compared with other popular prediction models.

The remainder of this paper is organized as follows. The relevant theoretical background is stated in Section 2. Then, the proposed DTP model is presented in Section 3. In Section 4, model validation, comparative experiments, and analysis are carried out. Conclusions and future work are presented in Section 5.

2. Theoretical Background

2.1. Maximal Information Coefficient

Compared with traditional correlation coefficients, MIC has generality and equitability. It not only captures linear, nonlinear, or even nonfunctional correlations (i.e., generality) but also assigns similar scores to any variables containing equal noise (i.e., equitability) [42]. Supposing a dataset of ordered pairs $D = \{X, Y\} = \{(x_i, y_i), i = 1, \cdots, N\}$, where X and Y are variables with length N, the MIC is calculated with the following steps:

Step 1: Divide the D into m-by-n grids G, where $m * n \leq B$, and B is set to $N^{0.6}$ [22] in this paper.

Step 2: Calculate the maximum mutual information (MI) of D under G $MI^*(D|G)$ by Equation (1); then, the (m, n)th term of characteristic matrix $M_{m,n}$ is obtained by normalizing $MI^*(D|G)$ as Equation (2).

$$MI^*(D|G) = \max MI(G) = \max \sum_{m,n} p(x_i, y_i) \log_2 \left(\frac{p(x_i, y_i)}{p(x_i) p(y_i)} \right) \tag{1}$$

$$M_{m,n} = \frac{MI^*(D|G)}{\log_2 \min(m, n)} \tag{2}$$

where $p(x_i, y_i)$ denotes the joint probability density, and $p(x_i)$ and $p(y_i)$ denote the marginal probability densities.

Step 3: Calculate $M_{m,n}$ for all grids that satisfy $m * n \leq B$; then, the MIC of D is the maximum term in the characteristic matrix, namely

$$\mathrm{MIC}(D) = \max_{m*n \leq B} M_{m,n} \tag{3}$$

where MIC ranges from 0 to 1. The larger the MIC, the stronger correlation.

2.2. Light Gradient Boosting Machine

Extreme gradient boosting (XGBoost) [43] and LGBM models are popular ensemble learning methods based on GDBT. Compared with XGBoost and GDBT, LGBM consumes fewer computational resources and has a faster training speed while obtaining a similar accuracy [20,44]. The superiority of LGBM is mainly reflected by the following technologies:

(a) Gradient-based one-side sampling (GOSS). Data with large gradients contribute more to the model and require more attention during training, while those with small gradients are already sufficiently learned by the model. GOSS is applied to make the model focus more on data with large gradients, while avoiding large variations in the distribution of training data. The process of GOSS is described as follows. Firstly, data are sorted according to the gradient by decreasing order. Afterwards, the top a% of data are retained, and b% of the remaining data is randomly selected. Finally, the information gain is calculated and the gradient of the selected b% data is multiplied by $\frac{1-a}{b}$.

(b) Exclusive feature bundling (EFB). EFB is effective when data are high-dimensional. It bundles mutually exclusive features to reduce the number of features, thus increasing the training speed without reducing the training accuracy.

(c) Histogram-based algorithm. The continuous features are discretized into K bins, which are utilized to generate the histogram during training, and the optimal segmentation point is found by traversing the discrete value in the histogram, as shown in Figure 1. This approach reduces the memory consumption.

(d) Leaf-wise growth strategy. The level-wise growth strategy splits plenty of redundant leaves with low gain, which excessively consumes computational resources [45], while the leaf-wise growth strategy achieves higher precision by splitting the leaf with the greatest gain. The comparison of the above growth strategies is shown in Figure 2.

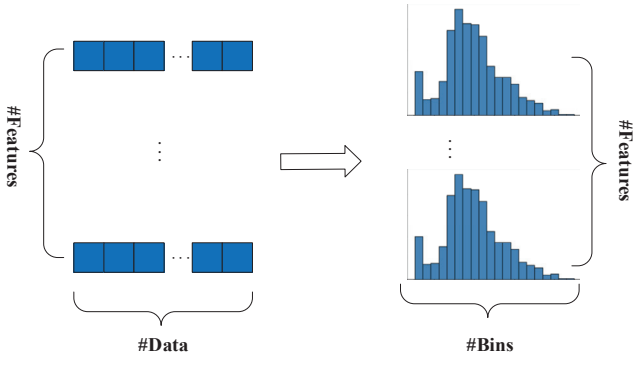

Figure 1. Histogram-based algorithm.

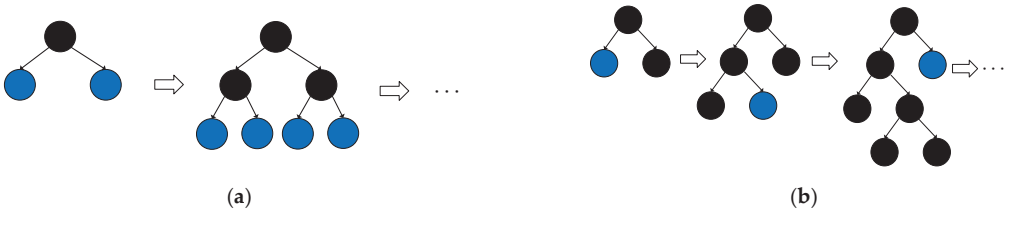

Figure 2. Comparison of (**a**) level-wise growth strategy and (**b**) leaf-wise growth strategy.

2.3. Variational Mode Decomposition

VMD is a non-recursive and adaptive signal decomposition method [37]. It obtains a series of approximately orthogonal modes by solving a variational optimization problem. The variational optimization problem is described as follows:

$$\min_{\{u_k\},\{w_k\}} \left\{ \sum_k \left\| \partial_t \left[\left(\delta(t) + \frac{j}{\pi t} \right) * u_k(t) \right] e^{-j\omega_k t} \right\|_2^2 \right\} \tag{4}$$

$$\text{s.t.} \sum_{k=1}^{K} u_k(t) = x(t) \tag{5}$$

where K denotes the number of modes, $x(t)$ is the original sequence, $\{u_k\} = \{u_1, \cdots, u_K\}$ and $\{w_k\} = \{w_1, \cdots, w_K\}$ are modes and center frequencies of modes, respectively, $\delta(t)$ is the Dirac distribution, and $*$ denotes convolution operation.

The Lagrange multiplier $\lambda(t)$ and quadratic penalty term are introduced to make the problem unconstrained; the augmented Lagrangian $\mathcal{L}$ is listed as follows:

$$\mathcal{L}(\{u_k\},\{w_k\},\lambda) = \alpha \sum_k \left\| \partial_t \left[\left(\delta(t) + \frac{j}{\pi t} \right) * u_k(t) \right] e^{-j\omega_k t} \right\|_2^2 + \left\| x(t) - \sum_{k=1}^{K} u_k(t) \right\|_2^2 + \lambda(t), x(t) - \sum_{k=1}^{K} u_k(t) \tag{6}$$

where α is the balance parameter.

The alternate direction method of multipliers (ADMM) [46] is adopted to solve the augmented Lagrangian $\mathcal{L}$. u_k, w_k are updated as follows:

$$\hat{u}_k^{n+1}(w) = \frac{\hat{x}(w) - \sum_{i<k} \hat{u}_i^{n+1}(w) - \sum_{i>k} \hat{u}_i^{n}(w) + \frac{\hat{\lambda}^n(w)}{2}}{1 + 2\alpha\left(\omega - \omega_k^n\right)^2} \tag{7}$$

$$\omega_k^{n+1} = \frac{\int_0^\infty w \left| \hat{u}_k^{n+1}(w) \right|^2 dw}{\int_0^\infty \left| \hat{u}_k^{n+1}(w) \right|^2 dw} \tag{8}$$

$$\hat{\lambda}^{n+1}(w) = \hat{\lambda}^n(w) + \tau \left(\hat{x}(w) - \sum_{k=1}^{K} \hat{u}_k^{n+1}(w) \right) \tag{9}$$

where τ is the iteration factor, and n denotes the number of iterations. $\hat{u}(w)$, $\hat{x}(w)$, and $\hat{\lambda}(w)$ are the Fourier transforms of $u(t)$, $x(t)$, and $\lambda(t)$, respectively.

The iteration is stopped when the following convergence condition is met:

$$\sum_{k=1}^{K} \frac{\| \hat{u}_k^{n+1}(w) - \hat{u}_k^n(w) \|_2^2}{\| \hat{u}_k^n(w) \|_2^2} < \varepsilon \tag{10}$$

where ε is the convergence threshold.

The number of modes K is key in VMD. On one hand, the modes are still complex if K is too small, which is inconducive to learning degradation trends; thus, the performance of the prediction model cannot be improved effectively. On the other hand, if K is too large, a great amount of computational resources is consumed, even the prediction accuracy is reduced due to the accumulation of prediction errors in sub-models. To determine a suitable K, the ratio of residual energy to the original signal energy R_{res} [47] is used as the criterion of decomposition. The R_{res} is defined as follows:

$$R_{res} = \frac{1}{T} \sum_{t=1}^{T} \left| \frac{x(t) - \sum_{k=1}^{K} u_k(t)}{x(t)} \right| \times 100\% \tag{11}$$

where T denotes the length of $x(t)$. The minimum K that satisfies $R_{res} < 1\%$ is the optimal number of modes.

2.4. Gated Recurrent Unit

A traditional recurrent neural network cannot effectively learn long-term dependence [48]. LSTM solves this shortcoming through the gating mechanism, while this structure increases the parameters of the network. GRU [49] is a simplified version of LSTM that only uses two gates, while the prediction accuracy is not reduced. The structure of a GRU cell is shown in Figure 3. Given the current input X_t and the previous hidden state H_{t-1}, the current hidden state H_t is calculated as follows.

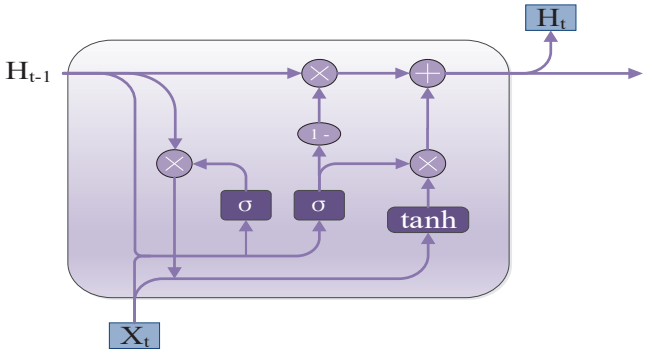

Figure 3. Structure of GRU cell.

Firstly, H_{t-1} and X_t are put into the reset gate R_t and generate the candidate hidden state $\overline{H}_t$:

$$R_t = sigmoid(W_{rx}X_t + U_{rh}H_{t-1}) \tag{12}$$

$$\overline{H}_t = tanh(W_{hx}X_t + U_{hh}(R_t \odot H_{t-1})) \tag{13}$$

where $\odot$ denotes the element-wise multiplication. W_{rx}, U_{rh}, W_{hx}, and U_{hh} are the weight matrices.

Afterwards, the update gate Z_t controls how much information in $\overline{H}_t$ is utilized to generate H_t:

$$Z_t = sigmoid(W_{zx}X_t + U_{zh}H_{t-1}) \tag{14}$$

$$H_t = (1 - Z_t) \odot H_{t-1} + Z_t \odot \widetilde{H_t} \tag{15}$$

where W_{zx} and U_{zh} are weight matrices.

3. The DTP Model Based on MIC-LGBM and VMD-GRU

To predict the degradation trend of a PSU precisely and provide support for condition-based maintenance, a MIC-LGBM and VMD-GRU-based combined model is proposed. On one hand, it generates a reliable PDI in a short time, only using few computational resources; on the other, its predicted degradation trend is accurate and has a strong correlation with the actual degradation trend. The overall flowchart of the proposed model is shown in Figure 4. Firstly, working parameters are screened by MIC, and the interference information is removed. Secondly, the data in the benchmark state, which represents the good running conditions of PSU, are utilized to generate the LGBM healthy model, and then the PDI sequence is obtained. Lastly, the VMD-GRU prediction model is constructed to predict the degradation trend of PSU.

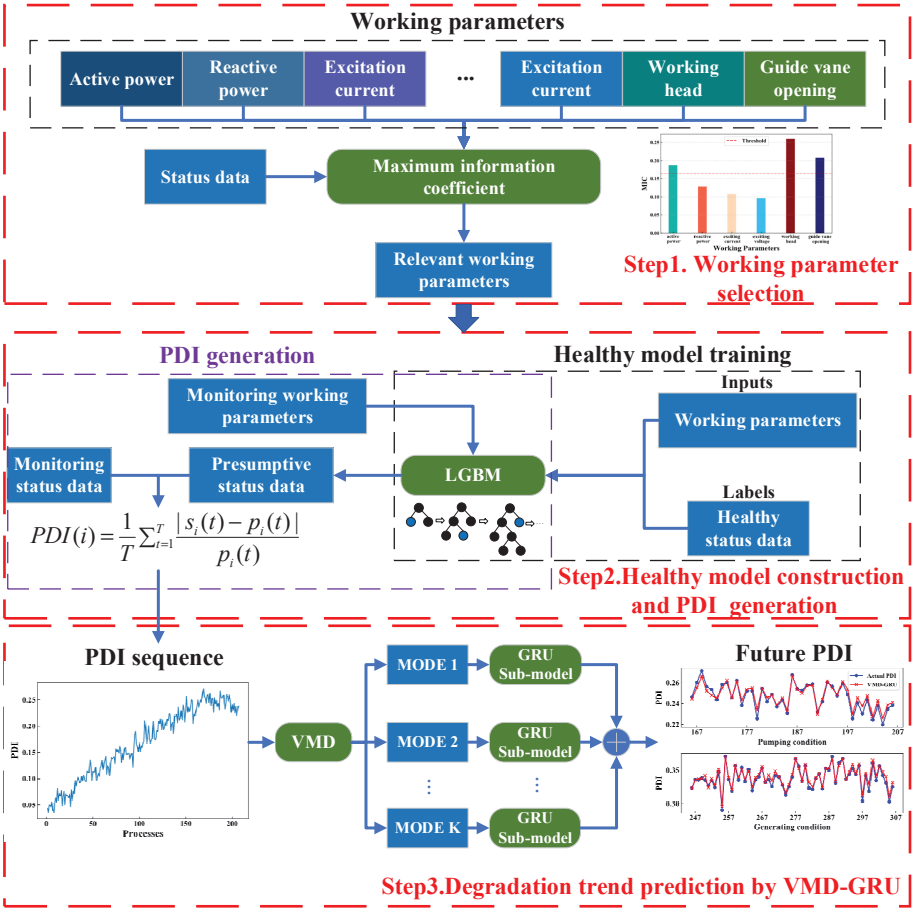

Figure 4. Proposed DTP model.

3.1. Working Parameters Selection by MIC

The status data, such as vibration, swing, etc., reflect the operating status of the PSU directly. Besides, the PSU behaves differently under different working parameters. Working parameters that are poorly correlated with the status data bring interference to the judgment of the PSU's status. Therefore, invalid operating parameters are excluded by MIC to ensure that the inputs to the healthy model are critical to determine the operating status of PSU. Given l working parameters $w^1(t), w^2(t), \cdots, w^l(t)$ and the status data $s(t)$ of PSU, the selection of working parameters is carried out as follows:

(1) Calculate the correlation $c(i), i = 1, \cdots, l$ between $w^i(t), i = 1, \cdots, l$ and $s(t)$ by the MIC in Section 2.1.

(2) Obtain the selection threshold δ as follows:

$$\delta = \frac{1}{l}\sum_{i=1}^{l} c(i) \tag{16}$$

(3) The working parameter $w^i(t)$ is selected as input of the healthy model if $c(i) \geq \delta$.

3.2. Healthy Model Construction and PDI Generation

3.2.1. Part A: Healthy Model Construction

After selecting the input, the status data are used as the output of the healthy model. Thus, the LGBM healthy model is built as follows:

(1) The period when the PSU is running well is selected as the benchmark state. The selected working parameters under benchmark state $w^1(t), w^2(t), \cdots, w^m(t)$ are used as the input of the LGBM healthy model, and the corresponding healthy status data $h(t)$ are adopted as the output of the LGBM healthy model. Thus, the nonlinear mapping relationship is established as follows:

$$h(t) = f\left(w^1(t), w^2(t), \cdots, w^m(t)\right) \tag{17}$$

(2) The trial-and-error method is utilized to determine the optimal parameters of LGBM.

The absolute average ($|AVG|$) and standard deviation (STD) of the fitting errors $E = \{e(i), i = 1, \cdots, N\}$ on the test set are introduced to evaluate the effectiveness of the LGBM healthy model. The definition of $|AVG|$ and STD are presented as follows:

$$|AVG| = \left| \frac{1}{N} \sum_{i=1}^{N} e(i) \right| \tag{18}$$

$$STD = \sum_{i=1}^{N} \frac{(e(i) - \bar{e})^2}{N - 1} \tag{19}$$

where N is the number of fitting errors E and $\bar{e}$ denotes the average of E. The smaller the $|AVG|$, the smaller fitting error. The smaller the STD, the more stable the healthy model performance.

Moreover, the training time of the healthy model $TIME$ is recorded to illustrate the computational resource consumption.

$$TIME = t_{end} - t_{start} \tag{20}$$

where t_{end} and t_{start} represent the start time and end time of model training, respectively. The smaller the $TIME$, the smaller the cost of computational resources.

3.2.2. Part B: PDI Generation

The performance degradation of the PSU mainly occurs in the pumping condition and generation condition. Therefore, a single pumping or generation process is used as the basis unit of PDI generation in this paper. The PDI $PDI(i)$ of the ith process is calculated as follows:

$$p_i(t) = f\left(w_i^1(t), w_i^2(t), \cdots, w_i^m(t)\right) \tag{21}$$

$$PDI(i) = \frac{1}{T} \sum_{t=1}^{T} \frac{|s_i(t) - p_i(t)|}{p_i(t)} \tag{22}$$

where $s_i(t)$ is the monitoring status data, $w_i^1(t), w_i^2(t), \cdots, w_i^m(t)$ are the monitoring working parameters selected by the MIC, f denotes the mapping relationship learned by the LGBM healthy model, $p_i(t)$ implies the presumptive status data under corresponding working parameters when the PSU is running well, and T denotes the number of points in the ith process.

3.3. Degradation Trend Prediction with VMD-GRU

The VMD-GRU prediction model is constructed after obtaining PDI. As shown in the bottom of Figure 4, the PDI sequence is decomposed into a series of modes at first. Then, the GRU sub-models are built for each mode separately. Finally, the predicted values of all modes are added to obtain the future PDI. The structure of the GRU sub-model is

shown in Figure 5. The long-term dependence of the PDI sequence is extracted by the GRU layer; then, the output of the final GRU cell is sent to the full connected layers to obtain the predicted value of mode.

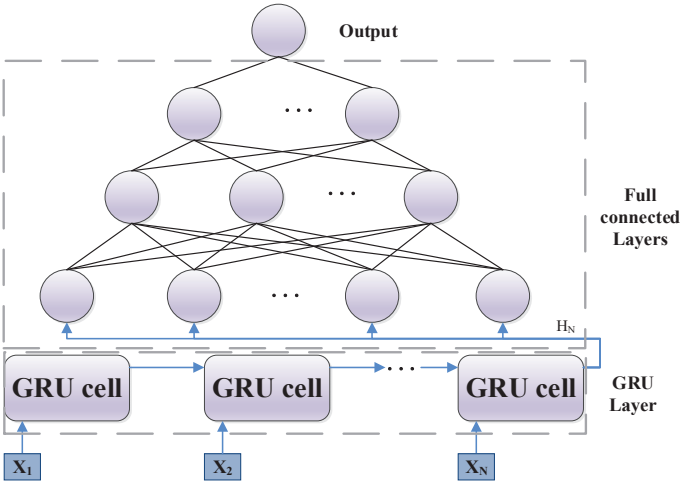

Figure 5. Structure of the GRU sub-model.

RMSE, MAE, and R^2 are selected as metrics for evaluating the performance of the prediction model.

(a) RMSE:

$$\mathrm{RMSE} = \sqrt{\sum_{i=1}^{N} \frac{(y_i - \widetilde{y}_i)^2}{N}} \tag{23}$$

(b) MAE:

$$\mathrm{MAE} = \frac{1}{N} \sum_{i=1}^{N} |y_i - \widetilde{y}_i| \tag{24}$$

(c) R^2:

$$R^2 = 1 - \frac{\sum_{i=1}^{N} (y_i - \widetilde{y}_i)^2}{\sum_{i=1}^{N} (y_i - \overline{y})^2} \tag{25}$$

where y_i and $\widetilde{y}_i$ denote the actual PDI and predicted PDI, respectively. N is the length of the actual PDI, and $\overline{y}$ is the average of y_i.

4. Case Study

The proposed DTP model was verified on a PSU located in China, and comparison experiments were conducted to illustrate the superiority of components of the proposed model. All experiments were carried out in the Python 3.6.4 environment running on a computer with R7 5800h CPU, GTX3060ti GPU.

4.1. Data Source

The structure of the PSU is shown in Figure 6. It has a single-stage mixed-flow pump-turbine unit with a capacity of 375 MW. The single-shaft vertical-stage pump-turbine is concatenated with the power generating motor, which has a rated speed of 375 r/min, through the main shaft. The monitoring system has worked since 19 May 2017. According to the operation reports, no abnormalities or accidents occurred from 15 January 2018 to 15 February 2018, which means the PSU ran well. This period was chosen as the benchmark state. The PSU had poor performance between 1 March 2019 to 1 October 2019, and this

period was used for generating the PDI. Besides, the PSU has different characteristics under different operating conditions, and DTP was carried out on the pumping condition and generating conditions, respectively. There were 207 pumping processes and 307 generating processes during PDI generation.

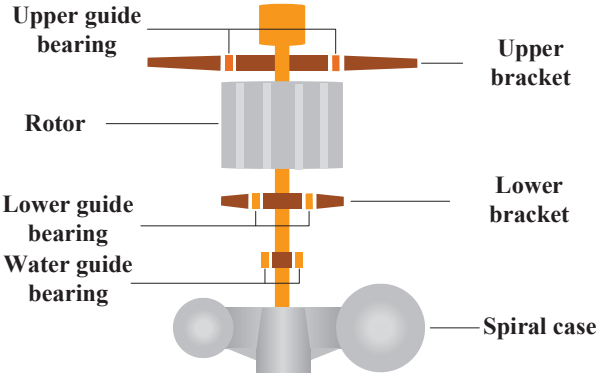

Figure 6. The structure of the PSU.

4.2. Working Parameter Selection Based on MIC

Among the status data, swing and vibration reflect the operating status of the PDU significantly [9]. The swing of the upper guide bearing was chosen to reflect the status of the PSU in this paper. Therefore, the output of the healthy model was determined as swing. The working parameters, such as active power, reactive power, excitation recurrent, excitation voltage, working head, guide vane opening, etc., determine the operation mode of the PSU. The working parameters have different effects on the swing; however, they also have different correlations with the swing. The relationships between the swing and the working parameters under the benchmark state are shown in Figure 7.

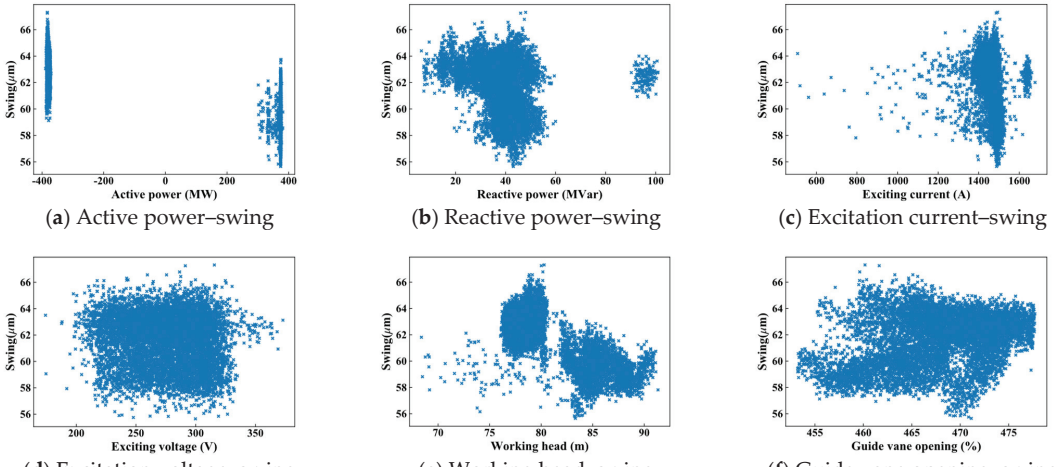

(**a**) Active power–swing (**b**) Reactive power–swing (**c**) Excitation current–swing

(**d**) Excitation voltage–swing (**e**) Working head–swing (**f**) Guide vane opening–swing

Figure 7. Relationships between working parameters and swing.

From Figure 7a, it can be seen that swing was distributed from 59.12–67.31 μm and 55.64–63.75 μm under the pumping condition and generating condition, respectively. This

indicates that PSU has different vibration characteristics under these operating conditions, and it is necessary to generate a PDI for all operating conditions separately to ensure consistency. Figure 7b shows that the reactive power of PSU is mostly distributed between 6.33 MVar and 60 Mvar, while a small amount is distributed from 91.2 Mvar to 102.3 MVar. Moreover, the relationships between the swing and the above working parameters are not linear and are difficult to discern directly; the same conclusions can be drawn in Figure 7c–f. Thus, MIC was utilized to extract the complex relationships between the swing and the working parameters; then, the selection threshold δ was calculated by Equation (16) to exclude the working parameters that have weak correlations with the swing. The MIC and δ are shown in Figure 8, where $\delta = 0.553$. The active power, working head, and guide vane opening were selected as the inputs of the healthy model since their MICs are greater than δ.

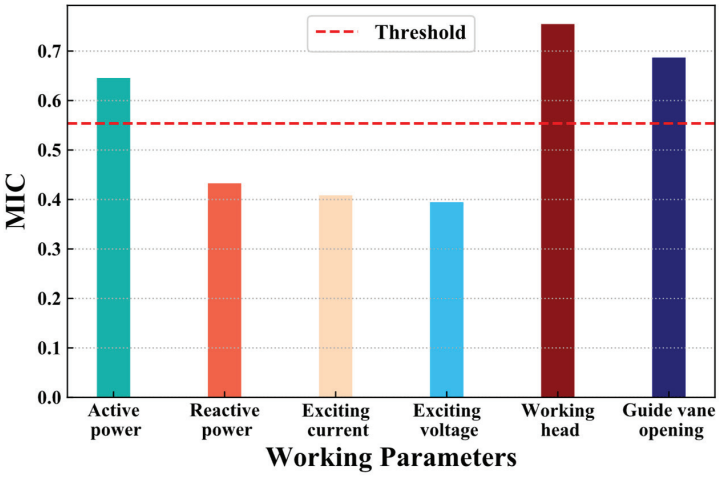

Figure 8. MIC between swing and working parameters.

4.3. Healthy Model Establishment and PDI Construction

4.3.1. Comparative Healthy Models and Parameter Settings

After determining the input and output of the healthy model, the LGBM healthy models were built under two operating conditions, respectively. In the benchmark state, there were 5009 samples under the pumping condition and 3175 samples under the generating condition. In total, 90% of the benchmark state was used for training, and the remaining 10% was applied for testing. The GPR, Classification and Regression Tree (CART) [50], and XGBoost are small and effective; thus, they were adopted for the comparison with the LGBM. The optimal parameters of healthy models were obtained through the trial-and-error method, as listed in Table 1. Moreover, ablation experiments were conducted to illustrate the importance of working parameter selection; i.e., all working parameters were taken as the input of the healthy model.

Table 1. Parameter setting of healthy models.

Model	Parameter Settings
GPR	Kernel = 'RBF', alpha = '1e-9'.
CART	Criterion = 'MSE', Min_samples_split = 2, Min_samples_leaf = 1.
XGBoost	Booster = 'gbtree', eta = 0.1, Max_depth = 7, Min_child_weight = 1, Sub_sample = 0.82.
LGBM	Max_depth = 8, Num_leaves = 19, Min_child_samples = 30, Sub_sample = 0.85.

4.3.2. Performance Analysis and Discussion of Healthy Models

The evaluation metrics of different healthy models on the testing set are listed in Table 2. The bolded values represent the best metrics. The box plots of fitting errors on the testing set are shown in Figure 9, and the mean values of evaluation metrics of two operating conditions are presented in Figure 10.

Table 2. Fitting errors of healthy models.

Parameter Selection	Healthy Model	Pumping Condition			Generating Condition		
		$\lvert AVG \rvert$	*STD*	*TIME*	$\lvert AVG \rvert$	*STD*	*TIME*
NO MIC	GPR	0.065	1.033	2.317	0.014	1.037	1.700
	CART	0.093	1.246	0.182	0.036	1.127	0.096
	XGBoost	0.384	1.174	1.539	0.030	1.128	0.937
	LGBM	0.082	1.055	0.755	0.028	0.994	0.652
MIC	GPR	0.049	0.985	2.261	0.029	1.071	1.553
	CART	0.056	1.169	**0.023**	0.023	1.063	**0.036**
	XGBoost	0.040	0.994	0.314	0.023	0.970	0.612
	LGBM	**0.036**	**0.911**	0.302	**0.019**	**0.938**	0.563

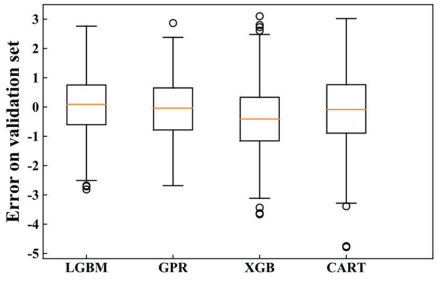

(**a**) Fitting errors under pumping condition (NO MIC)

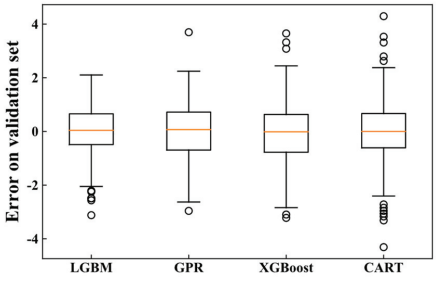

(**b**) Fitting errors under generating condition (NO MIC)

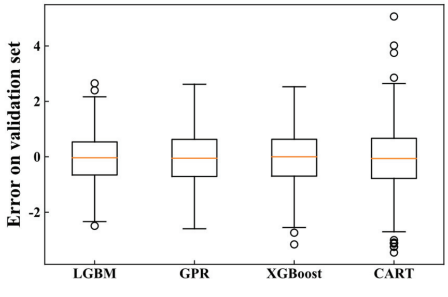

(**c**) Fitting errors under pumping condition (MIC)

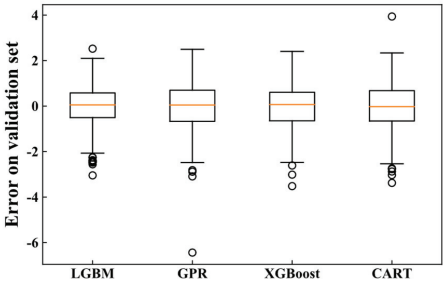

(**d**) Fitting errors under generating condition (MIC)

Figure 9. The box plots of fitting errors on the testing set.

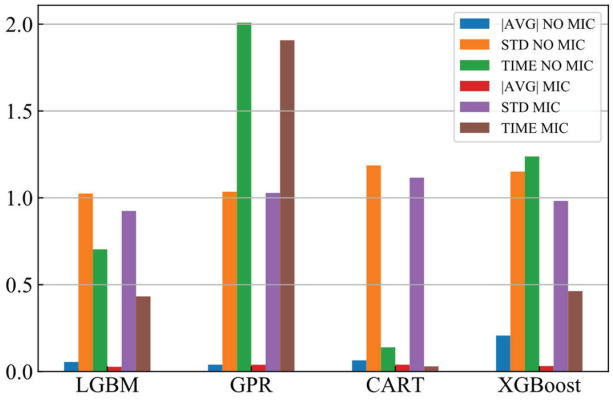

Figure 10. Average evaluation metrics under two conditions.

When the working parameters were selected by MIC, LGBM achieved the minimum $|AVG|$ and STD among all healthy models under both the pumping condition and generating condition. This reveals that LGBM has the smallest fitting error and the most stable performance. The $|AVG|$ and $TIME$ of XGBoost are close to those of LGBM, while STD is 6.2% higher than LGBM on average for two operating conditions. This indicates that XGBoost is more likely to produce outliers. CART takes the shortest training time among healthy models, while $|AVG|$ and STD are larger than XGBoost and LGBM. Although it trains quickly, its fitting error is not satisfactory. GPR took the longest time for training and consumed the most computational resources but performed the worst under the generating condition. The above conclusions are also verified in Figure 9c,d.

As shown in Table 2, when working parameters were not selected by MIC (NO MIC), most of healthy models had a larger $|AVG|$ and STD and required a longer training time. This shows that the redundant components in the working parameters not only decrease the accuracy and stability of healthy models but also cost more in terms of computational resources. Interestingly, the working parameter selection improves the performance of GPR under the pumping condition while its capability reduces under the generating condition. The working parameter selection makes the distributions of fitting errors on the testing set more concentrated, as shown in Figure 9. From Figure 10, it can be seen that parameter selection improved the average performance of GPR, CART, XGBoost, and LGBM under two operating conditions, where $|AVG|$ improved by 1.2%, 38.9%, 84.7%, and 50%, STD improved by 0.6%, 5.9%, 14.6%, and 9.7%, and $TIME$ improved by 5.1%, 78.8%, 62.6%, and 38.5%. MIC greatly improves the capability of XGBoost and LGBM.

4.3.3. PDI Construction with LGBM Healthy Model

Based on the reliable LGBM healthy model, the effective PDI sequences are generated. For the ith process, the presumptive status data $p_i(t)$ are obtained by Equation (21); then, the $PDI(i)$ is calculated by Equation (22). The PDI sequences of two operating conditions are shown in Figure 11. The PDI sequences of two operating conditions have similar overall increasing trends. This indicates that the degradation of PSU gradually increases with operation time, which is consistent with the records in the operating reports. In addition, the PDI sequences are so complex that there are plenty of recursive components and nonlinear components. These components are clearly demonstrated in the PDI sequence under the generating condition, as shown in Figure 12b. They seriously affect the performance of the prediction model.

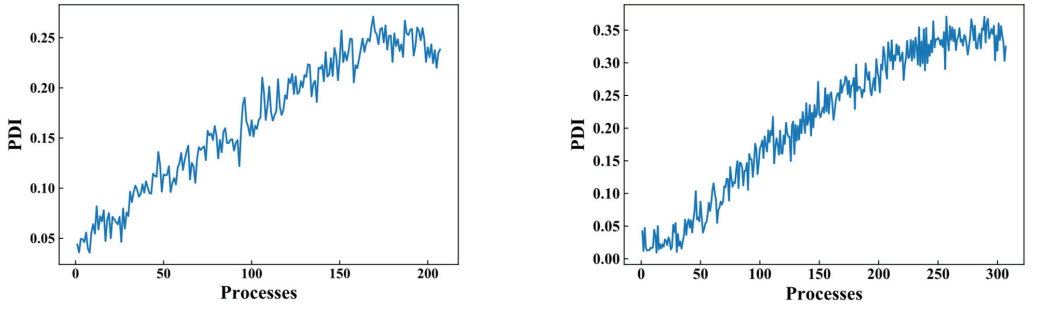

(**a**) PDI sequence under pumping condition (**b**) PDI sequence under generating condition

Figure 11. PDI sequences under (**a**) pumping and (**b**) generating conditions.

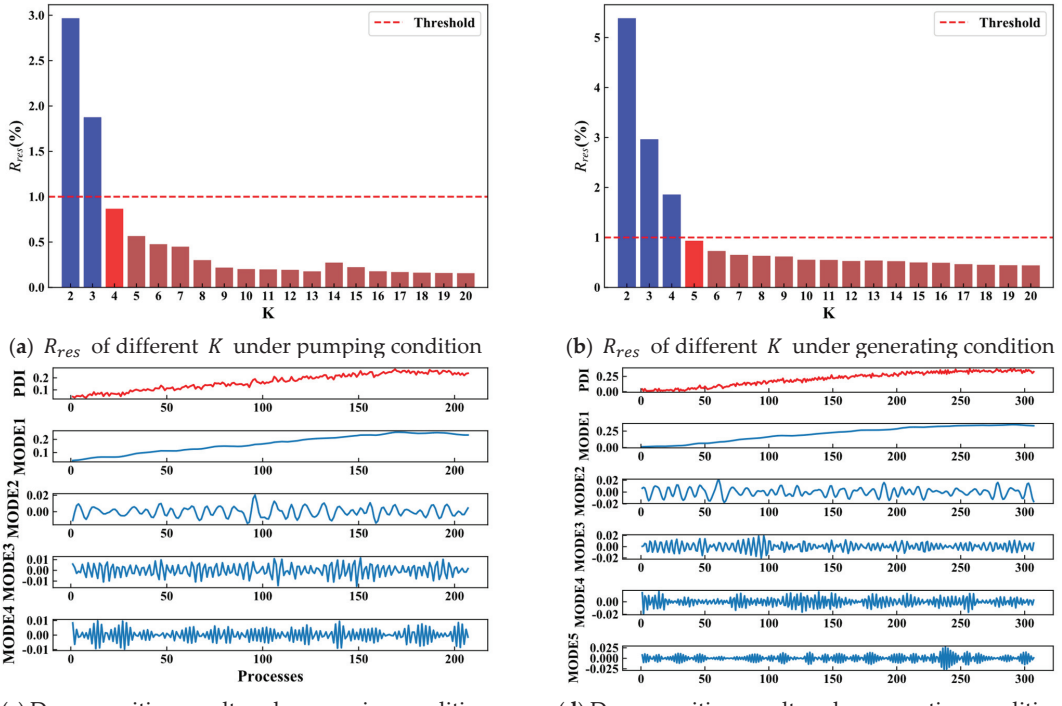

(**a**) R_{res} of different K under pumping condition (**b**) R_{res} of different K under generating condition

(**c**) Decomposition result under pumping condition (**d**) Decomposition result under generating condition

Figure 12. Decomposition results of PDI sequences by VMD.

4.4. Degradation Trend Prediction of PSU

4.4.1. Comparative Prediction Models and Parameter Settings

The complex PDI sequence brings challenges for predicting degradation trends accurately. To solve this problem, the VMD-GRU prediction model was constructed in this paper. VMD was utilized to decompose the PDI sequence into a series of simple modes; then, GRU sub-models were built for each mode separately, and the predicted values of the sub-models were summed to obtain the future PDI at last. The following comparative experiments were conducted to confirm the superiority of VMD-GRU. Firstly, the popular prediction models were used to illustrate the challenge brought by the complexity of

the PDI sequence, including ANN [27], SVR [26], LSTM [29], and GRU [33]. Afterwards, VMD-ANN, VMD-LSTM, and VMD-GRU were compared with ANN, LSTM, and GRU, respectively, to demonstrate the performance improvement resulting from decomposition; then, the EMD-ANN, EMD-LSTM, and EMD-GRU prediction models were set up to demonstrate the effectiveness of VMD. Lastly, the validity of GRU was proved by comparing GRU, EMD-GRU, and VMD-GRU with corresponding models. The optimal structures and parameter settings of prediction models were determined by the trial-and-error method, as shown in Table 3.

Table 3. Parameter setting of prediction models.

Model	Parameter Settings
ANN	Four full connected layers, number of neurons: 256, 64, 4, 1.
SVR	C = 0.8, Kernel = 'RBF', Epsilon = 0.001, Tol = 0.001.
LSTM	(a) LSTM Layer, 128 units. (b) Three full connected layers, number of neurons: 256, 64, 1.
GRU	(a) GRU Layer, 128 units. (b) Three full connected layers, number of neurons: 256, 32, 1.
EMD-ANN	(a) EMD: Decompose until meeting the stopping condition in [51]. (b) ANN sub-model: it has same structure as ANN prediction model.
EMD-LSTM	(a) EMD: Decompose until meeting the stopping condition in [51]. (b) LSTM sub-model: The structure is same as LSTM prediction model.
EMD-GRU	(a) EMD: Decompose until meeting the stopping condition in [51]. (b) GRU sub-model: The structure is same as GRU prediction model.
VMD-ANN	(a) VMD : K is set to 4 under pumping condition, while $K = 5$ under generating condition. (b) ANN sub-model: it has same structure as ANN prediction model.
VMD-LSTM	(a) VMD : K is set to 4 under pumping condition, while $K = 5$ under generating condition. (b) LSTM sub-model: The structure is same as LSTM prediction model.
VMD-GRU	(a) VMD : K is set to 4 underpumping condition, while $K = 5$ under generating condition. (b) GRU sub-model: The structure is same as GRU prediction model.

The time step was set to 5 in all prediction models; i.e., $PDI(i-5), PDI(i-4), \cdots, PDI(i-1)$ were used to predict $PDI(i)$. The first 80% of the PDI sequence was employed for training and the remaining 20% was utilized for testing. To eliminate randomness, all prediction results were the averages of 10 repeated experiments.

To determine the optimal number of modes for VMD, the R_{res} of different numbers of modes K was calculated under two conditions, respectively. The R_{res} is shown in Figure 12a,b. It can be seen that $R_{res} < 1\%$ when $K \geq 4$ under the pumping condition and $K \geq 5$ under the generating condition. Therefore, K was set to 4 and 5 under the pumping condition and generating condition, respectively. The decomposition results under an optimal K are presented in Figure 12c,d. These demonstrate that the smooth and simple modes are obtained by VMD, and they store different information of the PDI sequence. Additionally, the decomposition results of EMD are illustrated in Figure 13. EMD suffers from the mode mixing severely that multiple frequency components appear in the same mode. This reveals that the modes generated by EMD are more complex than those of VMD. Thus, we can conclude that VMD makes PDI sequences simpler, and it provides a better decomposition compared with EMD.

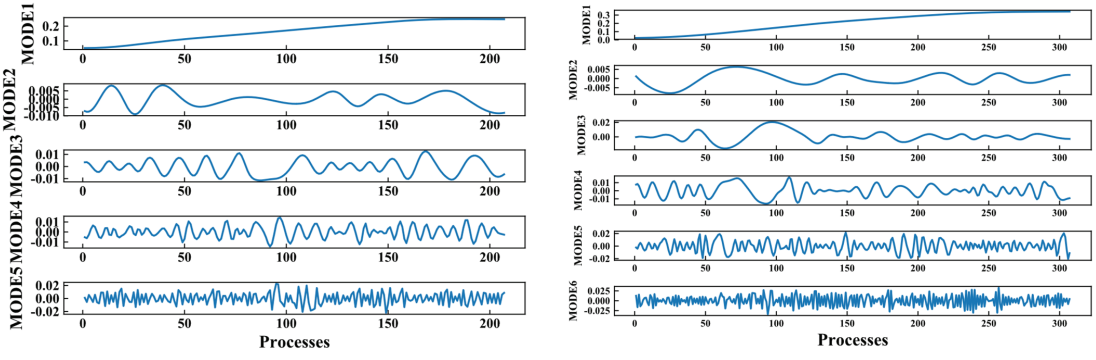

(**a**) Decomposition result under pumping condition

(**b**) Decomposition result under generating condition

Figure 13. Decomposition result of PDI sequences by EMD.

4.4.2. Performance Analysis and Discussion of Prediction Models

The prediction results of VMD-GRU on the testing sets are shown in Figure 14, and those of comparative experiments are shown in Figure 15. The RMSE, MAE, and R^2 are listed in Table 4. The bolded values indicate the optimal metrics. The analysis of the results and discussion are presented below.

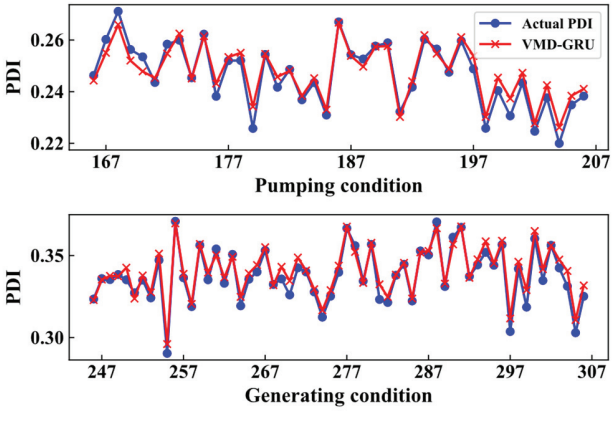

Figure 14. Performance of VMD-GRU.

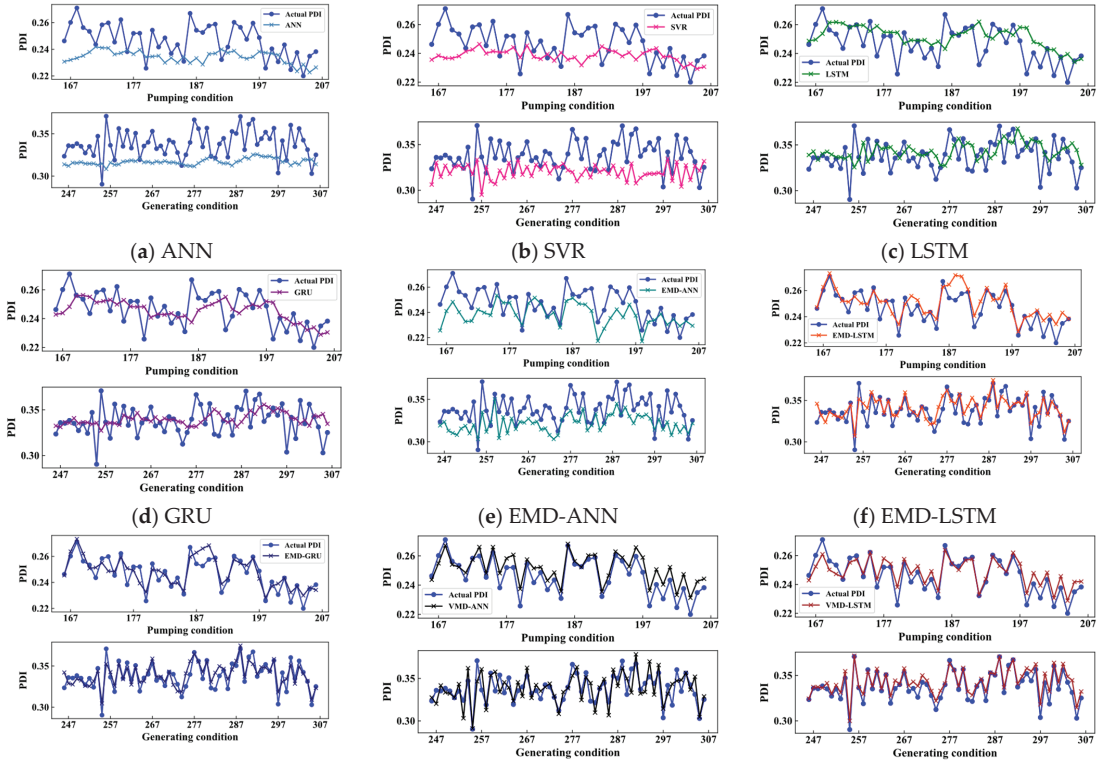

Figure 15. Performance of the comparative prediction models.

Table 4. Performance of prediction models.

Prediction Models	Pumping Condition			Generating Condition		
	RMSE	MAE	R^2	RMSE	MAE	R^2
ANN	0.0173	0.0149	−0.9761	0.0271	0.0232	−1.7304
SVR	0.0147	0.0125	−0.4360	0.0249	0.0208	−1.3031
LSTM	0.0129	0.0095	−0.1060	0.0190	0.0146	−0.3337
GRU	0.0118	0.0096	0.0677	0.0178	0.0136	−0.1780
EMD-ANN	0.0124	0.0106	−0.0187	0.0206	0.0177	−0.5713
EMD-LSTM	0.0076	0.0061	0.6160	0.0099	0.0078	0.6305
EMD-GRU	0.0062	0.0050	0.7457	0.0085	0.0068	0.7328
VMD-ANN	0.0065	0.0056	0.7234	0.0123	0.0100	0.4435
VMD-LSTM	0.0053	0.0045	0.8131	0.0066	0.0053	0.8405
VMD-GRU	**0.0035**	**0.0029**	**0.9171**	**0.0044**	**0.0035**	**0.9281**

(1) Challenges brought by the complex PDI sequence

From Table 4, the R^2 values of ANN, SVR, LSTM, and GRU are less than 0.07 under two operating conditions. This shows that the predicted PDI is poorly correlated with the actual PDI; thus, the developing trend of PDI is not effectively learned by these prediction models. The RMSE and MAE of four models are large; additionally, their prediction results can only fall roughly between the upper and lower envelopes of the actual PDI, as shown in Figure 15a–d. These show that the prediction models have large deviations. As shown in Figure 11 and Table 4, the PDI sequence is more complex under generating condition, and the prediction models perform worse under the generating condition than pumping

condition. These factors reveal that the performance of prediction models is inversely proportional to the complexity of the PDI sequence.

Thus, we can conclude that the complexity of the PDI sequence increases the difficulty of accurate prediction. In this case, even popular prediction models are not effective. The more complex the PDI sequence, the worse the performance.

(2) Comparison of VMD-based models with other models

VMD-ANN, VMD-LSTM, and VMD-GRU are compared with ANN, LSTM, and GRU, respectively, to verify the prediction performance improvement due to PDI sequence simplification by VMD. As listed in Table 4, the VMD-based models show a significant performance improvement. Compared with GRU, the RMSE and MAE of VMD-GRU are improved by 237.1% and 231% under the pumping condition and 304.5% and 288.5% under the generating condition. VMD-LSTM improves RMSE by 143.3% and 187.8% and MAE by 111.1% and 175.4% under the two conditions compared with LSTM. Similar results can be obtained by comparing VMD-ANN with ANN. These indicate that simple modes are more conducive to learning PDI sequences and reducing the prediction bias. In addition, the R^2 values of VMD-based models are greatly increased compared to the corresponding models. VMD-GRU reaches the optimal R^2, reaching 0.917 under the pumping condition and 0.928 under the generating condition, while the R^2 values of most benchmark prediction models are less than 0. Similar results can be acquired by comparing EMD-based models with ANN, LSTM, and GRU. These results show that decomposition is helpful to learning the long-term dependence in a PDI sequence.

As listed in Table 4, the VMD-based models have smaller errors and learn more long-term dependence in the PDI sequence compared with the EMD-based models. For example, the RMSE, MAE, and R^2 of the VMD-GRU are improved by 85.2%, 83.3%, and 19.9% compared with those of the EMD-GRU on average for the two operating conditions. This indicates that the VMD-based prediction models perform better, so the modes obtained by VMD are more effective.

Therefore, it can be concluded that the simple modes obtained by decomposition are helpful to learning the trend of PDI sequences and reducing the prediction error. Besides, the modes generated by VMD are more efficient than those of EMD.

(3) Comparison of GRU-based models with other models

Compared with ANN, SVR, and LSTM, GRU achieves the smallest RMSE and MAE and the largest R^2. Under the two operating conditions, the RMSE of GRU improved by 49.4% and 62.9% on average and MAE improved by 32.2% and 41.6% on average compared to ANN and SVR. This indicates that GRU has a smaller prediction bias and better learning ability compared with these models. The performance of LSTM is much better than ANN and SVR, yet the RMSE and MAE of LSTM are still larger than GRU by 7.42% and 2.89%. Besides, LSTM has more parameters and requires more time and computational resources. Therefore, GRU has the best prediction performance when the PDI sequence is not decomposed.

Under the two operating conditions, the EMD-GRU achieves the optimal evaluation metrics and performs best among EMD-based models. Compared with EMD-ANN and EMD-LSTM, the RMSE is improved by 121.1% and 19.5% on average, and the MAE is improved by 136.1% and 18.4% on average. Moreover, the R^2 of EMD-GRU is also the best among EMD-based models, reaching 0.7457 and 0.7328 under the pumping condition and generating condition, respectively. Comparing the VMD-based models, it can be seen that the RMSE and MAE of VMD-GRU are improved by 137.9% and 143.7% on average over VMD-ANN and 50.6% and 53.1% over VMD-LSTM under the two operating conditions. The R^2 of VMD-GRU is also the best among VMD-based models. These factors show that the GRU-based models learn the degradation trend most fully among the corresponding models when the PDI sequence is decomposed.

VMD-GRU achieves the largest R^2 among all prediction models, which are greater than 0.9 under the two operation conditions. This shows that the predicted values of VMD-

GRU have a strong correlation with the actual PDI. Besides, VMD-GRU has the smallest RMSE and MAE among all prediction models. These factors indicate that VMD-GRU has the smallest prediction error and learns the information in PDI sequence most adequately.

Based on the above analysis, we can conclude that VMD-GRU learns the long-term dependence of PDI sequence best, achieves the highest prediction accuracy, and every component of it is indispensable.

5. Conclusions

To predict the degradation trend of PSU reliably, a novel combined model based on MIC-LGBM and VMD-GRU is proposed in this paper. Firstly, MIC is utilized to eliminate the working parameters that have weak correlations with the status of PSU. Secondly, the LGBM healthy model is built to establish the mapping relationship between the selected working parameters and status data under good running conditions; then, the PDI is obtained on the basis of the LGBM healthy model and monitoring data. Lastly, the VMD-GRU prediction model is designed to predict the degradation trend reliably. Experimental validation and comparative analysis show that the proposed model requires less computational resources while establishing the most accurate and stable healthy model and predicts the degradation trend most reliably.

However, all hyperparameters are adjusted by the trial-and-error method in this paper, which consumes a great deal of time. The intelligent optimization algorithms perform outstandingly in hyperparameter tuning and will be used in our future work. Besides, the more reliable the degradation trend prediction, the greater the reference for decision-making. Building a more effective prediction model will also be a research focus in the future.

Author Contributions: Conceptualization, methodology, software, writing—original draft preparation, P.C.; validation, P.C., Y.D. and X.Z.; formal analysis, Y.W.; investigation, L.M.; resources, Y.Y.; writing—review and editing and funding acquisition, C.L. All authors have read and agreed to the published version of the manuscript.

Funding: This work was supported by the National Natural Science Foundation of China (No. 51879111) and the Hubei Provincial Natural Science Foundation of China (No. 2019CFA068).

Data Availability Statement: No new data were created or analyzed in this study. Data sharing is not applicable to this article.

Conflicts of Interest: The authors declare that they have no known competing financial interests or personal relationships that could have appeared to influence the work reported in this paper.

References

1. Wu, G.; Shao, X.; Jiang, H.; Chen, S.; Zhou, Y.; Xu, H. Control strategy of the pumped storage unit to deal with the fluctuation of wind and photovoltaic power in microgrid. *Energies* **2020**, *13*, 415. [CrossRef]
2. Hydropower Status Report 2021. Available online: https://www.hydropower.org/status-report (accessed on 3 January 2022).
3. Lai, X.; Li, C.; Zhou, J.; Zhang, N. Multi-objective optimization of the closure law of guide vanes for pumped storage units. *Renew. Energy* **2019**, *139*, 302–312. [CrossRef]
4. Zhao, Z.; Yang, J.; Yang, W.; Hu, J.; Chen, M. A coordinated optimization framework for flexible operation of pumped storage hydropower system: Nonlinear modeling, strategy optimization and decision making. *Energy Convers. Manag.* **2019**, *194*, 75–93. [CrossRef]
5. Zheng, Y.; Chen, Q.; Yan, D.; Liu, W. A two-stage numerical simulation framework for pumped-storage energy system. *Energy Convers. Manag.* **2020**, *210*, 112676. [CrossRef]
6. Lei, Y.; Li, N.; Guo, L.; Li, N.; Yan, T.; Lin, J. Machinery health prognostics: A systematic review from data acquisition to RUL prediction. *Mech. Syst. Signal Process.* **2018**, *104*, 799–834. [CrossRef]
7. Shan, Y.; Liu, J.; Xu, Y.; Zhou, J. A combined multi-objective optimization model for degradation trend prediction of pumped storage unit. *Measurement* **2021**, *169*, 108373. [CrossRef]
8. Hu, X.; Li, C.; Tang, G. In A hybrid model for predicting the degradation trend of hydropower units based on deep learning. In Proceedings of the 2019 Prognostics and System Health Management Conference (PHM-Qingdao), Qingdao, China, 25–27 October 2019; pp. 1–5.

9. Zhou, J.; Shan, Y.; Liu, J.; Xu, Y.; Zheng, Y. Degradation tendency prediction for pumped storage unit based on integrated degradation index construction and hybrid CNN-LSTM model. *Sensors* **2020**, *20*, 4277. [CrossRef]
10. An, X.; Pan, L. Characteristic parameter degradation prediction of hydropower unit based on radial basis function surface and empirical mode decomposition. *J. Vib. Control.* **2015**, *21*, 2200–2211. [CrossRef]
11. An, X.; Yang, L.; Pan, L. Nonlinear prediction of condition parameter degradation trend for hydropower unit based on radial basis function interpolation and wavelet transform. *Proc. Inst. Mech. Eng. Part C J. Mech. Eng. Sci.* **2015**, *229*, 3515–3525. [CrossRef]
12. An, X.; Pan, L.; Yang, L. Condition parameter degradation assessment and prediction for hydropower units using Shepard surface and ITD. *Trans. Inst. Meas. Control.* **2014**, *36*, 1074–1082. [CrossRef]
13. Sagi, O.; Rokach, L. Ensemble learning: A survey. *WIREs Data Mining Knowl Discov.* **2018**, *8*, e1249. [CrossRef]
14. Cai, R.; Xie, S.; Wang, B.; Yang, R.; Xu, D.; He, Y. Wind speed forecasting based on extreme gradient boosting. *IEEE Access* **2020**, *8*, 175063–175069. [CrossRef]
15. Zheng, H.; Wu, Y. A XGBoost model with weather similarity analysis and feature engineering for short-term wind power forecasting. *Appl. Sci.* **2019**, *9*, 3019. [CrossRef]
16. Tao, T.; Liu, Y.; Qiao, Y.; Gao, L.; Lu, J.; Zhang, C.; Wang, Y. Wind turbine blade icing diagnosis using hybrid features and Stacked-XGBoost algorithm. *Renew. Energy* **2021**, *180*, 1004–1013. [CrossRef]
17. Trizoglou, P.; Liu, X.; Lin, Z. Fault detection by an ensemble framework of extreme gradient boosting (XGBoost) in the operation of offshore wind turbines. *Renew. Energy* **2021**, *179*, 945–962. [CrossRef]
18. Alsaleh, A.; Binsaeedan, W. The influence of salp swarm algorithm-based feature selection on network anomaly intrusion detection. *IEEE Access* **2021**, *9*, 112466–112477. [CrossRef]
19. Truong, D.; Tran, D.; Nguyen, L.; Mac, H.; Tran, H.A.; Bui, T. Detecting web attacks using stacked denoising autoencoder and ensemble learning methods. In Proceedings of the Tenth International Symposium on Information and Communication Technology, Association for Computing Machinery, Hanoi, Vietnam, 4–6 December 2019; pp. 267–272.
20. Ke, G.; Meng, Q.; Finley, T.; Wang, T.; Chen, W.; Ma, W.; Ye, Q.; Liu, T.-Y. LightGBM: A highly efficient gradient boosting decision tree. In Proceedings of the 31st International Conference on Neural Information Processing Systems, Curran Associates Inc., Long Beach, CA, USA, 4–6 December 2017; pp. 3149–3157.
21. Cerrada, M.; Sánchez, R.-V.; Li, C.; Pacheco, F.; Cabrera, D.; Valente de Oliveira, J.; Vásquez, R.E. A review on data-driven fault severity assessment in rolling bearings. *Mech. Syst. Signal Process.* **2018**, *99*, 169–196. [CrossRef]
22. Reshef David, N.; Reshef Yakir, A.; Finucane Hilary, K.; Grossman Sharon, R.; McVean, G.; Turnbaugh Peter, J.; Lander Eric, S.; Mitzenmacher, M.; Sabeti Pardis, C. Detecting novel Associations in large data sets. *Science* **2011**, *334*, 1518–1524. [CrossRef]
23. Jiang, Y.; Li, C.; Yang, Z.; Zhao, Y.; Wang, X. Remaining useful life estimation combining two-step maximal information coefficient and temporal convolutional network with attention mechanism. *IEEE Access* **2021**, *9*, 16323–16336. [CrossRef]
24. Ji, H.; Huang, S.; Wu, Y.; Hui, Z.; Lv, X. In A New attribute selection method based on maximal information coefficient and automatic clustering. In Proceedings of the 2017 International Conference on Dependable Systems and Their Applications (DSA), Beijing, China, 31 October–2 November 2017; pp. 22–28.
25. Zhao, L.; Zhang, Y.; Li, J. Research on constructing a degradation index and predicting the remaining useful life for rolling element bearings of complex equipment. *J. Mech. Sci. Technol.* **2021**, *35*, 4313–4327. [CrossRef]
26. Liu, F.; Li, L.; Liu, Y.; Cao, Z.; Yang, H.; Lu, S. HKF-SVR optimized by Krill Herd algorithm for coaxial bearings performance degradation prediction. *Sensors* **2020**, *20*, 660. [CrossRef]
27. Liu, Z.; Guo, Y. In A neural network approach for prediction of bearing performance degradation tendency. In Proceedings of the 2017 9th International Conference on Modelling, Identification and Control (ICMIC), Kunming, China, 10–12 July 2017; pp. 204–208.
28. Bao, H.; Yan, Z.; Ji, S.; Wang, J.; Jia, S.; Zhang, G.; Han, B. An enhanced sparse filtering method for transfer fault diagnosis using maximum classifier discrepancy. *Meas. Sci. Technol.* **2021**, *32*, 085105. [CrossRef]
29. Park, K.; Choi, Y.; Choi, W.J.; Ryu, H.; Kim, H. LSTM-based battery remaining useful life prediction with multi-channel charging profiles. *IEEE Access* **2020**, *8*, 20786–20798. [CrossRef]
30. Xia, J.; Feng, Y.; Lu, C.; Fei, C.; Xue, X. LSTM-based multi-layer self-attention method for remaining useful life estimation of mechanical systems. *Eng. Fail. Anal.* **2021**, *125*, 105385. [CrossRef]
31. Wu, S.; Jiang, Y.; Luo, H.; Yin, S. Remaining useful life prediction for ion etching machine cooling system using deep recurrent neural network-based approaches. *Control Eng. Pract.* **2021**, *109*, 104748. [CrossRef]
32. Cho, K.; Merrienboer, B.V.; Gulcehre, C.; Ba Hdanau, D.; Bougares, F.; Schwenk, H.; Bengio, Y.J.C.S. Learning phrase representations using RNN encoder-decoder for statistical machine translation. In Proceedings of the 2014 Conference on Empirical Methods in Natural Language Processing (EMNLP), Doha, Qatar, 25–29 October 2019; pp. 1724–1734.
33. Chen, J.; Jing, H.; Chang, Y.; Liu, Q. Gated recurrent unit based recurrent neural network for remaining useful life prediction of nonlinear deterioration process. *Reliab. Eng. Syst. Saf.* **2019**, *185*, 372–382. [CrossRef]
34. Du, B.; He, Y.; An, B.; Zhang, C. Remaining useful performance estimation for complex analog circuit based on maximal information coefficient and bidirectional gate recurrent unit. *IEEE Access* **2020**, *8*, 102449–102466. [CrossRef]
35. Lu, Y.-W.; Hsu, C.-Y.; Huang, K.-C. An autoencoder gated recurrent unit for remaining useful life prediction. *Processes* **2020**, *8*, 1155. [CrossRef]

36. Huang, N.E.; Shen, Z.; Long, S.R.; Wu, M.C.; Shih, H.H.; Zheng, Q.; Yen, N.C.; Tung, C.C.; Liu, H.H.J.P.M.P.; Sciences, E. The empirical mode decomposition and the Hilbert spectrum for nonlinear and non-stationary time series analysis. *Proc. R. Soc. Lond. A* **1998**, *454*, 903–995. [CrossRef]
37. Dragomiretskiy, K.; Zosso, D. Variational mode decomposition. *IEEE Trans. Signal Process.* **2014**, *62*, 531–544. [CrossRef]
38. He, X.; Luo, J.; Zuo, G.; Xie, J. Daily runoff Forecasting using a hybrid model based on variational mode decomposition and deep neural networks. *Water Resour. Manag.* **2019**, *33*, 1571–1590. [CrossRef]
39. Xiao, F.; Yang, D.; Guo, X.; Wang, Y. VMD-based denoising methods for surface electromyography signals. *J. Neural Eng.* **2019**, *16*, 056017. [CrossRef] [PubMed]
40. He, X.; Luo, J.; Li, P.; Zuo, G.; Xie, J. A hybrid model based on variational mode decomposition and gradient boosting regression tree for monthly runoff forecasting. *Water Resour. Manag.* **2020**, *34*, 865–884. [CrossRef]
41. Ali, M.; Khan, A.; Rehman, N.U. Hybrid multiscale wind speed forecasting based on variational mode decomposition. *Int. Trans. Electr. Energy Syst.* **2018**, *28*, e2466. [CrossRef]
42. Liang, T.; Zhang, Q.; Liu, X.; Lou, C.; Liu, X.; Wang, H. Time-frequency maximal information coefficient method and its application to functional corticomuscular coupling. *IEEE Trans. Neural Syst. Rehabil. Eng.* **2020**, *28*, 2515–2524. [CrossRef] [PubMed]
43. Chen, T.; Guestrin, C. In XGBoost: A scalable tree boosting system. In Proceedings of the 22nd ACM SIGKDD International Conference, Association for Computing Machinery, San Francisco, CA, USA, 13–17 August 2016; pp. 785–794.
44. Wang, Y.; Wang, T. Application of improved lightGBM model in blood glucose prediction. *Appl. Sci.* **2020**, *10*, 3227. [CrossRef]
45. Zhang, Y.; Zhu, C.; Wang, Q. LightGBM-based model for metro passenger volume forecasting. *IET Intell. Transp. Syst.* **2021**, *14*, 1815–1823. [CrossRef]
46. Bertsekas, D.P. *Constrained Optimization and Lagrange Multiplier Methods. Constrained Optimization and Lagrange Multiplier Methods*; Academic Press: Cambridge, MA, USA, 1982.
47. Liu, Y.; Yang, C.; Huang, K.; Gui, W. Non-ferrous metals price forecasting based on variational mode decomposition and LSTM network. *Knowl. Based Syst.* **2020**, *188*, 105006. [CrossRef]
48. Wang, Y.; Zou, R.; Liu, F.; Zhang, L.; Liu, Q. A review of wind speed and wind power forecasting with deep neural networks. *Appl. Energy* **2021**, *304*, 117766. [CrossRef]
49. Li, C.; Tang, G.; Xue, X.; Saeed, A.; Hu, X. Short-Term Wind Speed Interval Prediction Based on Ensemble GRU Model. *IEEE Trans. Sustain. Energy* **2020**, *11*, 1370–1380.
50. Yu, J.; Jang, J.; Yoo, J.; Park, J.H.; Kim, S. A fault isolation method via classification and regression tree-based variable ranking for drum-type steam boiler in thermal power plant. *Energies* **2018**, *11*, 1142. [CrossRef]
51. Lei, Y.; Lin, J.; He, Z.; Zuo, M.J. A review on empirical mode decomposition in fault diagnosis of rotating machinery. *Mech. Syst. Signal Process.* **2013**, *35*, 108–126. [CrossRef]

energies

MDPI

Article

Piecewise Causality Study between Power Load and Vibration in Hydro-Turbine Generator Unit for a Low-Carbon Era

Lianda Duan [1,2], Dekuan Wang [1,2], Guiping Wang [1,2], Changlin Han [1,2], Weijun Zhang [1,2], Xiaobo Liu [1,2], Cong Wang [1,3,*], Zheng Che [1] and Chang Chen [1,2]

[1] China Institute of Water Resources and Hydropower Research, Beijing 100038, China; duanldiwhr@163.com (L.D.); wdk@iwhr.com (D.W.); wang_gp@iwhr.com (G.W.); jkhancl@iwhr.com (C.H.); jkzhangwj@iwhr.com (W.Z.); liuxb@iwhr.com (X.L.); chezheng0314@163.com (Z.C.); chenciwhr@163.com (C.C.)
[2] Beijing IWHR Technology Co., Ltd., Beijing 100038, China
[3] CREC Cloud Net Information Technology Co., Ltd., Beijing 100039, China
* Correspondence: hywangcong@163.com

Abstract: With the rapid development of wind and photovoltaic power generation, hydro-turbine generator units have to operate in a challenging way, resulting in obvious vibration problems. Because of the significant impact of vibration on safety and economical operation, it is of great significance to study the causal relationship between vibration and other variables. The complexity of the hydro-turbine generator unit makes it difficult to analyze the causality of the mechanism. This paper studied the correlation based on a data-driven method, then transformed the correlation into causality based on the mechanism. In terms of correlation, traditional research only judges whether there is a correlation between all data. When the data with correlation are interfered with by the data without correlation, the traditional methods cannot accurately identify the correlation. A piecewise correlation method based on change point detection was proposed to fill this research gap. The proposed method segmented time series pairs, then analyzed the correlation between subsequences. The causality between power load and vibration of a hydro-turbine generator unit was further analyzed. It indicated that when the power load is less than 200 MW, the causality is weak, and when the power load is greater than 375 MW, the causality is strong. The results show that the causality between vibration and power load is not fixed but piecewise. Furthermore, the piecewise correlation method compensated for the limitation of high variance of the maximum information coefficient.

Keywords: high proportional renewable power system; active power; change point detection; maximum information coefficient; cosine similarity; anomaly detection

Citation: Duan, L.; Wang, D.; Wang, G.; Han, C.; Zhang, W.; Liu, X.; Wang, C.; Che, Z.; Chen, C. Piecewise Causality Study between Power Load and Vibration in Hydro-Turbine Generator Unit for a Low-Carbon Era. *Energies* **2022**, *15*, 1207. https://doi.org/10.3390/en15031207

Academic Editors: Chaoshun Li, Yun Zeng, Beibei Xu, Chirag Trivedi and Dong Liu

Received: 3 January 2022
Accepted: 3 February 2022
Published: 7 February 2022

1. Introduction

Under the guidance of carbon peak and carbon neutralization, many renewable energy sources such as wind power and photovoltaic have grown rapidly in recent years [1,2]. As renewable energy is easily affected by the natural environment, power load often fluctuates [3]. This requires the power grid to have reliable peak and frequency regulation capabilities [4]. The hydro-turbine generator units (HTGUs) are essential equipment for peak and frequency regulation [5,6]. Moreover, hydropower accounts for a large proportion in Southwest China [7,8].

In this context, HTGUs have to operate in a challenging way, which is in contradiction with the goal of safe and stable operation. Under the challenging operation mode, the vibration of HTGUs is a problem worthy of study. Approximately 90% of the failures are reflected in vibration [9,10]. Vibration may cause an unstable rotation speed of the HTGUs and unbalanced flow channel pressure, which eventually causes the unit to fail to operate safely and stably [11]. In addition, vibration also affects the efficiency of HTGUs [12]. Therefore, there is an urgent need to study vibration.

In general, HTGUs can be divided into three subsystems: hydraulic, mechanical, and electrical subsystem. The three subsystems are coupled together, forming a complex nonlinear system [13,14]. The vibration of this kind of complex system has induced scholars to carry out a lot of research, most of which studies vibration from the view of dynamic models.

Xu et al. proposed a finite element dynamic model to simulate vibration [15]. Zeng et al. established a generalized Hamiltonian system including the lateral vibration equation of the shaft system and the generator equation [16]. Li et al. constructed the stator pack structural model and the electrical model of the generator and used the finite element method for electrical simulation. The source of abnormal vibration can be found by comparing the generated vibration data with real data. [17]. Li et al. constructed a nonlinear dynamic model considering the gyroscopic effect [18]. Zhao et al. proposed a condition indicator called artificial damage index based on dynamic analysis, which can be used to detect the vibration of Pelton turbines [1]. Xu et al. used nonlinear modal methods to analyze the interaction between subsystems [13]. Sun et al. proposed a method to study the overall nonlinear dynamics of the generator-shaft-foundation coupling system and studied the influence of the foundation system and related parameters on vibration [19]. Shi et al. proposed a mathematical model of HTGU unbalanced rotor bending-torsional coupling vibration considering the arcuate whirl of the shafting [20].

The above studies explained the mechanism of vibration from the view of dynamic models. However, building a comprehensive model is complex and difficult [11]; for example, draft tube pressure pulsation is difficult to model [21]. The data-driven approach is a new direction. Bi et al. used data-driven methods to analyze the correlation between vibration and other variables, and used highly correlated variables and historical vibration data to predict vibration [22]. However, correlation does not imply causation. In addition, the operation and maintenance personnel of the power plant are more concerned about the main factors causing the vibration and the time series causality between the vibration and other variables. Recently, studies on causality have been very fruitful. So, studying the cause of vibration from the perspective of causality can ascertain the cause of vibration and lay the foundation for anomaly detection.

Many studies on time series causality have been conducted. Granger introduced time flow into the study of causality and proposed a method to evaluate causality in a two-variable time series [23]. On this basis, a number of Granger-like causality detection methods have been developed [24–27]. Schreiber first introduced transfer entropy in information theory into the study of causality [28]. On this basis, a number of causality detection methods based on information theory have been developed [29,30]. Sugihara et al. proposed a convergent cross map suitable for detecting nonlinear causality [31]. However, none of the above methods were designed for vibration research. Granger causality studied the causality in the economic field, and convergence cross-mapping studied the causality between the prey and the predator.

In general, the more data, the better, but this is not necessarily the case in actual situations. The state of HTGUs is changeable. Here, three reasons behind the change are analyzed. First, an installation error occurs when installing the shaft [32]. Second, when the power load changes, the deformation of the shaft [33] also changes. Third, with the accumulation of operation time, the parameters of HTGUs may change [34,35]. The above reasons lead to the fact that the causality between vibration and other variables is not fixed but presents piecewise characteristics. A piecewise causality analysis method is proposed to study this complex causality. It should be noted that this paper only studies the causal relationship between vibration and a single variable, but does not study the causal relationship between vibration and multiple variables.

This paper has three main innovations compared with previous studies:

1. A kind of piecewise causality was proposed. According to the mechanism of HTGU, piecewise correlation was used to replace piecewise causality.

2. A piecewise correlation analysis method based on change point detection and correlation analysis was proposed. The interference of data without correlation was effectively avoided.
3. It was found that MIC has the problem of high variance. This paper used cosine similarity instead of MIC to avoid high variance.

2. Methods

This paper studies causality piecewise by utilizing piecewise correlation. The difference between the correlation and causality of the two variables is that the latter has directional information, which reveals whether the variable is cause or consequence. The piecewise causality can be obtained based on piecewise correlation and directional information. Section 2.1 gets the directional information from the mechanism, and Section 2.2 investigates the piecewise correlation quantitatively.

2.1. Mechanism Analysis

From the perspective of unbalanced forces, three kinds of unbalanced forces: unbalanced hydraulic force, unbalanced electrical force, and unbalanced mechanical force, act together to cause the vibration of the HTGU [36]. The unbalanced hydraulic force refers to the disturbing force generated by the water flow to the flow parts of the turbine. The hydraulic unbalance is mainly caused by cavitation occurring on the draft tube and runner. Cavitation is closely related to power load [12,37,38]. In other words, the power load affects the hydraulic imbalance.

The unbalanced mechanical force refers to the inertia and friction of the mechanical part. The unbalanced mechanical force is mainly caused by the misalignment of the rotor shaft system and insufficient shaft system rigidity. After the installation of the HTGU is completed, the degree of shafting misalignment can be considered unchanged when the HTGU is at a standstill. However, when the HTGU is rotating, the shaft system will be deformed [33]. Moreover, as the power load becomes larger, the shafting force becomes larger, resulting in greater bearing deformation and further aggravation of shaft misalignment, leading to greater unbalanced mechanical force [39].

The unbalanced electrical force refers to the radial unbalanced magnetic force caused by the uneven air gap of the generator. The uneven air gap is mainly caused by the misalignment of the shafting, and the misalignment of the shafting is closely related to the power load [39]. In addition, as the excitation current increases, the unbalanced electrical force becomes larger. The excitation current mainly depends on the change of power load and reactive power [40].

From the analysis of the above three types of unbalanced forces, the power load affects the three kinds of unbalanced force simultaneously, and finally affects the vibration of the HTGU. The power load has made the main contribution to the unbalanced force, so the paper studies the influence of the power load on the vibration.

2.2. Piecewise Causality Based on Change Point Detection

This paper proposes a combined algorithm (CPDC) based on change point detection [41] and correlation analysis. The change point detection acts as a segmenter, and the correlation analysis acts as a comparator. CPDC is used to explore the piecewise causality between power load and vibration. The exploration process can be divided into four steps: change point detection, change point matching, correlation analysis, and causality detection.

To clearly illustrate the proposed CPDC method, change point detection is briefly introduced first. Change point detection assumes piecewise stationary to segment the time series. A series of change points divide the time series into a subseries, in which the data in each subseries have similar statistical characteristics. In this paper, the number of change points in time series is uncertain. The change point detection used in this paper is an optimization problem with constraints. Linear penalty function and kernel-based loss

function are used to construct the objective function to deal with constrained optimization problems. Fortunately, this objective function can be optimized by the PELT algorithm, which has linear complexity [41].

1. Change point detection. Change points can be obtained by change point detection. The change point detection method based on the Gaussian kernel is selected for the unknown number of change points in the time series of interest and the unclear probability distribution. Taking the active power time series as an example, the number of active power changes is uncertain and random [14,42]. The specific change point detection algorithm can be found in Ref. [41].
2. Change point matching. When the difference between the two change points from the two-variable time series does not exceed the threshold, the two change points are said to match each other. Change points that cannot match each other often appear in actual situations. The augmented change point is proposed to divide the two-variable time series into subsequences aligned. When the change points can match each other, the larger change point is taken as the augmented change point; when the change points cannot match, the two change points are both used as the augmented change points. All augmented change points are arranged in ascending order to form an augmented change point sequence. As shown in Figure 1, the first change points of two lines P_1 and P_2 are relatively close and can match each other. Therefore, P_2 can replace P_1 and P_2 as the augmented change point. The second change points of two lines P_3 and P_4 are far apart and cannot match each other. Therefore, both P_3 and P_4 are kept as augmented change points. The augmented change point sequence formed by the change points in Figure 1 is $\{P_2, P_3, P_4\}$.
3. Correlation analysis. The augmented change point sequence obtained above can extract subsequences from the time series. According to a time range, two subsequences are extracted from the time series x and y. The time range of the subsequence x_{i} and y_{i} corresponding to the augmented change point $\mathrm{P_i}$ is $\mathrm{P_{i-1}}$ to $\mathrm{P_{i+1}}$. Then, x_{i} and y_{i} are normalized by MinMaxScaler, respectively. Finally, cosine similarity s_i between x_{i} and y_{i} is calculated by formulation:

$$s_i = \frac{x_i \cdot y_i}{\|x_i\| \|y_i\|}$$

   forming the cosine similarity sequence s.
4. Causality detection. It is considered that the causality between the subsequences is weak when the cosine similarity is less than the set threshold. On the contrary, it is believed that the causality is strong.

Although only CPCD mentioned in Section 2.2 is used in calculating piecewise causality, the mechanism analysis in Section 2.1 is the basis of CPCD, which builds a bridge between correlation and causality. This will be explained in detail in Section 4.2. In general, a data-driven approach based on domain knowledge is proposed, which is different from the model-based approach.

The proposed method obtains directional information from domain knowledge and piecewise correlations from the data, and fuses the two to obtain piecewise causality. This fusion is an effective use of domain knowledge and data. Significantly, the proposed piecewise correlations effectively solve the problems of traditional correlations. Figure 2 is a simple example that cannot be analyzed by the traditional correlation method. There is no correlation between the two curves in the left half, but there is a correlation between the two curves in the right half. The traditional method arbitrarily considers that there is no correlation between these two curves or that there is a correlation between these two curves. This problem can be handled well using the piecewise correlation method.

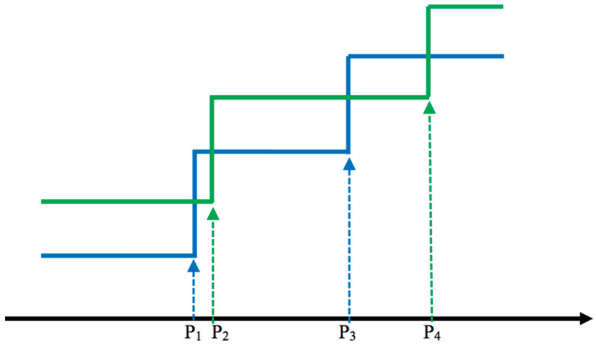

Figure 1. Schematic diagram of augmented change point.

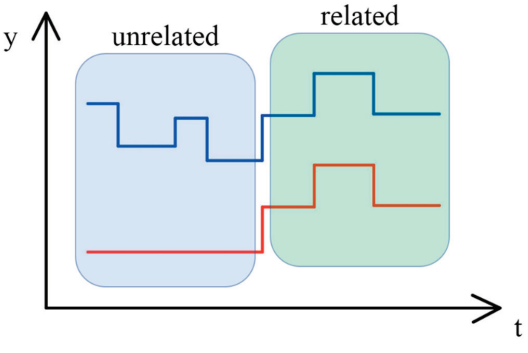

Figure 2. Schematic diagram of augmented change point.

3. Results

The measured data came from an HTGU, consisting of a Francis turbine and a vertical-shaft semi-umbrella generator, with a rated speed of 125 r/min and a rated power of 600 MW.

We used active power (P) and the peak-to-peak value of vibration in the X direction of the upper guide bearing (V_{ugx}) to quantify power load and vibration, respectively, and then studied the piecewise causality between power load and vibration based on these two variables. The following explains why these two variables were used for research.

For an HTGU, under a specific water head, both the turbine's flow rate and the generator's P can be used to measure the power load. However, since the relative error of P is less than that of the flow rate, and the water head is often time changing, P is selected to measure the power load.

There are two main types of vibration: radial vibration and axial vibration. This paper focuses on radial vibration, including upper guide swing, lower guide swing, and water guide swing. Figure 3 is used to explain why the upper guide was chosen for the study. It shows that the peak-to-peak value of the upper guide is almost twice as large as that of the lower guide and water guide. In addition, the sensors for measuring the three X-direction vibrations are with the same measurement accuracy. V_{ugx} was chosen to measure the vibration, considering that the relative error of V_{ugx} is the smallest.

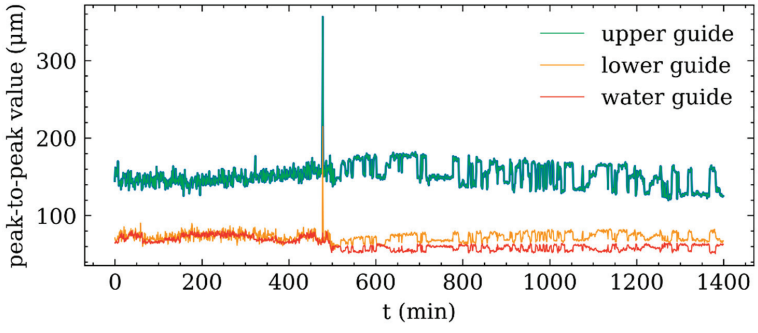

Figure 3. The peak-to-peak value of the swing of the three guide bearings.

We collected P and V_{ugx} time series data with a time length of 1400 and a sampling interval of 1 min. The collected data are shown in Figure 4a,b, which shows that the relationship between V_{ugx} and P is complex. The following content analyzes this complex relationship in detail.

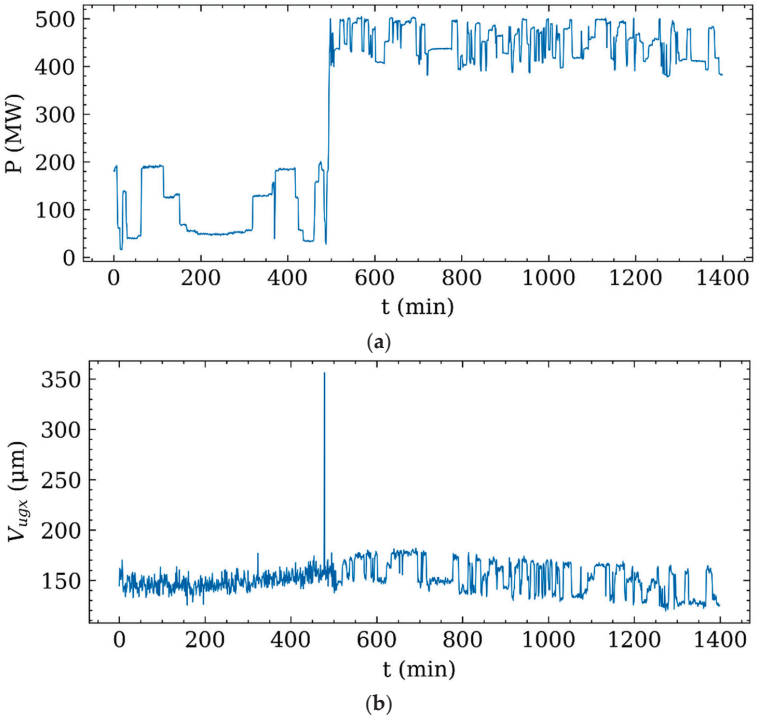

Figure 4. (**a**) Line graph of P. (**b**) Line graph of V_{ugx}. Although there is a spike in the figure, a single abnormal point has almost no effect on the change point detection and correlation calculation. Therefore, no special treatment is required for this spike.

In the change point detection step, the kernel change point detection (kernelCPD) in the Python package ruptures was used to segment the time series [41]. The specific parameter selection is shown in Table 1.

Table 1. Key parameters in change point detection.

Item	Parameter
kernel function	$k(x,y) = exp(-\gamma\|x-y\|^2)$
kernel parameter γ	0.1
minimum segment length	10
penalty value	3

The change point difference threshold is 5 in the change point matching step. The correlation threshold is 0.95 in the causal detection step.

The results of segmenting P and V_{ugx} are shown in Figure 5a,b, respectively. They show that the change points of P are very different from those of V_{ugx} in the first 509 data.

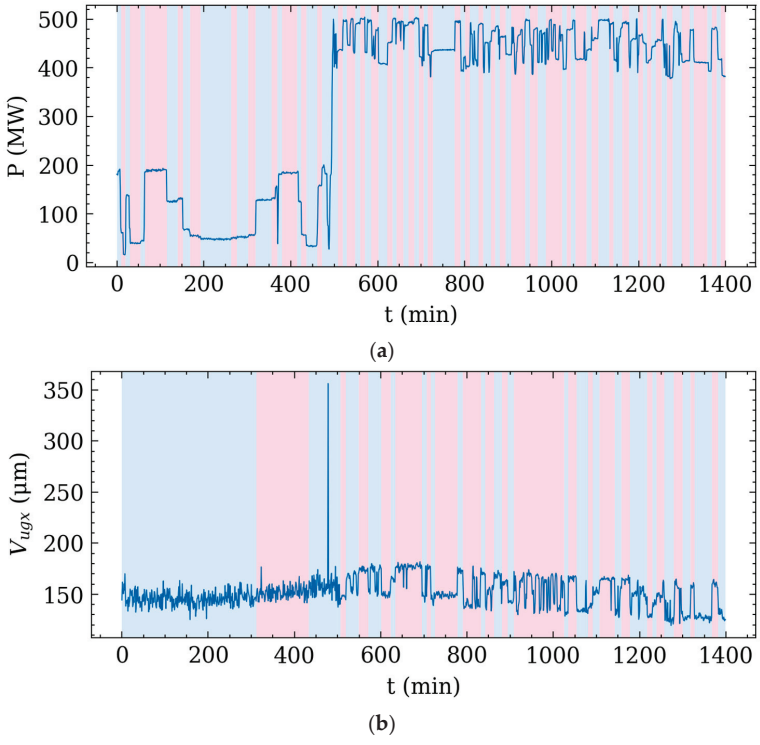

Figure 5. (**a**) The result obtained by segmenting P. (Different background colors for different segments.) (**b**) The result obtained by segmenting V_{ugx}. (Different background colors are used to distinguish different segments).

Figure 5a,b present the intermediate results of the piecewise causality analysis. They show that the number of change points of P is much more than that of V_{ugx}. Firstly, the fluctuation of P is relatively small, which makes the change points of P easier to find. Secondly, the change of P does not necessarily cause the change of V_{ugx}.

P and V_{ugx} are segmented according to the same change point sequence by change point matching. Then, the cosine similarities between the subsequences of P and the V_{ugx} are calculated, as shown in Figure 6. The larger the correlation coefficient, the stronger the causality between the subsequence of P and that of V_{ugx}.

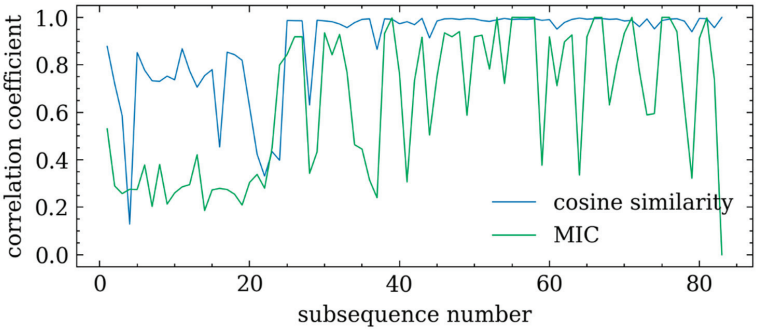

Figure 6. The correlation coefficient between P and V_{ugx} subsequence.

Figure 6 also implements the MIC [43] method to calculate the correlation between the two sequences for comparison. Judging from the line graph of cosine similarity, the first 24 pieces of data are within correlation threshold 0.95, and most of the later data exceed it. From the value of MIC, a similar conclusion can hardly be drawn because the fluctuation of the MIC line graph is greater than the cosine similarity. This will be discussed in detail in Section 4.2.

Figure 6 shows that the causality between P and V_{ugx} is weak in the time range corresponding to 1–24 subsequences, and the causality between P and V_{ugx} is strong in the time range corresponding to 25–83 subsequences. To observe this rule intuitively, the broken line diagrams of 1–23 subsequences, 25–83 subsequences, and 24 subsequences of P and V_{ugx} are presented in Figure 7a–c, respectively.

Figure 7a–c visually reveal when the causality is stronger and when it is weaker. Figure 7a,b show that P corresponding to 1~472 min is smaller, and P corresponding to 509–1400 min is larger. The influence of power load on vibration obtained in Section 2.1 plays a fundamental role here. There is weak causality between P and V_{ugx} when $P < 200$ MW. There is strong causality between P and V_{ugx}, and it reveals that V_{ugx} is predominantly affected by P when $P > 375$ MW. In addition, Figure 7c shows that the causality between P and V_{ugx} is weak when P changes from a small value to a large value.

For comparison, we calculated the correlation coefficients between P and V_{ugx} in the three time periods, and the results are shown in Table 2. Observing by row, it is easy to find that the value gradually increases. This implies that if the segmentation processing is not used, it is likely to be mistaken for simple causality between P and V_{ugx}. P and V_{ugx} only have strong causality during 509–1400 min.

Table 2. The correlation coefficients between P and V_{ugx} in the three time periods.

	1–472 min	**1–1400 min**	**509–1400 min**
cosine	0.867	0.892	0.999
MIC	0.227	0.611	0.886

From the last row of Table 2, it is easy to mistakenly believe that there is no causality between P and V_{ugx} if segmentation is not carried out. In fact, P and V_{ugx} have piecewise causality. The proposed method is a useful supplement to the MIC method.

Finally, it shows that the relationship between power load and the vibration is not a simple causality but a complex piecewise causality.

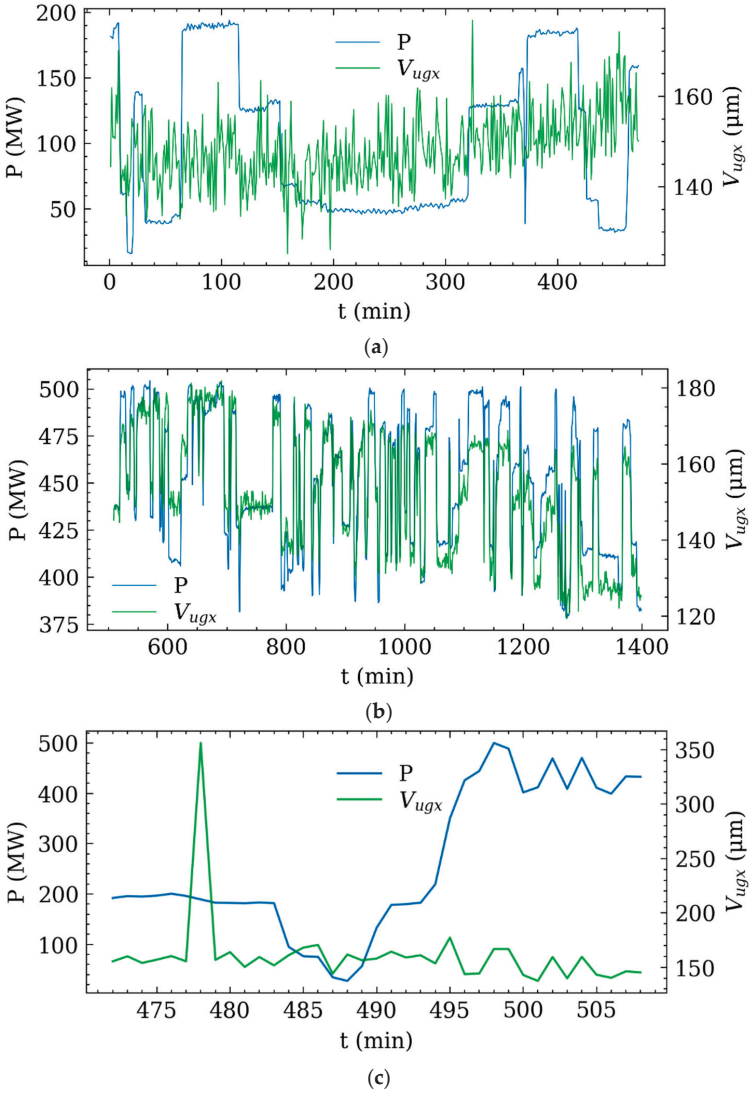

Figure 7. (**a**) P and V_{ugx} corresponding to subsequences 1–23. (**b**) P and V_{ugx} corresponding to subsequences 25–83. (**c**) P and V_{ugx} corresponding to the 24th subsequence.

4. Discussion

4.1. Compare the Difference of MIC and Cosine Similarity Based on Variance

Both MIC [43] and cosine similarity can measure the degree of correlation between the two sets of data, but from Figure 5, the value of MIC fluctuates far more than the cosine similarity. This kind of fluctuation brings great difficulties to the analysis of piecewise causality.

We used simulated data to evaluate the variance of MIC and cosine similarity. Take three random variables x, y, and z, where $y = 2x + 0.5\varepsilon$, $z = 2x + \varepsilon$, and x and ε both obey the standard normal distribution. Randomly generate x, y, and z samples $\{x_1, x_2, \ldots x_n\}$, $\{y_1, y_2, \ldots y_n\}$, and $\{z_1, z_2, \ldots z_n\}$, where n is the sample size. Here, we set $n = 100$. Normalize the three sets of samples by MaxMinScaler, respectively. Calculate the MIC and cosine similarity. Repeat the test 100 times, and the results are shown in Figure 8.

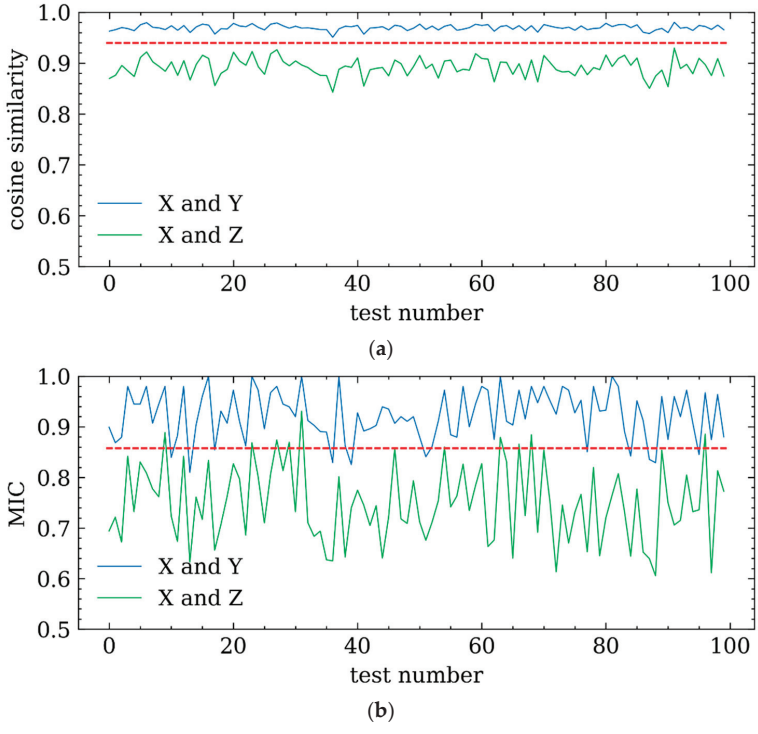

Figure 8. (**a**) Cosine similarity calculated by simulation test. (**b**) MIC calculated by simulation test.

Figure 8a,b can intuitively reveal why cosine similarity is better than MIC. In Figure 8a, the blue line represents the cosine similarity between X and Y obtained in 100 trials, and the green line represents the cosine similarity between X and Z obtained in 100 trials. In Figure 8b, the blue line represents the MIC between X and Y obtained in 100 trials, and the green line represents the MIC between X and Z obtained in 100 trials. The dotted line in Figure 8a can distinguish the blue line and the green line well, but the dotted line in Figure 8b cannot. This implies that the cosine similarity is more capable of distinguishing the strength of the correlation relationship than the MIC. The blue and green lines in Figure 8b fluctuate greatly and are intertwined together, which makes it impossible to distinguish well. The fluctuation of the line can be measured by variance. Next, from the perspective of variance, further, we analyze the difference between MIC and cosine similarity.

The following only considers the correlation coefficient between X and Z. The variance of the MIC and cosine similarity calculation results are calculated under different sample sizes to further study fluctuation. Table 3 shows that the larger the sample size n, the smaller the variance. When the sample size n is the same, the variance of the cosine similarity is smaller than that of MIC. It shows that cosine similarity can more stably measure the correlation than MIC. For this paper, where the amount of data is small, cosine similarity is more appropriate.

Table 3. The variance of cosine similarity and MIC calculated from the samples.

Variance	n = 10	n = 100	n = 1000
cosine	7.89×10^{-3}	3.77×10^{-4}	4.565×10^{-5}
MIC	4.94×10^{-2}	4.83×10^{-3}	6.48×10^{-4}

4.2. Correlation and Causality

Cosine similarity is an uncentralized Pearson correlation coefficient [44]. Correlation is one of the main methods to quantify causality but loses the causal relationship's directional information [45]. For example, there is a strong correlation between M and N. Still, from the strong correlation alone, it cannot be concluded that M leads to N or N leads to M. Section 2.1 clarifies how power load affects vibration by qualitatively studying the causality between power load and vibration. With the directional information provided by a qualitative study, correlations can reveal causality to a certain extent.

4.3. Piecewise Causality

Figures 5–7 show that the causality between P and V_{ugx} is strong when P is large. In addition, the causality between P and V_{ugx} is weak when P is small. This seems to be somewhat contradictory to the analysis in Section 2.1, but this is normal. This is because when P is small, the HTGU is in an unstable zone. This leads to large fluctuations of V_{ugx}, and V_{ugx} does not change with P.

The above complex causality is piecewise causality. This segmented operation is necessary and meaningful in the changeable industrial environment.

4.4. Advantages and Limitations

Bi et al. [22] believe that there is a strong correlation between P and V_{ugx}. However, the results show that the relationship between P and V_{ugx} is not stable but has a piecewise causality. In other words, the causality is strong in one section and weak in another section. The stable relationship between P and V_{ugx} is the basis for predicting V_{ugx} based on data such as P. This instability will affect some data processing tasks and deserves attention.

CPDC is suitable for analyzing piecewise causality. In addition, CPDC focuses on the data around the change point instead of the entire data, which reduces the amount of data that needs to be processed. The limitation of CPDC is that the change point detection method assumes that the data is piecewise stationary, and further research is needed for situations that do not meet this assumption.

5. Conclusions

Based on the domain knowledge and data-driven method of HTGUs, this paper proposed CPDC to study the piecewise causal relationship between vibration and power load. In this paper, the active power and vibration peak value of the upper guide bearing of HTGU were selected as the typical observation of power load and vibration, respectively. The piecewise correlation between vibration and power load was quantitatively studied by change point detection and correlation analysis methods. Further, based on the domain knowledge of HTGUs, the piecewise causal relationship between vibration and power load was clarified. The traditional correlation method cannot handle the case of segmentation of correlation, and the proposed piecewise correlation method solved this problem well. Three main conclusions are drawn. Firstly, from the qualitative analysis of mechanical, electrical, and hydraulic aspects, there is a causal relationship between power load and vibration. Among them, the power load is the cause, and the vibration is the result. Secondly, for a specific HTGU, the causal relationship between power load and the vibration is piecewise. Specifically, when the power load is small, the causal relationship between power load and the vibration is weak. When the power load is large, the causal relationship between the two is vital. Thirdly, from the perspective of statistical calculation, the variance of cosine similarity estimated by samples is less than that of MIC. The CPDC method proposed can find the piecewise correlation without being disturbed by the part without correlation. CPDC has value in studying the complex causality between vibration and other variables, and may also be applied to similar complex correlation studies.

Author Contributions: Conceptualization, L.D.; funding acquisition, G.W., C.H., and W.Z.; methodology, L.D.; project administration, D.W., X.L., and C.W.; validation, L.D.; visualization, C.C.; writing—

original draft, L.D.; writing—review and editing, D.W., C.W., X.L., and Z.C. All authors have read and agreed to the published version of the manuscript.

Funding: This research was funded by the IWHR Research & Development Support Program of China under grant AU0145B022021 and AU0145B032021.

Institutional Review Board Statement: Not applicable.

Informed Consent Statement: Not applicable.

Data Availability Statement: Not applicable.

Conflicts of Interest: The authors declare no conflict of interest.

Nomenclature

CPDC	change point detection and correlation analysis
HTGU	hydro-turbine generator units
kernelCPD	kernel change point detection
MIC	maximum information coefficient
P	active power
V_{lgx}	peak-to-peak value of vibration in X direction of the lower guide bearing
V_{ugx}	peak-to-peak value of vibration in X direction of the upper guide bearing
V_{wgx}	peak-to-peak value of vibration in X direction of the water guide bearing

References

1. Zhao, W.; Egusquiza, M.; Estevez, A.; Presas, A.; Valero, C.; Valentín, D.; Egusquiza, E. Improved damage detection in Pelton turbines using optimized condition indicators and data-driven techniques. *Struct. Health Monit.* **2021**, *20*, 3239–3251. [CrossRef]
2. Yang, Z.; Sun, G.; Behrens, P.; Østergaard, P.A.; Egusquiza, M.; Egusquiza, E.; Xu, B.; Chen, D.; Patelli, E. The potential for photovoltaic-powered pumped-hydro systems to reduce emissions, costs, and energy insecurity in rural China. *Energy Convers. Manag. X* **2021**, *11*, 100108. [CrossRef]
3. Saeed, A.; Li, C.; Gan, Z.; Xie, Y.; Liu, F. A simple approach for short-term wind speed interval prediction based on independently recurrent neural networks and error probability distribution. *Energy* **2022**, *238*, 122012. [CrossRef]
4. Feng, C.; Zheng, Y.; Li, C.; Mai, Z.; Wu, W.; Chen, H. Cost advantage of adjustable-speed pumped storage unit for daily operation in distributed hybrid system. *Renew. Energy* **2021**, *176*, 1–10. [CrossRef]
5. Zhao, W.; Egusquiza, M.; Valero, C.; Valentín, D.; Presas, A.; Egusquiza, E. On the use of artificial neural networks for condition monitoring of pump-turbines with extended operation. *Measurement* **2020**, *163*, 107952. [CrossRef]
6. Xiong, H.; Egusquiza, M.; Alberg Østergaard, P.; Pérez-Díaz, J.I.; Sun, G.; Egusquiza, E.; Patelli, E.; Xu, B.; Duan, H.; Chen, D.; et al. Multi-objective optimization of a hydro-wind-photovoltaic power complementary plant with a vibration avoidance strategy. *Appl. Energy* **2021**, *301*, 117459. [CrossRef]
7. Wang, C.; Wang, D.; Zhang, J. Experimental Study on the Optimal Strategy for Power Regulation of Governing System of Hydropower Station. *Water* **2021**, *13*, 421. [CrossRef]
8. Wang, C.; Wang, D.; Zhang, J. Experimental study on isolated operation of hydro-turbine governing system of Lunzua hydropower station in Zambia. *Renew. Energy* **2021**, *180*, 1237–1247. [CrossRef]
9. Kahraman, G.; Ozdemir, O. Mathematical modeling of vibration failure caused by balancing effect in hydraulic turbines. *Mech. Based Des. Struct. Mach.* **2021**. [CrossRef]
10. Luo, J.; Wang, X.; Xu, Y. Vibration fault diagnosis for hydroelectric generating unit based on generalized S-transform and QPSO-SVM. In Proceedings of the 2019 IEEE Sustainable Power and Energy Conference (iSPEC), Beijing, China, 21–23 November 2019; pp. 2133–2137. [CrossRef]
11. Xu, B.; Zhang, J.; Egusquiza, M.; Chen, D.; Li, F.; Behrens, P.; Egusquiza, E. A review of dynamic models and stability analysis for a hydro-turbine governing system. *Renew. Sustain. Energy Rev.* **2021**, *144*, 110880. [CrossRef]
12. Celebioglu, K.; Altintas, B.; Aradag, S.; Tascioglu, Y. Numerical research of cavitation on Francis turbine runners. *Int. J. Hydrog. Energy* **2017**, *42*, 17771–17781. [CrossRef]
13. Xu, B.; Luo, X.; Egusquiza, M.; Ye, W.; Liu, J.; Egusquiza, E.; Chen, D.; Guo, P. Nonlinear modal interaction analysis and vibration characteristics of a francis hydro-turbine generator unit. *Renew. Energy* **2021**, *168*, 854–864. [CrossRef]
14. Zhang, H.; Chen, D.; Xu, B.; Patelli, E.; Tolo, S. Dynamic analysis of a pumped-storage hydropower plant with random power load. *Mech. Syst. Signal Process.* **2018**, *100*, 524–533. [CrossRef]
15. Xu, Y.; Li, Z.; Lai, X. Dynamic Model for Hydro-Turbine Generator Units Based on a Database Method for Guide Bearings. *Shock Vib.* **2013**, *20*, 426849. [CrossRef]
16. Zeng, Y.; Zhang, L.; Guo, Y.; Qian, J.; Zhang, C. The generalized Hamiltonian model for the shafting transient analysis of the hydro turbine generating sets. *Nonlinear Dynam.* **2014**, *76*, 1921–1933. [CrossRef]

17. Li, R.; Li, C.; Peng, X.; Wei, W. Electromagnetic Vibration Simulation of a 250-MW Large Hydropower Generator with Rotor Eccentricity and Rotor Deformation. *Energies* **2017**, *10*, 2155. [CrossRef]
18. Li, J.; Chen, D.; Liu, G.; Gao, X.; Miao, K.; Li, Y.; Xu, B. Analysis of the gyroscopic effect on the hydro-turbine generator unit. *Mech. Syst. Signal Process.* **2019**, *132*, 138–152. [CrossRef]
19. Sun, W.; Guo, Z. Mathematical modeling and nonlinear vibration analysis of a coupled hydro-generator shaft-foundation system. *Commun. Nonlinear Sci. Numer. Simul.* **2021**, *98*, 105776. [CrossRef]
20. Shi, Y.; Zhou, J.; Lai, X.; Xu, Y.; Guo, W.; Liu, B. Stability and sensitivity analysis of the bending-torsional coupled vibration with the arcuate whirl of hydro-turbine generator unit. *Mech. Syst. Signal Process.* **2021**, *149*, 107306. [CrossRef]
21. Zhang, L.; Wu, Q.; Ma, Z.; Wang, X. Transient vibration analysis of unit-plant structure for hydropower station in sudden load increasing process. *Mech. Syst. Signal Process.* **2019**, *120*, 486–504. [CrossRef]
22. Bi, Y.; Zheng, B.; Zhang, Y.; Zhu, X.; Jiang, Y.; Li, C. Vibration trend prediction of hydroelectric generating unit based on MIC and BiGRU. *J. Hydraul. Eng.* **2021**, *52*, 612–621, 632. [CrossRef]
23. Granger, C. Investigating Causal Relations by Econometric Models and Cross-Spectral Methods. *Econometrica* **1969**, *37*, 424–438. [CrossRef]
24. Hu, M.; Liang, H. A copula approach to assessing Granger causality. *Neuroimage* **2014**, *100*, 125–134. [CrossRef]
25. Montalto, A.; Stramaglia, S.; Faes, L.; Tessitore, G.; Prevete, R.; Marinazzo, D. Neural networks with non-uniform embedding and explicit validation phase to assess Granger causality. *Neural Netw.* **2015**, *71*, 159–171. [CrossRef] [PubMed]
26. Siggiridou, E.; Kugiumtzis, D. Granger Causality in Multivariate Time Series Using a Time-Ordered Restricted Vector Autoregressive Model. *IEEE T. Signal Process.* **2016**, *64*, 1759–1773. [CrossRef]
27. Yang, G.; Wang, L.; Wang, X. Reconstruction of Complex Directional Networks with Group Lasso Nonlinear Conditional Granger Causality. *Sci. Rep.* **2017**, *7*, 2991. [CrossRef] [PubMed]
28. Thomas, S. Measuring Information Transfer. *Phys. Rev. Lett.* **2000**, *85*, 461–464. [CrossRef]
29. Kugiumtzis, D. Direct-coupling information measure from nonuniform embedding. *Phys. Rev. E* **2013**, *87*, 062918. [CrossRef]
30. Kugiumtzis, D. Partial transfer entropy on rank vectors. *Eur. Phys. J. Spec. Top.* **2013**, *222*, 401–420. [CrossRef]
31. Sugihara, G.; May, R.; Ye, H.; Hsieh, C.h.; Deyle, E.; Fogarty, M.; Munch, S. Detecting Causality in Complex Ecosystems. *Science* **2012**, *338*, 496–500. [CrossRef]
32. An, X. *Vibration Characteristics and Fault Diagnosis for Hydraulic Generator Units*; Huazhong University of Science & Technology: Wuhan, China, 2009.
33. Pennacchi, P.; Borghesani, P.; Chatterton, S. A cyclostationary multi-domain analysis of fluid instability in Kaplan turbines. *Mech. Syst. Signal Process.* **2015**, *60–61*, 375–390. [CrossRef]
34. Xu, B.; Chen, D.; Li, H.; Yan, D. Effects of parameter variation on a Pelton hydropower station system's shafting vibration. *J. Vib. Shock* **2019**, *38*, 10–18. [CrossRef]
35. Xu, B.; Chen, D.; Zhang, H.; Li, C.; Zhou, J. Shaft mis-alignment induced vibration of a hydraulic turbine generating system considering parametric uncertainties. *J. Sound Vib.* **2018**, *435*, 74–90. [CrossRef]
36. Yan, D.; Chen, Q.; Zheng, Y.; Liu, W. Parameter sensitivity and dynamic characteristic analysis of bulb hydro generating unit with shaft crack fault. *Mech. Syst. Signal Process.* **2021**, *158*, 107732. [CrossRef]
37. Pereira, J.G., Jr.; Favrel, A.; Andolfatto, L.; Landry, C.; Alligné, S.; Nicolet, C.; Avellan, F. Procedure for predicting part load resonance in Francis turbine hydropower units based on swirl number and local cavitation coefficient similitude. *Mech. Syst. Signal Process.* **2019**, *132*, 84–101. [CrossRef]
38. Yu, Z.F.; Wang, W.Q.; Yan, Y.; Liu, X.S. Energy loss evaluation in a Francis turbine under overall operating conditions using entropy production method. *Renew. Energy* **2021**, *169*, 982–999. [CrossRef]
39. Guo, B.; Xu, B.; Chen, D.; Ye, W.; Li, H. Vibration Characteristics of a Hydroelectric Generating System During the Load Rejection Process. *J. Comput. Nonlinear Dyn.* **2019**, *14*, 071006. [CrossRef]
40. Yan, Z.A.; Cui, X.; Su, S. *Electrical Machinery*, 2nd ed.; Xi'an Jiaotong University Press: Xi'an, China, 2006.
41. Truong, C.; Oudre, L.; Vayatis, N. Selective review of offline change point detection methods. *Signal Process.* **2020**, *167*, 107299. [CrossRef]
42. Xu, B.; Chen, D.; Zhang, H.; Li, H. Stability of a hydro-turbine governing system under stochastic fluctuating speed. *J. Vib. Shock* **2018**, *37*, 226–231. [CrossRef]
43. Reshef, D.N.; Reshef, Y.A.; Finucane, H.K.; Grossman, S.R.; McVean, G.; Turnbaugh, P.J.; Lander, E.S.; Mitzenmacher, M.; Sabeti, P.C. Detecting Novel Associations in Large Data Sets. *Science* **2011**, *334*, 1518–1524. [CrossRef]
44. Liang, J.; Feng, C.; Song, P. A Survey on Correlation Analysis of Big Data. *Chin. J. Comput.* **2016**, *39*, 1–18. [CrossRef]
45. Wang, T. Causality in big data and its philosophical connotation. *Soc. Sci. China* **2016**, *05*, 22–42.

energies

MDPI

Article

Research on Thermodynamic Characteristics of Hydraulic Power Take-Off System in Wave Energy Converter

Yubo Niu [1], Xingyuan Gu [1], Xuhui Yue [1], Yang Zheng [1], Peijie He [2] and Qijuan Chen [1,2,*]

[1] Key Laboratory of Transients in Hydraulic Machinery, Ministry of Education, Wuhan University, Wuhan 430072, China; niuyubo@whu.edu.cn (Y.N.); a386871202@126.com (X.G.); yuexh@whu.edu.cn (X.Y.); zhengy1991@foxmail.com (Y.Z.)

[2] School of Power and Mechanical Engineering, Wuhan University, Wuhan 430072, China; hepeijie@whu.edu.cn

* Correspondence: qjchen@whu.edu.cn; Tel.: +027-68772163

Abstract: Hydraulic power-take-off (PTO) systems which utilize high-pressure oil circuits to transmit energy are widely applied in wave energy generation. The properties of hydraulic oil are significantly influenced by environmental conditions, and its dynamic viscosity is sensitive to temperature, especially in relatively low-temperature cases. This paper studies the characteristics of the hydraulic PTO when started in different temperature conditions via numerical analysis and experimental verification. An improved numerical model of the hydraulic PTO system is proposed, in which the effects of temperature on the hydraulic oil viscosity and hydraulic motor efficiency are quantitatively investigated, and consequently, the thermal-hydraulic characteristics can be sufficiently considered. The performances of the hydraulic PTO in start-up processes with different initial temperatures and in long term operation are assessed. The results show that the presented model can reasonably describe the hydraulic PTO characteristics. The efficiency of hydraulic PTO degrades when it starts at low temperatures. The efficiency increases in relatively high temperature, while larger fluctuations of the flow rate and output power are observed. This study can provide guidance for enhancing the efficiency and consistency of hydraulic PTO operating in actual sea conditions.

Keywords: thermal-hydraulic characteristics; hydraulic oil viscosity; hydraulic PTO; wave energy converter

Citation: Niu, Y.; Gu, X.; Yue, X.; Zheng, Y.; He, P.; Chen, Q. Research on Thermodynamic Characteristics of Hydraulic Power Take-Off System in Wave Energy Converter. *Energies* **2022**, *15*, 1373. https://doi.org/10.3390/en15041373

Academic Editors: Duarte Valério, Mohamed Benbouzid and Eugen Rusu

Received: 10 December 2021
Accepted: 10 February 2022
Published: 14 February 2022

1. Introduction

As a widespread renewable energy source, ocean wave energy has gradually received extensive attention from scientists since the oil crisis broke out in the 1870s [1,2]. Waves have irregular motion and their power is largely discontinuous, which makes it difficult to obtain wave energy. An important feature of ocean waves is that they have the highest energy density among all renewable energy sources [2]. If wave energy can be effectively used, it will make a great contribution to alleviating the world energy crisis [3].

Some European countries were the first to carry out the research of wave energy conversion technology. At present, a large number of wave energy conversion devices have been designed and manufactured, some of which have been tested in actual sea conditions [2]. The wave energy converters are usually composed of a wave energy capture (WEC) system and a power take-off (PTO) system. There are many ways to classify wave energy converters currently, according to the different working principles of wave energy captures. They can be mainly divided into three types, the oscillating water column, overtopping, and oscillating body [4]. The role of the WEC system is to absorb wave energy, while the role of the PTO system is to convert the energy captured by the WEC system into relatively consistent mechanical energy and then outputs electrical energy through the generator. Therefore, the PTO system is the core part of the wave energy converter. There is no doubt that it has become the research focus of many universities and energy institutions [5]. In general, the typical PTO system can be equipped with four types of drive

mechanisms including air turbines, low-head hydraulic turbines, linear generators, and hydraulic oil circuits [4–6]. Air turbines are mainly adopted in oscillating water column WEC due their special working principles [4]. Their structures are reliable, however, the compressibility of air and the inevitable deviation of the actual rotation speed to the optimal value may easily degrade their efficiencies [7,8]. With high efficiency and reliability, low-head turbines are mainly applied to overtopping devices. Nevertheless, their large-scale applications are still impeded by the inconvenient constructions of the overtopping WECs. The linear generators are also broadly utilized in WECs, which primarily benefits from their low mechanical complexity. However, the linear generator structures are vulnerable to damages from vibrations and impacts, especially in real irregular waves and extreme waves. In addition, the power outputs from the linear generators fluctuated, and consequently, the quality of the converted electricity cannot satisfy the criteria. In contrast, hydraulic PTO systems are frequently employed in oscillating body WECs, and they use hydraulic oil circuits to transmit energy, which can cope with low frequency-large torque inputs of waves and overload protection. Meanwhile, their advantages of stabilizing power output are attractive for engineering applications. However, the performances, e.g., the pressure consistency, the flow rate consistency, and the efficiency of the hydraulic PTO, are sensitive to operating conditions, and the aforementioned performances may significantly deteriorate when the system states deviate from the optimal states. Consequently, we focus on hydraulic PTO in this paper and investigate the influences of several key elements to their performances [9,10].

In the past few decades, universities and scientific research institutions have carried out a large amount of research work on hydraulic PTO systems, including structural design and system optimization [9]. Stephen Salter proposed a kind of wave energy generation device named the nodding duck [10]. A buoyant pendulum wave energy generation system was invented by Lancaster University in the United Kingdom [11]. Zhejiang University designed a kind of pendulum wave energy generation device [12]. The Guangzhou Energy Research Institute of the Chinese Academy of Sciences created the duck-type and eagle-type wave energy conversion devices [13]. The University of Edinburgh in the United Kingdom put forward a wave energy power generation device based on a new hydraulic transmission system [14,15]. Gaspar presented some incremental modifications to the PTO architecture, such as using more cylinder ports, installing more parallel cylinders, and assembling an oil bypass circuit [16]. The consistency and efficiency of the wave energy conversion device are two key factors that determine whether the wave energy can be effectively used. The PTO system in the Pelamis wave energy converter realizes the torque control of the hydraulic cylinder by improving the one-way valve into a control valve block, thereby achieving the purpose of high-efficiency energy capture [17,18]. Falcao introduced and implemented a latching control method to increase the captured mechanical energy by the hydraulic PTO [19]. Liu et al. improved the power capture ability of a two-raft-type WEC by optimizing several parameters of the hydraulic PTO, including the area of the piston, the displacement of the hydraulic motor, and the effective damping of the generator [20]. Cargo et al. realized the maximization of the generated power in different wave period situations by optimizing the size of the hydraulic motor [21]. Chen and Jiang verified that the parameter settings of the key components play an important role in the consistent operation of the hydraulic PTO system through simulation and experiments [9]. Yue proposed integrated characteristic curves in constant voltage conditions, which are used to optimize system design and improve the operating efficiency of the PTO system [22]. Geng proposed a novel hydraulic PTO power module consisting of a pressure compensator and throttle valve by adjusting the parameters to improve the consistency of hydraulic motor speed and output power [23]. The focus of the research on the consistency and efficiency of the hydraulic PTO system is focused on how to select pivotal components and optimize parameters and control strategies, which ignored the influence of the characteristics of the working medium on the consistency of the output power and efficiency when the wave energy converters are running.

From the perspective of hydraulic oil characteristics, this paper studies the influence of temperature on the performance of the hydraulic PTO system during operation. The viscosity of hydraulic oil is an important property to measure the performance of hydraulic oil. If the viscosity of the hydraulic oil is too high, the internal friction force of the hydraulic oil will be relatively large when it flows, which will generate more heat energy during the energy transmission process and increase the total energy consumption. If the viscosity of hydraulic oil is too low, the leakage will increase, leading to a decrease in system pressure and affecting the consistency of the system. The viscosity of hydraulic oil is significantly affected by temperature changes [24]. Therefore, it is of great significance to study the effect of viscosity on the consistent operation and efficient work of the PTO system when it starts at different temperatures. According to the results of simulated analysis, the viscosity of hydraulic oil varies significantly within the range of −20 °C to 20 °C [24], considering that the seawater temperature in the sea area where electricity can be generated is above 0 °C, this paper selects the ambient temperature within the range of 0~20 °C to research the impact on the performance of the hydraulic PTO system.

The rest of this paper is organized as follows. Section 2 introduces the working principle of the hydraulic PTO system for a pendulum wave energy converter and the digital model of a hydraulic motor and simulation of hydraulic PTO system. Section 3 presents the components of the prototype test platform. The experimental results and analysis are arranged in Section 4. Finally, the corresponding conclusions are showed in Section 5.

2. Modeling and Simulation of Thermal Characteristics of Hydraulic PTO System

The hydraulic PTO system of a wave energy converter is mainly composed of a gear and rack mechanism, a single-acting hydraulic cylinder with single rod, four check valves, a relief valve, a high-pressure accumulator, a flow control valve, a permanent magnet synchronous generator, a hydraulic motor, resistor loads, and an oil tank [20]. The working principle is shown in Figure 1. The floating pendulum converts wave energy into its own mechanical energy and moves around the fulcrum [4]. The mechanical energy of the floating pendulum is transmitted to the single-acting horizontal bar hydraulic system by using the meshing gear and rack mechanism. Then the piston rod drives the piston to reciprocate to perform work on the hydraulic oil, which completes the conversion from mechanical energy to hydraulic energy. The four check valves integrate the two-way flow of hydraulic oil at the rod-less cavity oil port of the hydraulic cylinders into a one-way flow in the main oil circuit through rectification. The variable displacement hydraulic motor converts the hydraulic energy into rotating mechanical energy, which is then converted into electrical energy output by permanent magnet synchronous generator [3,25].

The main functions of the accumulator are to store energy, stabilize pressure, eliminate periodic fluctuations of the system pressure and flow generated when the cylinder is reversing, and enhance the consistency of the system. The overflow valve can avoid the high pressure in the pipeline, and the function of the flow control valve is to control the flow rate and participate in the control of the power; the oil tank is used to compensate for the leakage and short-term negative pressure that may occur in the system and to supplement the oil pressure in time [9,22,23,26].

2.1. The Temperature-Hydraulic Oil Viscosity-Efficiency Model of Hydraulic Motors

Hydraulic oil is most commonly used in hydraulic transmission, and most of the published literatures about hydraulic oil are selected in combination with specific engineering machinery. There are few theoretical studies on the external characteristics of hydraulic oil. The main physical properties of hydraulic oil include density, viscosity, elastic modulus, surface tension, etc. From the perspective of fluid movement and transmission force, viscosity is the main factor to prevent the flow of hydraulic oil. Therefore, it is of great significance to study the influence of fluid viscosity on the performance of the PTO system.

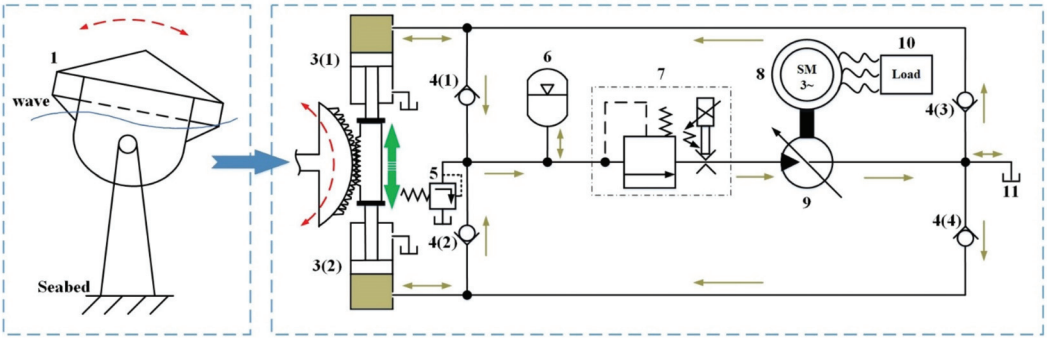

Figure 1. Schematic diagram of a hydraulic PTO system with a pendulum (**1**) wave energy capture device (**2**) rack and pinion mechanism (**3**) single-acting hydraulic cylinder with single rod (**4**) check valve (**5**) relief valve (**6**) high pressure accumulator (**7**) flow control valve (**8**) permanent magnet synchronous generator (**9**) hydraulic motor (**10**) resistor load (**11**) oil tank.

The law of internal friction proposed by Newton believes that the relative movement of two adjacent layers inside the flowing fluid produces internal friction, and its magnitude is proportional to the viscosity of the fluid, the velocity gradient of the relative movement, and the contact area. The mathematical expression is:

$$F = \mu A \frac{du}{dy} \tag{1}$$

The corresponding shear stress can be expressed as:

$$\tau = \frac{F}{A} = \mu \frac{du}{dy} \tag{2}$$

where μ refers to the dynamic viscosity of hydraulic oil, $Pa{\cdot}s$, τ is the internal friction shear stress of hydraulic oil, m^2/s, A means the contact area of hydraulic oil between two layers, m^2, and du/dy presents the velocity gradient of hydraulic oil, s^{-1}.

The greater the dynamic viscosity of the fluid is, the stronger the stickiness generated when it moves. The normal pressure has little effect on the viscosity of the fluid and can be almost ignored, while the temperature has a great influence on the viscosity of the fluid. The reason is that the viscosity of the fluid mainly comes from the attraction of molecules. The hydraulic oil belongs to the Newtonian fluid, so it conforms to the Newton internal friction law. In a constant temperature condition, the viscosity coefficient of this kind of fluid does not change, which is an oblique straight line through the origin of the coordinate in the $\tau \sim du/dy$ coordinate system. When the temperature increases, the molecular distance increases, the attractive force decreases, and the shear stress generated by the same shear deformation rate decreases; therefore, the dynamic viscosity decreases. The relationship between hydraulic oil viscosity and temperature can be expressed as:

$$\mu = \mu_{T_0} e^{-\lambda(T-T_0)} \tag{3}$$

where μ_{T_0} is the dynamic viscosity of hydraulic oil when T is equal to T_0, and $Pa{\cdot}s$, λ refers to the hydraulic oil viscosity coefficient.

According to the literature, the relationship between hydraulic motor torque loss and hydraulic oil viscosity [27] is:

$$M_L = K_\mu \mu n + K_P \Delta p + K_{\rho PSP} n^3 + \frac{K_{\rho VN} \Delta p \sqrt{\Delta p}}{n} + K_{P2} \Delta p^2 + M_{Lo} \tag{4}$$

where K_μ, K_P, $K_{\rho PSP}$, $K_{\rho VN}$, K_{P2}, and M_{Lo} are moment-loss-related performance characteristic coefficients, n represents speed of the hydraulic motor, r/min, Δp represents the pressure difference between inlet and outlet of hydraulic motor, Pa, ρ stands for hydraulic fluid density, and kg/m^3, M_L, and M_{Lo} delegate the torque loss and fixed torque loss of hydraulic motor, $N{\cdot}m$.

The relationship between hydraulic motor leakage loss and viscosity [27] is:

$$Q_L = C_\mu \frac{\Delta p}{\mu} + C_v n + C_{VN}\sqrt{\frac{\Delta p}{\rho}} + C_{PP}\frac{\rho n^3}{\Delta p} + C_C \frac{n\Delta p}{\beta} + Q_{Lo} \tag{5}$$

where C_μ, C_v, C_{VN}, C_{PP}, C_C, and Q_{Lo} are leakage-related performance characteristic coefficients, n represents the speed of hydraulic motor, r/min, Δp represents the pressure difference between inlet and outlet of hydraulic motor, Pa, ρ stands for hydraulic fluid density, and kg/m^3, Q_L, and Q_{Lo} delegate respectively leakage loss and fixed leakage loss of hydraulic motor, L/min.

The mechanical efficiency of a hydraulic motor can be expressed as:

$$\eta_m = \frac{M - M_L}{M} = 1 - \frac{M_L}{M} \tag{6}$$

where η_m stands for the hydro-mechanical efficiency and M is the theoretical output torque of a hydraulic motor, $N{\cdot}m$.

The volumetric efficiency of a hydraulic motor can be expressed as:

$$\eta_v = \frac{Q}{Q + Q_L} = \frac{1}{1 + \frac{Q_L}{Q}} \tag{7}$$

where η_v stands for the volumetric efficiency and Q represents the theoretical flow rate of a hydraulic motor, L/min.

The mechanical power loss of the hydraulic motor can be expressed as:

$$\varnothing_1 = 2\pi n M_L \tag{8}$$

The volumetric power loss of the hydraulic motor can be expressed as:

$$\varnothing_2 = \Delta p Q_L \tag{9}$$

When the temperature rises, the viscosity of the hydraulic oil decreases according to Formulas (3), (4), (6) and (8). Consequently, the torque loss of the hydraulic motor will decrease, which will increase the mechanical efficiency of the hydraulic motor. The mechanical power loss of the hydraulic motor is correspondingly reduced. It can be seen from Formulas (3), (5), (7) and (9) when the temperature rises, the viscosity of the hydraulic oil decreases, which will cause the leakage loss of the hydraulic motor to increase, thus the volumetric efficiency of the hydraulic motor decreases, and volumetric power loss of the hydraulic motor increases accordingly. The influence of viscosity on the efficiency of hydraulic motors mainly includes the influence of its mechanical efficiency and volumetric efficiency. It is very necessary to control the viscosity of hydraulic oil within a suitable range for the efficient operation of the PTO system. Therefore, this paper focuses on the influence of the viscosity of the hydraulic oil with the rise of temperature on mechanical loss, volumetric loss of the hydraulic motor, and system efficiency.

2.2. Simulation Model of Hydraulic PTO System

The hydraulic PTO system simulation model was established in AMESim, a software used for the modeling, simulation, and dynamic analysis of hydraulic systems, it is shown in Figure 2. The parameters for the simulation model are based on the design of the experiment platform and are shown in Table A1 of Appendix A.

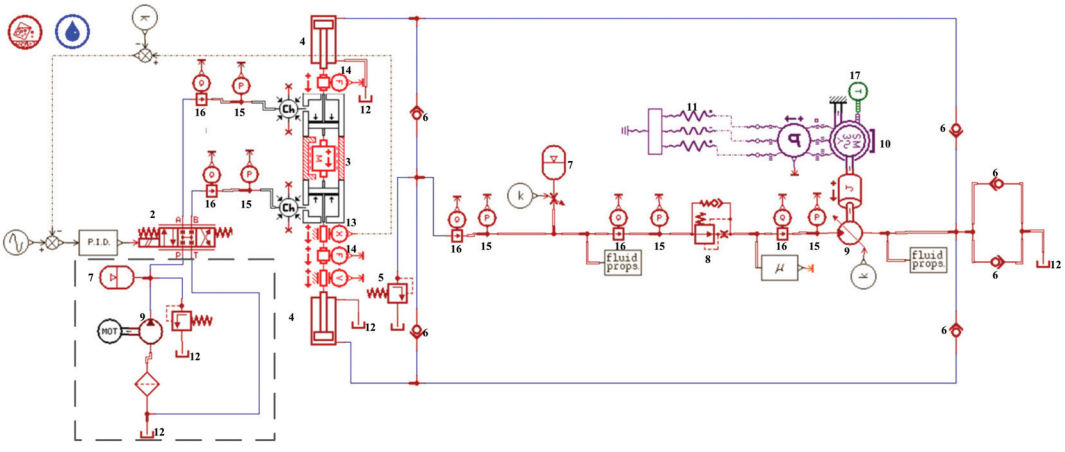

Figure 2. Schematic diagram of the experimental platform. (**1**) A pump station, (**2**) three-position and four-way reversing valve, (**3**) double-acting hydraulic cylinder with double rods, (**4**) single-acting hydraulic cylinder with single rod, (**5**) relief valve, (**6**) check valve, (**7**) high pressure accumulator, (**8**) flow control value, (**9**) hydraulic motor, (**10**) permanent magnet synchronous generator, (**11**) resistor loads, (**12**) oil tank, (**13**) a linear variable displacement transducer, (**14**) bidirectional force transducers, (**15**) pressure gauge, (**16**) flow rate sensor, (**17**) Torque tachometer.

Because the range of wave energy period is 6–8 s and the significant wave height distributes between 1.5 m and 3.5 m [23], we chose the typical sea state where the period was 8s, and the wave height was 1.5 m to carry out the simulation and experiments.; then controlling the pressure of the system kept in 7 MPa, and another sea state whose period was 6s and wave height was 1.5 m. The designed output powers of the hydraulic system were respectively about 1.2 KW and 1.5 KW.

3. Prototype Test Platform of Hydraulic Power Take-Off System

The verification test was completed by building a hydraulic PTO system prototype platform, shown in Figure 3, which consists of a drive system, a hydraulic PTO system, a data acquisition and monitoring system, and loads. The drive system, which simulates the motion of the wave energy capture device, realizes the reciprocating motion of the piston in the double-hydraulic-chamber double-rod cylinder through a hydraulic pump station and controls the direction of the piston by adjusting the three-position and four-way reversing valve, which guides the high-pressure oil into different chambers, and finally achieves the input of wave energy at different periods. The hydraulic PTO system utilizes the reciprocating movement of two single-acting hydraulic cylinders with single rods that are solidly connected to the double-acting hydraulic cylinder with double rods to discharge high-pressure oil from the rod-less cavity of the cylinders. The check valves integrate the two-way flow of hydraulic oil into a one-way flow, and then hydraulic oil enters the hydraulic motor through the flow control valve to drive the generator, which is rigidly connected with the motor to rotate. This process realizes the conversion of mechanical energy to electrical energy. The monitoring and control system was developed based on the LabVIEW software. A human-computer interaction interface was established in LabVIEW, and the serial communication technology of the computer and the programmable controller was applied to realize the condition monitoring of the PTO system and the real-time collection of data such as tubing pressure, system flow, hydraulic oil viscosity, and hydraulic motor speed and system while realizing the storage of data by using the database system.

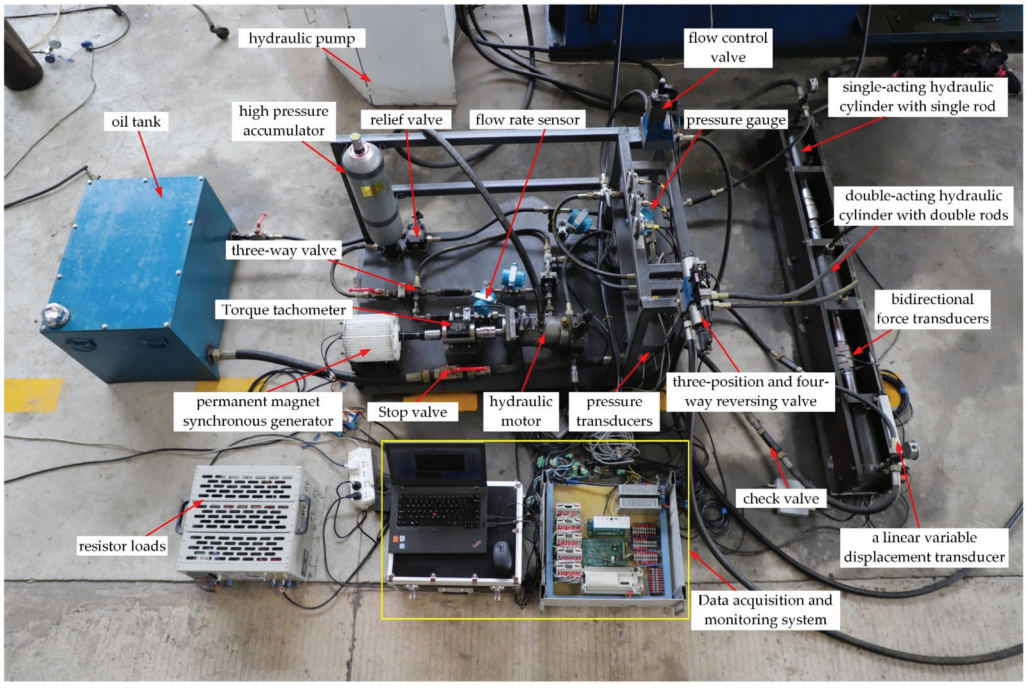

Figure 3. The composition of the experimental platform.

The research procedure was arranged as follows. Firstly, a prescribed piston motion with a period of 8 s and an amplitude of 0.075 m was used to validate the numerical model in this paper, and a comparison in system pressure was made, flow at variable temperatures and output power at 18 °C. Then the wave conditions with a period of 6 s and an amplitude of 0.075 m was used numerically to study the consistency of the PTO system. Finally, a long-running test was carried out at the temperature of 6 °C. Its purpose was to study the effect of temperature rise on the consistency and efficiency of the hydraulic PTO system.

The main component parameters are determined according to the designed working conditions, as shown in Table 1.

Table 1. Parameters of main components.

Components	Parameters	Value	Unit
Three-position and four-way reversing valve	Maximum pressure	31.5	MPa
	Maximum flow-rate	180	L/min
Double-acting double-rod cylinder	Maximum pressure	31.5	MPa
	Piston diameter	90	mm
	Rod diameter	63	mm
	Stroke	200	mm
Single-acting single-rod cylinder	Maximum pressure	31.5	MPa
	Piston diameter	80	mm
	Piston area	0.005	m^2

Table 1. *Cont.*

Components	Parameters	Value	Unit
	Rod diameter	63	mm
	Stroke	200	mm
Check valve	Maximum pressure	31.5	MPa
High-pressure accumulator	Maximum pressure	31.5	MPa
	Nominal volume	6.3	L
	Pre-charge gas pressure	4.5	MPa
Relief valve	Maximum cracking pressure	31.5	MPa
Flow control valve	Maximum pressure	31.5	MPa
	Adjuconsistent flow-rate range:	0~25	L/min
Hydraulic motor	Maximum pressure	35	MPa
	Maximum flow-rate	206	L/min
	Maximum displacement	54.8	mL/r
	Minimum displacement	16.4	mL/r
Low-pressure tank	Volume	175	L
Magnetic powder brake	Torque range	0~100	Nm
	Maximum power	10	kW
Bidirectional force transducer	Force range	−100~100	kN
Displacement transducer	Displacement range	0~225	mm
Flow-rate transducer	Flow-rate range	3.3~20	L/min
Pressure transducer	Pressure range	0~25	MPa
Torque-speed transducer	Torque range	0~100	Nm
	Speed range	0~1000	r/min

4. Results and Discussion

This section begins with experiments to validate the hydraulic PTO model proposed in Section 3. The experiments were conducted in a hydraulic PTO test platform and the ECD movements were simplified as prescribed piston motions. The PTO system start up tests were carried out at the ambient temperature of 6 °C, 12 °C, and 18 °C. Temperature is thought to be almost immutable when the PTO system starts up within a short of time. Thus, we studied the influence of different start-up temperatures on the characteristics of the PTO system. The system pressure, flow, and output power are tested in the numerical model and experimental conditions.

4.1. Simulation and Experiments of Hydraulic PTO System at Different Temperatures

The wave with a period of 8 s and an amplitude of 0.075 m was used to carry out the simulation and experiments. The pressure changes of the hydraulic PTO system within one minute of the startup process are shown in Figure 4. The three pictures (a), (b), and (c) respectively represent the corresponding system flow when the startup temperature is 6 °C, 12 °C, and 18 °C. It can be seen that the simulation results obtained by using the model in Section 3 generally agree with those obtained by experiments at different startup temperatures, °C, the system pressure dropped at the beginning. The analysis found that the accumulator was not working because of the low temperature at the beginning and the relatively high viscosity of the hydraulic oil. When the ambient temperature was 12 °C or 18 °C, there was little difference at the beginning. The system pressure in experimental conditions cannot reach the charging pressure because the compressibility of hydraulic oil was not considered in this model. However, the system pressure in the experimental condition was consistent with that in the simulation eventually.

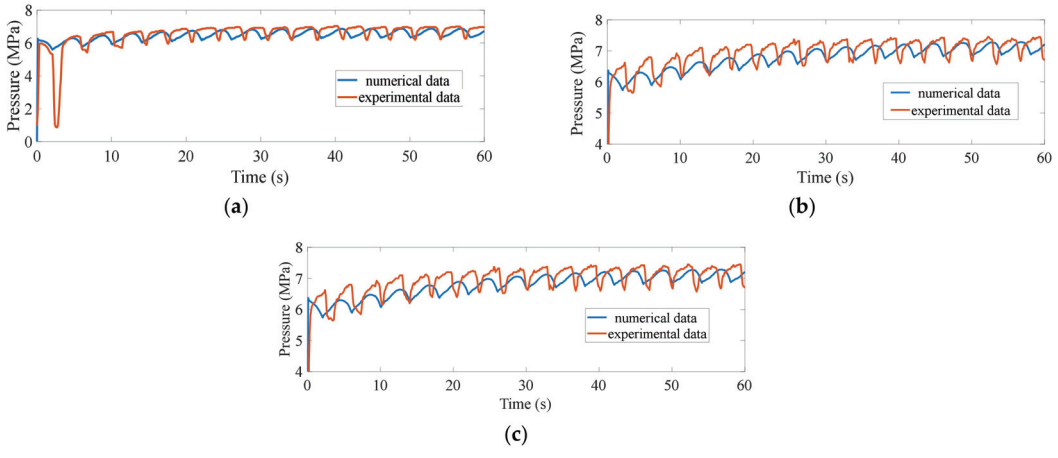

Figure 4. Comparison and experiment of hydraulic PTO system pressure between simulation at different temperatures. (**a**) ambient temperature is 6 °C. (**b**) ambient temperature is 12 °C. (**c**) ambient temperature is 18 °C.

The flow differences of the hydraulic PTO system at different temperatures in the start-up process are shown in Figure 5. The tested system flow is higher when the temperature is higher, close to the simulation results. Hence, within a certain temperature range, the higher the temperature the hydraulic oil is at the startup process, the greater the system flow rate will be.

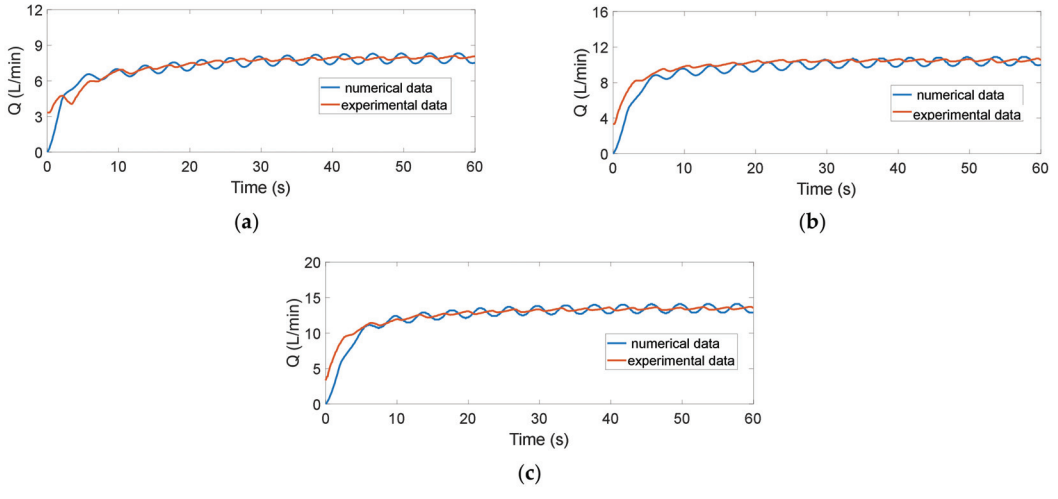

Figure 5. Comparison of hydraulic PTO system flow between simulation and experiment at different temperatures. (**a**) ambient temperature was 6 °C. (**b**) ambient temperature was 12 °C. (**c**) ambient temperature was 18 °C.

The output power changes of the hydraulic PTO system within one minute of the startup process are shown in Figure 6. Picture (a) presents the comparison of system output power at 18 °C between the numerical model and the experimental conditions, and they are generally on the way up, though they varied at the beginning. Picture (b) demonstrates that although the output power of the PTO system increased in volatility, the average value

only reached about 550 W when the initial temperature was 6 °C, which was much lower than the set system output power of 1200 W. In addition, the average value reached about 720 W and 1100 W when the initial temperature was 12 °C and 18 °C separately. Therefore, within the range of 6 °C to 18 °C, the higher the initial temperature, the greater the output power of the system, and it is closer to the designed output power.

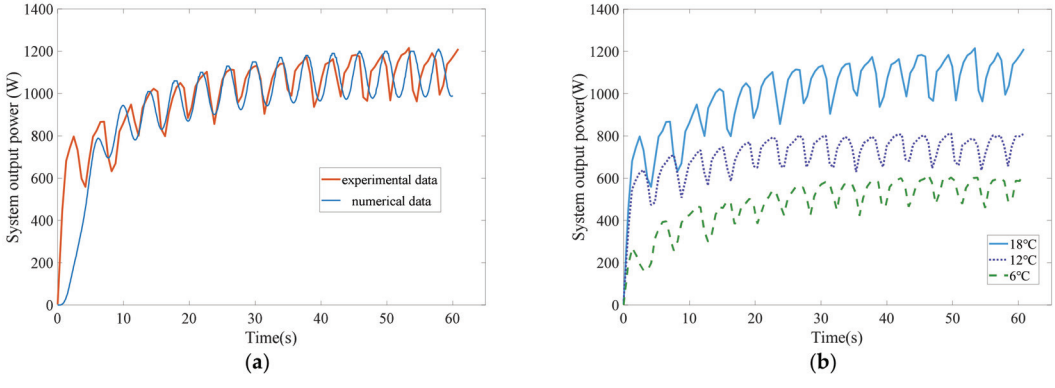

Figure 6. System output power at different start-up temperatures. (**a**) comparison of system output power at 18 °C between the numerical model and experimental conditions. (**b**) comparison of system output power at 6 °C, 12 °C, and 18 °C.

4.2. Simulation of Hydraulic PTO System at Different Temperatures

The wave with a period of 6 s and an amplitude of 0.075 m was considered in this simulation model. The pressure and flow changes of the hydraulic PTO system in the startup process are shown in Figures 7 and 8. The system pressure had no evident diversity when the period of the input wave had changed from 8s to 6s. Furthermore, when the ambient temperature was higher, it was faster to achieve the balance, and the volatility also increased in the meantime. At the same time, the flow would have a clear distinction if the temperature increased.

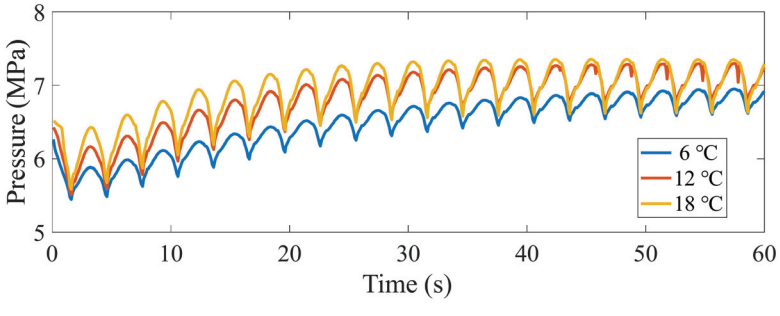

Figure 7. Comparison of the hydraulic PTO system pressure at different temperatures by simulation.

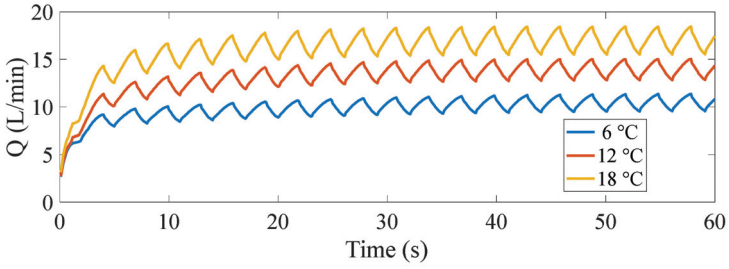

Figure 8. Comparison of hydraulic PTO system flow at different temperatures by simulation.

4.3. The Effect of Temperature Rise on the Consistency and Efficiency of Hydraulic PTO System

Since the output power of the PTO system at low temperature was much lower than at slightly higher temperatures, a long-running test was carried out at the temperature of 6 °C, controlling the input force constant and using the sensors and meters to record the system state data at runtime. The test results are shown in Figures 9 and 10. It can be seen that when the device was started, the temperature gradually rose, while the hydraulic motor speed, system flow, and pressure rose rapidly. Then, the temperature continued to rise, and when the system pressure was consistent, the system flow, speed, and torque of the hydraulic motor continued to increase. The rise in temperature reduced the viscosity and the flow resistance of the hydraulic oil, while the torque loss of the hydraulic motor decreased, which would eventually increase the mechanical efficiency of the system. Then, 6 minutes later, the temperature of the hydraulic oil continued to rise and eventually reached about 13 °C; the pressure fluctuated slightly. The fluctuations in flow rate and hydraulic motor speed were more obvious. The continuous rise of temperature caused the viscosity of the hydraulic oil to be too low, leading to an increase in leakage, and finally, the volumetric efficiency of the hydraulic PTO system decreased.

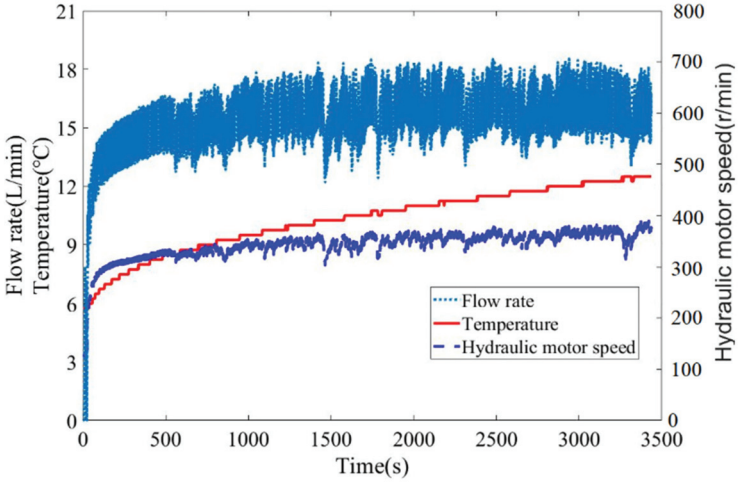

Figure 9. Changes of temperature, flow, and motor speed in the start-up to steady progress of power take-off system.

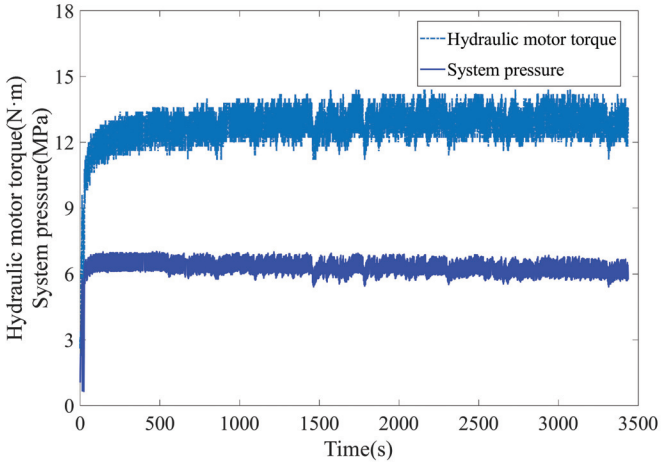

Figure 10. Changes in hydraulic motor torque and system pressure during long-term operation of the PTO system.

The changes in the mechanical efficiency and volumetric efficiency of the hydraulic motor with the operation of the PTO system are shown in Figure 11. The increase in the temperature of the hydraulic oil caused the mechanical efficiency to rise from about 80 percent to 97 percent, while the volumetric efficiency had a downward trend decreasing from around 93 percent to 85 percent. The total efficiency of the hydraulic motor shows a tendency that it increases firstly and then decreases, and the overall efficiency is maintained at the range of 70 percent to 88 percent.

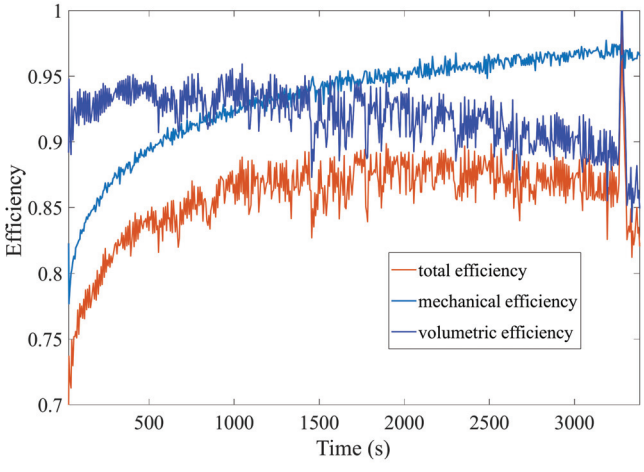

Figure 11. Mechanical, volumetric, and total efficiency of the hydraulic motor.

With the operation of the experimental device, the temperature of the hydraulic oil increased, the viscosity of the hydraulic oil decreased, and meanwhile, the hydraulic motor speed and system flow increased. Therefore, the influence of temperature on the system characteristics mainly altered the flow by affecting the hydraulic oil viscosity, thus acting on the hydraulic motor efficiency. This eventually had an impact on the system output power.

5. Conclusions

This paper focused on and studied the impact of start-up at variable temperatures and the rise of temperature on the characteristics of the hydraulic PTO system. The mathematical model of the temperature—hydraulic oil viscosity—hydraulic motor efficiency of the hydraulic PTO system was added into the simulation model of the hydraulic PTO system. Experiments were carried out to prove the correction of the simulation model, and different waves were emulated. The conclusions are as followed:

1. The system flow will increase owing to the rise of system temperature before it achieves the maximum, while system pressure can always reach a constant value;
2. The output power of the hydraulic PTO system is much lower than the designed one when it starts at low temperature, and it needs a reasonably long time for the system to heat up;
3. The results indicate that the thermal hydraulic model is reasonable and has high accuracy compared with to the real situation. For the cases of different wave excitation, the pressure of the hydraulic system is maintained at a relatively stable value, which ensures the consistent operation of the system at different input of energies;
4. The influence of temperature on the system characteristics is mainly altering the flow by affecting the hydraulic oil viscosity, thus acting on the hydraulic motor efficiency, eventually impacting the system output power.

In future work, we will study the operating characteristics of PTO in a larger range of temperatures and wave states and introduce a more accurate model to describe other components' performances to improve the efficiency of the hydraulic PTO system in different sea states.

Author Contributions: Conceptualization, Y.N. and Q.C.; methodology, X.G.; software, Y.N.; validation, Y.N., X.G. and X.Y.; formal analysis, Y.Z and P.H.; investigation, X.Y. and Y.Z.; resources, X.Y.; data curation, Y.N.; writing—original draft preparation, Y.N.; writing—review and editing, Q.C.; visualization, X.G. All authors have read and agreed to the published version of the manuscript.

Funding: This research was funded by the National Natural Science Foundation of China, grant number 52179088.

Institutional Review Board Statement: Not applicable.

Informed Consent Statement: Not applicable.

Conflicts of Interest: The authors declare no conflict of interest.

Appendix A

Table A1. Parameters of numerical model.

Components	Title	Unit	Value
Single-acting single-rod hydraulic cylinder	Piston diameter	mm	80
	Rod diameter	mm	63
High-pressure accumulator	Gas pre-charge pressure	bar	60
	Accumulator volume	L	6.3
	Polytropic index	□/	1.4
Flow control valve	Set flow	L/min	20
	Minimum operating pressure difference	bar	2
	Flow-rate pressure gradient	L/min/bar	0.05
	Valve hysteresis	bar	0
Hydraulic motor	Displacement	cc/rev	17.5

Table A1. *Cont.*

Components	Title	Unit	Value
Generator	Number of pole pairs	□/	5
	Reference temperature	degC	18
	Stator winding resistance at reference temperature	Ohm	0.05
	Corrective coefficient on stator winding resistance	1/K	0.2
	Stator cyclic inductance on Park's d axis	H	0.0035
	Stator cyclic inductance on Park's q axis	H	0.0018
	Permanent magnet flux linkage at reference temperature	Wb	0.4
Load	Resistance	Ohm	11
Oil	Density	kg/m^3	850
	Bulk modulus	bar	17,000
	Absolute viscosity	cP	51
Design operating parameters	Pressure	MPa	7
	Flow-rate	L/min	14.7
	Amplitude of piston motion	m	0.075
	Frequency of piston motion	Hz	1/8
	Rotational speed	r/min	600
	Output power	W	1200

References

1. Drew, B.; Plummer, A.R.; Sahinkaya, M.N. A review of wave energy converter technology. *Proc. Inst. Mech. Eng. Part A J. Power Energy* **2009**, *223*, 887–902. [CrossRef]
2. Clément, A.; McCullen, P.; Falcão, A.; Fiorentino, A.; Gardner, F.; Hammarlund, K.; Lemonis, G.; Lewis, T.; Nielsen, K.; Petroncini, S.; et al. Wave energy in Europe: Current status and perspectives. *Renew. Sustain. Energy Rev.* **2002**, *6*, 405–431. [CrossRef]
3. Lasa, J.; Antolin, J.C.; Angulo, C.; Estensoro, P.; Santos, M.; Ricci, P. Design, construction and testing of a hydraulic power Take-off for wave energy converters. *Energies* **2012**, *5*, 2060–2082. [CrossRef]
4. Falcão, A.F.d.O. Wave energy utilization: A review of the technologies. *Renew. Sustain. Energy Rev.* **2009**, *14*, 899–918. [CrossRef]
5. Hansen, R.H.; Kramer, M.M.; Vidal, E. Discrete displacement hydraulic power take-off system for the wave-star wave energy converter. *Energies* **2013**, *6*, 4001–4044. [CrossRef]
6. Jusoh, M.A.; Ibrahim, M.Z.; Daud, M.Z.; Albani, A.; Yusop, Z.M. Hydraulic power take-off concepts for wave energy conversion system: A review. *Energies* **2019**, *12*, 4510. [CrossRef]
7. Masuda, Y.; Miyazaki, T. Wave power electrical generation study in Japan. In Proceedings of the BHRA International Symposium on Wave and Tidal Energy, Canterbury, UK, 27–29 September 1978; pp. 85–92.
8. Whittaker, T.; Beattie, W.; Raghunathan, S.; Thompson, A.; Stewart, T.; Curran, R. The islay wave power project: An engineering perspective. *Proc. Inst. Civ. Eng.-Water Marit. Energy* **1997**, *124*, 189–201. [CrossRef]
9. Qijuan, C.; Wen, J.; Xuhui, Y.; Dazhou, G.; Donglin, Y.; Weiyu, W. Dynamic performance of key components for hydraulic power take-off of the wave energy converter. *IET Renew. Power Gener.* **2019**, *13*, 2929–2938. [CrossRef]
10. Ahamed, R.; McKee, K.; Howard, I. Advancements of wave energy converters based on power take off (PTO) systems: A review. *Ocean Eng.* **2020**, *204*, 107248. [CrossRef]
11. Cruz, J.M.B.P.; Salter, S.H. Numerical and experimental modelling of a modified version of the Edinburgh Duck wave energy device. *Proc. Inst. Mech. Eng. Part M J. Eng. Marit. Environ.* **2006**, *220*, 129–147. [CrossRef]
12. Orer, G.; Ozdamar, A. An experimental study on the efficiency of the submerged plate wave energy converter. *Renew. Energy* **2006**, *32*, 1317–1327. [CrossRef]
13. Zhang, D.; Li, W.; Lin, Y.; Bao, J. An overview of hydraulic systems in wave energy application in China. *Renew. Sustain. Energy Rev.* **2012**, *16*, 4522–4526. [CrossRef]
14. You, Y.; Sheng, S.; Wu, B.; He, Y. Wave energy technology in China. *Philos. Trans. R. Soc. Math. Phys. Eng. Sci.* **2012**, *370*, 472–480. [CrossRef]
15. Kim, B.-H.; Wata, J.; Zullah, M.A.; Ahmed, M.R.; Lee, Y.-H. Numerical and experimental studies on the PTO system of a novel floating wave energy converter. *Renew. Energy* **2015**, *79*, 111–121. [CrossRef]
16. Gaspar, J.F.; Calvário, M.; Kamarlouei, M.; Soares, C.G. Design tradeoffs of an oil-hydraulic power take-off for wave energy converters. *Renew. Energy* **2018**, *129*, 245–259. [CrossRef]

17. Henderson, R. Design, simulation, and testing of a novel hydraulic power take-off system for the Pelamis wave energy converter. *Renew. Energy* **2006**, *31*, 271–283. [CrossRef]
18. Dießel, D.; Bryans, G.; Verdegem, L.; Murrenhoff, H. Wavepod a transmission for wave energy converters—Set-up and testing. *Int. J. Fluid Power* **2015**, *16*, 75–82. [CrossRef]
19. Falcão, A.F.d.O. Phase control through load control of oscillating-body wave energy converters with hydraulic PTO system. *Ocean Eng.* **2007**, *35*, 358–366. [CrossRef]
20. Liu, C.; Yang, Q.; Bao, G.I. Influence of hydraulic power take-off unit parameters on power capture ability of a two-raft-type wave energy converter. *Ocean Eng.* **2018**, *150*, 69–80. [CrossRef]
21. Cargo, C.; Hillis, A.; Plummer, A. Strategies for active tuning of wave energy converter hydraulic power take-off mechanisms. *Renew. Energy* **2016**, *94*, 32–47. [CrossRef]
22. Chen, Q.; Yue, X.; Geng, D.; Yan, D.; Jiang, W. Integrated characteristic curves of the constant-pressure hydraulic power take-off in wave energy conversion. *Int. J. Electr. Power Energy Syst.* **2020**, *117*, 105730. [CrossRef]
23. Geng, D.; Zheng, Y.; Chen, Q.; Yue, X.; Yan, D. Novel hydraulic mechanism-based output power regulation for the wave energy converter. *Appl. Ocean Res.* **2021**, *110*, 102587. [CrossRef]
24. Chen, Q.; Yu, H.; Yue, X.; Ye, Z.; Geng, D. Thermal-hydraulic modeling and simulation on wave energy power take-off system. *Acta Energ. Sol. Sin.* **2020**, *41*, 237–243. (In Chinese)
25. Antolín-Urbaneja, J.C.; Cortés, A.; Cabanes, I.; Estensoro, P.; Lasa, J.; Marcos, M. Modeling innovative power take-off based on double-acting hydraulic cylinders array for wave energy conversion. *Energies* **2015**, *8*, 2230–2267. [CrossRef]
26. Penalba, M.; Ringwood, J.V. A Review of wave-to-wire models for wave energy converters. *Energies* **2016**, *9*, 506. [CrossRef]
27. Jeong, H.-S.; Kim, H.-E. A novel performance model given by the physical dimensions of hydraulic axial piston motors: Experimental analysis. *J. Mech. Sci. Technol.* **2007**, *21*, 630–641. [CrossRef]

energies

MDPI

Article

Noise Reduction Study of Pressure Pulsation in Pumped Storage Units Based on Sparrow Optimization VMD Combined with SVD

Yan Ren [1,*], Linlin Zhang [1], Jiangtao Chen [2], Jinwei Liu [3], Pan Liu [1], Ruoyu Qiao [1], Xianhe Yao [1], Shangchen Hou [1], Xiaokai Li [4], Chunyong Cao [5] and Hongping Chen [4]

1 School of Electric Power, North China University of Water Resources and Electric Power, Zhengzhou 450045, China; 15638296728@163.com (L.Z.); 201411210@stu.ncwu.edu.cn (P.L.); 19937720813@163.com (R.Q.); jms20151834@163.com (X.Y.); houshangchen888@163.com (S.H.)
2 Energy and Power Engineering Institute, Zhengzhou Electric Power College, Zhengzhou 450000, China; chenjt-1@163.com
3 China Nuclear Power Engineering Co., Ltd., Shenzhen 518124, China; liujinwei@cgnpc.com.cn
4 State Grid Hunan Electric Power Co., Ltd., Changsha 410004, China; lixiangvictory@126.com (X.L.); ftchenhp@163.com (H.C.)
5 Hunan Heimifeng Pumped Storage Power Co., Ltd., State Grid Xin Yuan Company, Changsha 410213, China; ccy.mm@163.com
* Correspondence: renyan@ncwu.edu.cn

Abstract: The unbalanced forces generated by pumped storage units operating under non-ideal operating conditions can cause pressure pulsations. Due to the noise interference, the feature information reflecting the operating state of the unit in the pressure pulsation is difficult to extract. Therefore, this paper proposes a noise reduction method based on sparrow search algorithm (SSA) optimized variational mode decomposition (VMD) combined with singular value decomposition (SVD). Firstly, SSA is used to realize the adaptive optimization of VMD parameters for ideal decomposition of the signal. Then, the noise reduction of the decomposed signal is performed by using the sensitivity of the Permutation Entropy (PE) for small mutations. The noise reduction and reconstruction of the decomposed signal are carried out again by using SVD. The experimental and comparison results show that the mean square error of the signal after VMD-SVD feature extraction is reduced from 1.0068 to 0.0732 and the correlation coefficient is increased from 0.2428 to 0.9614. It is proved that the method achieves better results in the pressure pulsation signal of pumped storage units and has some application significance for the fault diagnosis of pumped storage units.

Keywords: pumped storage units; pressure pulsation; noise reduction; variational mode decomposition; sparrow search algorithm

Citation: Ren, Y.; Zhang, L.; Chen, J.; Liu, J.; Liu, P.; Qiao, R.; Yao, X.; Hou, S.; Li, X.; Cao, C.; et al. Noise Reduction Study of Pressure Pulsation in Pumped Storage Units Based on Sparrow Optimization VMD Combined with SVD. *Energies* **2022**, *15*, 2073. https://doi.org/10.3390/en15062073

Academic Editors: Helena M. Ramos, Chaoshun Li, Yun Zeng, Beibei Xu and Dong Liu

Received: 3 February 2022
Accepted: 10 March 2022
Published: 11 March 2022

1. Introduction

Vibration in pumped storage units poses a significant threat to the safe and stable operation of the units [1,2]. Pumped storage units have the characteristics of rapid start-up and shutdown, peak cutting and valley filling, etc., which play an important supporting role in the construction of a new power system with new energy as the main body [3,4]. In order to smooth the new energy output, pumped storage units often deviate from the optimal operating conditions into the vibration zone when operating in new power systems. Pumped storage units operating in the vibration zone can cause strong draft tube pressure pulsations resulting in fatigue damage to the unit and affecting its performance [5]. The draft tube pressure pulsation signal is disturbed by ambient noise, the effective features are often masked by a large amount of noise, and the non-linearity and non-smoothness of the vibration signal is increasing. Noise reduction and feature extraction of draft tube pressure pulsations can increase unit operating efficiency and reduce economic losses [6].

A lot of research has been done on noise reduction and feature extraction of vibration signals [7–9]. Among them, short-time Fourier transform (STFT) [10,11], wavelet transform (WT) [12–14], empirical mode decomposition (EMD) [15,16], ensemble empirical mode decomposition (EEMD) [17,18], and other signal decomposition methods are more common. However, all of the above methods have certain limitations. STFT enables time-frequency analysis, but the fixed window function makes time-frequency analysis lack in adaptability. The WT makes use of the scalable nature of the wavelet basis functions to give good resolution, but some of the wavelet basis and threshold functions can cause unsatisfactory noise reduction results. EMD is achieved by time-scale transformation of the signal, which often results in mode mixing due to the uncertainty of the frequency and bandwidth of each mode during decomposition. The EEMD solves the mode mixing problem posed by EMD by adding random white noise to the original signal. However, the signal decomposition of EEMD is often accompanied by end effects that may cause signal deficiencies and affect the processing effect [19]. Based on the above analysis, it is important to propose a time-frequency signal processing method that is applicable to non-smooth non-linear signals. Singular value decomposition (SVD) is a noise reduction method based on phase space reconstruction, which achieves noise reduction by removing the reconstructed signal components corresponding to smaller singular values [20]. Reference [21] proposes an optimal wavelet demodulation method based on singular value decomposition (SVD), which can accurately detect the shock component in vibration signals. In [22], a combined adaptive local iterative filtering (ALIF) and SVD method was used for dual noise reduction and feature extraction of draft tube pressure pulsation, which was verified in simulation experiments and measured draft tube pressure pulsation data. Dragomiretskiy [23–26] proposed a variational mode decomposition (VMD) method based on non-recursive signals to achieve better results in the decomposition of vibration signals. Reference [27] used VMD to decompose the vibration signal, avoiding the mode mixing problem caused by EMD, and extracted a wealth of information on fault characteristics. Furthermore, [28] proposed a noise reduction method based on VMD and quantum particle swarm optimization adaptive stochastic resonance to achieve good noise reduction in early faint fault features. However, the effect of VMD decomposition is influenced by the iteration K and the penalty factor a. Too large a value of K or a can easily lead to over-decomposition of mode mixing; too small a value of K or a can easily lead to under-decomposition. Some of the literature is based on experience or observation to determine parameter combinations, which is subjective and random [29]. In recent years, some scholars have proposed to seek the optimal parameters of VMD by optimization algorithms. Traditional optimization algorithms [30–32] are well established but often fall into local optima when solving, making it difficult to achieve satisfactory results for the complexity of vibration signals. It is important to implement an adaptive decomposition of the VMD parameters using an algorithm with a strong global search capability.

Based on the above analysis, the SSA [33] has a flexible and efficient global search capability, with stronger convergence and better optimization accuracy and stability. Adaptive optimization of VMD parameters can be achieved using SSA. VMD and SVD have been applied to non-stationary vibration signals and have effectively avoided the problem of mode mixing in the decomposed signal, considering that the draft tube pressure pulsation contains a wealth of characteristic information about the unit's operating conditions for the pressure pulsation characteristics of the draft tube of pumped storage units [34,35]. In this paper, we propose a study on pressure pulsation reduction of pumped storage units based on sparrow optimization VMD combined with SVD.

This paper takes pumped storage units as the research object, and the main contributions are as follows: (1) By comparing the computational cost of envelope entropy (EE), sample entropy (SE), and permutation entropy (PE), it is determined that the EE is used as the fitness function of the SSA to achieve adaptive optimization of the VMD parameters. (2) Using the EE as the fitness function, the SSA, the particle swarm optimization (PSO), and the genetic algorithm (GA) were compared in terms of their ability to find the optimal

VMD parameters, and the SSA was determined as the optimization algorithm for the VMD parameters. (3) By comparing the noise reduction ability of different entropies, it was determined that PE would be used as the feature extraction method. (4) Calculate the PE after VMD decomposition and select the optimal PE parameter by comparing the entropy values under different embedding dimensions and delay time conditions. The signal components whose PE values are less than the set threshold are retained for reconstruction to achieve preliminary noise reduction of the noisy signal. (5) The signal after the initial noise reduction is noise reduced again by using SVD, and the effectiveness of various feature extraction methods is evaluated by using the correlation coefficient and mean square error as evaluation indexes.

The rest of the paper is as follows: Section 2 introduces the basic principles of the noise-carrying signal noise reduction method based on SSA optimization VMD combined with SVD and establishes the framework flow chart of the research method. Section 3 constructs a simulation signal based on the pressure pulsation characteristics of the draft tube of pumped storage units and determines the optimal parameters of the proposed method in this paper. Section 4 compares the proposed method with reported noise reduction methods using simulated signals and evaluation metrics to demonstrate the effectiveness of the method.

2. Methods

2.1. VMD

VMD is a new method for non-recursive signal decomposition proposed by Dragomiretskiy [36]. Constraints are used as the theoretical basis for constructing the overall framework and searching for variational modes by iteration. The decomposition of a signal consisting of multiple components into K intrinsic mode functions with fixed central frequencies ω_k. The mode mixing problems are avoided and local features are highlighted for subsequent signal analysis.

(1) Mode components u_k of the analytic signal

After Hilbert's method calculation, each intrinsic mode function is considered as an FM-AM mode function.

$$u_k(t) = \mathrm{A}_k(t)\cos(\varnothing_k(t)) \tag{1}$$

where $\mathrm{A}_k(t)$ is the instantaneous amplitude of $u_k(t)$, $\varnothing_k(t)$ is the instantaneous phase of $u_k(t)$. The derivative of the instantaneous phase with respect to time is the instantaneous frequency $\omega_k(t) = \mathrm{d}\varnothing_k(t)/\mathrm{d}t$.

(2) Estimation of the frequency bandwidth of each intrinsic mode function

Using Hilbert's transformation of the mode component $u_k(t)$, one can obtain the one-sided spectral equation. Gaussian smoothing is used to obtain the bandwidth of the analytic signal after frequency shift, that is, the square root of the norm gradient L^2. The variational problem is constructed as follows:

$$\begin{cases} \min\left\{ \sum\limits_{k=1}^{k} \left\| \partial_t \left(\delta(t) + \frac{j}{\pi t} \right) u_k\,(t)\, \mathrm{e}^{-jw_k\,(t)} \right\} \right\|_2^2 \\ s.\,t.\ \sum\limits_{k=1}^{k} u_k = f(t) \end{cases} \tag{2}$$

where ∂_t is the partial derivative of the function with respect to time t, $\delta(t)$ is the unit time impulse function, $\mathrm{e}^{-jw_k\,(t)}$ is the correction exponent, and $f(t)$ is the signal input function.

(3) Introduction of the Lagrange quadratic constraint and solution using alternating operators

The unconstrained variational solution is established by augmenting Lagrange method as in Equation (3). After that, the alternating direction multiplier algorithm is used to continuously iteratively update the solution to obtain the generalized function as in Equation (4):

$$\begin{array}{c} \mathrm{L}(\{u_k\},\{\omega_k\},\check{}) = a\sum_k \left\|\partial_t\left[\left(\delta(t)+\frac{j}{\pi t}\right)u_k(t)\right]\mathrm{e}^{-jw_k(t)}\right\|_2^2 + \|f(t) \\ -\sum_k u_k(t)\|_2^2 + <\check{}(t), f(t)\sum_k u_k(t)> \end{array} \tag{3}$$

where a is the penalty factor, and $\lambda(t)$ is the Lagrangian multiplier.

$$\begin{array}{c} \hat{u}_k{}^{\mathrm{n}+1} = \frac{-\hat{f}(w)-\sum_{i\neq k}\hat{u}_i{}^{\mathrm{n}+1}(\omega)+\frac{\hat{\lambda}(t)}{2}}{1+2a(\omega-\omega_k{}^2)} \\ \omega_k{}^{\mathrm{n}+1} = \frac{\int_0^\infty \omega|\hat{u}_k(\omega)|^2\,\mathrm{d}_\omega}{\int_0^\infty|\hat{u}_k(\omega)|^2\,\mathrm{d}_\omega} \end{array} \tag{4}$$

(4) Termination conditions

$$\sum_{k=1}^{k}\left(\|\hat{u}_k{}^{\mathrm{n}+1}-\hat{u}_k{}^{\mathrm{n}}\|_2^2\,/\,\|\hat{u}_k{}^{\mathrm{n}}\|_2^2\right) < \varepsilon \tag{5}$$

The iteration ends when the constraint satisfies the above equation, otherwise a circular iteration is performed and a series of intrinsic mode functions are obtained at the end of the iteration.

2.2. Adaptive Optimization of VMD Parameters

2.2.1. SSA Principles

The SSA is a group intelligence optimization algorithm that simulates the foraging and anti-predatory act of sparrows. The algorithm is built by simulating the following acts: finders search for food while avoiding the danger of predation; joiners compete for food resources by monitoring the finders. Assume that the sparrow population size is N, the number of iterations is t, the dimensionality of the optimization variables is d_{min}, and the fitness is f. The sparrow's ability to search for food is strongest when the fitness is best.

Assuming that the finder searches for the widest range of food, the iterative process updates the finder's location search as follows:

$$X_{i,j}^{t+1} = \begin{cases} X_{i,j}^{t}\cdot\exp\left(-\frac{i}{a\cdot iter_{\max}}\right) if\ R_2 < ST \\ X_{i,j}^{t}+Q\cdot L\ if\ R_2 \geq ST \end{cases} \tag{6}$$

where t is the number of iterations, $iter_{\max}$ is the current maximum number of iterations, $X_{i,j}$ is the position information of i-th sparrow in the j-th dimension, R_2 is the warning value, ST is the safety value, a is the random number of (0, 1], Q is a random number obeying normal distribution, and L denotes a $1 \times d$ matrix. When $R_2 < ST$, it means there is no predator in the foraging environment, and the finder can continue searching. When $R_2 \geq ST$, the predator appears and the sparrow needs to change the area to search.

Joiners compete for food resources with discoverers by monitoring their tracks, and a joiner's location search is updated as follows:

$$X_{i,j}^{t+1} = \begin{cases} Q\cdot\exp\left(\frac{X_{\mathrm{worst}}-X_{i,j}^{t}}{i^2}\right) if\ i > n/2 \\ X_p^{t+1}+\left|X_{i,j}^{t}-X_p^{t+1}\right|\cdot A^{+}\cdot L\ \text{ otherwise} \end{cases} \tag{7}$$

where X_p is the optimal position of the current discoverer, X_{worst} is the worst position currently searched, and A denotes a $1 \times d$ matrix. When $i > n/2$, it means that the joiner cannot obtain food resources due to low adaptation.

The locations of some of the individual sparrows in the sparrow population that realized the approaching danger and made a zone change were updated as follows:

$$X_{i,j}^{t+1} = \begin{cases} X_{\text{best}}^{t} + \beta \cdot \left| X_{i,j}^{t} - X_{best}^{t} \right| if\ f_{\ i} > f_{\ g} \\ X_{i,j}^{t} + K \cdot \left(\frac{\left| \ X_{i,j}^{t} - X_{\text{worst}}^{t} \ \right|}{(f_{\ i} - f_{w}) + \varepsilon} \right) if\ \ f_{\ i} = f_{\ g} \end{cases} \tag{8}$$

where X_{best} is the current global optimal position, $f_{\ i}$ is the i-th individual sparrow fitness, $f_{\ g}$ is the current global best fitness, f_w is the current global worst fitness value, β is a random number obeying normal distribution, K is a random number of $[-1, 1]$, and ε is a constant.

2.2.2. VMD Parameter Optimization Based on SSA

The EE can measure the extent to which a signal contains fault information based on the sparsity of the signal. If the signal contains more noise, the signal is less sparse and has a higher EE. The signal X_i has the following expression for the EE.

$$\begin{cases} E_p = -\sum\limits_{i=1}^{N} p_i \lg\ p_i \\ p_i = a(i) / \sum\limits_{i=1}^{N} a(i) \end{cases} \tag{9}$$

where E_p is the signal X_i of the EE, $a(i)$ is the signal X_i the envelope signal after Hilbert calculation, and p_i is the normalized form of the $a(i)$.

Reference [37] used EE as a fitness function to optimize the VMD parameters in order to make the SSA process of optimizing the VMD parameters more accurate. Firstly, the VMD parameters are initialized, using the parameters $[a, K]$ as particle positions. The EE is used as the fitness function to calculate the EE value of each particle under the VMD decomposition. The positions of sparrow discoverers, joiners, and other individuals are calculated according to Equations (6)–(8) for individual and global search. The particle positions are continuously updated and the combination of parameters with the smallest EE is recorded. When the number of iterations is satisfied, the loop is jumped out at the end of the iteration and the optimal parameter combination $[a, K]$ is output.

2.3. PE

PE is an effective calculation method proposed by Christophet et al. to detect signal dynamic mutation and time series randomness [38]. PE can be used to filter the mode information and distinguish the noise dominant component from the effective signal component with rich feature information. The noise interference components with relatively high entropy values are removed by preset threshold for the purpose of denoising. The principle of the algorithm is as follows:

(1) Suppose a time series X_i and reconstruct its phase space; the matrix is obtained as follows:

$$\begin{cases} X_1 = \left\{ X_1, X_{1+\tau}, \ldots, X_{1+(m-1)\tau}, \right\} \\ X_2 = \left\{ X_2, X_{2+\tau}, \ldots, X_{2+(m-1)\tau}, \right\} \\ \vdots \\ X_r = \left\{ X_r, X_{r+\tau} \ldots, X_{r+(m-1)\tau} \right\} \end{cases} \tag{10}$$

where m is the embedding dimension and τ is the delay time. r is the number of row vectors to reconstruct.

(2) Each row of the matrix is considered as a reconstructed component, and the elements are rearranged in ascending order to obtain:

$$X_i = \{X(i+(\varepsilon_1-1)\times\tau)\} \le X(i+(\varepsilon_2-1)\times\tau) \le \cdots \le X(i+(\varepsilon_m-1)\times\tau)\ \} \tag{11}$$

where $\varepsilon_1, \varepsilon_2, \cdots, \varepsilon_m$ is the column index of each element in the reconstructed component.

(3) Calculate the probability of indexing P_1 , $P_2, \cdots P_3$ at different positions. Define the normalized PE of the indexed series at different positions of the time series according to the form of entropy.

$$H = (-\sum_{i=1}^{r} P_i \cdot \lg_p) \lg(m!) \tag{12}$$

2.4. SVD

SVD is a noise reduction method based on phase space reconstruction. As the noise signal has a different correlation to the original signal, by observing the singular value SVD spectrum, the singular value components representing the noise after decomposition are zeroed out and the singular values of the valid signal are retained [39]. Noise reduction of the characteristic matrix is achieved by the inverse of the SVD. For the signal X_i, the Hankel matrix is constructed as follows:

$$H = \begin{bmatrix} X(1) & \cdots & X(q) \\ \vdots & \ddots & \vdots \\ X(d) & \cdots & X(N) \end{bmatrix} \tag{13}$$

The SVD decomposition of the H matrix is as follows:

$$Q = U \begin{bmatrix} \sum K & 0 \\ 0 & 0 \end{bmatrix} V^T \tag{14}$$

where U, V are orthogonal matrices. $\sum K = \mathrm{diag}(\sigma_1, \sigma_2, \cdots \sigma_3)$ forms the fault feature vector.

The PE value of the components after VMD decomposition is calculated, and the effective components smaller than the PE threshold are retained for reconstruction. The VMD-PE denoised signal is constructed as a Hankel matrix for SVD decomposition to achieve noise reduction again.

2.5. Noise Reduction Steps

Figure 1 shows the flow chart of the SSA–VMD–SVD framework, and the specific steps are shown below:

Step 1: Acquisition of vibration signals, setting the number of sampling points and sampling frequency.

Step 2: Determine the fitness function and establish an adaptive decomposition method for VMD parameters based on SSA, setting the population size to 10 and the maximum number of iterations to 20.

Step 3: Initialize the VMD parameters, using the parameters [a, K] as particle positions. The range of a is [1000, 3000] and the range of K is [2, 10]. The optimal combination of parameters with the smallest fitness function is obtained by SSA global search.

Step 4: Perform a VMD decomposition according to the optimal combination of parameters [a, K] to obtain K IMF components.

Step 5: Calculate the PE value of each component according to Equations (10)–(12) and set the PE threshold based on multiple simulations to achieve the initial noise reduction of the noisy signal.

Step 6: The initial noise reduction signal is decomposed by SVD according to Equation (14) to achieve the noise reduction of the reconstructed signal again.

Step 7: Extract the fault feature vector and perform a spectrum analysis to identify the cause of the fault.

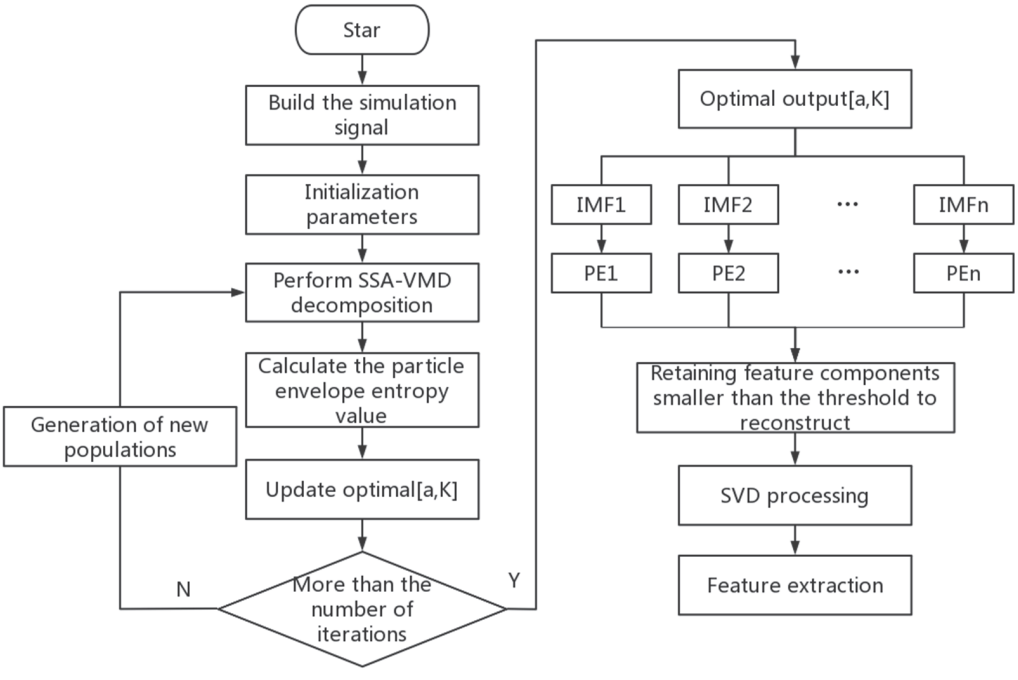

Figure 1. The framework flow chart of the proposed method.

3. Results

3.1. Simulation Signal

The main cause of the draft tube pressure pulsation is the low frequency vortex band, but there is also a certain amount of medium and high frequency pressure pulsation. The low-frequency pulsation frequency is about 0.15–0.30 times, and the medium-high frequency pressure pulsation frequency is close to the unit rotation frequency. In order to verify the effectiveness of the algorithm in extracting the pressure pulsation signal in the draft tube in this paper, the simulation signal A expression is established as follows:

$$\begin{aligned} X_1 = \ & 0.3 \cdot \sin(2\pi t\ f_1) + 0.2 \cdot \sin(2\pi t\ f_2) + 0.1 \sin \cdot (2\pi t\ f_3) \\ X_2 = \ & \text{rand}\ (1,\ 5000) \\ X_t = \ & X_1 + X_2 \end{aligned} \tag{15}$$

where f_1 is 0.6 Hz, f_2 is 2 Hz, and f_3 is 22 Hz; set the sampling frequency to 500 and the number of sampling points N to 5000.

3.2. Vibration Signal Analysis

The simulation graph is shown in Figure 2. Figure 2a,b show the original signal waveform and spectrum, while Figure 2c,d show the waveform and spectrum under strong noise interference. Under strong noise interference, the periodic pulses reflecting the fault characteristics are obliterated. In Figure 2d, it is also not possible to identify the obvious shock components, making it difficult to determine the type of fault.

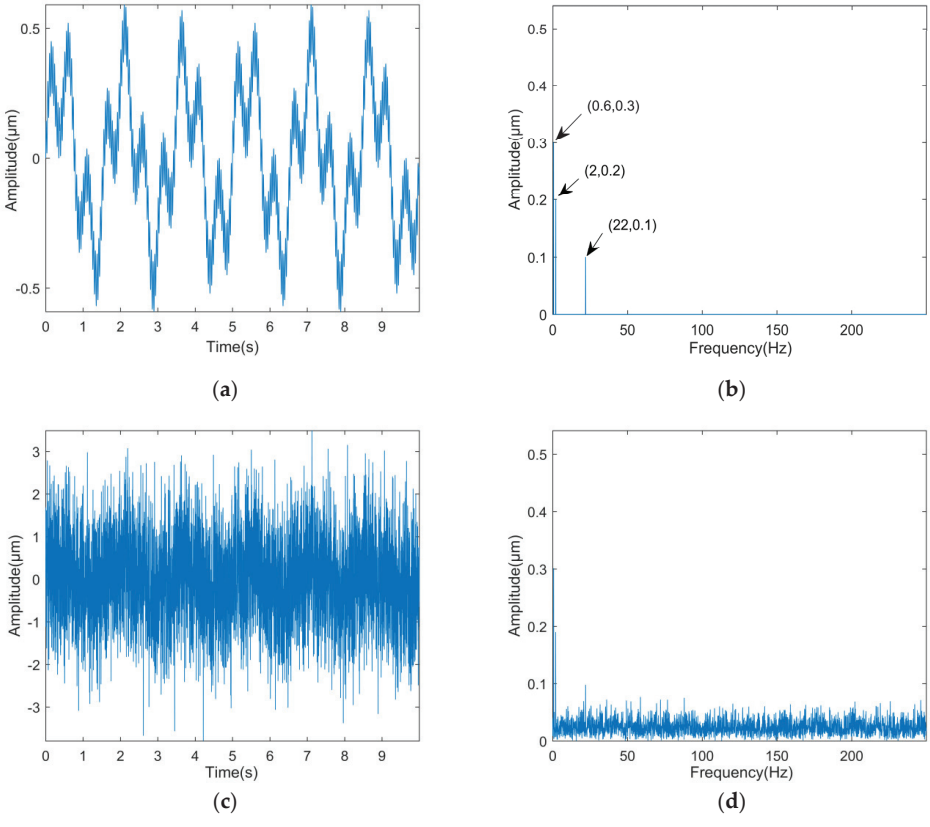

Figure 2. Simulated signal waveform and spectrum (**a**) Original signal waveform diagram; (**b**) Spectrum of the original signal; (**c**) Noise added signal waveform diagram; (**d**) Noise added signal spectrum.

3.3. Noise Reduction Based on SSA–VMD–SVD

3.3.1. Fitness Function

Entropy, as a measure of signal disorder, can be used as a fitness function for SSA–VMD. EE, SE, and PE can all be used as a fitness function. The lowest entropy value is used as the basis for preferring the parameters. Therefore, in order to reduce the computational cost of the algorithm, only the running times of the different types of entropies are compared. The results are shown in Table 1. It can be seen that the running time and iteration times of EE are the smallest among the three kinds of entropies, while their corresponding optimal parameters are similar, so the EE is used as the final fitness function.

Table 1. Table of optimization parameters for different fitness functions.

Fitness Functions	[a, K]	Number of Iterations	Minimum Entropy Value	Running Time (s)
EE	[2853, 10]	2	6.1766	4705
PE	[2996, 10]	2	0.4562	17150
SE	[2898, 10]	5	0.2221	10762

3.3.2. Optimization Algorithms

To highlight the global search capability of SSA algorithm, SSA is compared with GA and PSO. Using the EE as the fitness function and setting the same population size, number of iterations, and range of optimization parameters, the optimization results are shown in Figure 3.

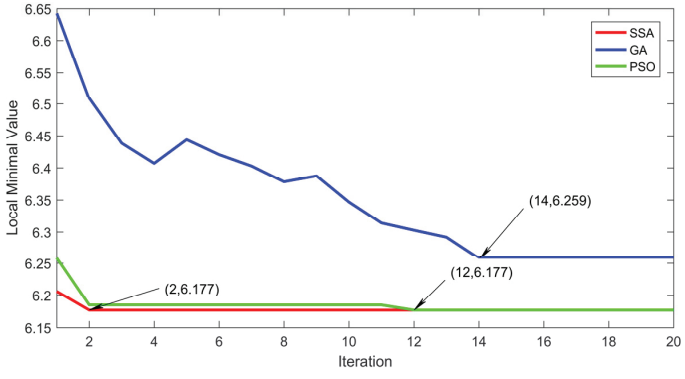

Figure 3. Iterative adaptation under different algorithms.

As can be seen from Figure 3, in the process of SSA optimization, the local minimum 6.177 appears in the second iteration, and the output parameter is [2853, 10]. In the process of PSO optimization, the local minimum 6.177 appears in the 12th iteration, and the output parameter is [2854, 10]. The local minimum value 6.259 in GA optimization appears in the 14th iteration, and the output parameter is [2902, 10]. When the output parameter value is close to the decomposition effect, the number of iterations of SSA is small and the fitness function is small, which proves that the convergence speed and global search ability of SSA are superior to GA and PSO.

Considering the randomness of the algorithm, the SSA-VMD algorithm with the envelope entropy as the fitness function was optimized for 10 times and the average value was taken as the output result, and the parameter combination was [2853, 10].

3.3.3. PE Parameter

The embedding dimension of the PE affects the construction accuracy, the embedding dimension m usually ranges from 3 to 7, and the delay time τ is usually set to 1 [40]. In order to select the PE parameters suitable for the pressure pulsation signal of the pumped storage unit, the PE values of the simulated signal with m [2, 10] and τ [1, 10] are compared and analyzed. The results are shown in Figure 4.

As can be seen from the Figure 4, when the embedding dimension is a fixed value, the curves in the figure mostly overlap.

Proof. The delay time has little effect on the PE value, and sufficient information can be obtained with a delay time of 1. □

Therefore, the delay time τ of 1 is chosen in this paper. When the embedding dimension m is [2,6], the entropy value remains within a stable and small difference. When the m is greater than or equal to 7, the PE value appears to be more volatile, which will cause some interference to the evaluation of the random degree of the signal. Considering the length of the data, the m should be as large as possible without distortion, so the m is chosen to be 6 and the τ is 1.

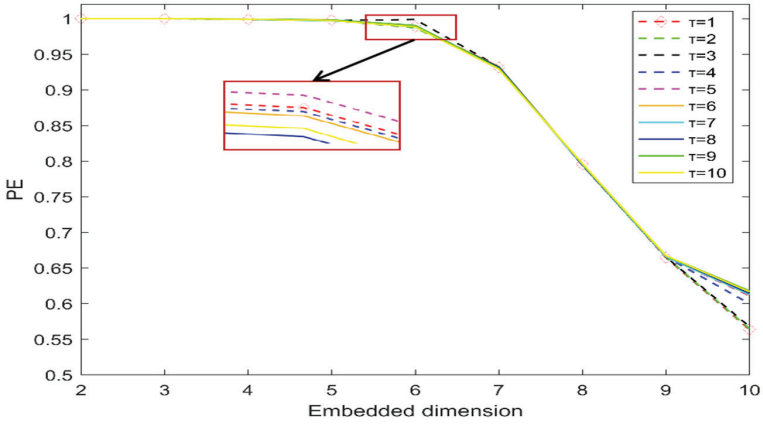

Figure 4. The relationship between the PE parameters.

3.3.4. The Comparison of Entropy

Entropy can distinguish between the noise component and the effective component to achieve primary noise reduction of the simulated signal [41]. The PE, SE, and EE are combined with VMD for a single noise reduction comparison respectively. The correlation coefficient and mean square error were also introduced to reflect the relationship between the noise-reduced signal and the original signal to evaluate the noise reduction effect of the PE. The calculation results are shown in Table 2.

Table 2. Noise reduction test with three types of entropy.

Feature Extraction Methods	Correlation Coefficient	Mean Square Error
VMD-PE	0.6210	0.3169
VMD-SE	0.4931	0.4368
VMD-EE	0.4945	0.4494

As seen in Table 2, the correlation coefficient of the VMD–PE processed signal is the largest and the mean square error is the smallest, and the noise reduction preserves the original signal more completely. It proves that PE has the best noise reduction effect among the three entropies.

3.3.5. Simulation Results

With the above parameter discussion, the SSA–VMD–SVD processed waveform and spectrum are obtained. As seen in Figure 5a, the processed signal waveform becomes smooth and regular, with a large amount of noise removed without distortion. From Figure 5b, it can be seen that the amplitude of the spectral lines representing the shock component is strong. The f_1, f_2, and f_3 frequencies reflecting the fault characteristics were basically extracted effectively. This demonstrates that the SSA–VMD–SVD decomposition works well and that there is no mode mixing problem.

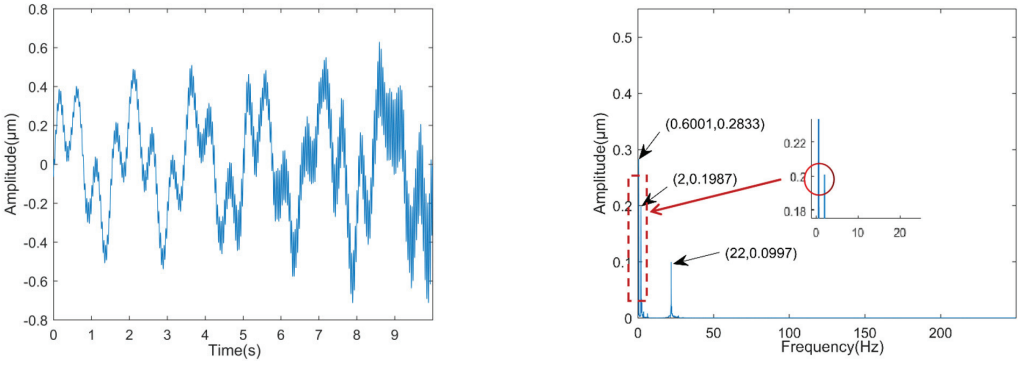

Figure 5. Simulated signal after SSA-VMD–SVD processing. (**a**) Waveform diagram after noise reduction; (**b**) Spectrum after noise reduction.

4. Discussion

4.1. Comparison of Methods

4.1.1. Comparative Analysis

In order to highlight the effectiveness and reliability of the proposed method, other methods are used for noise reduction and feature extraction comparison. The signal processing method considering time domain or frequency domain cannot adapt to the non-stationarity and non-linearity of pressure pulsation signal. The representative time-frequency signal decomposition method (CEEMD ALIF VMD) combined with PE was selected to carry out the primary noise reduction of the simulation signal. However, the effect of primary denoising on complex signal denoising and feature extraction is not ideal, so on the basis of primary denoising, SVD secondary denoising process is added. Figures 6–9 show the simulated signal plots after CEEMD–PE, VMD–PE, ALIF–PE, and ALIF–SVD processing respectively.

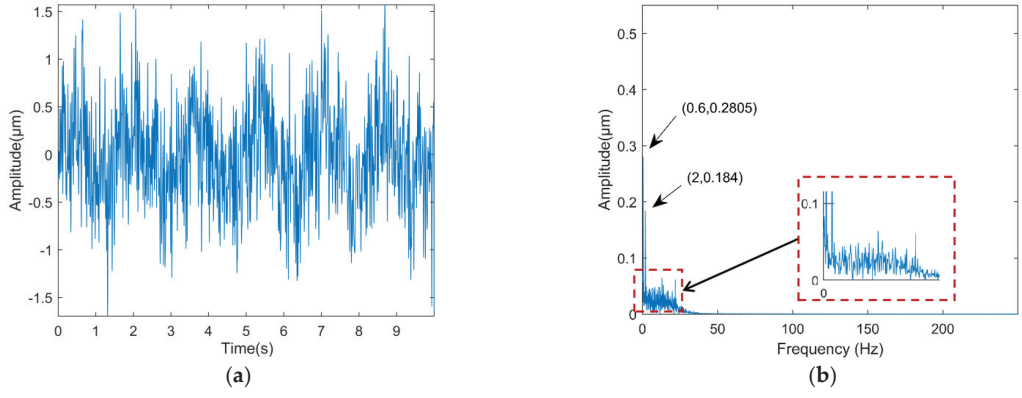

Figure 6. Simulated signal after CEEMD–PE processing. (**a**) Waveform diagram after noise reduction; (**b**) Spectrum after noise reduction.

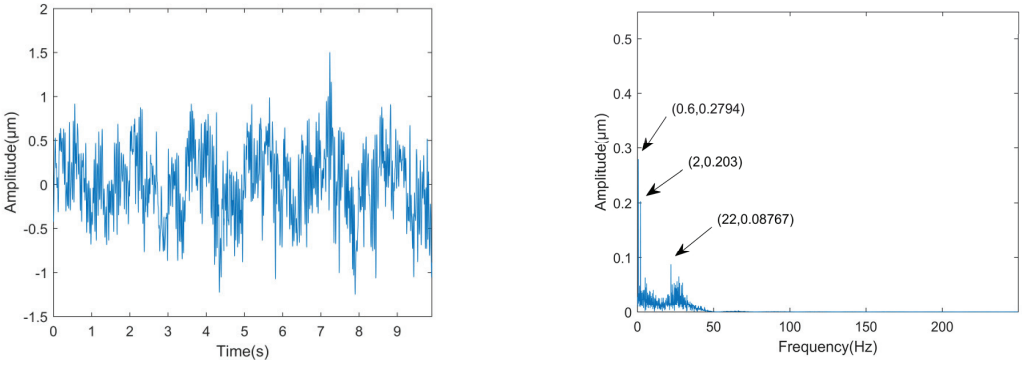

Figure 7. Simulated signal after VMD–PE processing. (**a**) Waveform diagram after noise reduction; (**b**) Spectrum after noise reduction.

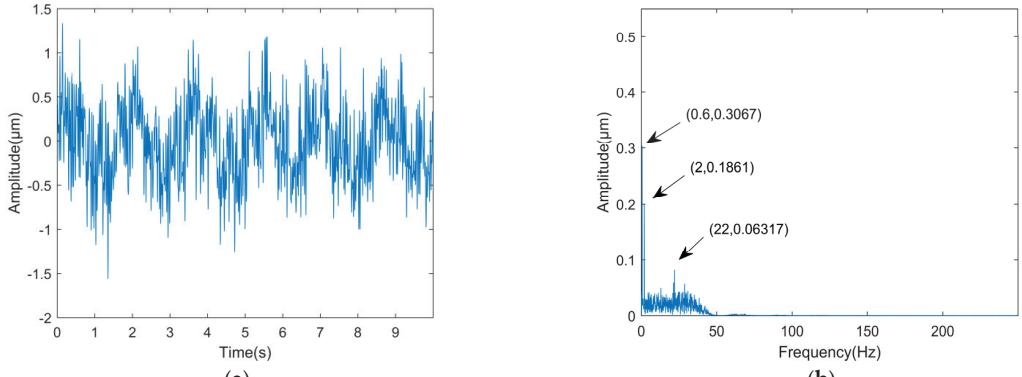

Figure 8. Simulated signal after ALIF–PE processing. (**a**) Waveform diagram after noise reduction; (**b**) Spectrum after noise reduction.

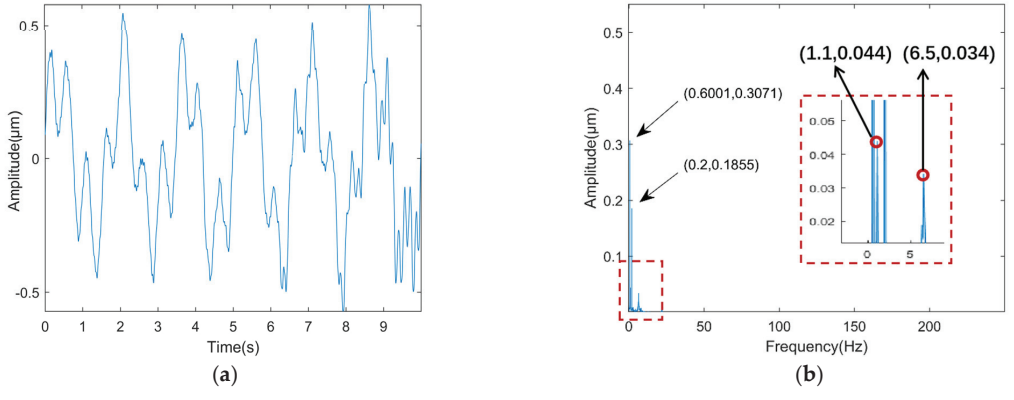

Figure 9. Simulated signal after ALIF–SVD processing. (**a**) Waveform diagram after noise reduction; (**b**) Spectrum after noise reduction.

The white noise added to the CEEMD decomposition is set at 0.2 times the standard deviation and 100 times the number of sets [42]. Due to the reconstruction bias caused by the addition of white noise resulting in some noise remaining in the signal after CEEMD processing, only two feature components are effectively extracted in Figure 6b. As seen in Figures 7 and 8, the burr is reduced in the waveform plots Figures 7a and 8a after VMD–PE and ALIF–PE processing, but the similarity to the original signal Figure 5a is not high. In Figures 7b and 8b, the three feature components are all extracted but the feature components are not accurate enough, there is bottom noise in the 0–50 Hz band, and the noise reduction effect is not satisfactory. The ALIF–SVD processed Figure 9a has a large amount of noise removed but appears distorted. In Figure 9b, only two low-frequency components are effectively extracted, and the full information reflecting the fault characteristics is not completely extracted.

4.1.2. Effectiveness Evaluation

To make the above conclusions more convincing, the correlation coefficient and mean square error were introduced to reflect the relationship between the processed signal and the original signal, and the results were calculated as shown in Table 3.

Table 3. Assessment table for different methods of noise reduction.

	Correlation Coefficient	Mean Square Error
Noisy signals	0.2428	1.0068
CEEMD–PE	0.5123	0.4227
VMD–PE	0.6210	0.3169
ALIF–PE	0.7024	0.2595
ALIF–SVD	0.9360	0.0940
VMD–SVD	0.9614	0.0732

As can be seen from Table 3, the correlation coefficient after VMD–SVD processing is the highest and the mean square error is the lowest among the methods, which proves that this method has the highest similarity to the original signal after denoising and reconstruction, retains the highest integrity of valid information, and is more effective for the extraction of early weak faults in the draft tube.

4.2. Analysis of Variable Working Conditions

In order to prove that VMD–SVD is not only suitable for noise reduction of vibration signal under single working conditions and fixed noise, change the characteristic frequency under the condition of invariable noise and change the noise size under the condition of invariable characteristic frequency, respectively, to demonstrate the applicability of the method under the condition of variable working conditions and random noise interference.

Construction of simulated signal B with the same noise but different frequencies:

$$\begin{aligned} X_1 = \ & 0.35\cdot\sin(2\pi t\ f_1)+0.3\cdot\sin(2\pi t\ f_2)+0.2\sin\cdot(2\pi t\ f_3)+0.2\sin\cdot(2\pi t\ f_3) \\ & X_2 = \text{rand}\ (1,\ 5000) \\ & X_t = X_1 + X_2 \end{aligned} \tag{16}$$

where f_1 is 0.5 Hz, f_2 is 1.1 Hz, and f_3 is 2 Hz; f_4 is 9.5 Hz.

Construction of simulated signal C with the same frequency but different noise:

$$\begin{aligned} X_1 = \ & 0.3\cdot\sin(2\pi t\ f_1)+0.2\cdot\sin(2\pi t\ f_2)+0.1\sin\cdot(2\pi t\ f_3) \\ & X_2 = 0.5\ \text{rand}\ (1,\ 5000) \\ & X_t = X_1 + X_2 \end{aligned} \tag{17}$$

where f_1 is 0.6 Hz, f_2 is 2 Hz, and f_3 is 22 Hz.

The constructed signals were subjected to VMD–SVD processing and the corresponding spectrums were obtained as shown in Figure 10. The correlation coefficients and mean

square errors of the three signals after VMD–SVD processing were compared and the results are shown in Table 4.

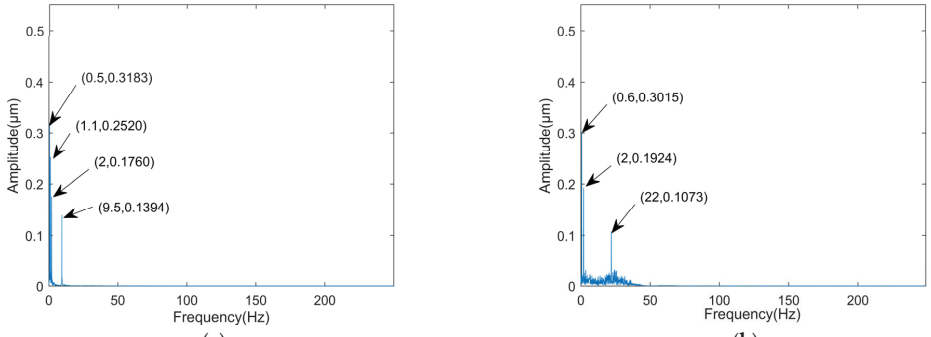

Figure 10. Spectra of the two simulated signals after VMD–SVD processing. (**a**) Spectrum of signal B after noise reduction; (**b**) Spectrum of signal C after noise reduction.

Table 4. Table of evaluation indicators for different signals.

Signal	Correlation Coefficient	Mean Square Error
A	0.9614	0.0732
B	0.9776	0.0901
C	0.9942	0.0285

As can be seen from Figure 10 and Table 4, the characteristic frequencies of signals B and C are basically extracted effectively, and the reconstructed signals maintain a good correlation with the original signals. This demonstrates that VMD–SVD is not only applicable to the noise reduction of vibration signals under single working conditions and fixed noise.

4.3. Examples

In order to verify the effectiveness of the algorithm in this paper, a pumped storage power plant draft tube pressure pulsation signal is used as an example for the unit test. The signal is collected using an AK–4D pressure sensor number N2186, as shown in Figure 11. The unit model is HLNTP–LJ–512, the rated output is 306.1 MW, the rated speed is 300 r/min, the sampling frequency is 500 Hz, and the number of intercepted data points is 5000. Figure 12 shows the measured pressure pulsation signal of a pumped storage power station, and the signal waveform plot is homogenized.

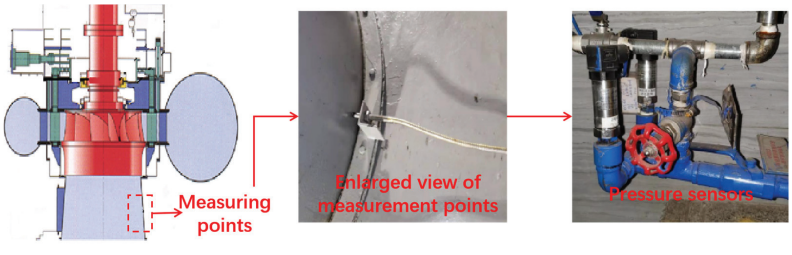

Figure 11. Sensor arrangement measurement diagram.

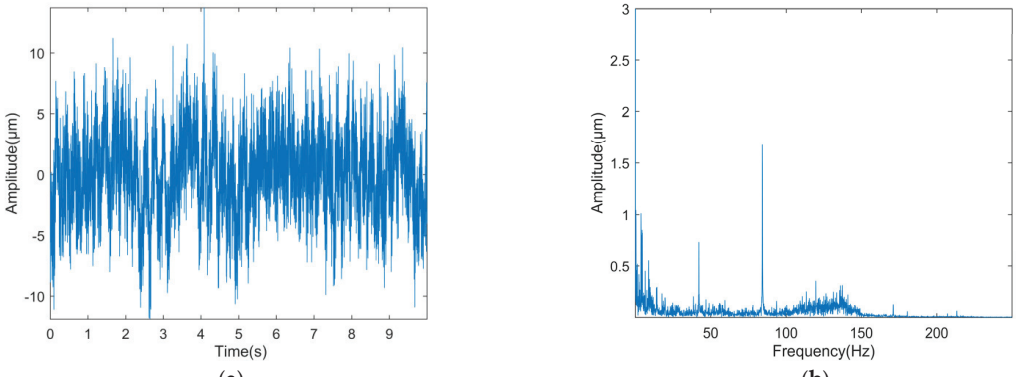

Figure 12. Measured pressure pulsation signal at a pumped storage power station. (**a**) Signal waveform diagram; (**b**) Signal spectrum.

As can be seen in Figure 12a, there is obviously non-periodic noise interference in the signal waveform, and the periodic pulse reflecting the characteristics of the fault is completely masked. As can be seen in Figure 12b, there are some spectral peaks in the middle and high frequency bands but there is no regularity, and there are many interference spectral lines around, making it difficult to accurately determine the cause of the unit fault.

The actual data were processed according to the simulation experiment of VMD–SVD. Figure 13a,b show the waveforms and spectrums after VMD–SVD processing, respectively. From Figure 13a, it can be seen that the processed signal waveform is smoother, the shock regularity is enhanced, and the interference noise is suppressed to a certain extent. As can be seen in Figure 13b, low frequency amplitudes that could not be identified before denoising appear, and the surrounding interference spectral lines are effectively removed. The shock component of $X = 0.61$ is consistent with the low frequency of the draft tube vortex band, and the shock component of $X = 4.5$ is close to the rotation frequency of the unit (as shown in the red dashed box), which meets the characteristics of the pressure pulsation of the draft tube vortex band. This proves that the fault characteristics masked by noise are effectively stripped out. The above analysis fully proves that the method in this paper can achieve effective extraction of early faint faults in pressure pulsation of pumped storage units.

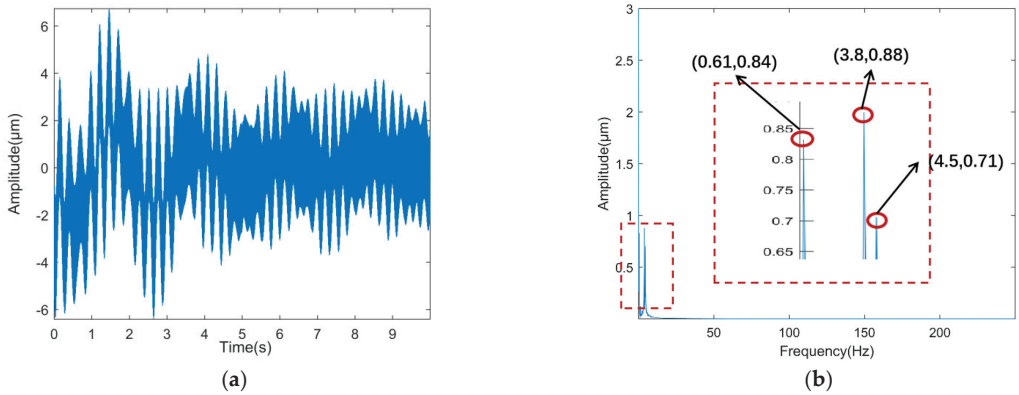

Figure 13. Graph of the actual data signal after VMD–SVD processing. (**a**) Waveform diagram after noise reduction; (**b**) Spectrum after noise reduction.

5. Conclusions

Against the background of strong noise interference and variable operating conditions of pumped storage units, and in view of the difficulty in extracting the early weak fault characteristics of pressure pulsations of pumped storage units, this paper proposes a sparrow-based optimization VMD combined with SVD for pressure pulsation noise reduction of pumped storage units, with the following conclusions.

(1) Applying the SSA algorithm with envelope entropy as the fitness function to the parameter decomposition of VMD overcomes the shortcomings of manual parameter selection of VMD and realizes the adaptive decomposition of VMD.
(2) The choice of the combined VMD–SVD noise reduction method effectively avoids the problem of post-reconstruction noise interference and can achieve good results in non-stationary signal decomposition.
(3) Through simulation comparison with CEEMD–PE, VMD–PE, ALIF–PE, and ALIF–SVD, it is proved that the noise reduction method of VMD–SVD can effectively remove noise, achieve the extraction of low frequency fault characteristics of pressure pulsation of pumped storage units under strong noise disturbance, and enhance fault-related characteristics.

Author Contributions: Supervision, writing—original draft preparation, Conceptualization, Y.R.; methodology, writing—original draft preparation, L.Z.; visualization, J.C.; formal analysis, J.L.; writing—review and editing, P.L.; data curation, R.Q., X.Y. and S.H.; software, X.L.; validation, investigation, C.C.; resources, H.C. All authors have read and agreed to the published version of the manuscript.

Funding: This research was funded by "Henan Province Key R & D and Promotion Project (Science and Technology Research), grant number No. 212102311054" and the Training Program for Young Key Teachers in Colleges and Universities of Henan Province, grant number No. 2019GGJS097, as well as the Hunan Key Laboratory of Renewable Energy Power Technology (Changsha University of Technology) Open Fund Project, grant number No. 2016ZNDL001.

Institutional Review Board Statement: Not applicable.

Informed Consent Statement: Not applicable.

Data Availability Statement: The data that support the findings of this study are available from the corresponding author upon reasonable request.

Conflicts of Interest: The authors declare no conflict of interest.

References

1. Han, T.; Li, Y.F.; Qian, M. A Hybrid Generalization Network for Intelligent Fault Diagnosis of Rotating Machinery Under Unseen Working Conditions. *IEEE Trans. Instrum. Meas.* **2021**, *70*, 1–11. [CrossRef]
2. Cai, B.; Hao, K.; Wang, Z.; Yang, C.; Kong, X.; Liu, Z.; Ji, R.; Liu, Y. Data-driven early fault diagnostic methodology of permanent magnet synchronous motor. *Expert Syst. Appl.* **2021**, *177*, 115000. [CrossRef]
3. Liu, T.; Wang, C.; Chen, Z.; Chen, F.; Bi, H.; Luo, Y.; Wang, Z. Analysis of flow characteristics in pumped storage unit during start-up in turbine mode. *J. Phys. Conf. Ser.* **2021**, *1985*, 012051. [CrossRef]
4. Jowsey, E. A new basis for assessing the sustainability of natural resources. *Energy* **2007**, *32*, 906–911. [CrossRef]
5. Feng, Z.; Chu, F. Nonstationary Vibration Signal Analysis of a Hydroturbine Based on Adaptive Chirplet Decomposition. *Struct. Health Monit. Int. J.* **2007**, *6*, 265–279. [CrossRef]
6. Cai, B.; Liu, Y.; Xie, M. A Dynamic-Bayesian-Network-Based Fault Diagnosis Methodology Considering Transient and Intermittent Faults. *IEEE Trans. Autom. Sci. Eng.* **2017**, *6*, 11289–11300. [CrossRef]
7. Ren, Y.; Huang, J.; Hu, L.-M.; Chen, H.-P.; Li, X.-K. Research on Fault Feature Extraction of Hydropower Units Based on Adaptive Stochastic Resonance and Fourier Decomposition Method. *Shock Vib.* **2021**, *2021*, 6640040. [CrossRef]
8. Delina, M.; Nurhusni, P.A. Feature extraction of noise signal in motorcycle by Fast Fourier Transform. *J. Phys. Conf. Ser.* **2021**, *1869*, 12198. [CrossRef]
9. Guan, S.; Wang, X.; Hua, L.; Li, L. Quantitative ultrasonic testing for near-surface defects of large ring forgings using feature extraction and GA-SVM. *Appl. Acoust.* **2021**, *173*, 107714. [CrossRef]
10. Rybak, G.; Strzecha, K. Short-Time Fourier Transform Based on Metaprogramming and the Stockham Optimization Method. *Sensors* **2021**, *21*, 4123. [CrossRef]

11. Chui, C.K.; Jiang, Q.; Li, L.; Lu, J. Analysis of an adaptive short-time Fourier transform-based multicomponent signal separation method derived from linear chirp local approximation. *J. Comput. Appl. Math.* **2021**, *396*, 113607. [CrossRef]
12. Li, Y.; Wang, Z.; Li, Z.; Li, H. Research on Gear Signal Fault Diagnosis Based on Wavelet Transform Denoising. *J. Phys. Conf. Ser.* **2021**, *1971*, 012074. [CrossRef]
13. Zhang, K.; Ma, C.; Xu, Y.; Chen, P.; Du, J. Feature extraction method based on adaptive and concise empirical wavelet transform and its applications in bearing fault diagnosis. *Measurement* **2021**, *172*, 108976. [CrossRef]
14. Zhang, K.; Tian, W.; Chen, P.; Ma, C.; Xu, Y. Sparsity-guided multi-scale empirical wavelet transform and its application in fault diagnosis of rolling bearings. *J. Braz. Soc. Mech. Sci. Eng.* **2021**, *43*, 1–17. [CrossRef]
15. Pal, S.; Mitra, M. Empirical mode decomposition based ECG enhancement and QRS detection. *Comput. Biol. Med.* **2012**, *42*, 83–92. [CrossRef]
16. Jiang, Z.; Wu, Y.; Li, J.; Liu, Y.; Xu, X. Application of EMD and 1.5-dimensional spectrum in fault feature extraction of rolling bearing. *J. Eng.* **2019**, *2019*, 8843–8847. [CrossRef]
17. Chen, Y.; Sun, J. Fault Diagnosis of Rolling Bearing Based on EEMD and PSO-SVM. *Electr. Power Sci. Eng.* **2016**, *32*, 47.
18. Liu, X.; Zhang, X.; Luan, Z.; Xu, X. Rolling bearing fault diagnosis based on EEMD sample entropy and PNN. *J. Eng.* **2019**, *2019*, 8696–8700. [CrossRef]
19. Wang, W.; Chen, Q.; Yan, D.; Geng, D. A novel comprehensive evaluation method of the draft tube pressure pulsation of Francis turbine based on EEMD and information entropy. *Mech. Syst. Signal Process.* **2019**, *116*, 772–786. [CrossRef]
20. An, X.; Zeng, H.; Li, C. Demodulation analysis based on adaptive local iterative filtering for bearing fault diagnosis. *Measurement.* **2016**, *94*, 554–560. [CrossRef]
21. Zhao, L.; Liu, X.; Lou, L. The feature extraction method of non-stationary vibration signal based on SVD-complex analytical wavelet demodulation. *Zhendong Ceshi Yu Zhenduan/J. Vib. Meas. Diagn.* **2015**, *35*, 672–676.
22. Ren, Y.; Liu, P.; Hu, L.; Huang, J.; Huang, S. Research on Noise Reduction Method of Pressure Pulsation Signal of Draft Tube of Hydropower Unit Based on ALIF-SVD. *Shock Vib.* **2021**, *2021*, 5580319. [CrossRef]
23. Bai, Y.; Liu, M.D.; Ding, L.; Ma, Y.J. Double-layer staged training echo-state networks for wind speed prediction using variational mode decomposition. *Appl. Energy* **2021**, *301*, 117461. [CrossRef]
24. Gfa, B.; Hwa, B.; Tqa, B.; Xpa, B.; Hong, W.C. A Transient Electromagnetic Signal Denoising Method Based on An Improved Variational Mode Decomposition Algorithm—ScienceDirect. *Measurement* **2021**, *184*, 109815.
25. Zhu, X.; Huang, Z.; Chen, J.; Lu, J. Rolling bearing fault diagnosis method based on VMD and LSSVM. *J. Phys. Conf. Ser.* **2021**, *1792*, 12035. [CrossRef]
26. Zhang, Y.; Lian, Z.; Fu, W.; Chen, X. An ESR Quasi-Online Identification Method for the Fractional-Order Capacitor of Forward Converters Based on Variational Mode Decomposition. *J. IEEE Trans. Power Electron.* **2022**, *37*, 3685–3690. [CrossRef]
27. Song, X.; Wang, H.; Chen, P. Weighted kurtosis-based VMD and improved frequency-weighted energy operator low-speed bearing-fault diagnosis. *Meas. Sci. Technol.* **2021**, *32*, 035016. [CrossRef]
28. Gu, X.; Chen, C. Rolling Bearing Fault Signal Extraction Based on Stochastic Resonance-Based Denoising and VMD. *Int. J. Rotating Mach.* **2017**, *2017*, 3595871. [CrossRef]
29. Li, Y.; Cheng, G.; Liu, C.; Chen, X. Study on planetary gear fault diagnosis based on variational mode decomposition and deep neural networks. *Measurement* **2018**, *130*, 94–104. [CrossRef]
30. Wen, Y.; Luk, K.; Gazeau, M.; Zhang, G.; Chan, H.; Ba, J. An Empirical Study of Large-Batch Stochastic Gradient Descent with Structured Covariance Noise. *arXiv* **2019**, arXiv:1902.08234.
31. Li, K.; Su, L.; Wu, J.; Wang, H.; Peng, C. A Rolling Bearing Fault Diagnosis Method Based on Variational Mode Decomposition and an Improved Kernel Extreme Learning Machine. *Appl. Sci.* **2017**, *7*, 1004. [CrossRef]
32. Lee, Z.J.; Su, S.F.; Chuang, C.C.; Liu, K.H. Genetic algorithm with ant colony optimization (GA-ACO) for multiple sequence alignment. *Appl. Soft Comput.* **2008**, *8*, 55–78. [CrossRef]
33. Zhou, S.; Xie, H.; Zhang, C.; Hua, Y.; Sui, X. Wavefront-Shaping Focusing Based on a Modified Sparrow Search Algorithm. *Opt.-Int. J. Light Electron Opt.* **2021**, *244*, 167516. [CrossRef]
34. Litvinov, I.; Shtork, S.; Gorelikov, E.; Mitryakov, A.; Hanjalic, K. Unsteady regimes and pressure pulsations in draft tube of a model hydro turbine in a range of off-design conditions. *Exp. Therm. Fluid Sci. Int. J. Exp. Heat Transf. Thermodyn. Fluid Mech.* **2018**, *91*, 410–422. [CrossRef]
35. Su, W.T.; Binama, M.; Li, Y.; Zhao, Y. Study on the method of reducing the pressure fluctuation of hydraulic turbine by optimizing the draft tube pressure distribution. *Renew. Energy* **2020**, *162*, 550–560. [CrossRef]
36. Dragomiretskiy, K.; Zosso, D. Variational Mode Decomposition. *IEEE Trans. Signal Process.* **2014**, *62*, 531–544. [CrossRef]
37. Hua, L.; Tao, L.; Xing, W.; Qing, C. Application of EEMD and improved frequency band entropy in bearing fault feature extraction. *ISA Trans.* **2018**, *88*, 170–185.
38. Cao, Y.; Tung, W.; Gao, J.B.; Protopopescu, V.A.; Hively, L.M. Detecting dynamical changes in time series using the permutation entropy. *Phys. Rev. E* **2004**, *70*, 46217. [CrossRef]
39. Jiang, H.; Chen, J.; Dong, G.; Liu, T.; Chen, G. Study on Hankel matrix-based SVD and its application in rolling element bearing fault diagnosis. *Mech. Syst. Signal Process.* **2015**, *52–53*, 338–359. [CrossRef]
40. Zanin, M.; Zunino, L.; Rosso, O.A.; Papo, D. Permutation Entropy and Its Main Biomedical and Econophysics Applications: A Review. *Entropy* **2012**, *14*, 1553–1577. [CrossRef]

41. Li, Y.; Gao, X.; Wang, L. Reverse Dispersion Entropy: A New Complexity Measure for Sensor Signal. *Sensors* **2019**, *19*, 5203. [CrossRef] [PubMed]
42. Yeh, J.R.; Shieh, J.S.; Huang, N.E. Complementary ensemble empirical mode decomposition: A novel noise enhanced data analysis method. *Adv. Adapt. Data Anal.* **2011**, *2*, 135–156. [CrossRef]

energies

MDPI

Article

Research on the Operational Strategy of the Hybrid Wind/PV/Small-Hydropower/Facility-Agriculture System Based on a Microgrid

Yan Ren [1,2,*], Linmao Ren [3], Kai Zhang [4], Dong Liu [5,*], Xianhe Yao [1] and Huawei Li [1]

[1] School of Electric Power, North China University of Water Resources and Electric Power, Zhengzhou 450045, China; jms20151834@163.com (X.Y.); lihuawei033@163.com (H.L.)
[2] Yellow River Engineering Consulting Co., Ltd., Zhengzhou 450003, China
[3] Railway Police College, Zhengzhou 450053, China; renlinmao@rpc.edu.cn
[4] Henan Province Agricultural Science and Technology Exhibition Hall, Zhengzhou 450002, China; nlttzhangkai@126.com
[5] School of Civil and Hydraulic Engineering, Huazhong University of Science and Technology, Wuhan 430074, China
* Correspondence: renyan@ncwu.edu.cn (Y.R.); liudongwhu@126.com (D.L.)

Abstract: The use of renewable energy sources, such as wind, photovoltaics (PV), and hydropower, to supply facility agriculture may effectively mitigate food and environmental pollution problems and ensure continuity of the energy supply. The operating conditions of a hybrid system are complex, so the operating strategy is very important for system configuration and scheduling purposes. In the current study, first, a hybrid wind/PV/small-hydropower/facility-agricultural system was constructed. Then, the chaotic particle swarm method was applied to optimize hybrid system operation, and a scheduling strategy of the hybrid system was proposed. Finally, combined with an example, according to wind and PV power output and load curves, supply-to-load curves for wind, PV, and small hydropower were obtained. The operational strategy proposed in this study maximizes the utilization of wind and solar resources and rationally allocates hydropower resources. The aforementioned operational strategy provides a basis for hybrid system capacity allocation and scheduling.

Keywords: hybrid system; facility agriculture; chaotic particle swarms method; operation strategy

Citation: Ren, Y.; Ren, L.; Zhang, K.; Liu, D.; Yao, X.; Li, H. Research on the Operational Strategy of the Hybrid Wind/PV/Small-Hydropower/Facility-Agriculture System Based on a Microgrid. *Energies* **2022**, *15*, 2466. https://doi.org/10.3390/en15072466

Academic Editors: Dimitrios Katsaprakakis and Athanasios I. Papadopoulos

Received: 15 March 2022
Accepted: 21 March 2022
Published: 27 March 2022

1. Introduction

1.1. Literature Review

Food is the major necessity of human beings. As the global population continues to grow, people need increasing quantities of grains and vegetables [1]. Therefore, promoting the efficient and sustainable development of agricultural production methods and improving technology to increase the crop yield per unit area has attracted increasing attention, including in smart agriculture and facility agriculture [2]. These approaches can create a more suitable environment for plant growth, making it possible to grow crops and vegetables out of season and accelerate their growth [3,4]. However, high efficiency has led to increased energy consumption and higher costs [5]. With the increasing pressure on energy conservation and emission reduction, governments have introduced various policies and guidelines to carry out clean energy research and practices. Consideration of the use of renewable and clean energy sources applied to agricultural production can help solve the problem of energy consumption, in addition to effectively mitigating carbon emissions and reducing the pollution of the environment from fossil fuels [6,7].

In recent years, a lot of research has been conducted on clean energy, and renewable clean energy sources such as wind power, PV power and hydropower have received attention. However, wind and PV resources are affected by natural climatic conditions and

are characterized by significant randomness and volatility, leading to inefficient energy development and, consequently, to difficulties in accessing the power grid, reducing power quality and reliability [8,9]. Therefore, many people have proposed a mixture of multiple energy sources to compensate for the fluctuations of wind and PV power generation through the advantages of rapid start–stop and the strong peaking ability of hydropower [10]. The study [11] makes full use of the flexibility of hydropower, integrates wind/PV/hydropower, identifies the sites of each power plant, and analyzes the complementary power output benefits of the system. In the combined operation of various energy sources, the power quality of the whole year and the whole day is effectively guaranteed. In the study [12], a hybrid system containing wind, PV, and hydropower plants with pumped storage was established and the impact on the national power system was studied. The results show that the hybrid system can effectively reduce the volatility of the grid. In fact, reducing the instability of wind and PV output by complementing hydro and pumped storage can effectively improve the power quality and system reliability.

New clean energy inputs are obvious and necessary for the development of modern and efficient facility agriculture [13], and wind power/PV power/hydropower is widely used around the world due to its good applicability [14], and there have been many applications of multi-energy complementary participation in agriculture. The study [15] used a combination of wind power and energy storage in agriculture. The study [16] used PV power generation to solve the problem of agricultural irrigation. The study [17] studied hybrid energy systems consisting of PV panels and other necessary accessories to provide electricity to cool greenhouses without the need to obtain energy from the grid. In these studies, the practicality and very promising applications of new energy sources integrated into facility agriculture were predicted.

Scholars of various countries have analyzed the economy and practicability of coordination of various energy sources and output power. Most of the early solution methods were based on linear programming, nonlinear programming, and dynamic programming [18,19]. Due to the depth of research, a class of heuristic algorithms based on biological evolution or natural phenomena, represented by genetic algorithms [20], ant colony algorithms [21], and particle swarm algorithms [22], have been greatly developed, effectively solving the shortcomings of the past algorithms in terms of low adaptability to the objective function and constraints and poor efficiency. In the study [23], an optimal distribution method for multi-energy power supply systems was established with the total cost minimization as the optimization objective. The relationship between the complementary characteristics of multiple energy sources and the planning cost was quantitatively analyzed using two important indicators, energy loss rate and hourly loss rate of distributed generation, and solved by a hybrid genetic algorithm and pattern search algorithm. In the study [24], power loss minimization and voltage profile enhancement in radial distribution networks were considered as the key objectives of the study, and selective particle swarm optimization (SPSO) was used to determine the installation size and location of network capacity enhancement. In the study [25], a multi-objective particle swarm optimization algorithm (MOPSO) was used to optimize a hybrid PV-wind-pumped storage system to obtain the optimal configuration with reduced initial investment cost. By comparison, many new evolutionary algorithms have been proposed or improved and applied to solve the optimal scheduling problem, mainly including the hybrid swarm algorithm [26], the slime mode algorithm [27], and the harmony search [28]. Therefore, proposing or improving algorithms is a key scientific problem for optimizing the coordination of multiple energy sources with each other. Solving this problem can provide technical support for obtaining better convergence and distribution of multi-energy complementary systems.

1.2. Research Gap and Motivation

Indeed, the application of wind/PV energy supports operations that are integrated into facility agriculture [17,29]. In addition, due to the development of large-scale facility agriculture [1,30], it is necessary to develop new approaches to the hybrid use of

renewable energy sources and the grid. In the literature, combining electricity generation with agriculture through independent wind and PV has also been studied, but there is little research on the coordinated integration of multiple energy sources with agricultural facilities. Meanwhile, the operating conditions of hybrid energy systems are complicated, especially in regard to systems based on microgrids, for which the operating strategy is very important. The studies [31–33] examined energy management strategies based on distributed microgrids and proposed an economic dispatching strategy of hybrid PV/storage/hydro/diesel microgrids without considering the operation characteristics of wind power. The studies [34,35] proposed an optimal microgrid scheduling method considering a hybrid wind/light/diesel/battery/desalination system but did not consider the operation strategy. The studies [36,37] investigated the impact of the operation strategy and operational characteristics of energy storage devices on the reliability of microgrids but only the energy storage aspect was studied. The study [38] examined the control strategy of a wind/PV/storage microgrid based on hybrid energy, considering the randomness and volatility of the output power and voltage of intermittent power sources, such as wind and PV power generation, and the complexity of microgrid control, but they did not consider the load impact.

In previous work, we conducted an in-depth study of the hybrid PV/wind/pumped storage system and optimized the system design using particle swarm optimization algorithms. Furthermore, the output smoothing of the hybrid hydro/wind/PV system was studied and analyzed [39,40]. The stability and economy of the multi-energy complementary system were confirmed [41]. In addition, the combination of clean energy and facility agriculture can improve the efficiency of land and energy use [42] and compensate for the energy demand of facility agriculture by directly providing productive energy through clean energy generation [43]. Related practical applications have already appeared in some countries, such as India and Canada [44,45]. Therefore, in this study, a mathematical model of a wind/PV/small-hydropower/facility-agriculture system was established, the operation strategy of the system was proposed, and an example was derived and analyzed using a chaotic particle swarm optimization (CPSO) algorithm. Compared with other algorithms, the CPSO algorithm avoids complex operations and has stronger global convergence and robustness, and it can be used as a new evolutionary algorithm to solve a large number of nonlinear, non-trivial, and multi-peak complex optimization problems [46,47]. The algorithm ensures the optimal capacity allocation of each energy source and establishes the optimal scheduling strategy, which can further enhance the advantages of complementary characteristics among various energy sources.

1.3. Contribution and Paper Organization

The main contributions of this paper are as follows:

(1) A mathematical model of the wind/PV/small-hydropower/facility-agriculture system was established with the load matching degree as the objective function and the power supply reliability as the constraint.
(2) Through the actual data, the control strategy and operation strategy of the wind/PV/small-hydropower/facility-agriculture system were proposed.
(3) The wind/PV/small-hydropower/facility-agriculture system was solved using the CPSO algorithm for the hybrid system, and the operation of the system was analyzed and is discussed.

The rest of this paper is organized as follows. A mathematical model of the wind/PV/small-hydropower/facility-agriculture system is established in Section 2. In addition, the specific steps and calculation process of the CPSO method for the composite system are introduced. In Section 3, the operation strategy flow of the hybrid system is depicted by example analysis, and the calculation results are discussed and analyzed. The conclusions are summarized in the final section.

2. Methods

2.1. System Optimization Design Model

2.1.1. System Optimization Model Building

Mathematically described as Equation (1):

$$\begin{cases} minf(x) \\ g_k(x) < \varepsilon_x \end{cases} \tag{1}$$

where:

$f(x)$—Optimization of the objective function;
$g_k(x)$—Constraint condition function;
ε_x—Tolerance factor of the constraint function, $\varepsilon_x \geq 0$;
x—Optimization variables.

2.1.2. Objective Function

With the load matching degree of the wind/PV/small-hydropower/facility-agriculture system as the optimization objective, using a supply–demand balance calculation model and the error evaluation of the supply–demand difference value root-mean-square, the objective function is expressed by Equation (2):

$$\sigma = \sqrt{\frac{\sum_{t=1}^{T}\left(P_S^t - P_L^t\right)}{T}} \tag{2}$$

where:

P_S^t—The total system power output during calculation period t, kW;
P_L^t—The system load value during calculation period t, kW;
T—Total number of hours, h.

That is, the optimization objective function $f(x) = \sigma$, and the optimization objective is to minimize σ.

2.1.3. Constraints

The power supply reliability of the system is selected as the constraint.

A reliability model of the composite generation system is established to evaluate the reliability of the system's power supply using the loss of power supply probability ($LPSP$), the accumulated power deficit, and the number of continuous days with guaranteed cloudy and windless weather, as follows:

(1) Loss of Load Power Rate

The calculation of the load loss of the power rate for a total time period can be defined as the ratio of the deficit power (LPS) to the total power required by the load during that time period, expressed by Equation (3):

$$LPSP = \frac{\sum_{t=1}^{T} LPS(t)}{\sum_{t=1}^{T} P_L(t)\Delta t} \tag{3}$$

where:

LPS—Insufficient power at time t, kWh;
$P_L(t)$—Total load at time t, kW;
T—Running time, h;
Δt—Calculation step size, h.

The $LPSP$ value is between 0 and 1, and the smaller the value, the higher the reliability. $LPSP = 0$ means that the load needs can be met at all times; $LPSP = 1$ means that the load needs cannot be met at all times. In fact, even the public grid can supply power to large cities with an $LPSP = 10^{-2}$ order of magnitude only, and it is obviously unreasonable to

require relatively expensive wind and solar power systems to achieve 100% reliability. Most of the failures that occur during the operation of stand-alone power supply systems are not due to the lack of capacity of the system components, but due to component failures, poor line contact, and operational errors, so the reliability requirements for wind and solar complementary power systems should be reasonable.

(2) Accumulated power deficit

The deficit ΔE can be expressed as:

$$\Delta E = E_W + E_{PV} + E_H - E_L \quad (4)$$

where:

E_W is the power generation of the wind turbine during the calculation period, kWh;

E_{PV}—The power generation of the PV array during the calculation period, kWh;

E_H—The power generation of small hydropower during the calculation period, kWh;

E_L—The power consumption of the load during the calculation period, kWh.

If ΔE is positive, it means that the system power generation during the calculation period is greater than the load power consumption, that is, the surplus amount, and can be used for battery charging; if ΔE is negative, it means that the system power generation during the calculation period is less than the load power consumption, that is, the deficit amount, and can be supplied by small hydropower generation first.

(3) Number of days with guaranteed continuous rainy and windless weather

The number of days with guaranteed continuous rainy and windless weather can be taken according to the reliability requirements of residential electricity consumption, generally n = 3 to 5 days (specific values are determined according to local meteorological data).

That is, the constraints are:

$g(x_1) = LPSP$, taking the tolerance factor of the constraint function $\varepsilon_1 = LPSP_{req}$ ($LPSP_{req}$ is the required value of load loss rate);

$g(x_2) = \Delta E$, taking the tolerance factor of the constraint function $\varepsilon_2 = \Delta E_{req}$ (ΔE_{req} is the cumulative deficit requirement value);

$g(x_3) = n$, taking the tolerance factor of the constraint function $\varepsilon_3 = n_{req}$ (n_{req} is to ensure the required value of the number of days of guaranteed continuous rainy and windless weather).

2.1.4. Selection of Optimization Variables

The power side mainly contains wind power, PV power, battery and pumped storage, and their operation and complementary methods affect the overall output and power balance of the system; thus, we use the capacity of different power sources (i.e., wind power, PV) and different forms of energy storage (i.e., pumped storage, battery) as optimization variables.

2.2. CPSO Method for Composite Systems

2.2.1. Detailed Steps

The basic idea of the CPSO algorithm is to use chaotic sequences to initialize the positions and velocities of particles; first, a chaotic search is performed for the optimal particle in the current particle population, and then the result of the chaotic search is replaced with a random particle in the particle population. The specific steps of composite system optimization using CPSO are as follows:

(1) Initializing the particles

A population containing n_s particles is randomly generated, the particles are initialized (i.e., the optimization variables: capacity of the wind turbine, PV array, pumped storage, and battery), each particle is given a random velocity (i.e., the step size of the change

in the capacity of the wind turbine, PV array, pumped storage, and battery during the optimization), and the number of iterations is set to N.

(2) Update the velocity and position of the particles

Update the velocity and position of the particle according to Equations (5) and (6):

$$\vec{v}_i^{k+1} = \omega \vec{v}_i^{k} + c_1 r_1 \left(\vec{x}_{pbest,i}^{k} - \vec{x}_i^{k} \right) + c_2 r_2 \left(\vec{x}_{gbest,i}^{k} - \vec{x}_i^{k} \right) \tag{5}$$

$$\vec{x}_i^{k+1} = \vec{x}_i^{k} + \vec{x}_i^{k+1} \tag{6}$$

where:
$\vec{v}_i^{k}$—the velocity of the kth iteration of the ith ($i = 1, 2, ..., m$) particle;
$\vec{x}_i^{k}$—the position of the kth iteration of the ith ($i = 1, 2, ..., m$) particle;
$\vec{x}_{pbest,i}^{k}$—individual optimal position of particle i for the kth iteration;
$\vec{x}_{gbest,i}^{k}$—the population optimal position for the kth iteration;
ω—inertia weights;
c_1—cognitive coefficient;
c_2—social coefficient;
r_1, r_2—random number between [0, 1].

(3) Chaotic optimization of particle swarm optimal positions $\vec{x}_{gbest}$:

① Mapping $\vec{x}_{gbest}$ to the definition domain [0, 1] of the logistic equation $\vec{y}_{n+1}^{k} = \mu \vec{y}_n^{k} \left(1 - \vec{y}_n^{k} \right)$ through Equation (7):

$$\vec{y}_1^{k} = \frac{\vec{x}_{gbest}^{k} - R_{min}^{k}}{R_{max}^{k} - R_{min}^{k}} \tag{7}$$

where μ is the control parameter, R_{max}^{k} and R_{min}^{k} are the upper and lower bounds of the value of $\vec{x}_i^{k}$, respectively.

② The chaotic sequence $\vec{y}_n^{k}$ is obtained by performing M iterations of the logistic equation for $\vec{y}_1^{k} (n = 1, 2, ..., m)$.

③ The chaotic sequence is mapped back to the original solution space by the inverse of Equation (8):

$$\vec{x}_{gbest,m}^{*k} = R_{min}^{k} + (R_{max}^{k} - R_{min}^{k}) \vec{y}_m^{k} \tag{8}$$

thus generating a sequence of feasible solutions in chaotic variables $\vec{x}_{gbest,m}^{*k} (m = 1, 2, ..., M)$.

④ Calculate the adaptation value of each feasible solution vector in the feasible solution sequence, and keep the feasible solution vector corresponding to the optimal adaptation value, denoted as $\vec{x}_g^{*k}$.

(4) A particle is randomly selected from the current particle population, and the position vector of $\vec{x}_g^{*k}$ is used to replace the position vector of the selected particle.

(5) Skip to step (2) until the algorithm reaches the maximum number of iterations N or the optimal solution is obtained, i.e., the capacity of the wind turbine, PV array, pumped storage, and battery when the load loss rate of the system is minimized and the initial investment cost of the system is lowest.

The flow chart of the algorithm of CPSO is shown in Figure 1.

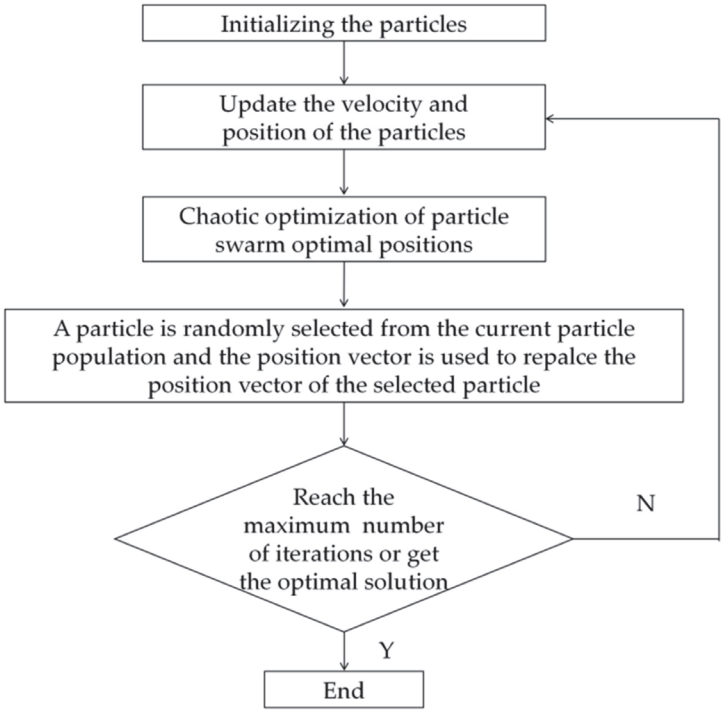

Figure 1. CPSO algorithm flow chart.

2.2.2. Calculation Process

The input raw data are the technical parameters of each component of the system (including the height of the wind turbine rotor, the power curve of the wind turbine, the short-circuit current and open-circuit voltage of the PV arrays, the current and voltage of the maximum power point, and the maximum and minimum head of the small hydropower plant), the wind speed data, the solar radiation data, the load data, and the allowable power loss rate. The initial position of the set particle population includes the capacity of the wind turbine, PV array, pumped storage, and battery.

The power generation of the wind turbine, the power generation of the PV arrays, the power consumption of the load, and the constraints are calculated.

During the optimal configuration of the system, if the reliability condition of $LPSP \leq LPSP_{req}$ cannot be met, the position of each particle, i.e., the capacity of the wind turbines, PV arrays, pumped storage, and battery, is adjusted by the CPSO algorithm until the system load loss rate $LPSP$ meets the requirements. For the given $LPSP_{req}$, the optimization algorithm allows the system to technically meet the requirements. However, the final optimized system to simultaneously achieve the lowest σ can be obtained by building a supply and demand balance calculation model.

3. Example Analysis

3.1. System Construction

The hybrid wind/PV/small-hydropower/facility-agriculture system based on a microgrid is shown in Figure 2, including wind turbines, PV arrays, small hydropower units, batteries, dispatch center, inverters, vegetable multispan greenhouses, orchards, and flower beds. The wind turbines and PV arrays comprise the system power supply. Small hydropower units can be employed as both the system power supply and energy storage

devices. Batteries are the main energy storage devices of the system. The system load consists of the loads of vegetable multispan greenhouses, orchards, curtain cooling systems, filling-light systems, ventilation drives, energy-saving lamps, sprinkler system drives, and other daily electricity demands.

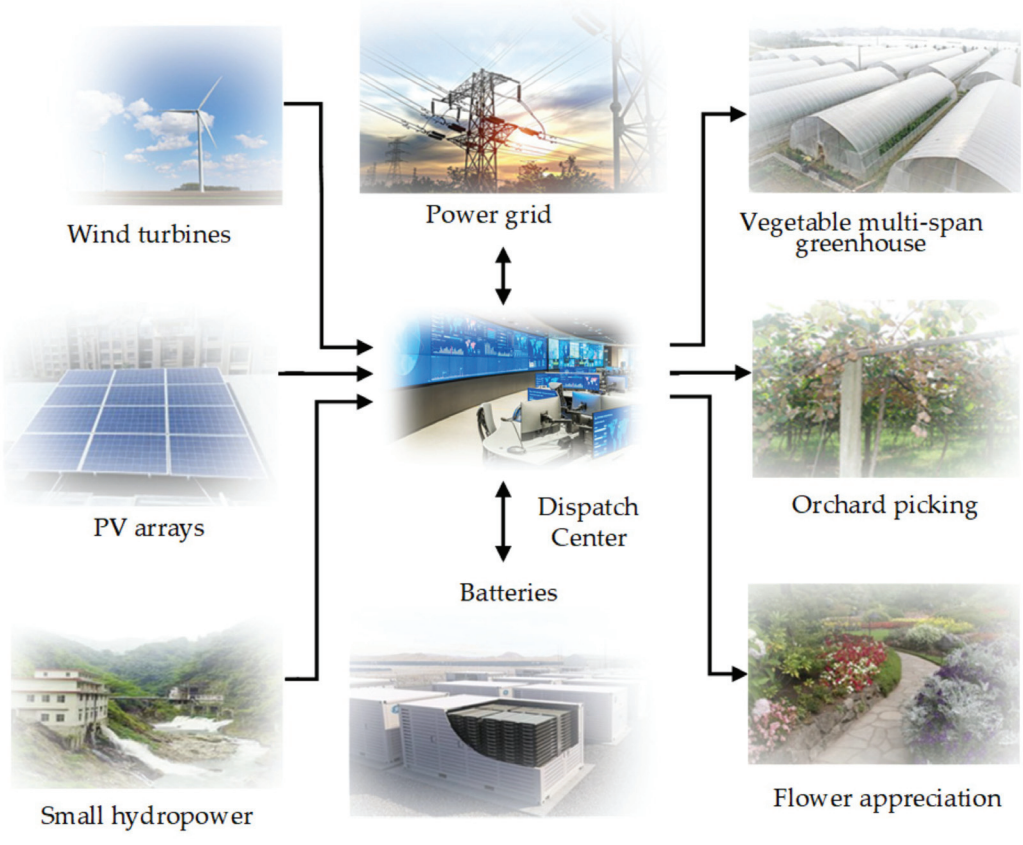

Figure 2. Hybrid wind/PV/small-hydropower/facility-agriculture system based on a microgrid.

Wind turbines are commonly installed in areas with good wind resources. The PV arrays are set up in agricultural greenhouses, higher than the normal elevation of 20 cm, and they span the gaps between adjacent greenhouses, thereby blocking direct sunlight and providing shade to vegetables, while translucent shed walls at a small angle allow sunlight to reach vegetables. In addition, PV arrays are installed along farm corridors and on the roof of the production plant.

3.2. Optimization of the Scheduling Method of the Hybrid System

The chaotic particle swarm method is applied to optimize hybrid system scheduling. The optimization goal load matching degree maximization, namely, the energy consumption and energy supply, should be lower than the allowable value. The optimization condition involves maximizing wind and solar resource utilization.

3.3. Operating Strategy of the Hybrid System

3.3.1. Wind and PV Power Generation Strategies

The wind turbines are operated under the maximum wind energy capture control strategy according to the available wind energy resources, and the PV arrays are operated via the MPPT control method according to the available solar resources.

If the generated wind and PV power meet the load demand, i.e., if $P_W + P_{PV} - P_L > 0$, wind and PV power are first supplied to the batteries to be charged. If the batteries are fully charged and a surplus occurs, power is supplied to the small hydropower system to pump water and then to the power grid.

If the generated wind and PV power do not satisfy the load demand, i.e., if $P_W + P_{PV} - P_L < 0$, the load is supplemented with other power sources.

3.3.2. Operation Strategy of the Small Hydropower Stations

Small hydropower stations are operated according to the water supply. First, the small hydropower stations supply power to satisfy the load, and if there is a surplus, power is supplied to the batteries and then to the power grid.

(1) When wind and PV power cannot meet the load demand, i.e., $P_W + P_{PV} - P_L < 0$, the small hydropower stations supply power to satisfy the load.
   - ① If $P_W + P_{PV} + P_H - P_L > 0$, the small hydropower stations supply power to the batteries to be charged. If a surplus occurs after the batteries have been fully charged, power is supplied to the power grid.
   - ② If $P_W + P_{PV} + P_H - P_L < 0$, other power resources supplement the load.

(2) When wind and PV power do satisfy the load demand, i.e., $P_W + P_{PV} - P_L > 0$.
   - ① If the batteries are fully charged, the small hydropower stations supply power to the grid.
   - ② If the batteries are not fully charged, the small hydropower stations first supply power to the batteries, after which power is supplied to the power grid when the batteries are fully charged.

3.3.3. Operation Strategy of the Batteries

If $P_W + P_{PV} + P_H - P_L < 0$, the batteries supply power to satisfy the load.

3.3.4. Operation Strategy of the System

(1) Generation power strategy
   - ① Wind and PV power first satisfy the load. If there is a surplus, power is supplied to the batteries to be charged. Any remaining power is then supplied to the small hydropower stations for water pumping purposes and finally to the power grid.
   - ② Small hydropower stations first meet the load demand, and surplus power is then supplied to the batteries to be charged and finally to the power grid.

(2) Consumption power strategy

The load is first satisfied via wind and PV power, and if the generated power is insufficient, power is then provided by the small hydropower stations, followed by the batteries and finally by the power grid.

(3) Battery charging strategy

The batteries are first charged via wind and PV power, and if the supplied power is insufficient, the small hydropower stations provide power.

(4) Pumping strategy of the pumps of the small hydropower stations

Only wind and PV power are consumed (only if a wind and PV power surplus occurs is power supplied to the batteries for charging purposes).

A flowchart of the system operating strategy is shown in Figure 3, where t is the charging time of the batteries, and T is the maximum charging time of the batteries to obtain a full charge.

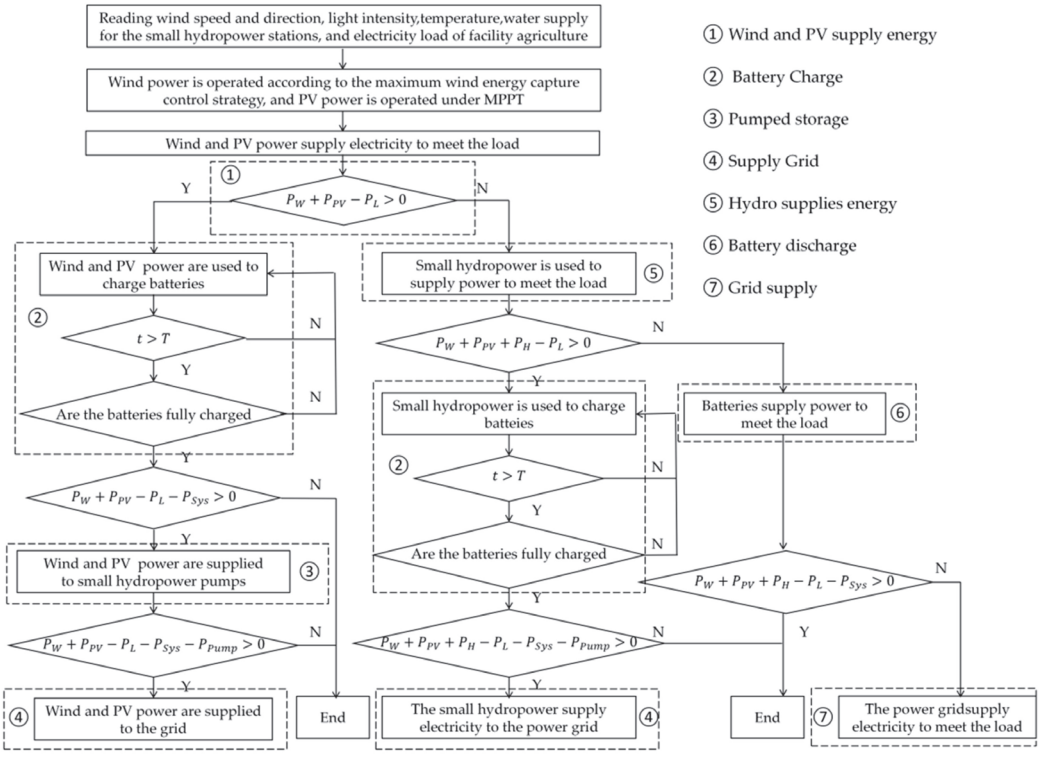

Figure 3. Flow chart of the hybrid system operation strategy.

3.4. Calculation Results and Discussion

In this study, we developed a mathematical model of the hybrid system in Section 2.1, elaborated the chaotic particle swarm optimization algorithm in Section 2.2.1, and explained the optimization problem in Section 2.2.2. The power side mainly contains wind turbines, PV arrays, batteries, and pumped storage units, and their operation and complementary methods affect the overall output and power balance of the system. Therefore, their input or output power are used as the optimization variables. Then, in Section 3, the operating processes of different power sources in the system are described. In a hybrid system, pumped storage and batteries are discharged when wind power and PV are insufficient and charged when wind power and PV are sufficient. The flow chart of the hybrid system operation strategy is shown in Figure 3.

After inputting the optimization variables, P_S is obtained by running the flow in Figure 3, and then the objective function σ is obtained according to Equation (2), after which the optimization is performed by the CPSO algorithm to obtain a better σ. If the maximum number of iterations is reached or the optimal solution is obtained, the calculation is terminated; otherwise the velocity and position of the particle are updated and calculated again. The application of the CPSO algorithm for the optimal operation of the hybrid system is shown in Figure 4.

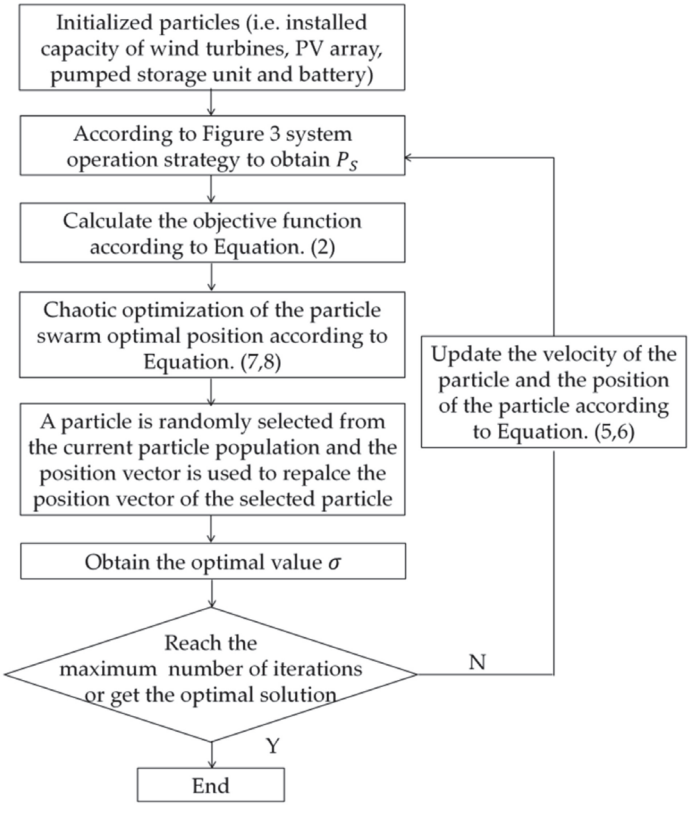

Figure 4. Application of the CPSO algorithm for the optimal operation of the hybrid system.

In the wind/PV/small-hydropower/facility-agriculture system, the installed capacity of wind power is 300 kW, that of the PV arrays is 312 kW, that of the small hydropower stations is 200 kW without regulation, and that of the batteries is 420 kWh. Wind and PV power curves and daily load curves are shown in Figure 5.

A wind and PV power supply-to-load curve is shown in Figure 6. Above the 0 kW line, a surplus occurs after wind and PV power satisfy the load, namely, from 1 to 3 h and 23.5 to 24 h, wind and PV power are supplied to satisfy the load, and any surplus power charges the batteries. Below the 0- W line, wind and PV power are insufficient to meet the load, i.e., from 3 to 23.5 h, other power sources are required to meet the load demand. In this example, no surplus electricity is supplied to the power grid.

From 1 to 3 h and 23.5 to 24 h, wind and PV power and the small hydropower stations supply electricity to satisfy the load. The profit–loss curve of the small hydropower station output after meeting the load demand is shown in Figure 7a. Above the 0 kW line, there is a surplus in the small hydropower station output, i.e., from 1 to 3.9 h and 22 to 24 h, the small hydropower stations first charge the batteries, and any surplus electric energy is then supplied to the grid. Below the 0 kW line, wind, PV power and small hydropower generation cannot meet the load. First, the batteries are used to supply power to satisfy the load, and the power deficit is supplied by the power grid. Figure 7b shows wind and PV power and small hydropower station supply-to-load curves. From 1 to 1.25 h, the small hydropower stations supply power to the grid.

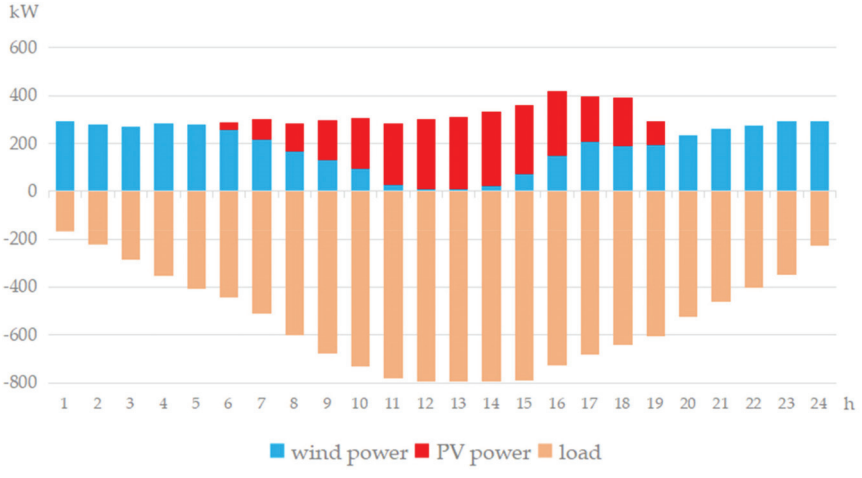

Figure 5. Wind and PV power curves and daily load curve.

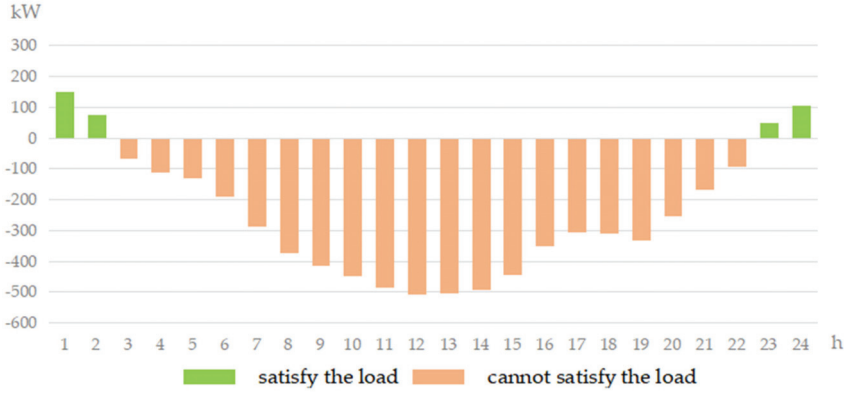

Figure 6. Supply-to-load curve of wind and PV power.

(**a**)

Figure 7. *Cont.*

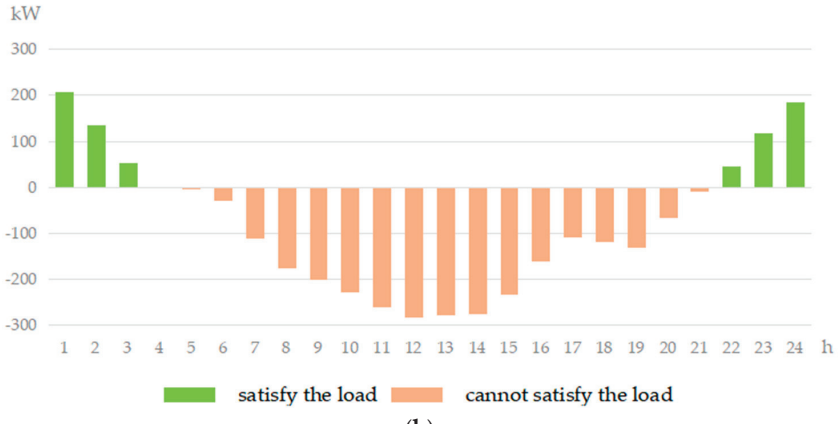

Figure 7. Supply-to-load curves of wind and PV power and small hydropower stations: (**a**) small hydropower station output after meeting the load demand; (**b**) wind and PV power and small hydropower station supply-to-load curves.

4. Conclusions

The hybrid wind/PV/small-hydropower/facility-agriculture system may effectively mitigate food and environmental pollution problems and ensure continuity of the energy supply.

(1) The maximum wind power capture control strategy is adopted in wind power generation, and the MPPT control approach is applied in PV power generation, which maximizes wind and solar energy resource utilization. The considered small hydropower generating and pumping systems are independent systems, which increase the system's operational flexibility.

(2) The operational strategy of the hybrid system is considered in terms of four aspects: power generation strategy, operation strategy, battery charging strategy, and small hydropower pumping strategy. The load should be prioritized in terms of electricity consumption, batteries should be the second priority, and the power grid should be the final priority. This approach guarantees the electricity required for facility agriculture and fully utilizes the various resources.

(3) As China's largest industry, there are many research results in the field of combining agriculture with clean energy. The research in this paper responds to the carbon peak and carbon neutral requirements proposed by China. Clean energy is certain to be vigorously developed in the agricultural industry, and the development model of "multiple complementary clean energy sources + agriculture" will have far-reaching implications for the sustainable green development of China and the world.

At present, it is still difficult to fully characterize the system operation and control strategies due to the complexity of the model and the limited available data. In order to further improve the effectiveness of the coordinated operation strategy, a more comprehensive simulation of the optimal operation of the system considering water quantity constraints, economics, and other factors is needed in future studies, and the synergy among wind, PV, and water energy sources should be further explored.

Author Contributions: Y.R.: conceptualization, methodology, writing of the original draft. L.R. and K.Z.: revision, visualization, software, formal analysis. D.L. and X.Y.: investigation, data curation, validation. H.L.: literature collation. All authors have read and agreed to the published version of the manuscript.

Funding: The authors acknowledge financial support from the Henan Province Key R & D and Promotion Project (Science and Technology Research) (Grant No. 212102311054), the China Postdoctoral Science Foundation (Grant No. 2020M682416), the Training Program for Young Key Teachers in Colleges and Universities of Henan Province (Grant No. 2019GGJS097), the Key Scientific Research Projects of Colleges and Universities in Henan Province (Grant No. 17A480006) and Supported by Key Scientific and Technological Projects in Henan (Grant No. 192102310515).

Institutional Review Board Statement: Not applicable.

Informed Consent Statement: Not applicable.

Data Availability Statement: The data that support the findings of this study are available from the corresponding author upon reasonable request.

Conflicts of Interest: The authors declare no conflict of interest.

References

1. Wang, T.; Wu, G.; Chen, J.; Cui, P.; Chen, Z.; Yan, Y.; Zhang, Y.; Li, M.; Niu, D.; Li, B.; et al. Integration of solar technology to modern greenhouse in China: Current status, challenges and prospect. *Renew. Sustain. Energy Rev.* **2017**, *70*, 1178–1188.
2. Martínez-Rodríguez, B.; Bilbao-Arechabala, S.; Jorge-Hernandez, F. Security Architecture for Swarms of Autonomous Vehicles in Smart Farming. *Appl. Sci.* **2021**, *11*, 4341.
3. Gupta, M.; Abdelsalam, M.; Khorsandroo, S.; Mittal, S. Security and privacy in smart farming: Challenges and opportunities. *IEEE Access* **2020**, *8*, 34564–34584.
4. Wang, Y.; Niu, H.; Yang, L.; Wang, W.; Liu, F. An optimization method for local consumption of photovoltaic power in a facility agriculture micro energy network. *Energies* **2018**, *11*, 1503.
5. Symeonaki, E.G.; Arvanitis, K.G.; Piromalis, D.D. Current trends and challenges in the deployment of IoT technologies for climate smart facility agriculture. *Int. J. Sustain. Agric. Manag. Inform.* **2019**, *5*, 181–200.
6. Tabor, D.P.; Roch, L.M.; Saikin, S.K.; Kreisbeck, C.; Sheberla, D.; Montoya, J.H.; Dwaraknath, S.; Aykol, M.; Ortiz, C.; Tribukait, H.; et al. Accelerating the discovery of materials for clean energy in the era of smart automation. *Nat. Rev. Mater.* **2018**, *3*, 5–20.
7. Hou, R.; Li, S.; Chen, H.; Ren, G.; Gao, W.; Liu, L. Coupling mechanism and development prospect of innovative ecosystem of clean energy in smart agriculture based on blockchain. *J. Clean. Prod.* **2021**, *319*, 128466.
8. Ma, T.; Javed, M.S. Integrated sizing of hybrid PV-wind-battery system for remote island considering the saturation of each renewable energy resource. *Energy Convers. Manag.* **2019**, *182*, 178–190.
9. Zhang, H.; Lu, Z.; Hu, W.; Wang, Y.; Dong, L.; Zhang, J. Coordinated optimal operation of hydro–wind–solar integrated systems. *Appl. Energy* **2019**, *242*, 883–896.
10. Peng, Z.; Chen, X.; Yao, L. Research status and future of hydro-related sustainable complementary multi-energy power generation. *Sustain. Futures* **2021**, *3*, 100042.
11. Tang, Y.; Fang, G.; Tan, Q.; Wen, X.; Lei, X.; Ding, Z. Optimizing the sizes of wind and photovoltaic power plants integrated into a hydropower station based on power output complementarity. *Energy Convers. Manag.* **2020**, *206*, 112465. [CrossRef]
12. Jakub, J.; Jerzy, M.; Magdalena, K.; Bartłomiej, C.; Mirosław, J. Integrating a wind- and PV-powered hybrid to the power system by coupling it with a hydroelectric power station with pumping installation. *Energy* **2018**, *144*, 549–563.
13. Golzar, F.; Heeren, N.; Hellweg, S.; Roshandel, R. A comparative study on the environmental impact of greenhouses: A probabilistic approach. *Sci. Total Environ.* **2019**, *675*, 560–569.
14. Martinho, V.J.P.D. Energy consumption across European Union farms: Efficiency in terms of farming output and utilized agricultural area. *Energy* **2016**, *103*, 543–556.
15. Calderon, J.; Cureg, J.; Diaz, M.; Guzman, J.; Rudd, C.; Le, H.T. Smart Agriculture: An Off-Grid Renewable Energy System for Farms using Wind Power and Energy Storage. In Proceedings of the 2019 IEEE Power & Energy Society Innovative Smart Grid Technologies Conference (ISGT), Washington, DC, USA, 17–20 February 2019; pp. 1–5.
16. Narvarte, L.; Fernández-Ramos, J.; Martínez-Moreno, F.; Carrasco, L.; Almeida, R.; Carrêlo, I. Solutions for adapting photovoltaics to large power irrigation systems for agriculture. *Sustain. Energy Technol. Assess.* **2018**, *29*, 119–130.
17. Marucci, A.; Cappuccini, A. Dynamic photovoltaic greenhouse: Energy balance in completely clear sky condition during the hot period. *Energy* **2016**, *102*, 302–312.
18. Li, C.; Zhou, J.; Ouyang, S.; Ding, X.; Chen, L. Improved decomposition-coordination and discrete differential dynamic programming for optimization of large-scale hydropower system. *Energy Convers. Manag.* **2014**, *84*, 363–373.
19. Preitl, Z.; Precup, R.E.; Tar, J.K.; Takács, M. Use of multi-parametric quadratic programming in fuzzy control systems. *Acta Polytech. Hung.* **2006**, *3*, 29–43.

20. Chen, L.; Chang, F. Applying a real-coded multi-population genetic algorithm to multi-reservoir operation. *Hydrol. Processes* **2007**, *21*, 688–698.
21. Moeini, R.; Afshar, M. Arc-based constrained ant colony optimisation algorithms for the optimal solution of hydropower reservoir operation problems. *Can. J. Civ. Eng.* **2011**, *38*, 811–824.
22. Čiča, Đ.; Zeljković, M.; Tešić, S. Dynamical contact parameter identification of spindle-holder-tool assemblies using soft computing techniques. *Facta Univ. Ser. Mech. Eng.* **2020**, *18*, 565–577.
23. Xu, W.; Zhou, D.; Huang, X.; Lou, B.; Liu, D. Optimal allocation of power supply systems in industrial parks considering multi-energy complementarity and demand response. *Appl. Energy* **2020**, *275*, 115407.
24. Kefale, H.A.; Getie, E.M.; Eshetie, K.G. Optimal design of grid-connected solar photovoltaic system using selective particle swarm optimization. *Int. J. Photoenergy* **2021**, *2021*, 6632859.
25. Xu, X.; Hu, W.; Cao, D.; Huang, Q.; Chen, C.; Chen, Z. Optimized sizing of a standalone PV-wind-hydropower station with pumped-storage installation hybrid energy system. *Renew. Energy* **2020**, *147*, 1418–1431.
26. Zapata, H.; Perozo, N.; Angulo, W.; Contreras, J. A hybrid swarm algorithm for collective construction of 3D structures. *Int. J. Artif. Intell.* **2020**, *18*, 1–18.
27. Precup, R.E.; David, R.C.; Roman, R.C.; Szedlak-Stinean, A.I.; Petriu, E.M. Optimal tuning of interval type-2 fuzzy controllers for nonlinear servo systems using Slime Mould Algorithm. *Int. J. Syst. Sci.* **2021**, 1–16. [CrossRef]
28. Assad, A.; Deep, K. A Hybrid Harmony search and Simulated Annealing algorithm for continuous optimization. *Inf. Sci.* **2018**, *450*, 246–266.
29. Colantoni, A.; Monarca, D.; Marucci, A.; Cecchini, M.; Zambon, I.; Di Battista, F.; Maccario, D.; Saporito, M.G.; Beruto, M. Solar Radiation Distribution inside a Greenhouse Prototypal with Photovoltaic Mobile Plant and Effects on Flower Growth. *Sustainability* **2018**, *10*, 855.
30. Alayi, R.; Mohkam, M.; Seyednouri, S.R.; Ahmadi, M.H.; Sharifpur, M. Energy/Economic Analysis and Optimization of On-Grid Photovoltaic System Using CPSO Algorithm. *Sustainability* **2021**, *13*, 12420.
31. Xue, M.D.; Zhao, B.; Zhang, X.S.; Gao, X.; Jiang, Q. Economic Dispatch of Stand-alone Photovoltaic-Battery-Hydro-Diesel Hybrid Microgrid Based on Distributed Control. *Autom. Electr. Power Syst.* **2014**, *38*, 1–7.
32. Poudel, S.; Dubey, A. Critical Load Restoration Using Distributed Energy Resources for Resilient Power Distribution System. *IEEE Trans. Power Syst.* **2018**, *34*, 52–63.
33. Abdelkader, A.; Rabeh, A.; Ali, D.M.; Mohamed, J. Multi-objective genetic algorithm based sizing optimization of a stand-alone wind/PV power supply system with enhanced battery/supercapacitor hybrid energy storage. *Energy* **2018**, *163*, 351–363.
34. Fang, L.; Niu, Y.; Zu, Q.; Wang, S. Energy management strategy based on energy storage equalization technology and transferable load. *Int. Trans. Electr. Energy Syst.* **2018**, *28*, e2599.
35. Wu, B.; Maleki, A.; Pourfayaz, F.; Rosen, M.A. Optimal design of stand-alone reverse osmosis desalination driven by a photovoltaic and diesel generator hybrid system. *Sol. Energy* **2018**, *163*, 91–103.
36. Chen, L.; Mou, L.; Xu, X.; Liu, S. Influences of energy storage operational strategy and characteristic on microgrid reliability. *Electr. Power Autom. Equip.* **2017**, *37*, 70–76.
37. Ding, H.; Zhang, W.; Chen, M.; Li, S.; Hou, T.; Zhou, X.; Fu, Y.; Liu, Z. Multi-Objective optimial configuration of distributed wind-solar generation considering energy storage. In Proceedings of the 2018 2nd IEEE Conference on Energy Internet and Energy System Integration (EI2), Beijing, China, 20–22 October 2018; pp. 1–6.
38. Lan, G.J.; Li, W.Y.; Yin, K. Control strategy of wind/photovoltaic/storage micro-grid based on combined energy storage solutions. *China J. Power Sci.* **2015**, *39*, 2503–2506.
39. Yan, R.; Yuan, Z. Optimal design of PV/wind/pumped-storage hybrid system based on improved particle swarm optimization. *Adv. Sci. Lett.* **2012**, *6*, 660–663.
40. Ren, Y.; Zheng, Y.; Li, C.; Zhou, B.; Mao, Z.H. Intelligent optimization of hybrid wind/PV/pumped-storage power system. In *Advanced Materials Research*; Trans Tech Publications Ltd.: Hamburg, Germany, 2012; pp. 719–722.
41. Ren, Y.; Yao, X.; Liu, D.; Qiao, R.; Zhang, L.; Zhang, K.; Jin, K.; Li, H.; Ran, Y.; Li, F. Optimal design of hydro-wind-PV multi-energy complementary systems considering smooth power output. *Sustain. Energy Technol. Assess.* **2021**, *50*, 101832.
42. Zhang, K.; Yu, J.; Ren, Y. Demand side management of energy consumption in a photovoltaic integrated greenhouse. *Int. J. Electr. Power Energy Syst.* **2021**, *134*, 107433.
43. Zhang, K.; Yu, J.; Ren, Y. Research on the size optimization of photovoltaic panels and integrated application with Chinese solar greenhouses. *Renew. Energy* **2021**, *182*, 536–551.
44. Tuballa, M.L.; Abundo, M.L. A review of the development of Smart Grid technologies. *Renew. Sustain. Energy Rev.* **2016**, *59*, 710–725.
45. Morris, D.W.; Blekkenhorst, N. Wind energy versus sustainable agriculture: An Ontario perspective. *J. Rural. Community Dev.* **2017**, *12*, 23–33.
46. Petrović, M.; Vuković, N.; Mitić, M.; Miljković, Z. Integration of process planning and scheduling using chaotic particle swarm optimization algorithm. *Expert Syst.* **2016**, *64*, 569–588.
47. Dursun, E.H.; Koyuncu, H.; Kulaksiz, A. A novel unified maximum power extraction framework for PMSG based WECS using chaotic particle swarm optimization derivatives. *Eng. Sci. Technol. Int. J.* **2021**, *24*, 158–170.

energies

MDPI

Article

Impacts of Yield and Seasonal Prices on the Operation of Lancang Cascaded Reservoirs

Mengfei Xie [1], Suzhen Feng [2], Jinwen Wang [2], Maolin Zhang [1] and Cheng Chen [2,*]

[1] Kunming Power Exchange Center Co., Ltd., Kunming 650011, China; xiemengfeihust@foxmail.com (M.X.); zhangmaolin_9901@163.com (M.Z.)
[2] School of Civil & Hydraulic Engineering, Huazhong University of Science and Technology, Wuhan 430074, China; szfeng@hust.edu.cn (S.F.); jinwen.wang@hust.edu.cn (J.W.)
* Correspondence: chencheng410@hust.edu.cn

Abstract: This work formulates a stochastic dynamic programming (SDP) model that incorporates seasonal electricity prices and can handle a constraint on power yield, which is assumed to be satisfied at any time it is possible, thus allowing for an analysis of their impacts on the operational performances of cascaded reservoirs. The model is applied to the Lancang Cascade, specifically its two largest reservoirs, Xiaowan and Nuozhadu. The results show that increasing the power yield of the cascade will reduce energy production unfavorably but will impact water spillage favorably, with a power yield of 2000 MW and with a 91% reliability suggested as being a satisfactory operational target. The case study also suggests that using seasonal electricity prices makes the power generation very unstable during weeks 12–20, which is a period of time that is critical to transferring from dry to flooding seasons.

Keywords: stochastic dynamic programming (SDP); power yield; seasonal price; reliability; cascaded reservoirs

Citation: Xie, M.; Feng, S.; Wang, J.; Zhang, M.; Chen, C. Impacts of Yield and Seasonal Prices on the Operation of Lancang Cascaded Reservoirs. *Energies* **2022**, *15*, 3247. https://doi.org/10.3390/en15093247

Academic Editor: Alban Kuriqi

Received: 14 March 2022
Accepted: 18 April 2022
Published: 28 April 2022

1. Introduction

Due to the stochastic characteristics of inflow into reservoir and electricity prices, long-term hydropower operation is generally interpreted as a stochastic sequential decision-making process. Additionally, the nonlinear factors that involve hydropower output are interconnected, including the water head, reservoir storage, release, generating capacity, and water rate, which raises challenges for long-term hydropower operation [1]. Stochastic dynamic programming (SDP) is the most conventional methodology that can be used to address these issues. SDP has long been studied and successfully implemented in reservoir operation [2–4], which is attributable to its capability for dealing with the nonlinearity of functions involved in the model as well as in terms of its structure being inherently compatible with the stage-by-stage decision-making procedure often employed in real-time reservoir operation. For example, the water balance expresses the relationship of storages between two successive time-steps [5], and the Markov chain is commonly used to represent the stochastic relationship of inflows also between two successive time-steps [6]. Both the water balance and the Markov chain can serve well as the transition equations in dynamic programming (DP).

SDP can derive a close-loop operating rule, which defines the optimal decision at any possible state and is usually represented by a combination of discrete values of the state variables that traditionally include the storage at the beginning of the current or decision-making stage and the local inflow during the current stage of each reservoir [7–9]. The discretization in even a decent resolution of the state variables makes it problematic for SDP to be applicable to a reservoir system on a large scale such as in instances with more than three reservoirs. Some scholars [10,11] call it a "dimensional curse" since enumerating to obtain the optimal decisions for all the possible combinations of the discrete values of the

state variables takes a very long computational time, which is intolerable in engineering practice. For a hydropower system with no more than three cascaded reservoirs, however, SDP is always one of the most favorable options.

In China, where the advancement of power marketization and the market-oriented electricity price plays a vital role in promoting the optimal allocation of power resources [12], electricity price is the most pivotal factor in regulating the activity of the power producer. In deregulated electricity markets, price uncertainty must also be included in the scheduling models [13]. Due to the influence of uncertain quantities including electricity price and inflow, reliability in the long-term hydropower is a meaningful measurement to evaluate the hydropower system [14]. For instance, Saadat and Asghari [15] employed the reliability concept to maximize the reservoir releases to satisfy downstream demands. Reliability is an important indicator for power supply in the electrical system [16].

This work will apply SDP to the Xiaowan and Nuozhadu, the two biggest cascaded hydropower reservoirs in the Lancang River. The problem size is small and can be easily handled with SDP, which, however, will still encounter great challenges in dealing with the probabilistic constraints, such as those relating to the reliability, vulnerability, and resilience of the system, due to the difficulty of formulating these constraints into ones that are adaptable to the structure of the DP [17]. The Lancang hydropower cascade that is to be studied is required to yield energy at a high reliability, which is essentially a probabilistic constraint that is originally unable to be explicitly included in the SDP formulation but is likely to be converted into a normal constrain by assuming that the power yield must be satisfied whenever possible.

This work aims to investigate how the power yield will affect the operation of lancing cascaded reservoirs in terms of reliability, power production and water spillages, the proper power yield the cascade should target, as well as how the implementation of seasonal electricity prices will have impacts on the hydropower generation, in addition to simultaneously deriving the operational policies of the cascaded hydropower reservoirs that meet different objectives.

2. Problem Formulation

The reservoir operation, when formulated into SDP, may use one or a few state variables, usually selected from the storage S_t at the beginning of time-step t, the local inflow Q_{t-1} in previous time-step $t-1$, the local inflow Q_t in current time-step t, and the forecasted inflow H_t in time-step t [18]. The recursive objective function in the SDP, for one reservoir and when using the H_t as the inflow state variable, can be expressed as follows:

$$f_t(S_t, H_t) = \underset{Q_t|H_t}{E}\left\{\max_{R_t}\left[B(S_t, Q_t, R_t) + \underset{H_{t+1}|H_t,Q_t}{E}[f_{t+1}(S_{t+1}, H_{t+1})]\right]\right\} \quad (1)$$

where $f_t(S_t, H_t)$ is the benefit-to-go function, representing the maximum expected benefit till the end of the planning horizon given the initial storage S_t at the beginning of time-step t and the hydrological state H_t in time-step t; $\underset{Q_t|H_t}{E}\{\cdot\}$ is the expectation operator at conditional probability of $P(Q_t \mid H_t)$; and $B(S_t, Q_t, R_t)$ is the stage benefit, determined by the initial storage S_t, the current inflow Q_t, and the release R_t in stage/time-step t.

This work applies SDP to a hydropower system involving two cascaded reservoirs, where the state variables include the storages S_{it} of reservoir i at the beginning of time-step t and the total inflow into the cascade in coming time-step $t-1$. The recursive objective function in SDP, when applied to two cascaded reservoirs, is expressed as follows:

$$f_t(S_{1t}, S_{2t}, Q_t) = \max\left\{\underset{Q_{t+1}|Q_t}{E}[B_{1t}(S_{1t}, I_{1t}, R_{1t}) + B_{2t}(S_{2t}, I_{2t}, R_{2t}) + f_{t+1}(S_{1,t+1}, S_{2,t+1}, Q_{t+1})]\right\} \quad (2)$$

where the local inflow I_{it} to an individual reservoir is assumed as being perfectly correlated to the total inflow Q_t to the whole cascade:

$$I_{it} = \lambda_i \cdot Q_t \tag{3}$$

in which λ_i is the proportional coefficient of local inflow into reservoir i to the total inflow into the whole cascade. The constraints include the following:

(1) The water balance

$$S_{i,t+1} = S_{it} + (I_{it} + \sum_{k \in \Omega(i)} R_{kt} - R_{it}) \cdot \Delta t \tag{4}$$

where the $\Omega(i)$ is the set of reservoirs immediately upstream of reservoir i and the Δt is the time length in time-step t.

(2) The lower $S_{it}^{\min}$ and upper bounds $S_{it}^{\max}$ on the storage

$$S_{it}^{\min} \le S_{it} \le S_{it}^{\max} \tag{5}$$

(3) The release being nonnegative

$$R_{it} \ge 0 \tag{6}$$

(4) The power yield Y at a certain reliability ε

$$\Pr\left(\sum_i P_{it} \ge Y\right) \ge \varepsilon \tag{7}$$

where the hydropower output P_{it} of i in time-step t is determined with

$$P_{it} = \eta_i \cdot \left[Z_i^{up}\left(\frac{S_{it} + S_{i,t+1}}{2}\right) - Z_i^{dn}(R_{it})\right] \cdot \min(R_{it}, U_i^{\max}) \tag{8}$$

with the final storage $S_{i,t+1}$ being determined via the water balance (4), the η_i being the coefficient of generation efficiency, and the $U_i^{\max}$ being the capacity of turbine discharge of hydropower reservoir i.

The stage benefit $B_{it}(S_{it}, I_{it}, R_{it})$, dependent of different operational objectives, could be the energy production, the revenue gained at seasonal prices, and power yield in current stage, etc. For a certain stage benefit function, the recursive equation in the SDP will evolve to the optimal reservoir operational policy, which can then be used in long-term real-time operation, month by month, for instance. This work will compare the following three objectives with each other, denoted as follows:

(1) SDP-1: to maximize the energy production without power yield;

$$B_{it}(S_{it}, Q_{it}, R_{it}) = P_{it} \cdot \Delta t \tag{9}$$

(2) SDP-2: to maximize the revenue at seasonal prices without power yield, where ζ_t is the seasonal price of electricity in time-step t;

$$B_{it}(S_{it}, Q_{it}, R_{it}) = \zeta_t \cdot P_{it} \cdot \Delta t \tag{10}$$

(3) SDP-3: to maximize the energy production with power yield (7).

3. Solution Procedures

The reservoir operation problem will be solved with discrete stochastic dynamic programming (DSDP), which requires state variables to be discretized and both the objective and constraints to be decoupled into every stage, with only the state variables coupled via state variables between two adjacent stages.

3.1. The Typical Inflows and Their Transition Probabilities

The coming inflow into the cascade, as one of the state variables, is a random variable that can be represented by some typical values, making the monthly inflows a stochastic

chain, with the Markov Chain as being specific when considering only the first-order correlation between the inflows in two successive time-steps. Generally, based upon the mean and standard deviation of the random inflow, its distribution space can be divided into five intervals: below dry, dry, average, wet, and above wet, commonly practiced due to the simplicity in engineering application [19]. To derive the inflow transition probabilities, four methods—counting, ordinary least-squares regression, robust linear model regression, and multi-variate conditional distributions—are evaluated to determine how they influence water system performance [20]. The most accessible counting method is selected to acquire inflow transition probabilities in this work. The number of typical inflows should be neither too small nor too large to balance the computational burden with the fullness of their representation. The inflow in this work is represented with 7 typical values, determined by following these steps:

(1) Suppose the number of typical inflows in time-step t is K, and there are Y years of historical inflows Q_t^y observed, which ensure n (=Y/K) historical inflows be represented by one typical inflow, determined as the average over these n historical inflows.

(2) Arrange the historical inflows Q_t^y for t = 1,2, . . . , T and y = 1,2, . . . , Y in order from the smallest to the largest: $Q_t^{y(1)} \le Q_t^{y(2)} \le \cdots \le Q_t^{y(Y)}$; the typical inflow for any interval k (k = 1,2, . . . , K) in time-step t is determined as the average over n historical inflows, expressed as

$$Q_t(k) = \frac{1}{n} \sum_{j=n(k-1)+1}^{nk} Q_t^{y(j)} \tag{11}$$

(3) Apparently, each historical inflow in any time-step t can be represented by one of the k typical inflows in this time-step, and the transition probability from the k-th in time-step t to the l-th in time-step t + 1 can be estimated as follows:

$$\Pr\left\{ Q_{t+1}^l \middle| Q_t^k \right\} = \frac{n_t(k,l)}{n} \tag{12}$$

where among n historical inflows represented by the k-th typical inflow in time-step t, there are $n_t(k,l)$ of their successive inflows that are represented by the l-th typical inflow in time-step t + 1.

3.2. The Representative Storages

The storage of a reservoir, which theoretically could be any value within its physically feasible region, is actually a continuous state variable that will also be discretized into a number of storage volume intervals representing the storage state at certain time. The number of the storage intervals should be good enough for the computational resolution. According to the work by Karamouz [21], increasing the number of storage intervals to more than 20 will help little in improving the operational results of a reservoir that has an active storage capacity 1.7 times more than the amount of its average annual runoff.

3.3. The Power Yield at Certain Reliability

As required by SDP, the constraints must be decoupled into every stage, with only the state variables coupled via state variables between two adjacent stages. The constraint (7) of power yield at certain reliability, however, cannot be easily decoupled into individual stages as the reliability of meeting the power yield is determined over the whole planning horizon and cannot be exactly enforced stage by stage. However, if assuming the power yield must be met whenever it is possible, then we have the following deterministic constraint:

$$\sum_i P_{it} \ge Y \tag{13}$$

to be satisfied in every stage, thereby making the constraint decoupled into individual stages. Under this assumption, the power yield actually determines the reliability, which

can be estimated by simulating the final optimal operation policy derived by solving the SDP.

3.4. Recursive Evolution

With the transition probabilities determined with (12), the recursive Equation (2) can be reformulated as follows:

$$f_t(S_{1t}^i, S_{2t}^j, Q_t^k) = \max_{R_{1t}, R_{2t}} \left\{ \sum_{l=1}^{K} \Pr(Q_{t+1}^l \middle| Q_t^k) \cdot \left[B_{1t}(S_{1t}, I_{1t}, R_{1t}) + B_{2t}(S_{2t}, I_{2t}, R_{2t}) + f_{t+1}(S_{1,t+1}, S_{2,t+1}, Q_{t+1}^l) \right] \right\} \quad (14)$$

which is a backward recursive equation and, given a stationary stochastic streamflow process, will evolve to a steady operational policy of the cascaded reservoirs. To be specific, let the benefit-to-go function at the end of the planning horizon (T) be zero so that the recursive equation finishes one iteration after evolving from T to 1 backward over time. Then, subtract the benefit-to-go function by a constant to avoid numerical overflow, and repeat this procedure until the convergence has been achieved.

4. Engineering Applications

4.1. Engineering Background

Xiaowan and Nuozhadu are two large, cascaded hydropower reservoirs located in the Lancang River basin; both are situated in the middle and lower reaches of the Lancang River, and the reginal location is depicted in Figure 1. The Xiaowan reservoir, with an active storage capacity close to 10 billion cubic meters, has a strong over-year regulation capacity, the same as its downstream Nuozhadu reservoir that, with a total of 5850 MW capacity installed, is one of the key strategic projects for the West-to-East and the Yunnan-to-outside power transmission thanks to its strong power generation capacity. This work studies the joined optimal operation of the cascaded Xiaowan and Nuozhadu reservoirs, which are two main regulatory hydropower stations under the Yunnan Provincial Power Grids. The dimension problem will not be an obstacle for the case study of two reservoirs.

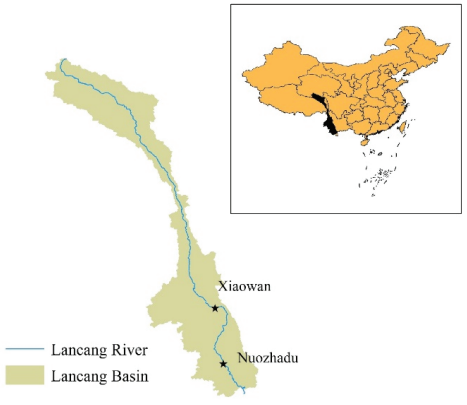

Figure 1. Reginal location of Xiaowan and Nuozhadu reservoir.

4.2. Data Preparation and Setting

There are 57 years of "Xunly" historical inflows during 1953–2009 available for the cascade. In China, a month is divided into three Xuns: the early, mid, and late, with each Xun being a period of about 10 days.

The number of inflow states are set to be 7 in each Xun; thus, the size of the transition probability matrix will be $7 \times 7 = 49$. It is worth noting that since the reservoir operational rule is annually periodic, the transition probability from the last Xun in a year is to the first Xun in its next year. The optimal reservoir operation rule derived with the SDP will

be simulated under the historical scenario of the inflows observed during 1953–2009. The basic parameters of both hydropower reservoirs are summarized in Table 1.

Table 1. The basic parameters of the reservoirs.

Parameters	Xiaowan	Nuozhadu
Dead storage capacity (bcm)	4.662	10.414
Normal storage capacity (bcm)	14.557	21.749
Minimum head (m)	164	152
Maximum head (m)	251	215
Generating discharge capacity (m^3)	2261	3429

This work studies the joint operational strategies of the cascaded Xiaowan and Nuozhadu hydropower reservoirs under three different objective conditions. The SDP-1 that maximizes the expected energy production is different from the SDP-2 that maximizes the expected revenue calculated based on seasonal electricity prices, which are given in Table 2.

Table 2. Monthly electricity prices.

Month	1	2	3	4	5	6	7	8	9	10	11	12
Price (CNY/KWh)	0.39	0.39	0.39	0.39	0.26	0.19	0.19	0.19	0.19	0.19	0.26	0.39

The SDP-2 is equivalent to the SDP-1 when keeping the electricity unchanged over the planning horizon. As for the SDP-3, the operational strategies with different power yields can be derived and then simulated over many years to statistically estimate the reliabilities in meeting the power yields. Figures 2 and 3 reveal the water level, inflow, and release process of Xiaowan and Nuozhadu for SDP-1, SDP-2, and SDP-3 models during 2000–2009. For SDP-2, due to the dynamic electricity price, water level fluctuations are more obvious. Similar trends can be presented for SDP-3 models with different power yield. Statistical analysis will be described as follows:

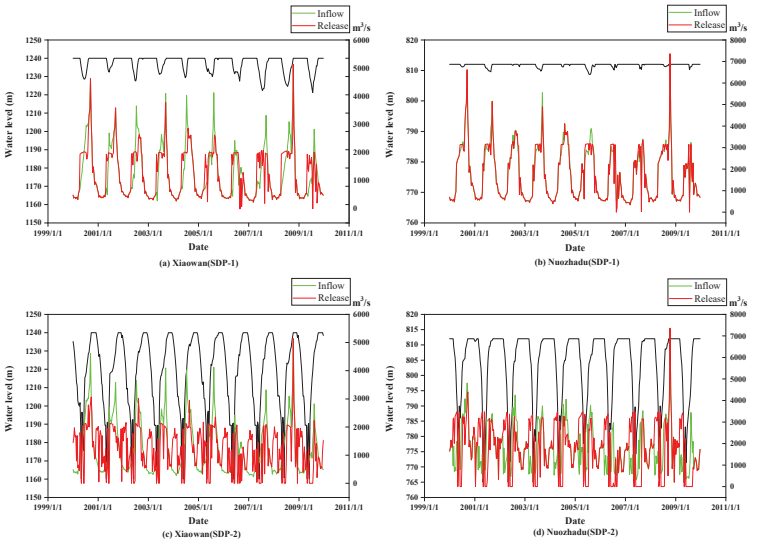

Figure 2. Water level, inflow, and release process of cascade reservoir for SDP-1 and SDP-2 during 2000–2009.

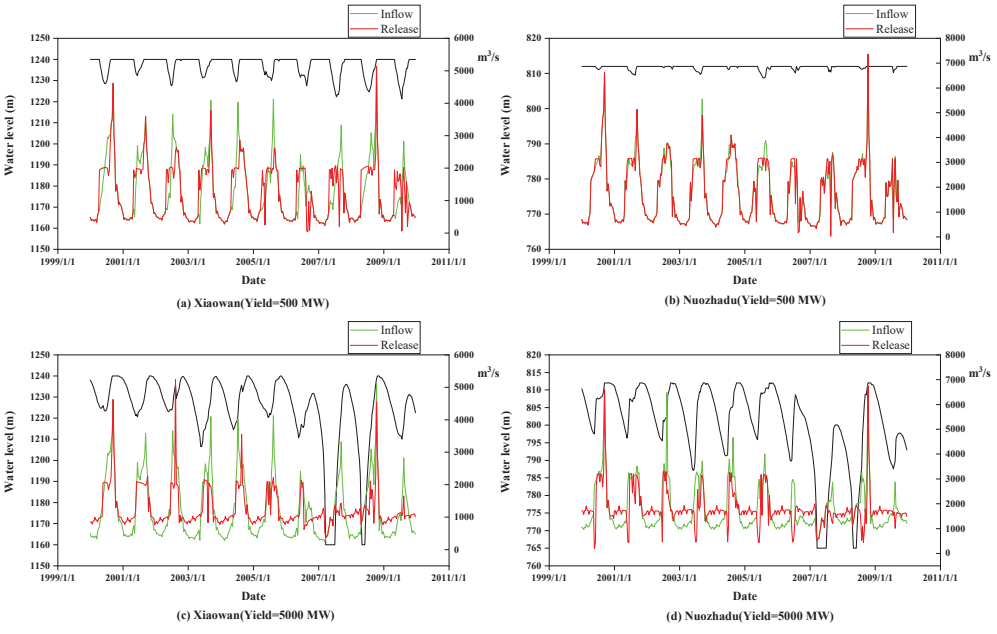

Figure 3. Water level, inflow, and release process of cascade reservoir for SDP-3 with power yield = 500 MW and 5000 MW during 2000–2009.

4.3. Comparison between the SDP-1 and SDP-2

Figure 4 compares the SDP-1 and SDP-2 of the annual energy production and revenue for both cascaded hydropower stations. When compared to the statistical average determined by simulating the operation strategies over many years, the SDP-1 gives an annual average energy production (AAEP) of 50,274,110 MWh, improved by 2.29% over the SDP-2 that produces an AAEP of 49,121,330 MWh. The SDP-2, however, gains an annual average revenue (AAR) of CNY 15,094 M, improved by 5.34% over the SDP-1 that will have an AAR of CNY 14,328 M when estimated at CNY 0.285/KWh, which is the average of the monthly electricity prices given in Table 2.

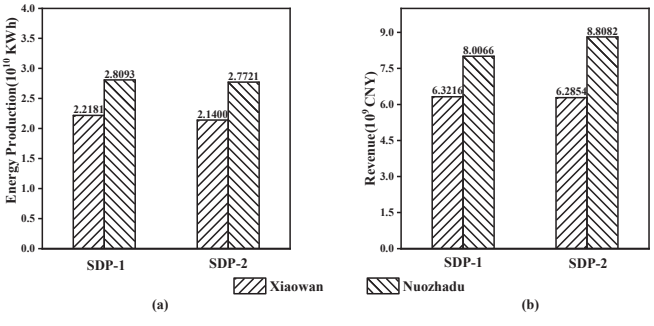

Figure 4. Comparison between the SDP-1 and SDP-2 on expected energy (**a**) and revenue (**b**).

Figure 5 shows the energy production processes from the SDP-1 and 2 for both the Xiaowan and Nuozhadu hydropower reservoirs. The SDP-1 that maximizes the expected energy production has a generation process that is similar to the inflow process in the trend, with less generation in dry seasons and more in wet seasons. However, the SDP-2

that maximizes the expected revenue will try to generate less in wet seasons when the electricity prices are low but will generate more in the dry seasons to take advantage of the higher electricity prices, which is particularly obvious from the Nuozhadu reservoir. The results suggest that using seasonal electricity prices makes the power generation very unstable during 12–20 Xun, which is a critical time period for transferring from dry to flooding seasons.

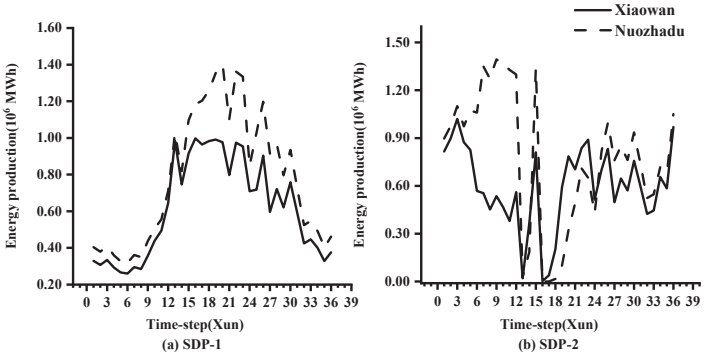

Figure 5. Comparison between the SDP-1 and SDP-2 on average energy production in each Xun (1/3 month).

4.4. The Results by the SDP-3

By setting the power yield to 500 MW, 1000 MW, 2000 MW, 3000 MW, 4000 MW, and 5000 MW, the SDP-3 problems are solved to derive the corresponding optimal operational strategies, which are then simulated over a time period of 1953–2009, when the historical inflows are available to estimate the reliabilities associated with the power yields. Table 3 summarizes the relationship between the power yield and its reliability, and Figure 6 illustrates the average energy production in each time-step or Xun (1/3 month), in this case. As Table 3 shows, when the power yield increase gradually, the reliability in meeting the power yield decrease gradually, and Figure 6 demonstrates that the energy production process becomes more even for both the Xiaowan and Nuozhadu hydropower reservoirs, with the higher reliability leading to more generation than the lower reliability in dry seasons. The reliability decreases sharply when increasing the power yield from 2000 MW to 3000 MW, suggesting the power yield of 2000 MW at 91% reliability should be a satisfactory operational target.

Table 3. The reliability of the power yield for the cascade.

Power Yield	500 MW	1000 MW	2000 MW	3000 MW	4000 MW	5000 MW
Reliability	99.4%	98.3%	90.7%	77.9%	69.8%	47.5%

The average annual energy productions and spillages under different power yields are summarized in Table 4, which shows that both the energy production and spillage of the Xiaowan and Nuozhadu decrease when the power yield of the hydropower cascade grows higher; in particular, the spillage from the Nuozhadu decreases sharply from 1073 to 595 million cubic meters when the power yield increases from 4000 to 5000 MW. Apparently, increasing the power yield of the cascade will reduce the energy production unfavorably but will affect the water spillage favorably.

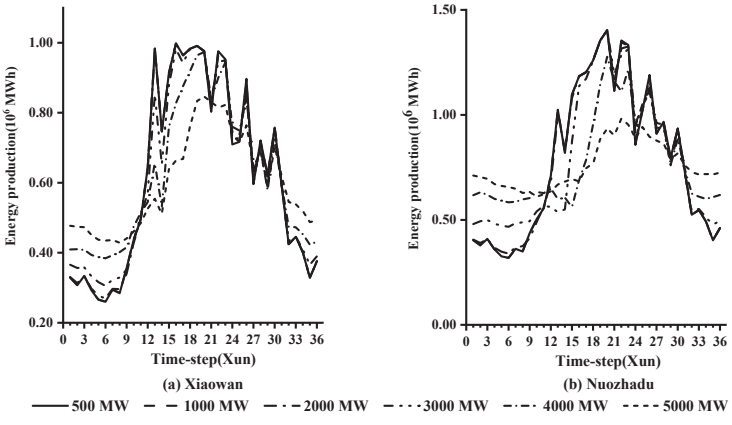

Figure 6. The average energy production of Xiaowan (**a**) and Nuozhadu (**b**) in each Xun (1/3 month) under different power yields for the cascade.

Table 4. Annual energy and spillage under different power yields by the SDP-3.

		500 MW	1000 MW	2000 MW	3000 MW	4000 MW	5000 MW
Energy (MWh)	Xiaowan	22,180,172	22,179,661	22,179,003	22,176,101	22,160,479	21,512,030
	Nuozhadu	28,093,066	28,093,517	28,092,104	28,071,902	27,933,721	27,214,184
Spillage (million m^3)	Xiaowan	1417.9	1416.8	1410.9	1367.1	1191.1	909.0
	Nuozhadu	1282.5	1280.8	1278.3	1231.6	1072.5	594.5

The average spillage processes derived by the SDP-3 under different power yields are illustrated in Figure 7, which demonstrates that spillage mainly occurs from early July to late August. With the power yield increased from 0 to 5000 MW, the spillages of Nuozhadu have a trend that is broadly similar to each other in terms of gradually increasing from early July, reaching the first peak in mid or late August, then decreasing until early September, reaching the second peak, then decreasing slowly. Xiaowan, however, has a different trend in spillage that reaches its peak in mid or late September when the power yield is 4000 MW and in mid or late June when it is 5000 MW.

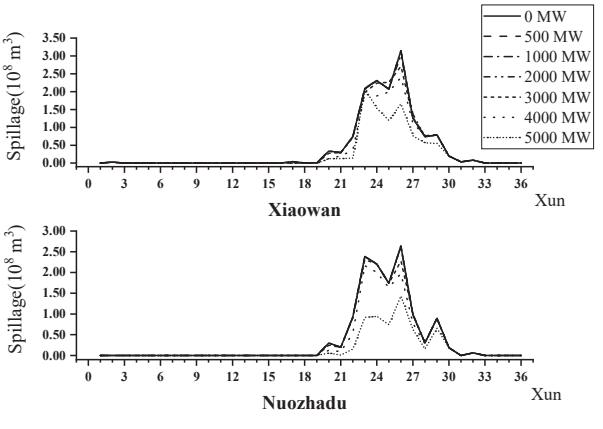

Figure 7. The average spillage in each Xun under different power yields.

5. Conclusions

This work formulates a stochastic dynamic programming (SDP) model that incorporates seasonal electricity prices and can handle the constraint on power yield at certain reliability that are assumed to be satisfied whenever it is possible. Despite the increasing number of reservoirs that will hinder the application of proposed SDP model to multi-reservoir operation, a cascade with two reservoirs in the case study makes it convenient to employ the proposed SDP model. When applied to the Lancang River consisting of its two major cascaded hydropower reservoirs, SDP derives the optimal operational strategies under three conditions: to maximize the energy production and revenue without power yield, and to maximize the energy production with power yield, both of which are compared with each other. The results show that increasing the power yield of the cascade will reduce the energy production unfavorably but will affect the water spillage favorably, with a power yield of 2000 MW with a 91% reliability being suggested as a satisfactory operational target. The case study also suggests that using seasonal electricity prices makes the power generation very unstable during weeks 12–20, which is a critical period of time for transferring from dry to wet seasons.

Author Contributions: M.X.—Conceptualization, formal analysis, writing—review and editing; S.F.—Writing—review and editing, visualization; J.W.—Methodology, software; M.Z.—Supervision, project administration; C.C.—Methodology, software, writing—original draft preparation, writing—review and editing. All authors have read and agreed to the published version of the manuscript.

Funding: This research received no external funding.

Data Availability Statement: Not applicable.

Conflicts of Interest: The authors declare no conflict of interest.

References

1. Kang, C.X.; Chen, C.; Wang, J.W. An Efficient Linearization Method for Long-Term Operation of Cascaded Hydropower Reservoirs. *Water Resour. Manag.* **2018**, *32*, 3391–3404. [CrossRef]
2. Stedinger, J.R.; Faber, B.A.; Lamontagne, J.R. Developments in Stochastic Dynamic Programming for Reservoir Operation Optimization. In Proceedings of the World Environmental and Water Resources Congress 2013: Showcasing the Future, Cincinnati, OH, USA, 19–23 May 2013; pp. 1266–1278.
3. Ben Alaya, A.; Souissi, A.; Tarhouni, J.; Ncib, K. Optimization of Nebhana Reservoir Water Allocation by Stochastic Dynamic Programming. *Water Resour. Manag.* **2003**, *17*, 259–272. [CrossRef]
4. Stedinger, J.R.; Sule, B.F.; Loucks, D.P. Stochastic dynamic programming models for reservoir operation optimization. *Water Resour. Res.* **1984**, *20*, 1499–1505. [CrossRef]
5. Turgeon, A. Stochastic optimization of multireservoir operation: The optimal reservoir trajectory approach. *Water Resour. Res.* **2007**, *43*. [CrossRef]
6. Scarcelli, R.O.C.; Zambelli, M.S.; Soares, S.; Carneiro, A.A.F.M. Ensemble of Markovian stochastic dynamic programming models in different time scales for long term hydropower scheduling. *Electr. Power Syst. Res.* **2017**, *150*, 129–136. [CrossRef]
7. Tejada-Guibert, J.A.; Johnson, S.A.; Stedinger, J.R. The Value of Hydrologic Information in Stochastic Dynamic Programming Models of a Multireservoir System. *Water Resour. Res.* **1995**, *31*, 2571–2579. [CrossRef]
8. Mousavi, S.J.; Mahdizadeh, K.; Afshar, A. A stochastic dynamic programming model with fuzzy storage states for reservoir operations. *Adv. Water Resour.* **2004**, *27*, 1105–1110. [CrossRef]
9. Feng, Z.K.; Niu, W.J.; Cheng, C.T.; Liao, S.L. Hydropower system operation optimization by discrete differential dynamic programming based on orthogonal experiment design. *Energy* **2017**, *126*, 720–732. [CrossRef]
10. Zhao, T.T.G.; Cai, X.M.; Lei, X.H.; Wang, H. Improved Dynamic Programming for Reservoir Operation Optimization with a Concave Objective Function. *J. Water Resour. Plan. Manag. Asce* **2012**, *138*, 590–596. [CrossRef]
11. Cheng, C.T.; Wang, S.; Chau, K.W.; Wu, X.Y. Parallel discrete differential dynamic programming for multireservoir operation. *Environ. Model. Softw.* **2014**, *57*, 152–164. [CrossRef]
12. Liu, S.; Yang, Q.; Cai, H.; Yan, M.; Zhang, M.; Wu, D.; Xie, M. Market reform of Yunnan electricity in southwestern China: Practice, challenges and implications. *Renew. Sustain. Energy Rev.* **2019**, *113*, 109265. [CrossRef]
13. Hongling, L.; Chuanwen, J.; Yan, Z. A review on risk-constrained hydropower scheduling in deregulated power market. *Renew. Sustain. Energy Rev.* **2008**, *12*, 1465–1475. [CrossRef]
14. Ware, A. Reliability-constrained hydropower valuation. *Energy Policy* **2018**, *118*, 633–641. [CrossRef]
15. Saadat, M.; Asghari, K. Reliability Improved Stochastic Dynamic Programming for Reservoir Operation Optimization. *Water Resour. Manag.* **2017**, *31*, 1795–1807. [CrossRef]

16. Li, X.; Liu, P.; Ming, B.; Huang, K.; Xu, W.; Wen, Y. Joint Optimization of Forward Contract and Operating Rules for Cascade Hydropower Reservoirs. *J. Water Resour. Plan. Manag.* **2022**, *148*, 04021099. [CrossRef]
17. Chen, C.; Kang, C.; Wang, J. Stochastic Linear Programming for Reservoir Operation with Constraints on Reliability and Vulnerability. *Water* **2018**, *10*, 175. [CrossRef]
18. Mujumdar, P.P.; Nirmala, B. A bayesian stochastic optimization model for a multi-reservoir hydropower system. *Water Resour. Manag.* **2007**, *21*, 1465–1485. [CrossRef]
19. Kim, Y.-O.; Palmer Richard, N. Value of Seasonal Flow Forecasts in Bayesian Stochastic Programming. *J. Water Resour. Plan. Manag.* **1997**, *123*, 327–335. [CrossRef]
20. Haguma, D.; Leconte, R.; Côté, P. Evaluating Transition Probabilities for a Stochastic Dynamic Programming Model Used in Water System Optimization. *J. Water Resour. Plan. Manag.* **2018**, *144*, 04017090. [CrossRef]
21. Karamouz, M.; Houck, M.H. Annual and monthly reservoir operating rules generated by deterministic optimization. *Water Resour. Res.* **1982**, *18*, 1337–1344. [CrossRef]

energies

MDPI

Article

Nonlinear Modeling and Stability of a Doubly-Fed Variable Speed Pumped Storage Power Station with Surge Tank Considering Nonlinear Pump Turbine Characteristics

Nan Zhang [1,*], Xiaoming Xue [1], Na Sun [1], Yanhui Gu [1], Wei Jiang [1] and Chaoshun Li [2,*]

[1] Jiangsu Key Laboratory of Advanced Manufacturing Technology, Huaiyin Institute of Technology, Huai'an 223003, China; xue_xiaoming@foxmail.com (X.X.); sunna1347@126.com (N.S.); jimgu@hyit.edu.cn (Y.G.); jw_hust@163.com (W.J.)

[2] School of Civil and Hydraulic Engineering, Huazhong University of Science and Technology, Wuhan 430074, China

* Correspondence: zhangnanhust@163.com (N.Z.); csli@hust.edu.cn (C.L.); Tel.: +86-132-9651-5285 (N.Z.); +86-158-7180-0142 (C.L.)

Abstract: This paper investigates the nonlinear modeling and stability of a doubly-fed variable speed pumped storage power station (DFVSPSPS). Firstly, the mathematical model of DFVSPSPS with surge tank considering nonlinear pump turbine characteristics was derived and established. Then, Hopf bifurcation analysis of DFVSPSPS was performed. The stable region was identified and verified by example analysis. Moreover, the effect mechanism of nonlinear pump turbine characteristics on the stability of DFVSPSPS was explored. Finally, the influence of factors on the stability and dynamic response of DFVSPSPS was studied. The results indicate that the emerged Hopf bifurcation of DFVSPSPS is supercritical and the region on the low side of the bifurcation line is the stable region. Nonlinear head characteristics have a significant influence on the stability and dynamic response of DFVSPSPS. Nonlinear speed characteristics have an obvious effect on the stability and dynamic response of DFVSPSPS only under positive load disturbance and unstable surge tank. Nonlinear head characteristics are unfavorable for the stability of DFVSPSPS under positive load disturbance and favorable under negative load disturbance. A smaller flow inertia of penstock, a smaller head loss of penstock and a greater unit inertia time constant are favorable for the stability of DFVSPSPS. The stable region under the positive disturbance of active power is larger than that under the negative disturbance of active power. The time constant of the surge tank presents a saturation characteristic on the stability of DFVSPSPS.

Keywords: doubly-fed variable speed pumped storage power station; nonlinear modeling; Hopf bifurcation; stability analysis; nonlinear pump turbine characteristics

Citation: Zhang, N.; Xue, X.; Sun, N.; Gu, Y.; Jiang, W.; Li, C. Nonlinear Modeling and Stability of a Doubly-Fed Variable Speed Pumped Storage Power Station with Surge Tank Considering Nonlinear Pump Turbine Characteristics. *Energies* **2022**, *15*, 4131. https://doi.org/10.3390/en15114131

Academic Editor: Javier Contreras

Received: 4 May 2022
Accepted: 2 June 2022
Published: 4 June 2022

1. Introduction

Vigorously developing renewable energy is an important strategic measure to deal with the problems of fossil fuel shortage, global warming and energy security. It is also an effective way of maintaining the sustainable development of national societies and economies. In recent years, the large-scale development and grid connection of intermittent renewable energy, such as wind power and photovoltaic, has created a serious threat to the safe and stable operation of the power grid [1,2]. Pumped storage power stations (PSPS) are the main regulating power supply in power systems [3]. It is of great importance to ensure the safety of the power grid, promote the consumption of renewable energy and promote the green and low-carbon transformation of energy [4,5]. Under the guidance of the goal of carbon peak and carbon neutralization, vigorously developing PSPS is an urgent task to implement the dual carbon goal [6].

At present, most PSPS use synchronous generators, which can only operate at a constant speed, resulting in a series of problems: (a) Under generator operation mode, the

power regulation of the unit is slow; (b) The constant speed PSPS (CSPSPS) can only operate stably at the rated synchronous speed. When the operating head or load change, the unit speed will deviate from the optimal speed and the efficiency of the pump turbine will decrease, resulting in the deterioration of the unit operation; (c) In pumping mode, the input electromagnetic power lacks controllability. The variable speed pumped storage unit (VSPSU) is a new type of PSU, where an AC-excited asynchronous motor is used to replace the traditional DC-excited synchronous motor. The speed control of the unit is realized by changing the excitation current, which overcomes the disadvantage that the speed of the traditional PSU is not adjustable. Compared with the CSPSPS, the variable speed PSPS (VSPSPS) has the following advantages: (a) Accelerated regulation of active power; (b) Increased operation efficiency of the pump turbine in generator and pumping modes; (c) Widened operating range of the pump turbine; (d) Reduced cavitation process; (e) Increased stability and flexibility of pump turbine [7–9]. However, the modeling and operation control of VSPSPS are more complex due to the use of an AC-excited asynchronous motor and converter.

Most of the research into VSPSPS are focused on mathematical modeling, numerical simulation, operation stability, reliability, dynamic characteristics and control. Mathematical modeling is the foundation of numerical simulation, operation stability, reliability, dynamic characteristics and control. Stability is the primary requirement for the normal operation of the system. The relevant research on modeling, control and stability of VSPSPS is presented below.

Kuwabara et al. [10] took the 400 MW VSPSU of the Ohkawachi PSPS as an example to study the principal design and actual performance of the machine. The excellent dynamic performance and significant potential for contribution to the power system have been verified by field test data. Unsteady numerical simulations of the VSPSPS and the CSPSPS were performed and the corresponding dynamic performance was compared [11]. The simulation results demonstrate that VSPSPS improves power system stability. Tests of the VSPSPS in the Hydraulics Laboratory of the Polytechnic University of Madrid were also performed [8]. The results show that the VSPSPS has greater flexibility under off-designed conditions, which is mainly reflected by the improvements in efficiency, operation performance and operating range. Integrated modeling of VSPSPS and wind power was established with MATLAB/Simulink and validated by on-site measurements [12]. The advantage of VSPSPS for mitigating wind was analyzed by performance assessment. The different control strategies for VSPSPS connected to an isolated power system with high penetration of intermittent renewable energy were studied. The effect mechanism of penstock length and initial operating point on the dynamic performance was then investigated [13].

Relevant scholars have conducted in depth research into modeling, numerical simulation and control, and have done a lot of work. However, there has been relatively little work conducted on the stability of VSPSPS [14]. Guo et al. [15] derived a nonlinear mathematical model of VSPSPS. The influence of factors on stability were studied. However, nonlinear pump turbine characteristics were ignored and a linear model was used. A novel mathematical model of VSPSPS concerning the electromechanical transient model of doubly-fed induction (DFIG) was established and the stability was investigated based on Hopf bifurcation theory under turbine and pump modes [16,17]. Unfortunately, the pump turbine model was still linear. Zhu et al. [18] studied the stability of VSPSPS considering nonlinear head loss and the parameter sensitivity analysis of the model was analyzed systematically. However, the model did not consider pump turbine nonlinear characteristics.

From the above literature review, it can be shown that pump turbine nonlinear characteristics are often ignored and the simplified linear model is used in most of the existing research. However, the stability of a VSPSPS is affected by all the components of the hydropower station. Among those components, the pump turbine is the core component of PSPS and has an important effect on the stability of VSPSPS [19]. On the other hand,

the surge tank also has an obvious influence on the stability and dynamic performance of VSPSPS but this influence is always neglected [20–22]. Therefore, it is difficult to fully understand the stability and dynamic characteristics of VSPSPS based on the simplified model; the effect mechanism of nonlinear pump turbine characteristics on stability and dynamic characteristics of VSPSPS can not be calculated. Moreover, most of the established models are focused on numerical simulation and control and are not suitable for stability analysis [14]. Therefore, a complete and reasonable mathematical model should be established for stability and dynamic characteristics analysis of VSPSPS. To overcome the above problems, using a doubly-fed VSPSPS (DFVSPSPS) as the research object, a novel nonlinear model of DFVSPSPS with surge tank and consideration of nonlinear pump turbine characteristics was established, and the dynamic performance and parameter sensitivity were studied. The novelty and innovation of the paper are:

(1) The establishment of a novel, nonlinear model of DFVSPSPS considering surge tank and nonlinear pump turbine characteristics.
(2) Clarification of the stability of DFVSPSPS based on theoretical analysis and numerical simulation.
(3) Revealing of the effect mechanism of nonlinear pump turbine characteristics on the stability of DFVSPSPS.
(4) Revealing of the influence of factors on the stability of DFVSPSPS.

The rest of this paper is organized as follows: The mathematical model of DFVSPSPS considering surge tank and nonlinear pump turbine characteristics is established in Section 2; in Section 3, the stability of DFVSPSPS is analyzed and verified by Hopf bifurcation theory and numerical simulation; in Section 4, the influence of nonlinear pump turbine characteristics on the stability and dynamic characteristics of DFVSPSPS are revealed; in Section 5, the influence of system parameters on the stability and dynamic characteristics of DFVSPSPS are studied; in Section 6, conclusions are given.

2. Nonlinear Modeling of DFVSPSPS

A typical layout schematic diagram of a DFVSPSPS is shown in Figure 1. In a DFVSPSPS system, the components include an upstream reservoir, headrace tunnel, surge tank, penstock, pump turbine, DFIG, converter and tailwater. The pump turbine is designed in a reversible way with high energy conversion efficiency in both power generation and pumping functions. The surge tank is set to decrease water hammer pressure in the penstock. The mathematical model of a DFVSPSPS is composed of the basic equations of components. The nomenclature for variables is shown in Appendix A.

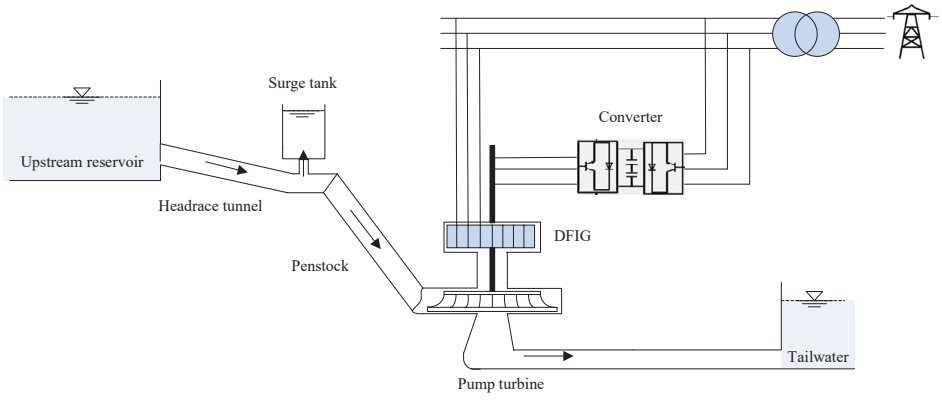

Figure 1. Schematic diagram of a DFVSPSPS.

2.1. Hydraulic System

The dynamic equations of the hydraulic system, including headrace tunnel, surge tank and penstock, are determined by Newton's Second Law of Motion.

Dynamic equation of headrace tunnel [23,24]:

$$h_s = -T_{wH}\frac{dq_H}{dt} - \frac{h_{H0}}{H_0} \tag{1}$$

Dynamic equation of surge tank [23,24]:

$$q = q_H + T_F\frac{dh_s}{dt} \tag{2}$$

Dynamic equation of penstock [19]:

$$T_w\frac{dq}{dt} = -h - h_s \tag{3}$$

2.2. Model of DFIG Control System

2.2.1. Model of DFIG

DFIG is a complex system with strong nonlinearity and high coupling, therefore, it is difficult to model. To facilitate the research, the model of DFIG was established in a two-phase *d-q* synchronous coordinate. The basic equations of stator voltage and rotor voltage are [16]:

$$\begin{cases} v_{ds} = R_s i_{ds} + \frac{d}{dt}\varphi_{ds} - \omega_1\varphi_{qs} \\ v_{qs} = R_s i_{qs} + \frac{d}{dt}\varphi_{qs} + \omega_1\varphi_{ds} \\ v_{dr} = R_r i_{dr} + \frac{d}{dt}\varphi_{dr} - (\omega_1 - \omega)\varphi_{qr} \\ v_{qr} = R_r i_{qr} + \frac{d}{dt}\varphi_{qr} + (\omega_1 - \omega)\varphi_{dr} \end{cases} \tag{4}$$

The equations of the stator and rotor flux linkages are represented as follows:

$$\begin{cases} \varphi_{ds} = L_s i_{ds} + L_m i_{dr} \\ \varphi_{qs} = L_s i_{qs} + L_m i_{qr} \\ \varphi_{dr} = L_m i_{ds} + L_r i_{dr} \\ \varphi_{qr} = L_m i_{qs} + L_r i_{qr} \end{cases} \tag{5}$$

The torque equation and motion equation of the DFIG are represented as follows:

$$\begin{cases} \frac{d\omega}{dt} = \frac{1}{T_a}(T_L - T_e - F\omega) \\ T_e = 1.5n_p(\varphi_{ds}i_{qs} - \varphi_{qs}i_{ds}) \end{cases} \tag{6}$$

2.2.2. Control System

An AC-DC-AC bidirectional converter was adopted for this paper. The rotor-side converter adopts vector control based on the stator flux direction to realize the decoupling of active and reactive power of DFIG and control the active and reactive power independently. The grid-side converter adopts double closed-loop control based on the voltage direction to keep the DC bus voltage constant.

The control of the rotor side is shown as follows:

$$\begin{cases} i_{dr\_ref} = \frac{L_s}{L_m}\left(K_{p3} + \frac{K_{i3}}{s}\right)\left(Q_{dref} - Q_d\right) + \frac{\varphi_1}{L_m} \\ v_{dr\_ref} = \left(K_{p4} + \frac{K_{i4}}{s}\right)\left(i_{dr\_ref} - i_{dr}\right) + v_{drc} \end{cases} \tag{7}$$

$$\begin{cases} i_{qr\_ref} = \frac{L_s}{L_m}\left(K_{p1} + \frac{K_{i1}}{s}\right)\left(P_{ref} - P\right) \\ v_{qr\_ref} = \left(K_{p2} + \frac{K_{i2}}{s}\right)\left(i_{qr\_ref} - i_{qr}\right) + v_{qrc} \end{cases} \tag{8}$$

v_{drc} and v_{qrc} are defined as follows:

$$v_{drc} = -\frac{1}{L_s}(L_r L_s - L_m L_m)(\omega_1 - \omega) i_{qr} \tag{9}$$

$$v_{qrc} = \frac{1}{L_s}(L_r L_s - L_m L_m)(\omega_1 - \omega_r) i_{dr} - \frac{L_m}{L_s}(\omega_1 - \omega)\varphi_1 \tag{10}$$

The control of the grid side is shown as follows:

$$\begin{cases} i_{dg\_ref} = \left(K_{p5} + \frac{K_{i5}}{s}\right)\left(Q_{g\_ref} - Q_g\right) \\ v_{dg\_ref} = \left(K_{p6} + \frac{K_{i6}}{s}\right)\left(i_{dg\_ref} - i_{dg}\right) \end{cases} \tag{11}$$

$$\begin{cases} i_{qg\_ref} = \left(K_{p7} + \frac{K_{i7}}{s}\right)\left(v_{dc\_ref} - v_{dc}\right) \\ v_{qg\_ref} = \left(K_{p8} + \frac{K_{i8}}{s}\right)\left(i_{qg\_ref} - i_{qg}\right) \end{cases} \tag{12}$$

Now, the mathematical model of the DFIG control system was established, and consisted of Equations (4)–(12).

2.2.3. Model Simplifying of DFIG Control System

The response time of the electromagnetic transient, including the switching action of the power electronic devices and the dynamic process of the power converter, is very short. The electromechanical transient process is relatively slow (hundreds of milliseconds). Therefore, the model of the DFIG control system can be simplified by ignoring the electromagnetic transient process.

Under the reference coordinate system of stator flux linkage orientation, the *d*-*q* axis voltage and flux linkage have the following constraints:

$$\begin{cases} v_{ds} = 0 \\ v_{qs} = -u_1 \\ \varphi_{ds} = \varphi_1 \\ \varphi_{qs} = 0 \end{cases} \tag{13}$$

Under operation, the voltage dip of the stator resistance is far less than the reactance voltage dip and counter electromotive force. Therefore, the stator resistance of the motor can be ignored. By substituting $R_s = 0$ and Equation (13) into Equations (4)–(5) we yield [16]:

$$\begin{gathered} \begin{bmatrix} \frac{di_{dr}}{dt} \\ \frac{di_{qr}}{dt} \end{bmatrix} = \begin{bmatrix} \frac{R_r L_s}{L_m^2 - L_s L_r} & \omega_1 \\ -\omega_1 & \frac{R_r L_s}{L_m^2 - L_s L_r} \end{bmatrix} \begin{bmatrix} i_{dr} \\ i_{qr} \end{bmatrix} + \omega \begin{bmatrix} 0 & -1 \\ 1 & 0 \end{bmatrix} \begin{bmatrix} i_{dr} \\ i_{qr} \end{bmatrix} + \\ \frac{L_s}{L_m^2 - L_s L_r} \begin{bmatrix} -1 & 0 \\ 0 & -1 \end{bmatrix} \begin{bmatrix} v_{dr} \\ v_{qr} \end{bmatrix} + \frac{L_m \varphi_1 (\omega_1 - \omega)}{L_m^2 - L_s L_r} \begin{bmatrix} 0 \\ 1 \end{bmatrix} \end{gathered} \tag{14}$$

where $\varphi_1 = -u_1/\omega_1$.

The dynamic characteristics of a DFVSPSPS are only related to the active power regulation. Therefore, under decoupling control, the grid voltage and the *d*-axis current can be considered constant. Consequently, in the study of stability and dynamic characteristics of DFVSPSPS, only the change of *q*-axis current is considered. For Equation (14), the equation for change of *q*-axis current can be obtained when the change of the d-axis current is ignored [16]:

$$\frac{di_{qr}}{dt} = \frac{R_r L_s}{L_m^2 - L_s L_r} i_{qr} - \frac{L_s}{L_m^2 - L_s L_r} v_{qr} + (\omega_1 - \omega)\left(\frac{L_m \varphi_1}{L_m^2 - L_s L_r} - i_{dr}\right) \tag{15}$$

The simplified model of DFIG can be obtained by combining Equations (6) and (15):

$$\begin{cases} \frac{di_{qr}}{dt} = \frac{R_r L_s}{L_m^2 - L_s L_r} i_{qr} - \frac{L_s}{L_m^2 - L_s L_r} v_{qr} + (\omega_1 - \omega)\left(\frac{L_m \varphi_1}{L_m^2 - L_s L_r} - i_{dr}\right) \\ T_e = -1.5 n_p \varphi_1 \frac{L_m}{L_s} i_{qr} \\ \frac{d\omega}{dt} = \frac{n_p}{J}(T_e - T_m) \end{cases} \tag{16}$$

The response time of the electromagnetic transient is far less than the electromechanical transient process. Therefore, the dynamic process of the converter and the inner current loop can be ignored. A simplified DFIG control system model can be obtained further by combining Equations (8), (10) and (16):

$$\begin{cases} \dot{x}_1 = p + \frac{3 n_p \varphi_1 L_m \omega_0}{2 L_s} i_{qr} + \frac{3 I_{qr0} n_p \varphi_1 L_m}{2 L_s} \omega + \frac{3 n_p \varphi_1 L_m}{2 L_s} \omega i_{qr} \\ \dot{i}_{qr} = -\frac{L_s}{L_m}\left(K_{p1} \dot{x}_1 + K_{i1} x_1\right) \\ \dot{\omega} = \frac{1}{T_a}\left(m_t + \frac{3 n_p \varphi_1 L_m}{2 L_s} i_{qr}\right) \end{cases} \tag{17}$$

2.3. Mechanical System

The governor is the core control component of the DFVSPSPS and consists of the controller and servosystem, which is mainly used to regulate the frequency, guide vane opening and power of a pump turbine. The traditional proportional-integral-derivative (PID) controller is used in the governor of a DFVSPSPS. The transfer function of the PID is defined as [25]:

$$G_{PID}(s) = K_P + \frac{K_I}{s} + K_D s \tag{18}$$

The servosystem is the actuator of the governor, which is used to convert the electrical signal from the controller output into a mechanical signal to provide power to operate the guide vane. The servosystem can be described by a typical first-order transfer function:

$$\frac{y(s)}{\sigma(s)} = \frac{1}{1 + T_y(s)} \tag{19}$$

The mechanical system consists of pump turbine and governor. The model for a pump turbine can be defined as a moment function and a flow function of guide vane opening, generator speed and water head, shown as follows [26]:

$$\begin{cases} M_t = f_t(\alpha, n, H) \\ Q = f(\alpha, n, H) \end{cases} \tag{20}$$

For small perturbation in the neighborhood of a steady-state operating point, the nonlinear pump turbine model shown in Equation (20) can be approximated as a linear model by using the Taylor series expansion without considering higher-order terms. Equation (20) can be rewritten as:

$$\begin{cases} \Delta M_t = \frac{\partial M_t}{\partial \alpha} \Delta\alpha + \frac{\partial M_t}{\partial n} \Delta n + \frac{\partial M_t}{\partial H} \Delta H \\ \Delta Q = \frac{\partial Q}{\partial \alpha} \Delta\alpha + \frac{\partial Q}{\partial n} \Delta n + \frac{\partial Q}{\partial H} \Delta H \end{cases} \tag{21}$$

The relative values of the above equations are obtained:

$$\begin{cases} \frac{\Delta M_t}{M_r} = \frac{\frac{\partial M_t}{M_r}}{\partial \frac{\alpha}{\alpha_{\max}}} \frac{\Delta\alpha}{\alpha_{\max}} + \frac{\frac{\partial M_t}{M_r}}{\partial \frac{n}{n_r}} \frac{\Delta n}{n_r} + \frac{\frac{\partial M_t}{M_r}}{\partial \frac{H}{H_r}} \frac{\Delta H}{H_r} \\ \frac{\Delta Q}{Q_r} = \frac{\frac{\partial Q}{Q_r}}{\partial \frac{\alpha}{\alpha_{\max}}} \frac{\Delta\alpha}{\alpha_{\max}} + \frac{\frac{\partial Q}{Q_r}}{\partial \frac{n}{n_r}} \frac{\Delta n}{n_r} + \frac{\frac{\partial Q}{Q_r}}{\partial \frac{H}{H_r}} \frac{\Delta H}{H_r} \end{cases} \tag{22}$$

Meanwhile, the six transfer coefficients are defined as follows:

$$\begin{cases} e_y = \frac{\partial M_t}{\partial \frac{\alpha}{\alpha_{\max}}} \frac{M_r}{} & e_x = \frac{\partial M_t}{\partial \frac{n}{n_r}} \frac{M_r}{} & e_h = \frac{\partial M_t}{\partial \frac{H}{H_r}} \frac{M_r}{} \\ e_{qy} = \frac{\partial Q}{\partial \frac{\alpha}{\alpha_{\max}}} \frac{Q_r}{} & e_{qx} = \frac{\partial Q}{\partial \frac{n}{n_r}} \frac{Q_r}{} & e_{qh} = \frac{\partial Q}{\partial \frac{H}{H_r}} \frac{Q_r}{} \end{cases} \tag{23}$$

Thus, Equation (22) can be expressed as [27,28]:

$$\begin{cases} m_t = e_y y + e_x \omega + e_h h \\ q = e_{qy} y + e_{qx} \omega + e_{qh} h \end{cases} \tag{24}$$

where six transfer coefficients of pump turbine e_x, e_y, e_h, e_{qx}, e_{qy} and e_{qh} are the partial derivatives of the torque and flow concerning speed n, guide vane opening y and water head h, respectively [29].

The mathematical model of the DFVSPSPS system not only includes the description of the dynamic characteristics of each component of the system, but also includes the control strategy, which is composed of Equations (1)–(3), Equations (17)–(19) and Equation (24). The control block diagram of the DFVSPSPS is shown in Figure 2.

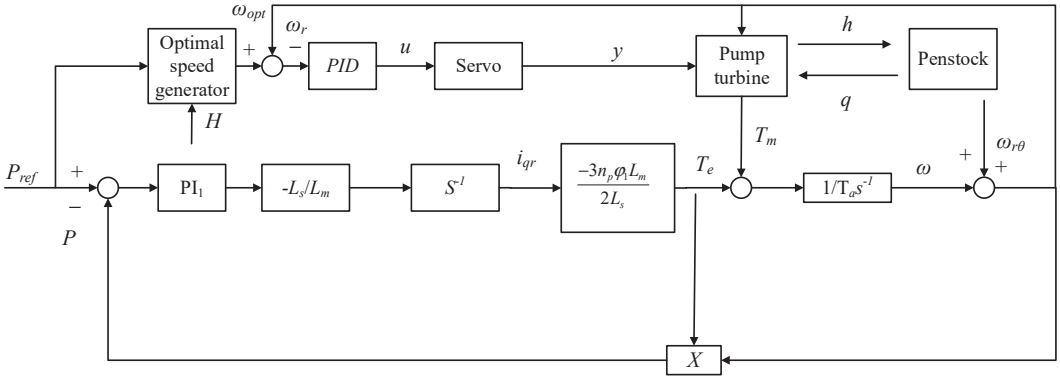

Figure 2. Control block diagram of the DFVSPSPS.

As shown in Figure 2, the optimal speed ω_{opt} is obtained from the power reference value P_{ref} and head h through the optimal speed generator, and the pump turbine can operate under the optimal working conditions. The control signal u of PID controller can be obtained from the difference between the optimal speed ω_{opt} and the real-time speed ω. The guide vane opening y can then be obtained through the hydraulic servosystem to control the mechanical torque of the hydraulic turbine unit. The rotor side controls the active output of the generator according to the difference between the power reference value P_{ref} and the real-time power P. The speed optimization of the optimal speed generator is used to obtain the optimal speed under different power reference value P_{ref} and head h.

Therefore, according to the control block diagram of the system, the state space equation of the DFVSPSPS can be obtained from Equation (25):

$$\begin{cases} \dot{q}_H = \frac{1}{T_{wH}} h_s - \frac{2h_{H0}}{T_{wH} H_0} q_H \\ \dot{h}_s = \frac{1}{T_F} \left(e_{qh} h + e_{qx} \omega + e_{qy} y - q_H \right) \\ \dot{h} = \frac{1}{e_{qh}} \left(-e_{qx} \dot{\omega} - e_{qy} \dot{y} - \frac{1}{T_w} h - \frac{1}{T_w} h_s \right) \\ \dot{x}_1 = p + \frac{3 n_p \varphi_1 L_m \omega_{r0}}{2 L_s} i_{qr} + \frac{3 i_{qr0} n_p \varphi_1 L_m}{2 L_s} \omega + \frac{3 n_p \varphi_1 L_m}{2 L_s} \omega i_{qr} \\ \dot{i}_{qr} = -\frac{L_s}{L_m} \left(k_{p1} \dot{x}_1 + k_{i1} x_1 \right) \\ \dot{\omega} = \frac{1}{T_a} \left(e_x \omega + e_y y + e_h h + \frac{1.5 n_p \varphi_1 L_m}{L_s} i_{qr} \right) \\ \dot{y} = \frac{1}{T_y} \left(k_p \dot{z} + k_i z - k_d \dot{\omega} - y \right) \\ \dot{z} = ap - \omega \end{cases} \tag{25}$$

Equation (25) is an eighth-order state equation with eight state variables, q_H, h_s, h, x_1, i_{qr}, ω, y and z. When the six transfer coefficients of pump turbine e_x, e_y, e_h, e_{qx}, e_{qy} and e_{qh} are considered as constants, the pump turbine is a linear model. The six transfer coefficients can be obtained from the model synthetic characteristic curve of the pump turbine. The synthetic characteristic curve of the pump turbine is shown in Figure 3. To calculate the six transfer coefficients in a certain steady operating point 0, the four neighboring operating points should be determined. In Figure 3, points 1 and 2 are located on the equal speed curve and points 3 and 4 are located on the equal guide vane opening curve. The six transfer coefficients can be defined as:

$$\begin{cases} e_x = \frac{(M_4 - M_3)/M_r}{(n_4 - n_3)/n_r} & e_y = \frac{(M_2 - M_1)/M_r}{(\alpha_2 - \alpha_1)/\alpha_{\max}} & e_h = \frac{(M_4 - M_3)/M_r}{(H_4 - H_3)/H_r} \\ e_{qx} = \frac{(Q_4 - Q_3)/Q_r}{(n_4 - n_3)/n_r} & e_{qx} = \frac{(Q_2 - Q_1)/Q_r}{(\alpha_2 - \alpha_1)/\alpha_{\max}} & e_{qh} = \frac{(Q_4 - Q_3)/Q_r}{(H_4 - H_3)/H_r} \end{cases} \tag{26}$$

$$\begin{cases} M = M_{11} D_1^3 H \\ Q = Q_{11} D_1^2 \sqrt{H} \\ n = n_{11i} \sqrt{H} / D_1 \\ H_i = \left(\frac{n D_1}{n_{11}} \right)^2 \end{cases} \tag{27}$$

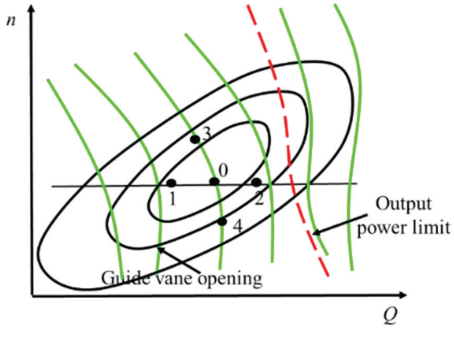

Figure 3. The synthetic characteristic curve of a pump turbine.

From the above analysis, it can be seen that the values of six transfer coefficients are dependent on the steady operating condition point and characteristic curve of the pump turbine.

In the above mathematical model of DFVSPSPS shown in Equation (25), the six coefficients are considered as constants. However, during the transient process, the system parameters and operating condition point will change. Therefore, the values of transfer coefficients of the pump turbine will change. Therefore, there are some limitations and inaccuracies in the analysis of stability and dynamic characteristic of DFVSPSPS based on the linear pump turbine model, resulting in a large deviation in the calculation results.

Considering the nonlinear characteristics of the pump turbine reflected by the changing six transfer coefficients with the change of operating conditions, the pump turbine nonlinear model should be deduced to analyze and reveal the influence of nonlinear pump turbine characteristics on the stability and dynamic characteristics of DFVSPSPS.

In the following paragraphs e_y is taken as an example to illustrate the derivation process of the nonlinear analytical expression [30].

$$\begin{array}{l} e_y = \frac{(M_2-M_1)/M_r}{(\alpha_2-\alpha_1)/\alpha_{\max}} = \frac{\left(M_{112}D_1^3H-M_{111}D_1^3H\right)/M_{11r}D_1^3H_r}{(\alpha_2-\alpha_1)/\alpha_{\max}} \\ = \frac{(M_{112}-M_{111})/M_{11r}}{(\alpha_2-\alpha_1)/\alpha_{\max}}\frac{H}{H_r} = e_{y0}(h+1) \end{array} \tag{28}$$

By using the same method, we can get [30]:

$$\left\{ \begin{array}{l} e_{qy} = \frac{(Q_2-Q_1)/Q_r}{(\alpha_2-\alpha_1)/\alpha_{\max}} = e_{qy0}\sqrt{h+1} \\ e_x = \frac{(M_4-M_3)/M_r}{(n_4-n_3)/n_r} = e_{x0}\sqrt{h+1} \\ e_{qx} = \frac{(Q_4-Q_3)/Q_r}{(n_4-n_3)/n_r} = e_{qx0} \\ e_h = \frac{(M_4-M_3)/M_r}{(H_4-H_3)/H_r} = e_{h0} \\ e_{qh} = \frac{(Q_4-Q_3)/Q_r}{(H_4-H_3)/H_r} = e_{qh0}\frac{1}{\omega+1} \end{array} \right. \tag{29}$$

Then the nonlinear pump turbine model can be obtained:

$$\left\{ \begin{array}{l} m = e_{h0}h + e_{x0}\sqrt{h+1}\omega + e_{y0}(h+1)y \\ q = e_{qh0}\frac{1}{\omega+1}h + e_{qx0}\omega + e_{qy0}\sqrt{h+1}y \end{array} \right. \tag{30}$$

From Equation (30), we can find that the moment equation and discharge equation are nonlinear and the six transfer coefficients can change with the head and speed. Therefore, the nonlinear pump turbine characteristics consist of nonlinear head characteristics and nonlinear speed characteristics. Considering the nonlinear pump turbine characteristics, a novel nonlinear DFVSPSPS is established in Equation (31):

$$\left\{ \begin{array}{l} \dot{q}_H = \frac{1}{T_{wH}}h_s - \frac{2h_{H0}}{T_{wH}H_0}q_H \\ \dot{h}_s = \frac{1}{T_F}\left(\frac{e_{qh0}}{\omega+1}h + e_{qx0}\omega + e_{qy0}\sqrt{h+1}y - q_H\right) \\ \dot{x}_1 = p + \frac{3n_p\varphi_1L_m\omega_{r0}}{2L_s}i_{qr} + \frac{3i_{qr0}n_p\varphi_1L_m}{2L_s}\omega + \frac{3n_p\varphi_1L_m}{2L_s}\omega i_{qr} \\ \dot{i}_{qr} = -\frac{K_{i1}L_sx_1}{L_m} - \frac{pK_{p1}L_s}{L_m} - 1.5K_{p1}n_p\varphi_1\omega_{ro}i_{qr} - 1.5K_{p1}n_p\varphi_1\omega i_{qr} - 1.5K_{p1}n_p\varphi_1i_{qr0}\omega \\ \dot{\omega} = \frac{1}{T_a}\left(e_{x0}\sqrt{h+1}\omega + e_{y0}(h+1)y + e_{h0}h + \frac{1.5n_p\varphi_1L_m}{L_s}i_{qr}\right) \\ \dot{y} = \left(-\frac{1}{T_y} - \frac{e_{y0}(h+1)K_d}{T_aT_y}\right)y + \left(-\frac{e_{x0}\sqrt{h+1}K_d}{T_aT_y} - \frac{K_p}{T_y}\right)\omega - \frac{e_{h0}K_d}{T_aT_y}h + \frac{K_i}{T_y}z - \frac{1.5K_dL_mn_p\varphi_1}{T_aL_sT_y}i_{qr} + \frac{apK_p}{T_y} \\ \dot{z} = ap - \omega \\ \dot{h} = \left(\frac{K_de_{h0}e_{qy0}\sqrt{h+1}}{T_ae_{qh0}T_y} - \frac{e_{h0}e_{qx0}}{T_ae_{qh0}} - \frac{1}{T_we_{qh0}}\right)(\omega+1)h + \left(\frac{1.5\varphi_1K_de_{qy0}\sqrt{h+1}L_mn_p}{T_ae_{qh0}L_sT_y} - \frac{1.5\varphi_1e_{qx0}L_mn_p}{T_ae_{qh0}L_s}\right)(\omega+1)i_{qr} \\ + \left(\frac{K_de_{qy0}\sqrt{h+1}e_{x0}\sqrt{h+1}}{T_ae_{qh0}T_y} + \frac{e_{qy0}\sqrt{h+1}K_p}{e_{qh0}T_y} - \frac{e_{qx0}e_{x0}\sqrt{h+1}}{T_ae_{qh0}}\right)(\omega+1)\omega \\ + \left(\frac{K_de_{qy0}\sqrt{h+1}e_{y0}(h+1)}{Tae_{qh0}T_y} - \frac{e_{qx0}e_{y0}(h+1)}{T_ae_{qh0}} + \frac{e_{qy0}\sqrt{h+1}}{e_{qh0}T_y}\right)(\omega+1)y \\ - \frac{e_{qy0}\sqrt{h+1}K_i}{e_{qh0}T_y}(\omega+1)z - \frac{1}{T_we_{qh0}}(\omega+1)h_s - \frac{ape_{qy0}\sqrt{h+1}K_p}{e_{qh0}T_y}(\omega+1) \end{array} \right. \tag{31}$$

3. Stability Analysis of DFVSPSPS

3.1. Hopf Bifurcation Theory

Hopf bifurcation theory is an effective method of investigating the stability of nonlinear systems, whose basic concept is described below [31,32].

For a nonlinear system expressed by differential equations $\dot{x} = f(x, \mu)$, x is the state vector and is the bifurcation parameter. The equilibrium point x_E of the system can be

found by setting $\dot{\boldsymbol{x}} = 0$. The Jacobian matrix of the system at the equilibrium point x_E can be obtained as $\boldsymbol{J}(\mu) = \boldsymbol{D}f_{\boldsymbol{x}}(\boldsymbol{x}_E, \mu)$, whose characteristic equation $\det(\boldsymbol{J}(\mu) - \lambda \boldsymbol{I}) = 0$ is:

$$a_0(\mu)\lambda^n + a_1(\mu)\lambda^{n-1} + \ldots + a_{n-2}(\mu)\lambda^2 + a_{n-1}(\mu)\lambda + a_n(\mu) = 0 \tag{32}$$

where $a_i(\mu)(i = 1, 2, \ldots, n)$ are the coefficients of characteristic equation and λ is the eigenvalue.

If the following conditions are met, the nonlinear system will achieve Hopf bifurcation [27]:

(i) $a_i(\mu_c) > 0 (i = 1, 2, \ldots, m)$

(ii) $\Delta_i(\mu_c) > 0 (i = 1, 2, \ldots, m-2), \Delta_{n-1}(\mu_c) = 0$

$$\Delta_j(\mu_c) = \begin{vmatrix} a_1 & 1 & 0 & \cdots & 0 \\ a_3 & a_2 & a_1 & \cdots & 0 \\ a_5 & a_4 & a_3 & \cdots & 0 \\ \vdots & \vdots & \vdots & \ddots & \vdots \\ a_{2j-1} & a_{2j-2} & a_{2j-3} & \cdots & a_j \end{vmatrix} \cdot (j = 1, 2, \ldots, m-1)$$

(iii) $\sigma'(\mu_c) = \mathrm{Re}\left(\frac{\mathrm{d}\lambda}{\mathrm{d}\mu}\big|_{\mu=\mu_c}\right) \neq 0$

If the bifurcation parameter $\mu = \mu_c$ satisfies the above conditions, then $\mu = \mu_c$ is the bifurcation point of the system. At $\mu = \mu_c$, the dynamic response of the system will oscillate periodically, and the phase space trajectory is a stable limit cycle. In addition, the type of bifurcation can be determined by the transversal coefficient $\sigma'(\mu_c)$. If $\sigma'(\mu_c) > 0$, the occurred Hopf bifurcation is supercritical and the system is stable when $\mu < \mu_c$. If $\sigma'(\mu_c) > 0$, the occurred Hopf bifurcation is subcritical and the system is stable when $\mu > \mu_c$.

3.2. Hopf Bifurcation Analysis of DFVSPSPS

For the eighth-order DFVSPSPS nonlinear model described by Equation (31) in this paper, the equilibrium point $x_E = (h_{sE}, q_{HE}, x_{1E}, i_{qrE}, \omega_E, y_E, z_E)$ can be obtained by setting:

$$\begin{cases} h_{sE} = -h_E \\ q_{HE} = \frac{-h_E H_0}{2h_{H0}} \\ x_{1E} = 0 \\ i_{qrE} = -\frac{L_s p}{1.5 n_p \varphi_1 L_m (\omega_{r0} + ap)} - \frac{ap I_{qr0}}{\omega_{r0} + ap} \\ \omega_E = ap \\ y_E = -\frac{1.5 n_p \varphi_1 L_m}{L_s e_{y0}(h_E+1)} i_{qrE} - \frac{e_{x0}\sqrt{h_E+1}\omega_E}{e_{y0}(h_E+1)} - \frac{e_{h0} h_E}{e_{y0}(h_E+1)} \\ z_E = \frac{y_E}{K_i} \end{cases} \tag{33}$$

Then the Jacobian matrix of the system $\dot{x} = f(x, \mu)$ at the equilibrium point x_E can be obtained and the detailed expression of $\boldsymbol{D}f_x(\boldsymbol{x}_E, \mu)$ is presented in Appendix B. The characteristic equation $\boldsymbol{J}(\mu)$ is:

$$a_0\lambda^8 + a_1\lambda^7 + a_2\lambda^6 + a_3\lambda^5 + a_4\lambda^4 + a_5\lambda^3 + a_6\lambda^2 + a_7\lambda + a_8 = 0 \tag{34}$$

$$\begin{cases} a_i > 0 \ (i = 1, 2, \ldots, 8), \Delta_i > 0 \ (i = 1, 2, \ldots, 7), \Delta_7 = 0 \\ \sigma'(\mu_c) \neq 0 \end{cases} \tag{35}$$

3.3. Stable Region of DFVSPSPS

The Hopf bifurcation criteria for DFVSPSPS has been obtained in Section 3.2 as shown in Equation (35). The bifurcation line can be obtained by solving Equation (35), which consists of all bifurcation points on the parameter plane and divides the whole parameter plane into a stable region and an unstable region. The stable region of DFVSPSPS can be determined based on the bifurcation line and transversal coefficient $\sigma'(\mu_c)$. In this section,

an actual DFVSPSPS is taken as a specific engineering example to present the application procedures of Hopf bifurcation analysis of DFVSPSPS. The stable region and dynamic response of DFVSPSPS can be clarified, and the essence and laws of stability of DFVSPSPS can be revealed based on the example analysis. The basic parameters of the DFVSPSPS are shown in Table 1.

Table 1. Parameters of the DFVSPSPS.

Parameters	Values	Parameters	Values
H_0	43.45	T_a	9.46
h_{H0}	3.8	a	0.373
T_{wH}	42.8	p	0.1
T_w	1.8	L_m	2.9
T_F	1500	L_s	3.08
e_x	−1	n_p	7
e_y	1	φ_1	1.0
e_h	1.5	ω_0	1.022
e_{qx}	0	i_{qr0}	−0.099

The governor parameters K_p, K_i and K_d are the important variables and are closely related to the stability and dynamic characteristic of the DFVSPSPS. Therefore, the K_p-K_i plane is selected as the parameter plane and K_d is considered as a constant. Usually, K_p is chosen as the abscissa, K_i is chosen as the ordinate and the bifurcation parameter. For a given value of K_p, the value of K_i can be obtained by Equation (35).

In actual applications, the stable region of DFVSPSPS is determined by the following procedure:

Step 1: For a specific engineering example of DFVSPSPS, the equilibrium point of the system (Equation (31)) is calculated based on Equation (33);

Step 2: Calculate the Jacobian matrix of the system at the equilibrium point;

Step 3: Calculate the coefficients of the characteristic equation of the Jacobian matrix;

Step 4: For a value of K_p, calculate the corresponding bifurcation parameter K_i using Equation (35)

Step 5: For all the values of K_p, the repetition of Step 4 yields all the bifurcation points. The bifurcation line is then determined.

Step 6: Calculate the transversal coefficient $\sigma'(\mu_c)$ for all the bifurcation points. The type of emerged Hopf bifurcation can then be determined.

The step disturbance of power is applied to excite the system, and the bifurcation line of the system can be determined based on the above six steps. The results are shown in Figure 4. Meanwhile, according to the obtained bifurcation points and the aforementioned definition of $\sigma'(\mu_c)$, the corresponding transversal coefficients $\sigma'(\mu_c)$ are calculated and shown in Figure 5.

From Figure 4, we can see that the bifurcation line is a smooth curve, and the controller parameter K_I of the bifurcation line presents a trend of first slowly increasing and then rapidly decreasing with the increase of K_P. The K_P-K_I plane is divided into three parts, namely, the unstable region, stable region and critical stable region (bifurcation line). Figure 5 shows that the values of $\sigma'(\mu_c)$ are greater than zero, which indicates that the emerged Hopf bifurcation of DFVSPSPS is supercritical. Therefore, the region at the lower side of the bifurcation line is the stable region and the other side is the unstable region. The bifurcation line and stable region can quantificationally and intuitively reflect the stability and dynamic characteristics of DFVSPSPS.

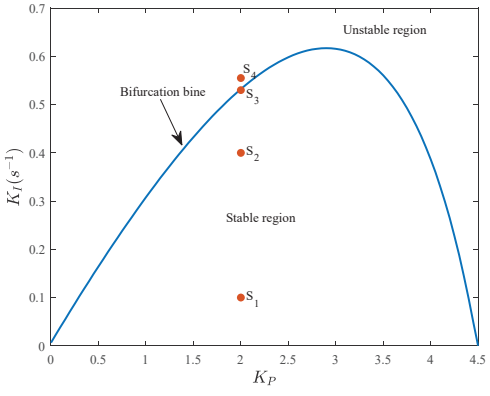

Figure 4. Stable region of the DFVSPSPS.

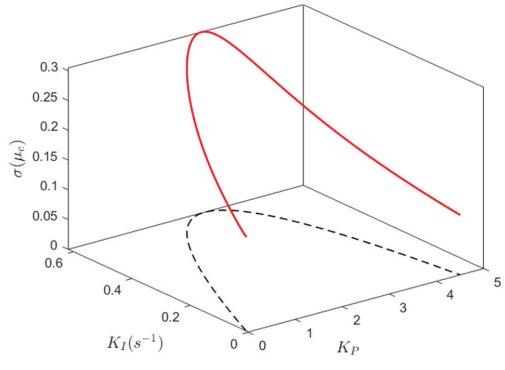

Figure 5. Values of $\sigma'(\mu_c)$ corresponding to the bifurcation line.

3.4. Numerical Simulation and Verification of Stability

To verify the correctness of the obtained stable region in Section 3.3, and investigate the dynamic characteristic of DFVSPSPS under different governor parameter values, there are three points S_1, S_2 and S_3 in Figure 4 which were selected as the representatives for numerical simulation of the dynamic response S_1 and S_2 are located within the stable region, S_3 is located on the bifurcation line and S_3 is located within the unstable region. To reflect the changes of state variables more intuitively, the phase space trajectories are also presented.

The Runge-Kutta method can be used to solve the nonlinear derivative equations of DFVSPSPS for numerical simulation, and the dynamic response process of the state variables x, y, and ω under the four points S_1, S_2, S_3 and S_4 are calculated, as shown in Figure 6. The corresponding phase space trajectories are shown in Figure 7. From Figures 6 and 7, we can conclude that the numerical simulation results are consistent with the Hopf bifurcation theory analysis. For the stable state points S_1 and S_2, the dynamic responses of state variables present a damped oscillation and finally converge to a steady state. The phase space trajectories of S_1 and S_2 stabilize to the equilibrium point after several periods of damped attenuated motion. For the bifurcation point S_3, the dynamic responses gradually enter a constant amplitude oscillation after several periods of oscillation. The corresponding phase space trajectory of S_3 stabilizes at the limit cycle. For the unstable state point S_4, the dynamic responses are divergent oscillation, and its phase space trajectory enters a gradually divergent motion.

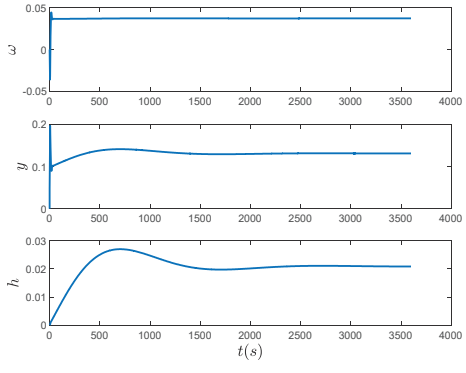

(**a**)

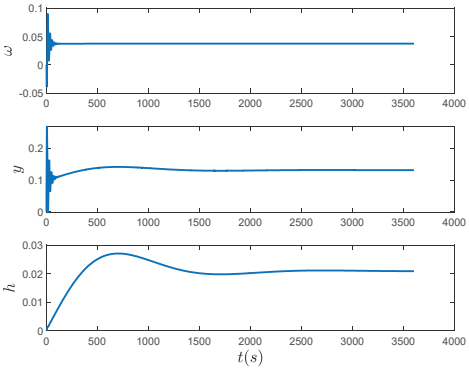

(**b**)

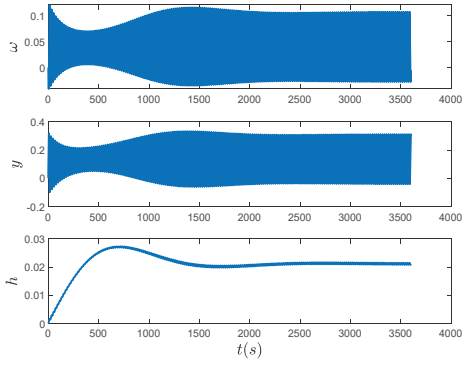

(**c**)

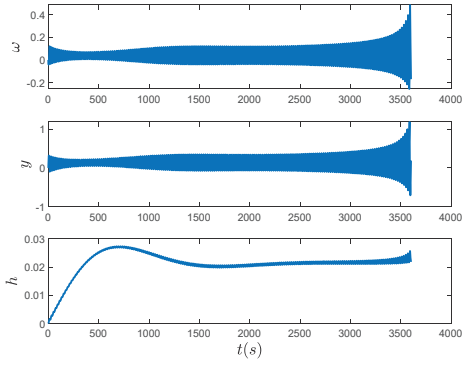

(**d**)

Figure 6. Dynamic responses of state variables x, y, ω for S_1, S_2, S_3 and S_4. (**a**) S_1; (**b**) S_2; (**c**) S_3; (**d**) S_4.

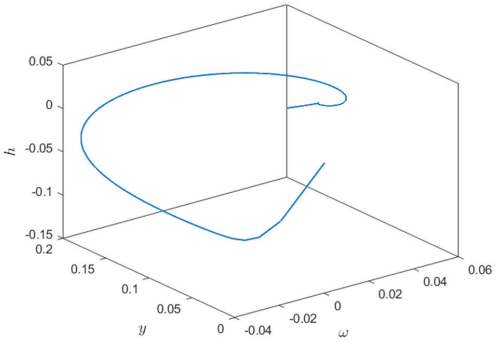

(**a**)

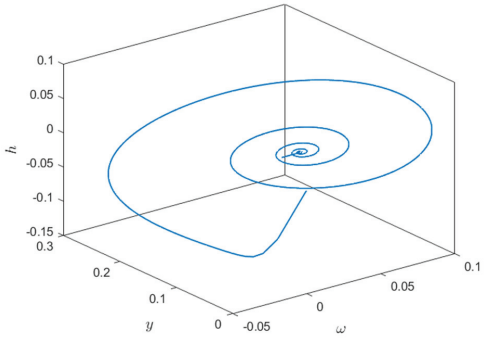

(**b**)

Figure 7. *Cont.*

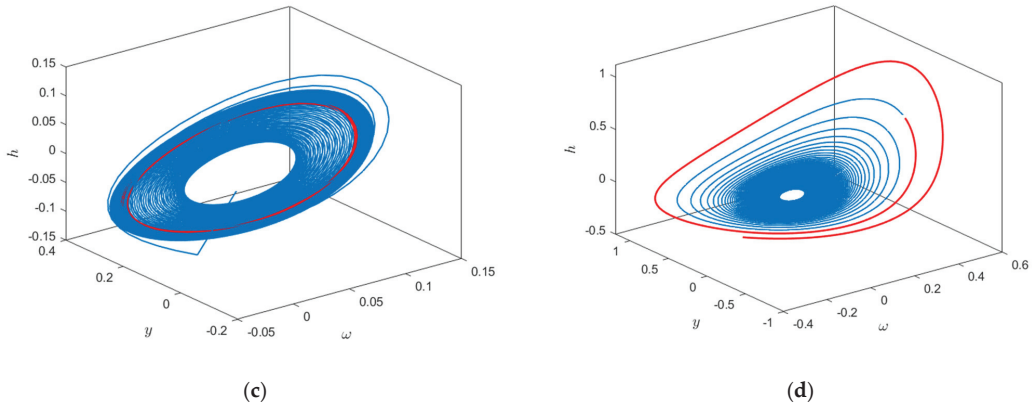

(**c**) (**d**)

Figure 7. Phase space trajectories of x, y, ω for S_1, S_2, S_3 and S_4. (**a**) S_1; (**b**) S_2; (**c**) S_3; (**d**) S_4.

4. Effect Mechanism of Nonlinear Pump Turbine Characteristics on Stability and Dynamic Characteristics

The stability and dynamic characteristics of DFVSPSPS have been investigated based on the engineering example in Section 3. In this section, we will focus on the effect mechanism of nonlinear pump turbine characteristics. In particular, the influence mechanism of nonlinear head characteristics and nonlinear speed characteristics on stability and dynamic characteristics of the DFVSPSPS are revealed.

A contrastive analysis is used to explore the effect mechanism of nonlinear head characteristics and nonlinear speed characteristics. Equation (30) is the nonlinear pump turbine model including nonlinear head characteristics and nonlinear speed characteristics, which is denoted as Model A. If nonlinear speed characteristics are ignored, the model of DFVSPSPS is denoted as Model B, where $e_{qh0}/(\omega+1)$ is replaced by e_{qh0}. If the pump turbine only considers nonlinear head characteristics, the model of DFVSPSPS is denoted as Model C. The state equation can be obtained by replacing $e_{x0}\sqrt{h+1}$, $e_{y0}(h+1)$ and $e_{qy0}\sqrt{h+1}$ with e_{x0}, e_{y0} and e_{qy0}, respectively. If both nonlinear head characteristics and nonlinear speed characteristics are ignored then a linear pump turbine model can be denoted as Model D, where $e_{qh0}/(\omega+1)$, $e_{x0}\sqrt{h+1}$, $e_{y0}(h+1)$ and $e_{qy0}\sqrt{h+1}$ are replaced by e_{qh0}, e_{x0}, e_{y0} and e_{qy0}, respectively. The corresponding equations of pump turbines of Model B, Model C and Model D are presented as follows:

$$\text{Model B}: \begin{cases} m = e_{h0}h + e_{x0}\sqrt{h+1}\omega + e_{y0}(h+1)y \\ q = e_{qh0}h + e_{qx0}\omega + e_{qy0}\sqrt{h+1}y \end{cases} \tag{36}$$

$$\text{Model C}: \begin{cases} m = e_{h0}h + e_{x0}\omega + e_{y0}y \\ q = e_{qh0}\frac{1}{\omega+1}h + e_{qx0}\omega + e_{qy0}y \end{cases} \tag{37}$$

$$\text{Model D}: \begin{cases} m = e_{h0}h + e_{x0}\omega + e_{y0}y \\ q = e_{qh0}h + e_{qx0}\omega + e_{qy0}y \end{cases} \tag{38}$$

The stability and dynamic characteristics of DFVSPSPS under Model A have been analyzed in Section 3. The same stability analysis method can be used for Model B, Model C and Model D. Most research shows that the surge tank and the external disturbance have a significant influence on the stability of DFVSPSPS [19]. Therefore, different time constants of the surge tank and step load disturbance are considered, i.e., T_F = 1500 s, T_F =250 s, p = 0,1 and $p = -0.1$. The stable region and dynamic responses for Model A, Model B, Model C and Model D are shown in Figures 8 and 9.

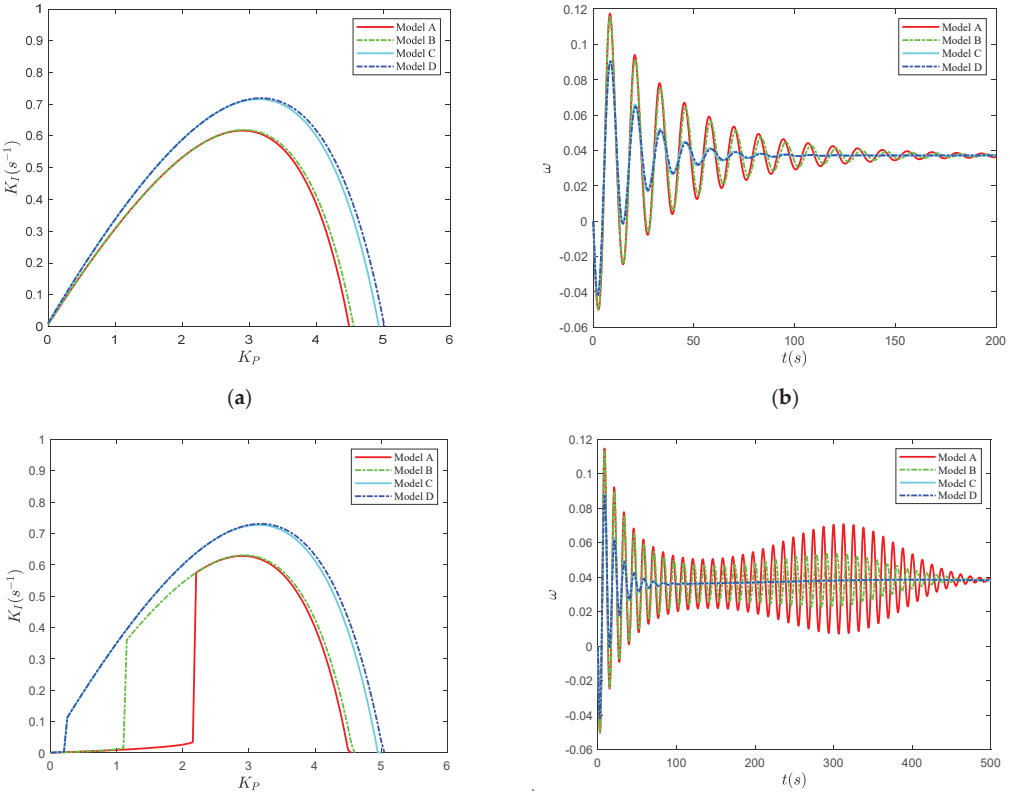

Figure 8. Stable region and dynamic responses of DFVSPSPS under p = 0.10: (**a**) T_F = 1500 s; (**b**) T_F = 1500 s; (**c**) T_F = 250 s; (**d**) T_F = 250 s.

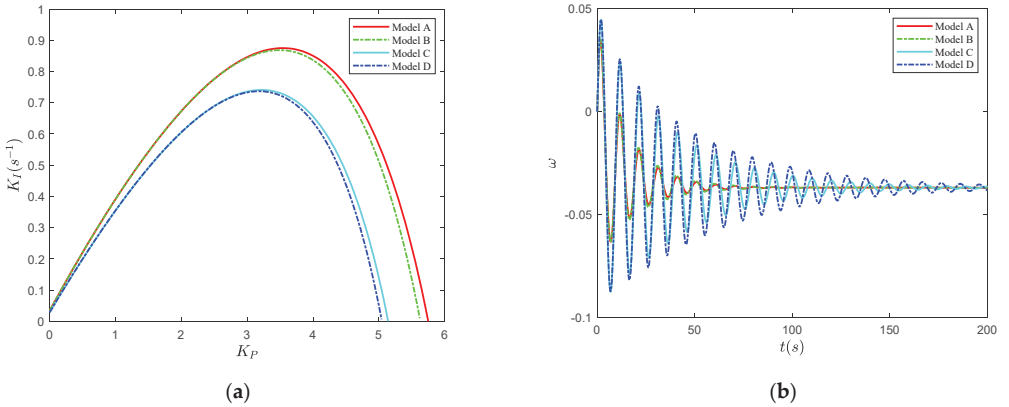

Figure 9. *Cont.*

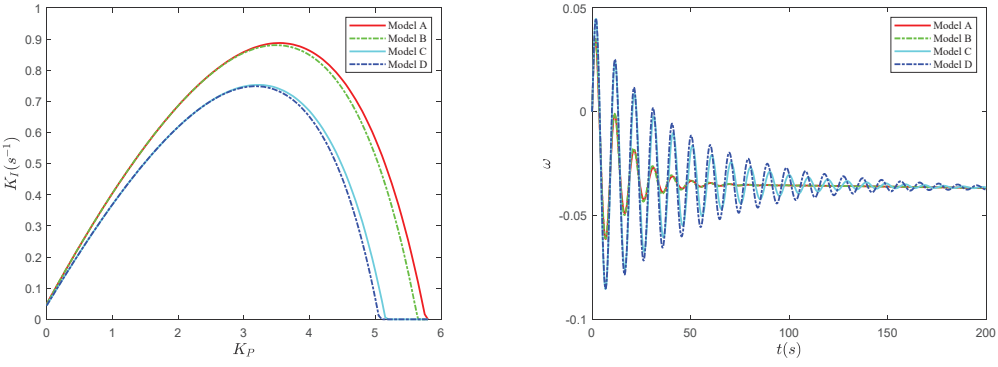

(**c**) (**d**)

Figure 9. Stable region and dynamic responses of DFVSPSPS under $p = -0.10$: (**a**) T_F = 1500 s; (**b**) T_F = 1500 s; (**c**) T_F = 250 s; (**d**) T_F = 250 s.

Figures 8 and 9 show that:

1. When p = 0.1 and T_F = 1500 s, the stable regions of Model A and Model B are almost coincident. Similarly, the stable regions of Model C and Model D are almost coincident. Moreover, the stable regions of Model A and Model B are significantly smaller than those of Model C and Model D. Therefore, under p = 0.1 and T_F = 1500 s, we can see that nonlinear speed characteristics have almost no effect on stability, but nonlinear head characteristics have a significant effect on stability. Therefore, nonlinear pump turbine characteristics are mainly realized by the nonlinear head and nonlinear head characteristics are unfavorable for the stability of DFVSPSPS. The same conclusion can be drawn for dynamic response. Nonlinear speed characteristics have almost no effect on dynamic response, but nonlinear head characteristics have a significant effect on dynamic response. Comparing the dynamic responses of Model A and Model C in Figure 8b, nonlinear head characteristics can increase the oscillation amplitude and prolong the stability time. Nonlinear head characteristics have a negative effect on the dynamic performance of DFVSPSPS.
2. For the DFVSPSPS under p = 0.1 and T_F = 250 s, the stable regions of Model A and Model B are obviously smaller than that under p = 0.1 and T_F = 1500 s. The stable regions of Model C and Model D are almost coincident with that under p = 0.1 and T_F = 1500 s. However, the stable region of Model A is obviously smaller than Model B. The results indicate that nonlinear head characteristics have a significant effect on stability. Nonlinear speed characteristics have no effect on stability when the pump turbine does not contain nonlinear head characteristics as seen by comparing the stable regions of Model C and Model D. However, nonlinear speed characteristics have an obvious effect on stability when the pump turbine model contains nonlinear head characteristics as seen by comparing the stable regions of Model A and Model B. Therefore, under p = 0.1 and T_F = 1500 s, nonlinear speed characteristics rely on nonlinear head characteristics. Nonlinear speed characteristics and nonlinear head characteristics are unfavorable for the stability of DFVSPSPS.
3. For the DFVSPSPS under $p = -0.1$ and T_F = 1500 s, the stable regions of Model A and Model B are almost coincident. The stable regions of Model C and Model D are also almost coincident. The stable region of Model C under p = 0.1 and T_F = 1500 s is the same as that under $p = -0.1$ and T_F = 1500 s. However, the stable regions of Model A and Model B are significantly larger than those of Model C and Model D. Therefore, under p $= -0.1$ and T_F = 1500 s, we can draw the same conclusion as that under p = 0.1 and T_F = 1500 s. Nonlinear speed characteristics have almost no

effect on the stability and dynamic characteristics, but nonlinear head characteristics have a significant effect on the stability and dynamic characteristics. Nonlinear pump turbine characteristics are mainly realized by the nonlinear head. Nonlinear head characteristics are favorable for the stability dynamic characteristics of DFVSPSPS. Moreover, external disturbance only has an obvious effect on the stability of Model A and Model B and has no effect on the stability of Model C and Model D. Therefore, the influence of external disturbance on stability relies on nonlinear head characteristics. From Figure 9, we can see that the results under T_F = 1500 s are the same as that under T_F = 250 s.

5. Analysis of Influence Factors on Stability of DFVSPSPS

The effect mechanism of nonlinear pump turbine characteristics on the stability and dynamic characteristics of DFVSPSPS was investigated in Section 4. In this section, the effect mechanism of influence factors of DFVSPSPS on the stability and dynamic characteristics are further explored. The analysis results clarify the effect mechanism of influence factors on the stability and dynamic characteristics of DFVSPSPS, and provide guidance for the improvement of stability and dynamic performance of DFVSPSPS. Five important parameters of DFVSPSPS, T_w, h_{H0}, T_a, p and T_F, were chosen as the influence factors. The different values of the five influence factors were considered, and the other parameters remained unchanged, as shown in Table 1. For each value of the influence factors, the stable region of DFVSPSPS was obtained and a state point under the stable region was chosen for numerical simulation of the dynamic response of ω. The stable region and dynamic response of DFVSPSPS are shown in Figures 10–14.

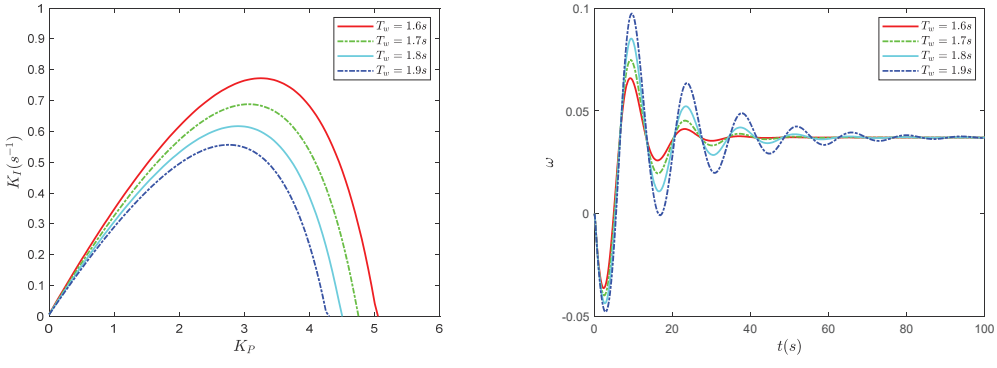

(**a**) (**b**)

Figure 10. Effect of T_w on stability and dynamic characteristics: (**a**) Stable region; (**b**) Dynamic response.

- Effect of T_w on stability and dynamic characteristics of DFVSPSPS

T_w was set as 1.6 s, 1.7 s, 1.8 s and 1.9 s, respectively. The stable regions and dynamic responses are shown in Figure 10. From Figure 10a, it can clearly be seen that T_w has a significant effect on stability. The stable region becomes obviously smaller as T_w increases. Therefore, a smaller T_w is favorable for the stability of DFVSPSPS. T_w also has a significant effect on the response process shown in Figure 10b. As T_w increases, the dynamic performance of DFVSPSPS becomes significantly worse.

- Effect of h_{H0} on stability and dynamic characteristics of DFVSPSPS

h_{H0} was set as 5 m, 6 m, 7 m and 8 m, respectively. The stable regions under different h_{H0} are shown in Figure 11a. Figure 11a shows that h_{H0} has an obvious effect on the stability of DFVSPSPS. The stable region becomes smaller as h_{H0} increases.Therefore, a

smaller h_{H0} is favorable for the stability of DFVSPSPS. However, from Figure 11b, the dynamic responses are coincident under different values of h_{H0}. Therefore, h_{H0} has almost no effect on the dynamic response of DFVSPSPS.

- Effect of T_a on stability and dynamic characteristics of DFVSPSPS

T_a was set as 7 s, 8 s, 9 s and 10 s, respectively. The stable regions and dynamic responses are shown in Figure 12. From Figure 12a, it can clearly be seen that T_a has a significant effect on stability. The stable region becomes obviously larger as T_a increases. Therefore, a larger T_a is favorable for the stability of DFVSPSPS. T_a also has a significant effect on the response as shown in Figure 12b. As T_a increases, the dynamic performance of DFVSPSPS becomes significantly improved.

- Effect of p on stability and dynamic characteristics of DFVSPSPS

p was set as -0.2, -0.1, 0.1 and 0.2, respectively. The stable regions and dynamic responses are shown in Figure 13. From Figure 13a, it can clearly be seen that p has a significant effect on stability. The stable region under $p < 0$ is larger than that under $p > 0$. Moreover, when $p < 0$, the stable region becomes obviously larger as p increases. However, when $p > 0$, the stable region becomes obviously smaller with increasing p. Therefore, a larger absolute value of p is favorable for the stability of DFVSPSPS.

p also has a significant effect on the response process of ω as shown in Figure 13b. When $p > 0$, the response process of ω first decreases and then increases. The oscillation amplitude becomes larger with increasing p. When $p < 0$, the response process of ω first increases and then decreases. The oscillation amplitude becomes larger with decreasing p. After several periods, the response process of ω stabilizes at a positive steady-state value. Therefore, the oscillation amplitude relies on the absolute value of p and the sign of the steady-state value depends on the sign of p.

- Effect of T_F on stability and dynamic characteristics of DFVSPSPS

T_F was set as 270 s, 280 s, 300 s, 350 s, 400 s and 1500 s, respectively. The stable regions under different T_F are shown in Figure 14a. Figure 14a shows that T_F has an obvious effect on the stability of DFVSPSPS when $T_F < 350$. The stable region becomes larger as T_F increases. However, when $T_F > 350$, the stable region keeps almost unchanged with increasing T_F. Therefore, a larger T_F is favorable for the stability of DFVSPSPS. However, from Figure 14b, the dynamic responses of ω are coincident under different values of T_F. Therefore, T_F has almost no effect on the dynamic responses of DFVSPSPS.

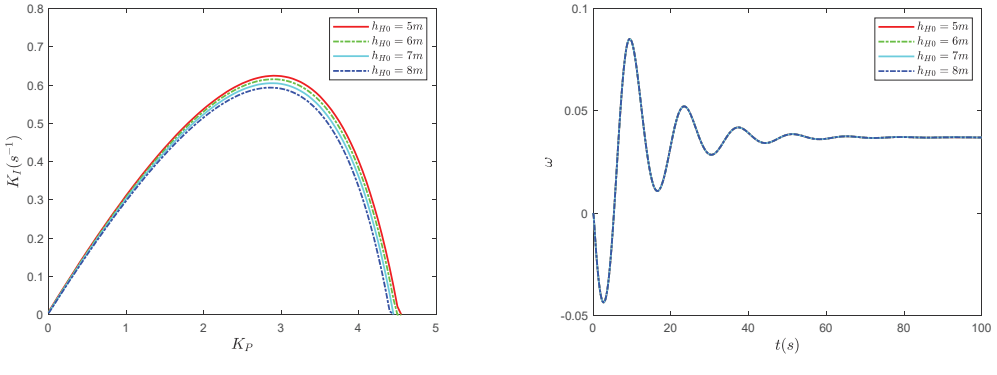

(**a**) (**b**)

Figure 11. Effect of h_{H0} on stability and dynamic characteristics: (**a**) Stable region; (**b**) Dynamic response.

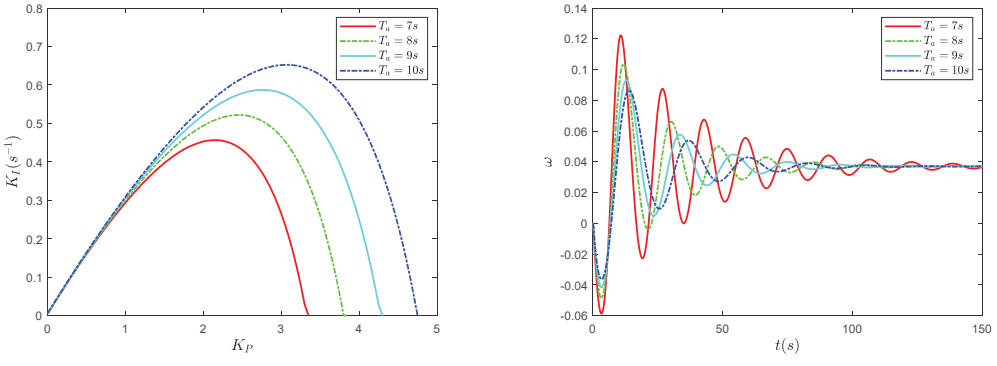

(**a**) (**b**)

Figure 12. Effect of T_a on stability and dynamic characteristics: (**a**) Stable region; (**b**) Dynamic response.

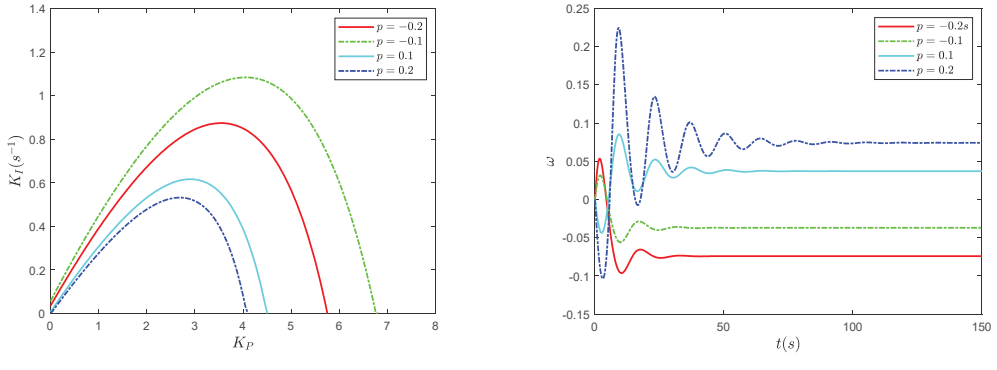

(**a**) (**b**)

Figure 13. Effect of p on stability and dynamic characteristics: (**a**) Stable region; (**b**) Dynamic response.

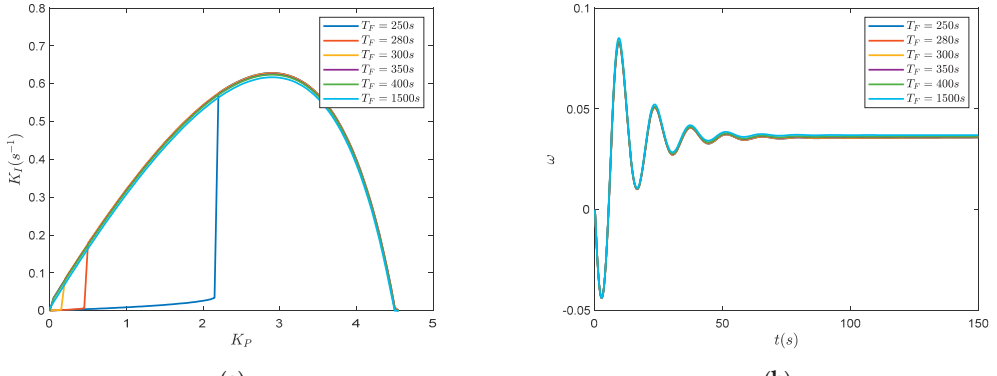

(**a**) (**b**)

Figure 14. Effect of T_F on stability and dynamic characteristics: (**a**) Stable region; (**b**) Dynamic response.

6. Conclusions

A novel nonlinear model of DFVSPSPS considering surge tank and nonlinear pump turbine characteristics was established. Hopf bifurcation analysis of the DFVSPSPS was carried out and the stability region was obtained. The effect mechanism of nonlinear pump turbine characteristics on the stability and dynamic characteristics of DFVSPSPS was studied. Finally, the influence factors on the stability and dynamic response of DFVSPSPS were analysed. The conclusions are as follows:

1. The mathematical model of the DFVSPSPS considering surge tank and nonlinear pump turbine characteristics is described by an eight-dimensional nonlinear state equation. The emerged Hopf bifurcation of DFVSPSPS is supercritical and the whole K_p-K_i plane is divided into two parts, where the region at the lower side of the bifurcation line is the stable region. This has been verified by numerical simulation.
2. Nonlinear head characteristics have a significant effect on the stability and dynamic characteristics of DFVSPSPS under all situations. However, nonlinear speed characteristics have obvious influence on the stability and dynamic characteristics of DFVSPSPS only under $p = 0.1$, $T_F = 250$ s due to the instability of the surge tank. Under other situations, nonlinear speed characteristics have no effect on the stability and dynamic characteristics of DFVSPSPS. The influence of nonlinear speed characteristics relies on nonlinear head characteristics. Nonlinear head characteristics are unfavorable for the stability of DFVSPSPS under positive load disturbance and favorable under negative load disturbance. The stable region of Model C and Model D are also almost coincident in all situations.
3. T_w has a significant influence on the stability and dynamic characteristics of DFVSPSPS. A smaller T_w is favorable for the stability and dynamic performance of DFVSPSPS. h_{H0} has a significant influence on stability but has no effect on the dynamic characteristics of DFVSPSPS. A smaller h_{H0} is favorable for the stability of DFVSPSPS. T_a has a significant influence on the stability and dynamic characteristics of DFVSPSPS. A greater T_a is favorable for the stability and dynamic performance of DFVSPSPS.
4. p has a significant effect on the stability of DFVSPSPS. The stable region under $p < 0$ is larger than that under $p > 0$. Under $p < 0$, the stable region becomes larger with increasing p. However, under $p > 0$, the stable region becomes smaller with increasing p. T_F has an obvious effect on the stability of DFVSPSPS and presents a saturation characteristic. Under $T_F < 350$the stable region becomes larger with increasing T_F. However, when $T_F > 350$, the stable region keeps almost unchanged with increasing T_F. Therefore, a larger T_F is favorable for the stability of DFVSPSPS. However, the T_F has almost no effect on the dynamic characteristics of DFVSPSPS.

A novel nonlinear mathematical model of DFVSPSPS considering surge tank and nonlinear pump turbine characteristics was established and stability was studied in this paper. However, there are still some limitations to the model of DFVSPSPS. There is only one pump turbine for one headrace tunnel considered in this paper, which is a simplified model. In an actual engineering application, in order to obtain a large water level drop and save project investment, the layout of the water conveyance system of PSPS mostly uses multiple units sharing one common tunnel. Additionally, there is hydraulic disturbance and interaction between different pump turbines for PSPS with multiple pump turbines. The hydraulic disturbance and interactions between different turbines have an obvious influence on the stability of PSPS. Therefore, a refined nonlinear model of the DFVSPSPS with a layout of multiple units sharing one common tunnel should be established and the stability needs to be investigated.

On the other hand, the specific nonlinearities in the governor system (delay, saturation, backlash and so on) are ignored in this paper and have a non-negligible impact on the stability and dynamic characteristics of DFVSPSPS. Therefore, it is necessary to consider the nonlinear characteristics of the governor and a more precise nonlinear mathematical model should be established to investigate the effect mechanism on the stability of system.

Author Contributions: Conceptualization, N.Z.; methodology, N.Z.; software, W.J.; validation, X.X.; formal analysis, Y.G.; investigation, W.J.; resources, N.S.; data curation, N.S.; project administration, C.L.; writing—original draft preparation, N.Z.; writing—review and editing, N.Z.; visualization, X.X.; supervision, N.Z.; funding acquisition, N.Z. All authors have read and agreed to the published version of the manuscript.

Funding: This work was supported by the Natural Science Foundation of Jiangsu Province (No. BK20201069, No. BK20201065), the National Natural Science Foundation of China (Grant No. 51709122), the Natural Science Foundation of the Jiangsu Higher Education Institutions of China (No. 20KJD480003) and the Major Program of National Natural Science Foundation of the Jiangsu Higher Education Institutions of China (No. 21KJA460010).

Conflicts of Interest: The authors declare no conflict of interest.

Appendix A

Nomenclature	
Q_H	discharge in headrace tunnel, m^3/s
Q	discharge in penstock, m^3/s
H_s	change of water level of surge tank, m
H	pump turbine net head, m
h_{H0}	head loss of headrace tunnel, m
T_{wH}	flow inertia time constant of headrace tunnel, s
T_F	time constant of surge tank, s
T_w	flow inertia time constant of penstock, s
M_t	kinetic moment
n	unit speed
α	guide vane opening
e_x, e_y, e_h	moment transfer coefficients of turbine
e_{qx}, e_{qy}, e_{qh}	discharge transfer coefficients of turbine
T_y	time constant of the servomotor
K_p, K_i, K_d	controller parameters of governor
v_{ds}, v_{qs}, v_{dr}, v_{qr}	d, q axis components of the stator and rotor voltage
i_{ds}, i_{qs}, i_{dr}, i_{qr}	d, q axis components of the stator and rotor current
φ_{ds}, φ_{qs}, φ_{dr}, φ_{qr}	d, q axis components of the stator and rotor flux
φ_1	the stator flux linkage
R_s, R_r	resistance of stator and rotor
ω_1	angular velocity of the synchronous rotation
ω	Unit speed
L_m	mutual inductance between the stator and rotor
L_s, L_r	self-inductance of the stator and rotor
T_a	unit inertia time constant
T_L, T_e	active torque and load torque of pump turbine
F	friction coefficient
n_p	number of pole pairs
i_{dr_ref}, i_{qr_ref}	d, q axis components of the rotor current reference
v_{dr_ref}, v_{qr_ref}	d, q axis components of the rotor voltage reference
v_{drc}, v_{qrc}	d, q axis voltage compensation of rotor
P, Q_d	active power and reactive power
P_{ref}, Q_{dref}	power reference
K_{p1}, K_{i1}, K_{p2}, K_{i2}, K_{p3}, K_{i3}, K_{p4}, K_{i4}	control parameters

Nomenclature	
s	Laplace operator
i_{dg_ref}, i_{qg_ref}	d, q axis current reference of grid-side
v_{dg_ref}, v_{qg_ref}	d, q axis voltage reference of grid-side
K_{p5}, K_{i5}, K_{p6}, K_{i6}, K_{p7}, K_{i7}, K_{p8}, K_{i8}	control parameters
v_{dc}, v_{dc_ref}	DC bus voltage and DC bus reference voltage
i_{dg}, i_{qg}	d, q axis current compensation of grid-side
Q_g, Q_{g_ref}	reactive power of grid side and reference value
u_1	grid voltage
x_1	intermediate variable

Definition of variates

$$\begin{cases} h_s = \frac{Hs-H_0}{H_r} & q_H = \frac{Q_H-Q_{H0}}{Q_r} & \omega = \frac{n-n_0}{n_r} & p = \frac{P_{ref}-P_{ref0}}{n_r} \\ h = \frac{H-H_0}{H_r} & q = \frac{Q-Q_0}{Q_r} & y = \frac{\alpha-\alpha_0}{\alpha_{\max}} & m_t = \frac{M_t-M_0}{M_r} \end{cases}$$

are the relative deviations of corresponding variables, where subscripts r and 0 denote the rated condition value and the initial value, respectively.

Appendix B

$$\boldsymbol{D}f_x(\boldsymbol{x}_E,\mu) = \begin{bmatrix} J_{11} & J_{12} & J_{13} & J_{14} & J_{15} & J_{16} & J_{17} & J_{18} \\ J_{21} & J_{22} & J_{23} & J_{24} & J_{25} & J_{26} & J_{27} & J_{28} \\ J_{31} & J_{32} & J_{33} & J_{34} & J_{35} & J_{36} & J_{37} & J_{38} \\ J_{41} & J_{42} & J_{43} & J_{44} & J_{45} & J_{46} & J_{47} & J_{48} \\ J_{51} & J_{52} & J_{53} & J_{54} & J_{55} & J_{56} & J_{57} & J_{58} \\ J_{61} & J_{62} & J_{63} & J_{64} & J_{65} & J_{66} & J_{67} & J_{68} \\ J_{71} & J_{72} & J_{73} & J_{74} & J_{75} & J_{76} & J_{77} & J_{78} \\ J_{81} & J_{82} & J_{83} & J_{84} & J_{85} & J_{86} & J_{87} & J_{88} \end{bmatrix} = \begin{bmatrix} \frac{\partial \dot{q}_H}{\partial q_H} & \frac{\partial \dot{q}_H}{\partial h_s} & \frac{\partial \dot{q}_H}{\partial x_1} & \frac{\partial \dot{q}_H}{\partial i_{qr}} & \frac{\partial \dot{q}_H}{\partial \omega} & \frac{\partial \dot{q}_H}{\partial y} & \frac{\partial \dot{q}_H}{\partial z} & \frac{\partial \dot{q}_H}{\partial h} \\ \frac{\partial \dot{h}_s}{\partial q_H} & \frac{\partial \dot{h}_s}{\partial h_s} & \frac{\partial \dot{h}_s}{\partial x_1} & \frac{\partial \dot{h}_s}{\partial i_{qr}} & \frac{\partial \dot{h}_s}{\partial \omega} & \frac{\partial \dot{h}_s}{\partial y} & \frac{\partial \dot{h}_s}{\partial z} & \frac{\partial \dot{h}_s}{\partial h} \\ \frac{\partial \dot{x}_1}{\partial q_H} & \frac{\partial \dot{x}_1}{\partial h_s} & \frac{\partial \dot{x}_1}{\partial x_1} & \frac{\partial \dot{x}_1}{\partial i_{qr}} & \frac{\partial \dot{x}_1}{\partial \omega} & \frac{\partial \dot{x}_1}{\partial y} & \frac{\partial \dot{x}_1}{\partial z} & \frac{\partial \dot{x}_1}{\partial h} \\ \frac{\partial \dot{i}_{qr}}{\partial q_H} & \frac{\partial \dot{i}_{qr}}{\partial h_s} & \frac{\partial \dot{i}_{qr}}{\partial x_1} & \frac{\partial \dot{i}_{qr}}{\partial i_{qr}} & \frac{\partial \dot{i}_{qr}}{\partial \omega} & \frac{\partial \dot{i}_{qr}}{\partial y} & \frac{\partial \dot{i}_{qr}}{\partial z} & \frac{\partial \dot{i}_{qr}}{\partial h} \\ \frac{\partial \dot{\omega}}{\partial q_H} & \frac{\partial \dot{\omega}}{\partial h_s} & \frac{\partial \dot{\omega}}{\partial x_1} & \frac{\partial \dot{\omega}}{\partial i_{qr}} & \frac{\partial \dot{\omega}}{\partial \omega} & \frac{\partial \dot{\omega}}{\partial y} & \frac{\partial \dot{\omega}}{\partial z} & \frac{\partial \dot{\omega}}{\partial h} \\ \frac{\partial \dot{y}}{\partial q_H} & \frac{\partial \dot{y}}{\partial h_s} & \frac{\partial \dot{y}}{\partial x_1} & \frac{\partial \dot{y}}{\partial i_{qr}} & \frac{\partial \dot{y}}{\partial \omega} & \frac{\partial \dot{y}}{\partial y} & \frac{\partial \dot{y}}{\partial z} & \frac{\partial \dot{y}}{\partial h} \\ \frac{\partial \dot{z}}{\partial q_H} & \frac{\partial \dot{z}}{\partial h_s} & \frac{\partial \dot{z}}{\partial x_1} & \frac{\partial \dot{z}}{\partial i_{qr}} & \frac{\partial \dot{z}}{\partial \omega} & \frac{\partial \dot{z}}{\partial y} & \frac{\partial \dot{z}}{\partial z} & \frac{\partial \dot{z}}{\partial y_2} \\ \frac{\partial \dot{h}}{\partial q_H} & \frac{\partial \dot{h}}{\partial h_s} & \frac{\partial \dot{h}}{\partial x_1} & \frac{\partial \dot{h}}{\partial i_{qr}} & \frac{\partial \dot{h}}{\partial \omega} & \frac{\partial \dot{h}}{\partial y} & \frac{\partial \dot{h}}{\partial z} & \frac{\partial \dot{h}}{\partial y_1} \end{bmatrix}$$

where:

$\frac{\partial \dot{q}_H}{\partial q_H} = -\frac{2h_{H0}}{T_{wH}H_0}$, $\frac{\partial \dot{q}_H}{\partial h_s} = \frac{1}{T_{wH}}$, $\frac{\partial \dot{q}_H}{\partial x_1} = 0$, $\frac{\partial \dot{q}_H}{\partial i_{qr}} = 0$, $\frac{\partial \dot{q}_H}{\partial \omega} = 0$, $\frac{\partial \dot{q}_H}{\partial y} = 0$, $\frac{\partial \dot{q}_H}{\partial z} = 0$, $\frac{\partial \dot{q}_H}{\partial h} = 0$;

$\frac{\partial \dot{h}_s}{\partial q_H} = -\frac{1}{T_F}$, $\frac{\partial \dot{h}_s}{\partial h_s} = 0$, $\frac{\partial \dot{h}_s}{\partial x_1} = 0$, $\frac{\partial \dot{h}_s}{\partial i_{qr}} = 0$, $\frac{\partial \dot{h}_s}{\partial \omega} = \frac{e_{qx0}}{T_F} - \frac{e_{qh0}h_E}{T_F(\omega+1)^2}$, $\frac{\partial \dot{h}_s}{\partial y} = \frac{e_{qy0}\sqrt{h_E+1}}{T_F}$, $\frac{\partial \dot{h}_s}{\partial z} = 0$,

$\frac{\partial \dot{h}_s}{\partial h} = \frac{e_{qh0}}{T_F(\omega_E+1)} + \frac{e_{qy0}}{2T_F\sqrt{h_E+1}}$; $\frac{\partial \dot{x}_1}{\partial q_H} = 0$, $\frac{\partial \dot{h}_s}{\partial h_s} = 0$, $\frac{\partial \dot{x}_1}{\partial x_1} = 0$, $\frac{\partial \dot{x}_1}{\partial i_{qr}} = \frac{3n_p\varphi_1 L_m\omega_{r0}}{2L_s} + \frac{3n_p\varphi_1 L_m}{2L_s}\omega_E$,

$\frac{\partial \dot{x}_1}{\partial \omega} = \frac{3i_{qr0}n_p\varphi_1 L_m}{2L_s} + \frac{3n_p\varphi_1 L_m}{2L_s}i_{qrE}$, $\frac{\partial \dot{x}_1}{\partial y} = 0$, $\frac{\partial \dot{x}_1}{\partial z} = 0$, $\frac{\partial \dot{x}_1}{\partial h} = 0$; $\frac{\partial \dot{x}_1}{\partial q_H} = 0$, $\frac{\partial \dot{h}_s}{\partial h_s} = 0$, $\frac{\partial \dot{i}_{qr}}{\partial x_1} = -\frac{K_{i1}L_s}{L_m}$,

$\frac{\partial \dot{i}_{qr}}{\partial i_{qr}} = -1.5K_{p1}n_p\varphi_1\omega_{ro} - 1.5K_{p1}n_p\varphi_1\omega_E$, $\frac{\partial \dot{i}_{qr}}{\partial \omega} = -1.5K_{p1}n_p\varphi_1 i_{qr0} - 1.5K_{p1}n_p\varphi_1 i_{qrE}$, $\frac{\partial \dot{i}_{qr}}{\partial y} = 0$,

$\frac{\partial \dot{i}_{qr}}{\partial z} = 0$, $\frac{\partial \dot{i}_{qr}}{\partial h} = 0$; $\frac{\partial \dot{x}_1}{\partial q_H} = 0$, $\frac{\partial \dot{h}_s}{\partial h_s} = 0$, $\frac{\partial \dot{\omega}}{\partial x_1} = 0$, $\frac{\partial \dot{\omega}}{\partial i_{qr}} = \frac{1.5n_p\varphi_1 L_m}{T_a L_s}$, $\frac{\partial \dot{\omega}}{\partial \omega} = \frac{e_{x0}\sqrt{h_E+1}}{T_a}$, $\frac{\partial \dot{\omega}}{\partial y} = \frac{e_{y0}(h+1)}{T_a}$,

$\frac{\partial \dot{\omega}}{\partial z} = 0$, $\frac{\partial \dot{\omega}}{\partial h} = \frac{e_{h0}+e_{y0}y_E}{T_a} + \frac{e_{x0}\omega_E}{2T_a\sqrt{h_E+1}}$; $\frac{\partial \dot{x}_1}{\partial q_H} = 0$, $\frac{\partial \dot{h}_s}{\partial h_s} = 0$, $\frac{\partial \dot{y}}{\partial x_1} = 0$, $\frac{\partial \dot{y}}{\partial i_{qr}} = -\frac{1.5K_d L_m n_p\varphi_1}{T_a L_s T_y}$,

$\frac{\partial \dot{y}}{\partial \omega} = -\frac{K_p}{T_y} - \frac{K_d e_{x0}\sqrt{h_E+1}}{T_a T_y}$, $\frac{\partial \dot{y}}{\partial y} = -\frac{1}{T_y} - \frac{K_d e_{y0}(h_E+1)}{T_a T_y}$, $\frac{\partial \dot{y}}{\partial z} = \frac{K_i}{T_y}$,

$\frac{\partial \dot{y}}{\partial h} = -\frac{K_d e_{h0}}{T_a T_y} - \frac{K_d e_{y0}y_E}{T_a T_y} - \frac{K_d e_{x0}\omega}{2T_a T_y\sqrt{h_E+1}}$; $\frac{\partial \dot{x}_1}{\partial q_H} = 0$, $\frac{\partial \dot{h}_s}{\partial h_s} = 0$, $\frac{\partial \dot{z}}{\partial x_1} = 0$, $\frac{\partial \dot{z}}{\partial i_{qr}} = 0$, $\frac{\partial \dot{z}}{\partial \omega} = -1$, $\frac{\partial \dot{z}}{\partial y} = 0$,

$\frac{\partial \dot{z}}{\partial z} = 0$, $\frac{\partial \dot{z}}{\partial h} = 0$; $\frac{\partial \dot{x}_1}{\partial q_H} = 0$, $\frac{\partial \dot{h}_s}{\partial h_s} = -\frac{\omega_E+1}{T_w e_{qh0}}$, $\frac{\partial \dot{h}}{\partial x_1} = 0$,

$\frac{\partial \dot{h}}{\partial i_{qr}} = \frac{1.5K_d L_m e_{qy0}n_p\varphi_1\sqrt{h_E+1}(\omega_E+1)}{L_s T_a T_y e_{qh0}} - \frac{1.5L_m e_{qx0}n_p\varphi_1(\omega_E+1)}{L_s T_a e_{qh0}}$,

$$\frac{\partial \dot{h}}{\partial \omega} = \omega_E \left(\frac{K_p e_{qy0}\sqrt{h_E+1}}{T_y e_{qh0}} - \frac{e_{qx0} e_{x0}\sqrt{h_E+1}}{T_a e_{qh0}} + \frac{K_d e_{qy0} e_{x0}(h_E+1)}{T_a T_y e_{qh0}} \right)$$
$$-h_E \left(\frac{1}{T_w e_{qh0}} + \frac{e_{h0} e_{qx0}}{T_a e_{qh0}} - \frac{K_d e_{h0} e_{qy0}\sqrt{h_E+1}}{T_a T_y e_{qh0}} \right)$$
$$-i_{qr E} \left(\frac{3 L_m e_{qx0} n_p \phi_1}{2 L_s T_a e_{qh0}} - \frac{3 K_d L_m e_{qy0} n_p \phi_1 \sqrt{h_E+1}}{2 L_s T_a T_y e_{qh0}} \right)$$
$$+y_E \left(\frac{e_{qy0}\sqrt{h_E+1}}{T_y e_{qh0}} - \frac{e_{qx0} e_{y0}(h_E+1)}{T_a e_{qh0}} + \frac{K_d e_{qy0} e_{y0}(h_E+1)^{3/2}}{T_a T_y e_{qh0}} \right)$$
$$-\frac{h_{sE}}{T_w e_{qh0}} - \frac{K_i e_{qy0} z_E \sqrt{h_E+1}}{T_y e_{qh0}} + \frac{K_p e_{qy0}\sqrt{h_E+1}(\omega_E+1)}{T_y e_{qh0}} - \frac{e_{qx0} e_{x0}\sqrt{h_E+1}(\omega_E+1)}{T_a e_{qh0}}$$
$$-\frac{K_p a e_{qy0} p\sqrt{h_E+1}}{T_y e_{qh0}} + \frac{K_d e_{qy0} e_{x0}(h_E+1)(\omega_E+1)}{T_a T_y e_{qh0}},$$

$$\frac{\partial \dot{h}}{\partial y} = \frac{e_{qy0}\sqrt{h_E+1}(\omega_E+1)}{T_y e_{qh0}} - \frac{e_{qx0} e_{y0}(h_E+1)(\omega_E+1)}{T_a e_{qh0}} + \frac{K_d e_{qy0} e_{y0}(h_E+1)^{3/2}(\omega_E+1)}{T_a T_y e_{qh0}},$$
$$\frac{\partial \dot{h}}{\partial z} = -\frac{K_i e_{qy0}\sqrt{h_E+1}(\omega_E+1)}{T_y e_{qh0}},$$
$$\frac{\partial \dot{h}}{\partial h} = y_E \left(\frac{e_{qy0}(\omega_E+1)}{2 T_y e_{qh0}\sqrt{h_E+1}} - \frac{e_{qx0} e_{y0}(\omega_E+1)}{T_a e_{qh0}} + \frac{3 K_d e_{qy0} e_{y0}\sqrt{h_E+1}(\omega_E+1)}{2 T_a T_y e_{qh0}} \right)$$
$$+\omega_E \left(\frac{K_p e_{qy0}(\omega_E+1)}{2 T_y e_{qh0}\sqrt{h_E+1}} - \frac{e_{qx0} e_{x0}(\omega_E+1)}{2 T_a e_{qh0}\sqrt{h_E+1}} + \frac{K_d e_{qy0} e_{x0}(\omega_E+1)}{T_a T_y e_{qh0}} \right)$$
$$-\frac{\omega_E+1}{T_w e_{qh0}} - \frac{e_{h0} e_{qx0}(\omega_E+1)}{T_a e_{qh0}} - \frac{K_i e_{qy0} z_E(\omega_E+1)}{2 T_y e_{qh0}\sqrt{h_E+1}} - \frac{K_p a e_{qy0} p(\omega_E+1)}{2 T_y e_{qh0}\sqrt{h_E+1}}$$
$$+\frac{K_d e_{h0} e_{qy0}\sqrt{h_E+1}(\omega_E+1)}{T_a T_y e_{qh0}} + \frac{K_d e_{h0} e_{qy0} h_E(\omega_E+1)}{2 T_a T_y e_{qh0}\sqrt{h_E+1}} + \frac{3 K_d L_m e_{qy0} i_{qr} n_p \varphi_1(\omega_E+1)}{4 L_s T_a T_y e_{qh0}\sqrt{h_E+1}}$$

References

1. Saeed, A.; Li, C.; Gan, Z.; Xie, Y.; Liu, F. A simple approach for short-term wind speed interval prediction based on independently recurrent neural networks and error probability distribution. *Energy* **2022**, *238*, 122012. [CrossRef]
2. Zhang, N.; Xue, X.; Jiang, W.; Shi, L.; Feng, C.; Gu, Y. A novel hybrid forecasting system based on data augmentation and deep learning neural network for short-term wind speed forecasting. *J. Renew. Sustain. Energy* **2021**, *13*, 066101. [CrossRef]
3. Zhao, Z.; Yang, J.; Chung, C.Y.; Yang, W.; He, X.; Chen, M. Performance enhancement of pumped storage units for system frequency support based on a novel small signal model. *Energy* **2021**, *234*, 121207. [CrossRef]
4. Javed, M.S.; Zhong, D.; Ma, T.; Song, A.; Ahmed, S. Hybrid pumped hydro and battery storage for renewable energy based power supply system. *Appl. Energy* **2020**, *257*, 114026. [CrossRef]
5. Xu, B.; Chen, D.; Venkateshkumar, M.; Xiao, Y.; Yue, Y.; Xing, Y.; Li, P. Modeling a pumped storage hydropower integrated to a hybrid power system with solar-wind power and its stability analysis. *Appl. Energy* **2019**, *248*, 446–462. [CrossRef]
6. Lyu, X.; Yang, K.; Fang, J. Utilization of resources in abandoned coal mines for carbon neutrality. *Sci. Total Environ.* **2022**, *822*, 153646. [CrossRef]
7. Sivakumar, N.; Das, D.; Padhy, N.P. Variable speed operation of reversible pump-turbines at Kadamparai pumped storage plant—A case study. *Energy Convers. Manag.* **2014**, *78*, 96–104. [CrossRef]
8. Fraile-Ardanuy, J.; Wilhelmi, J.R.; Fraile-Mora, J.J.; Perez, J.I. Variable-speed hydro generation: Operational aspects and control. *IEEE Trans. Energy Convers.* **2006**, *21*, 569–574. [CrossRef]
9. Ardizzon, G.; Cavazzini, G.; Pavesi, G. A new generation of small hydro and pumped-hydro power plants: Advances and future challenges. *Renew. Sustain. Energy Rev.* **2014**, *31*, 746–761. [CrossRef]
10. Kuwabara, T.; Shibuya, A.; Furuta, H.; Kita, E.; Mitsuhashi, K. Design and dynamic response characteristics of 400 MW adjustable speed pumped storage unit for Ohkawachi Power Station. *IEEE Trans. Energy Convers.* **1996**, *11*, 376–384. [CrossRef]
11. Padoan, A.C.; Kawkabani, B.; Schwery, A.; Ramirez, C.; Nicolet, C.; Simond, J.; Avellan, F. Dynamical Behavior Comparison Between Variable Speed and Synchronous Machines With PSS. *IEEE Trans. Power Syst.* **2010**, *25*, 1555–1565. [CrossRef]
12. Yang, W.; Yang, J. Advantage of variable-speed pumped storage plants for mitigating wind power variations: Integrated modelling and performance assessment. *Appl. Energy* **2019**, *237*, 720–732. [CrossRef]
13. Sarasúa, J.I.; Pérez-Díaz, J.I.; Torres Vara, B. On the Implementation of Variable Speed in Pump-Turbine Units Providing Primary and Secondary Load-Frequency Control in Generating Mode. *Energies* **2015**, *8*, 13559–13575. [CrossRef]
14. Vasudevan, K.R.; Ramachandaramurthy, V.K.; Venugopal, G.; Ekanayake, J.B.; Tiong, S.K. Variable speed pumped hydro storage: A review of converters, controls and energy management strategies. *Renew. Sustain. Energy Rev.* **2021**, *135*, 110156. [CrossRef]
15. Guo, W.; Zhu, D. Nonlinear modeling and operation stability of variable speed pumped storage power station. *Energy Sci. Eng.* **2021**, *9*, 1703–1718. [CrossRef]
16. Gao, C.; Yu, X.; Nan, H.; Men, C.; Fu, J. A Fast High-Precision Model of the Doubly-Fed Pumped Storage Unit. *J. Electr. Eng. Technol.* **2021**, *16*, 797–808. [CrossRef]

17. Gao, C.; Yu, X.; Nan, H.; Men, C.; Zhao, P.; Cai, Q.; Fu, J. Stability and dynamic analysis of doubly-fed variable speed pump turbine governing system based on Hopf bifurcation theory. *Renew. Energy* **2021**, *175*, 568–579. [CrossRef]
18. Zhu, Z.; Tan, X.; Lu, X.; Liu, D.; Li, C. Hopf Bifurcation and Parameter Sensitivity Analysis of a Doubly-Fed Variable-Speed Pumped Storage Unit. *Energies* **2022**, *15*, 204. [CrossRef]
19. Xu, X.; Guo, W. Stability of speed regulating system of hydropower station with surge tank considering nonlinear turbine characteristics. *Renew. Energy* **2020**, *162*, 960–972. [CrossRef]
20. Guo, W.; Yang, J.; Yang, W.; Chen, J.; Teng, Y. Regulation quality for frequency response of turbine regulating system of isolated hydroelectric power plant with surge tank. *Int. J. Electr. Power Energy Syst.* **2015**, *73*, 528–538. [CrossRef]
21. Peng, Z.; Guo, W. Saturation characteristics for stability of hydro-turbine governing system with surge tank. *Renew. Energy* **2019**, *131*, 318–332. [CrossRef]
22. Zhang, T.; Zhou, J.; Lai, X.; Huang, Y.; Li, M. Nonlinear stability and dynamic characteristics of grid-connected hydropower station with surge tank of a long lateral pipe. *Int. J. Electr. Power Energy Syst.* **2022**, *136*, 107654. [CrossRef]
23. Liu, Y.; Guo, W. Coupling dynamic characteristics and transient power angle instability of grid-connected hydropower station with surge tank. *Int. J. Electr. Power Energy Syst.* **2022**, *139*, 107984. [CrossRef]
24. Liu, Y.; Guo, W. Multi-frequency dynamic performance of hydropower plant under coupling effect of power grid and turbine regulating system with surge tank. *Renew. Energy* **2021**, *171*, 557–581. [CrossRef]
25. Li, C.; Zhang, N.; Lai, X.; Zhou, J.; Xu, Y. Design of a fractional-order PID controller for a pumped storage unit using a gravitational search algorithm based on the Cauchy and Gaussian mutation. *Inf. Sci.* **2017**, *396*, 162–181. [CrossRef]
26. Zhang, H.; Chen, D.; Xu, B.; Wang, F. Nonlinear modeling and dynamic analysis of hydro-turbine governing system in the process of load rejection transient. *Energy Convers. Manag.* **2015**, *90*, 128–137. [CrossRef]
27. Lai, X.; Li, C.; Guo, W.; Xu, Y.; Li, Y. Stability and dynamic characteristics of the nonlinear coupling system of hydropower station and power grid. *Commun. Nonlinear Sci. Numer. Simul.* **2019**, *79*, 104919. [CrossRef]
28. Zhang, N.; Li, C.; Li, R.; Lai, X.; Zhang, Y. A mixed-strategy based gravitational search algorithm for parameter identification of hydraulic turbine governing system. *Knowl.-Based Syst.* **2016**, *109*, 218–237. [CrossRef]
29. Zhao, Z.; Yang, J.; Huang, Y.; Yang, W.; Ma, W.; Hou, L.; Chen, M. Improvement of regulation quality for hydro-dominated power system: Quantifying oscillation characteristic and multi-objective optimization. *Renew. Energy* **2021**, *168*, 606–631. [CrossRef]
30. Chen, D.; Ding, C.; Ma, X.; Yuan, P.; Ba, D. Nonlinear dynamical analysis of hydro-turbine governing system with a surge tank. *Appl. Math. Model.* **2013**, *37*, 7611–7623. [CrossRef]
31. Lin, J.; Xu, R.; Li, L. Turing-Hopf bifurcation of reaction-diffusion neural networks with leakage delay. *Commun. Nonlinear Sci. Numer. Simul.* **2020**, *85*, 105241. [CrossRef]
32. Hassard, B.; Kazarinoff, N.; Wan, Y.-H. *Theory and Applications of Hopf Bifurcation*; Cambridge University Press: London, UK, 1981; p. 41.

energies

MDPI

Article

Dynamic Characteristics and Successive Start-Up Control Strategy Optimization of Pumped Storage Units under Low-Head Extreme Conditions

Yonggang Li [1,2], Jinjiao Hou [1,2], Juan Gu [1], Chaoshun Li [1,*] and Yanhe Xu [1,*]

[1] School of Civil and Hydraulic Engineering, Huazhong University of Science and Technology, Wuhan 430074, China; llxyfzg64li@163.com (Y.L.); hou_jj@hdec.com (J.H.); gujuanhust@163.com (J.G.)
[2] Huadong Engineering Corporation Limited, Hangzhou 311122, China
* Correspondence: csli@hust.edu.cn (C.L.); yh_xu@hust.edu.cn (Y.X.); Tel.: +86-158-7180-0142 (C.L.); +86-133-7786-4561 (Y.X.)

Abstract: With inherent 'S' characteristics and the one-tunnel-with-two-units arrangement of the pump-turbine, hydraulic transient changes in the successive start-up process are complex, and the optimal control is difficult. This paper aims to study the dynamic characteristics and successive start-up control strategy optimization of two hydraulic couplings pumped storage units (PSUs) under low-head extreme conditions. Firstly, an accurate model of two hydraulic coupling PSUs' successive start-up is established. Based on this model, the influence of the interval time of successive start-up on the dynamic characteristics of PSUs is carried out. It is shown that the change of the interval time of the successive start-up (ΔT) of the two PSUs has a significant impact on the dynamic response stability of the low-head start-up. If ΔT is more than 40 s, the hydraulic oscillation and speed fluctuation of the PSUs deteriorate. Secondly, with the different controller parameters for the two PSUs, a novel multi-objective optimization scheme with fractional order PID controller (FOPID) is proposed to figure out the best control scheme for the successive start-up. Furthermore, selecting the sum of the rise time (T_r) of the rotating speed of two PSUs and the sum of the integral time absolute error (ITAE) of two PSUs is the objective. Meanwhile, the optimization scheme of PID with different parameters (PIDDP) is used to compare and verify the optimization method proposed in this paper. The results for this extreme condition indicate that FOPID has more significant advantages in optimizing the instability of the successive start-up process, with the better Pareto front, and the optimized scheme has a more stable dynamic transition process of flow, water hammer pressure, and rotational speed.

Keywords: pumped storage units (PSUs); successive start-up; 'S' characteristics; low water head conditions; multi-objective optimization; fractional order PID controller (FOPID)

Citation: Li, Y.; Hou, J.; Gu, J.; Li, C.; Xu, Y. Dynamic Characteristics and Successive Start-Up Control Strategy Optimization of Pumped Storage Units under Low-Head Extreme Conditions. *Energies* **2022**, *15*, 5428. https://doi.org/10.3390/en15155428

Academic Editor: Helena M. Ramos

Received: 6 July 2022
Accepted: 24 July 2022
Published: 27 July 2022

1. Introduction

Wind and solar energy have become the consensus on sustainable development [1]. However, wind and solar energy exhibit obvious intermittency, and large-scale wind and solar energy connected to the electrical power grid constitutes a severe challenge to safety and stability [2]. A pumped storage unit (PSU), with superiority in switching operating conditions fast [3], can make up for the intermittency [4] and has been become the most well-established and commercially acceptable technology for utility-scale electrical power storage [5] and plays an irreplaceable role in improving the safety, stability, and flexibility of the electrical power system. Thus, the dynamic performance and the control quality of the PSU are very important [6].

Due to the existence of the large flow inertia in the long diversion pipeline and with a large number of nonlinear links, as well as the existence of the unique reverse 'S' characteristic instability region of the pump-turbine, the optimal control of the PSU presents

complex characteristics [7]. Particularly, in the reverse 'S' characteristic instability region, the full characteristic curve of the unit shows serious crossover, aggregation, and twisting.

Compared with other operating conditions, when the PSU starts up under low-head conditions, it is more likely to fall into this area, which will cause speed oscillation and is difficult to stabilize, and even a failure to start up [8]. Thus, focusing on the efficiency and stability of the start-up strategy under low-water-head extreme conditions has a great significance. Moreover, one tunnel for two units has become a typical layout of PSUs, and two units share the same water-diversion systems and tailrace tunnel. If the operating conditions of the two PSUs are different or the transition conditions are not synchronized, strong hydraulic interference will occur in the diversion system [9]. For example, when the two PSUs start up successively under the low-head condition, the hydraulic interference between the two units will further increase the risk of falling into the 'S' region, leading to the regulation quality deterioration of the control system [10].

Using an intelligent optimization algorithm to figure out a feasible solution has become an effective method to solve the above issues [11]. There are many kinds of intelligent optimization algorithms that have been proposed and used to improve the control performance of PSUs. Zhang et al. [12] improved NSGAS-III and used it to research the best control strategy for the pump-turbine regulating system. Xu et al. [13] used the improved gravitational search algorithm (GSA) to optimize the control strategy of PSUs operating under low-water-head conditions. In the above-published research, the author only considered a single optimization goal. However, in the actual production process, the evaluation of the control quality of the transition process of the PSU often needs to consider multiple performance indicators such as speed overshoot, adjustment time, and water hammer pressure. Hou et al. [14] used multiple objectives to obtain a superior successive start-up strategy of two coupling PSUs.

This paper focuses on the successive start-up strategy of two hydraulic coupling PSUs under low-head extreme conditions. The innovation is as follows: (1) establishing an accurate transition process model of the regulating system of PSUs based on one actual pumped storage station in China. The effects of the complex boundary conditions of the surge chamber, bifurcated pipe, and the nonlinear links are fully considered in this accurate model. In this way, the characteristics of the transition process of the PSUs can be described more realistically. (2) The multi-objective optimal method is applied to research the successive start-up of two PSUs under low-head extreme conditions. The multi-objective grey wolf optimal algorithm (MOGWO) [15] is used in this paper. (3) The interval time of a successive start-up is optimized to obtain the optimal moment after the first start-up to achieve better dynamic quality. (4) The two hydraulic coupling PSUs have their parameter of the fractional-order PID (FOPID) controller [16] compared and analyzed with traditional PID controller.

The overview of the rest of this paper is as follows. In Section 2, an accurate model of two hydraulic coupling PSUs' successive start-up under low-head extreme conditions has been established according to a real pumped storage station in Jiangxi province in China. In this model, the non-linear characteristics of the diversion system and hydraulic actuator are fully considered. Based on this model, the influence of interval time on successive start-up has been published, and the range of the most extreme condition of successive start-up is determined. In Section 3, introduced the optimization schemes, and the MOGWO are introduced. Section 4 shows the result of the numerical calculation experiment of a successive start-up under low-water-head extreme conditions with different control strategies, specifically, the PID controller with the two units with different parameters and the FOPID controller with the two units with different parameters. In Section 5, the conclusion and a summary of this paper are published.

2. Model of Two Hydraulic Coupling PSUs Regulating System

The typical layout of two hydraulic coupling PSUs is shown in Figure 1. It needs to declare that, during the process of the successive start-up of two hydraulic coupling PSUs,

the 1# PSU is the earlier one, and the 2# PSU is the later one. The parameters of each pipe section are shown in Table 1.

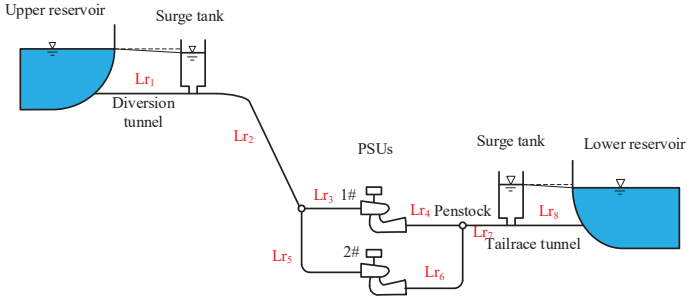

Figure 1. Typical layout of two hydraulic couplings pumped storage units (PSUs).

Table 1. The parameters of each pipe section.

Code	L(m)	D(m)
Lr_1	444.23	6.20
Lr_2	865.69	5.04
Lr_3	117.86	2.6
Lr_4	155.4	4.19
Lr_5	117.86	2.6
Lr_6	155.4	4.19
Lr_7	15	6.5
Lr_8	1065.2	6.58

The PSU regulating system is a complex closed-loop control system integrating hydraulic, mechanical, and electrical systems. As the important auxiliary equipment of the pumped storage power station is composed of a pressurized water-diversion system, pump-turbine, generator, and pump-turbine governor, as shown in Figure 2. The basic task is to complete the starting, power generation, pumping, load increase and load reduction, primary frequency modulation, and shutdown of the water turbine.

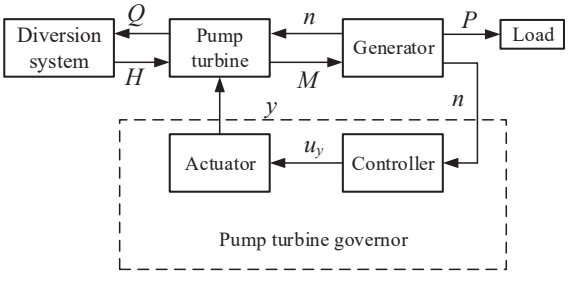

Figure 2. Structure diagram of the PSU speed-regulating system.

In Figure 2, Q represents the flow of the PSU; H represents the working water head of the PSU; n represents the rotation speed of the pump-turbine and the generator; M represents the torque of the pump-turbine; P represents the output power of the generator; y represents the opening of the guide vane; u_y represents the output of the controller and adjust guide vane opening accordingly.

2.1. Mathematical Model of Pressurized Water Diversion System

The model of the pressurized water system mainly focuses on the dynamic relationship between the flow pressure and flow rate. According to Newton's second law and the law of conservation of mass, the characteristics of water flow in pipes can be described by the momentum equation and continuity equation [17] and shown as follows in Equations (1) and (2).

$$\frac{\partial V}{\partial t} + V\frac{\partial V}{\partial L} + g\frac{\partial H}{\partial L} + \frac{f}{2D}V\left|V\right| = 0 \tag{1}$$

$$\frac{c^2}{g}\frac{\partial V}{\partial L} + V\left(\frac{\partial H}{\partial L} + \sin\alpha\right) + \frac{\partial H}{\partial t} = 0 \tag{2}$$

where V represents the average velocity of the flow at the pipe centerline; H represents the water head at time t of a certain flow section in the pipe; L represents the distance from the cross-section to the origin; f represents the hydraulic friction coefficient of the pipeline; D represents the pipe diameter; F represents pipeline cross-sectional area; c represents the velocity of the pressure wave; α represents the angle between the pipe centerline and the horizontal, and g represents the gravitational constant.

Due to the elastic water hammer and the flow friction of the non-constant flow in the water-diversion system, the characteristic-line method that was proposed in [18], has been used in this study. Moreover, the characteristics method could be adopted to solve these two differential equations and obtain the hydraulic pressure and water flow in the various parts of the water-diversion system [19]. Depending on whether the pressure wave is in the same direction as the water flow, we can get two kinds of hydraulic pressure characteristic lines, including a positive characteristic line and a negative characteristic line, with two characteristic line equations [20]:

$$C^+: Q_P^t = C_P - C_a H_P^t \tag{3}$$

$$C^-: Q_P^t = C_n + C_a H_P^t \tag{4}$$

where $Q^t{}_P$ represents the section flow of the point p, at the time t; H_P^t represents the section hydraulic head of the point p at time t; $C_p = Q_A^{t-\Delta t} + \frac{gA}{c}H_A^{t-\Delta t} - \frac{f\Delta L}{2DAc}Q_A^{t-\Delta t}\left|Q_A^{t-\Delta t}\right|$, $C_n = Q_B^{t-\Delta t} - \frac{gA}{c}H_B^{t-\Delta t} - \frac{f\Delta L}{2DAc}Q_B^{t-\Delta t}\left|Q_B^{t-\Delta t}\right|$, $C_a = \frac{gA}{c}$; the $Q_A^{t-\Delta t}$ represents the section flow of the point A, at the time $t-\Delta t$; $H_A^{t-\Delta t}$ represents the section hydraulic head of point A at time $t-\Delta t$; the $Q_B^{t-\Delta t}$ represents the section flow of point B at time $t-\Delta t$; $H_B^{t-\Delta t}$ represents the section hydraulic head of point B at time $t-\Delta t$.

The schematic diagram of the characteristic line method is shown in Figure 3.

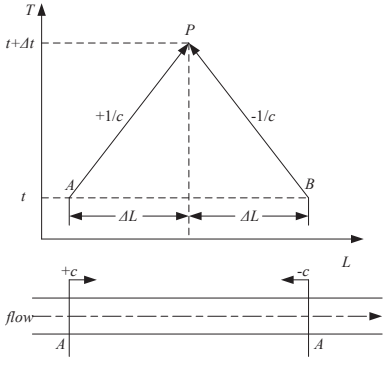

Figure 3. Schematic diagram of the characteristic line method.

2.2. Mathematical Model of Pump-Turbine

The pump-turbine is the core equipment of the pumped storage power station and the key to realizing the conversion from water energy to electric energy [21]. As the main component of the PSU, a lot of studies have been carried out on the modeling. However, due to the complex flow characteristics in the pump-turbine, the accurate expressions of the flow and output torque can not be obtained so far, so the accurate dynamic data of the unit can not be obtained. Researchers usually use the full-characteristic curves of the units to establish the mathematical model, which is composed of the torque curves and the flow curves [22,23], as shown in Figure 4.

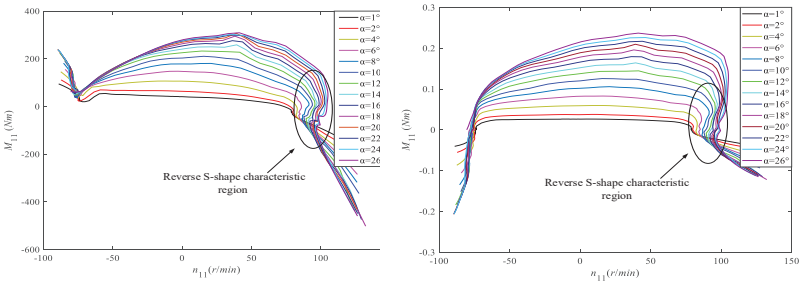

(**a**) Torque characteristic curve (**b**) Flow characteristic curve

Figure 4. Full-characteristic curves of pump-turbine.

Moreover, the unit is expressed as a torque function and a flow function is shown as Equations (5) and (6), respectively.

$$M_1' = f_M(a, n_1') \tag{5}$$

$$Q_1' = f_Q(a, n_1') \tag{6}$$

where M_1' represents the unit-torque of the pump-turbine; Q_1' represents the unit flow of the pump-turbine; a represents the angle of the guide vane opening, and n_1' represents the unit-rotational speed of the pump-turbine runner. Then the torque and the flow are calculated by Equation (7).

$$\begin{cases} M_t = M_1' D^3 H \\ Q_t = Q_1' D^2 \sqrt{H} \\ n = n_1' \sqrt{H}/D \end{cases} \tag{7}$$

where M_t and Q_t represent the torque and the flow of the pump-turbine at the time t, respectively. H represents the operating water head; D represents the diameter of the pump-turbine runner, and n represents the rotational speed of the pump-turbine runner.

As shown in Figure 4, there is a reverse 'S' region at the end of the full-characteristic curve, and with the problems of severe polymerization, distortions, and crossovers, which might lead to issues with various values of unit-torque and unit-flow at the same unit-speed [24]. Several researchers have published their studies on solving the multivalued problem of the 'S' region. In this paper, the improved Suter transformation method [25] is applied. The full-characteristic curves can be transformed into the W_H and W_M curves under the improved Suter transformation method, as shown in Figure 5.

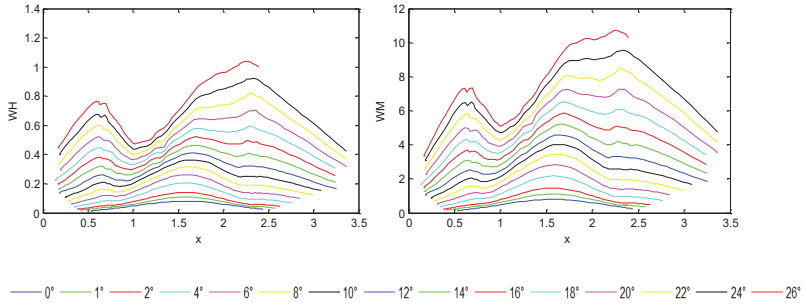

Figure 5. W_H and W_M curves under the improved Suter transformation method.

The W_H and W_M curves can be represented as Equations (8) and (9).

$$\begin{cases} WH(x,y) = \frac{h}{n^2+q^2+C_h \cdot h}(y+C_y)^2 \\ WM(x,y) = \frac{m+k_2 \cdot h}{n^2+q^2+C_h \cdot h}(y+C_y)^2 \end{cases} \tag{8}$$

$$\begin{cases} n \geq 0, x = \arctan[(q+k_1\sqrt{h})/n] \\ n < 0, x = \pi + \arctan[(q+k_1\sqrt{h})/n] \end{cases} \tag{9}$$

where $k_1 = 0.5 \sim 1.2, k_2 > \frac{|M_{11\max}|}{M_{11}}$, and the M_{11} represents the unit torque. $C_y = 0.1 \sim 0.3$, $C_h = 0.4 \sim 0.6$; n, q, h, and y represent relative rotational speed, relative flux, relative water head, and relative guide vane opening, respectively.

The relative-value equations can be solved according to Equations (8) and (9), as shown in Equation (10).

$$\begin{cases} h_{n+1} = W_H(y_{n+1}, x(q_{n+1}, n_{n+1})) \cdot (q_{n+1}^2 + n_{n+1}^2) \\ m_{n+1} = W_M(y_{n+1}, x(q_{n+1}, n_{n+1})) \cdot (q_{n+1}^2 + n_{n+1}^2) \end{cases} \tag{10}$$

2.3. First-Order Model of the Generator

In this study, the synchronous generator has been regarded as a rotating rigid body with a certain torque of inertia, and the first-order model is adopted [26], shown in Equation (11).

$$\begin{cases} (T_a + T_b)\frac{dn}{dt} + e_n n = M_t - M_g \\ e_n = e_g - e_x \end{cases} \tag{11}$$

where T_a represents the inertial time constant of the pump-turbine; T_b represents the inertial time constant of the load; e_n represents the comprehensive self-regulation coefficient of the pump-turbine unit; e_g represents the self-regulation coefficient of the synchronous generator, and n represents the relative rotational speed deviation.

During the progress of start-up, the electrical load equals 0, so that $Mg = 0$. The first-order model could be expressed as Equation (12).

$$\begin{cases} (T_a + T_b)\frac{dn}{dt} + e_n n = M_t \\ e_n = e_g - e_x \end{cases} \tag{12}$$

2.4. Model of the PSUs' Governor

The typical PSU governor consists of a crisis governor and an electro-hydraulic servo system. The basic structure of the governor is shown in Figure 6. The microcomputer regulator is the core of the speed control system. According to the collected information about the speed of the unit, power grid frequency, guide vane opening, and other relevant information, the control mode switching and control signal output functions are realized

through the control process and program calculation. The electro-hydraulic servo system converts the electrical output signal of the microcomputer regulator to the displacement signal of the servo motor and drives the water guide mechanism to change the guide vane opening, so as change the flow into the unit runner, finally realizing the regulation control of the unit.

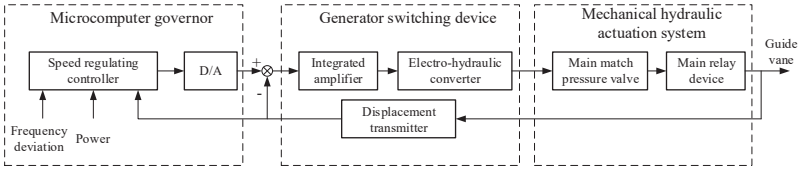

Figure 6. The basic structure of the PSU governor.

2.4.1. Model of Microcomputer Regulator

In this paper, the numerical simulation of the PSU under the condition of the lower water head is studied by using the microcomputer governor model based on FOPID, which could also be represented as $PI^{\lambda}D^{\mu}$.

With the development of fractional calculus theory, its application in the control system has been developed rapidly. The research shows that the $PI^{\lambda}D^{\mu}$ controller has good control performance. In this paper, the $PI^{\lambda}D^{\mu}$ controller is applied. The $PI^{\lambda}D^{\mu}$ controller proposed based on the fractional-order differential theory has one more fractional integral order λ and differential order μ than the traditional integral order PID controller. Usually, the λ and μ could be any real numbers in the range of [0, 2] [27]. The structure diagram of the $PI^{\lambda}D^{\mu}$ controller is shown in Figure 7.

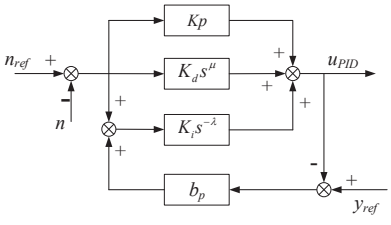

Figure 7. Structure diagram of the $PI^{\lambda}D^{\mu}$.

The transfer function of the $PI^{\lambda}D^{\mu}$ controller is shown as Equation (13).

$$C(s) = \frac{u(s)}{e(s)} = K_p + \frac{K_i}{s^{\lambda}} + K_d s^{\mu} \tag{13}$$

From the above equation, it can be easily concluded that, when both λ and μ are equal to 1, the $PI^{\lambda}D^{\mu}$ controller equals the traditional *PID* controller. With two more adjustable parameters, the $PI^{\lambda}D^{\mu}$ controller not only has all the advantages of the PID controller but also has better flexibility and applicability and can obtain a better control effect.

2.4.2. Model of Electro-Hydraulic Servo Motor System

In this paper, the PSUs work in the large fluctuation transition process, and the parameters of the PSU governor change greatly. The nonlinear characteristics of the elector-hydraulic system must be fully taken into account. Therefore, the dead zone, the saturation effect of the main distribution valve, and the main servomotor must be thought about. The structure of the electro-hydraulic servo motor system is shown in Figure 8.

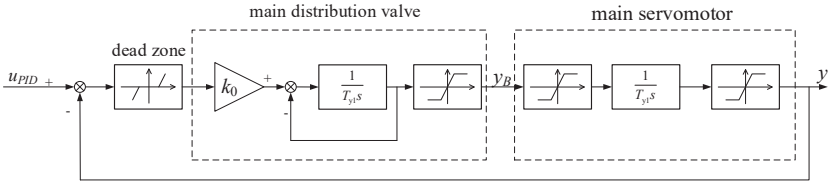

Figure 8. Structure of the electro-hydraulic servo motor system.

The mathematical expressions are shown as follows:

(1) the mathematical expression of the dead zone

$$d_{out} = \begin{cases} d_{in} - b, \ d_{in} \geq b \\ 0, \ -a < d_{in} < b \\ d_{in} + b, \ d_{in} \leq -b \end{cases} \tag{14}$$

where b represents the rage of the dead zone; d_{in} represents the input of the dead zone; d_{out} represents the output of the dead zone.

(2) the mathematical expression of the saturation effect

$$s_{out} = \begin{cases} s_{in}, \ s_{min} < s_{in} < s_{\max} \\ s_{\min}, \ s_{in} < s_{min} \\ s_{\max}, \ s_{in} > s_{\max} \end{cases} \tag{15}$$

where s_{in} represents the input of the saturated nonlinear link; $s_{\max}$ and $s_{\min}$ represents the upper and lower bounds of the saturated nonlinear link, respectively.

In conclusion, in this section, the schematic of the numerical simulation model is shown in Figure 9.

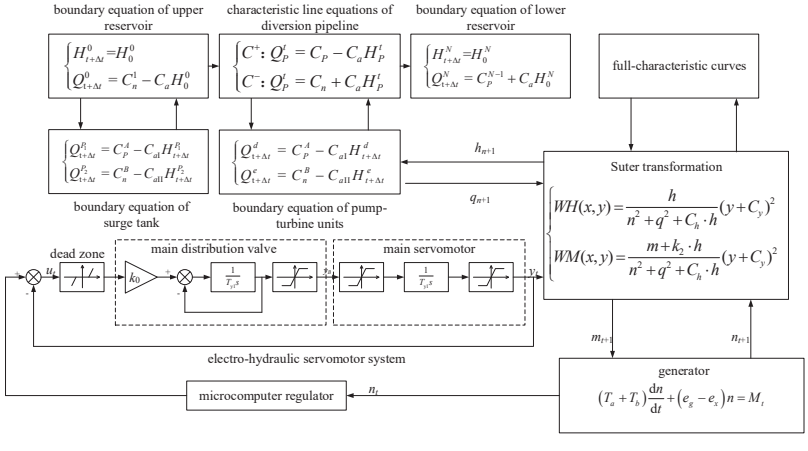

Figure 9. Schematic of the numerical simulation model.

2.5. The Influence of the Interval Time of Successive Start-Up on the Dynamic Characteristics of PSUs

There are hydraulic connections between the two PSUs of the same hydraulic unit in the steady-state operation and transition process. During the process of successive start-up, the hydraulic disturbance in the system will aggravate the change of flow and water pressure in the system, which means a more unfavorable dynamic process. The

hydraulic interference will lead to the different transition processes of the two units with different successive start-up interval times.

To figure out the most adverse starting interval time, when the two hydraulic coupling units start up successively under low-water-head conditions. The simulation research about the influence of the interval time ΔT has been carried out based on a model of two hydraulic coupling PSU regulation systems. The physical parameters and working-condition parameters of the model are shown in Table 2. Under the different water-head operating conditions, with different interval times, the rapidity and stationarity of the units are analyzed during the progress of successive start-ups. The simulation tests are based the MATLAB 9.2. The rapidity is quantitatively characterized by the rise time T_r of the rotating speed, while stationarity is quantitatively characterized by the integral time absolute error (ITAE) of the rotating speed, a relatively comprehensive index. Then the dynamic process of the evaluation index of the unit successive start-up process when the ΔT takes on different values is recorded and compared. The results of the simulation study are as follows.

Table 2. The physical parameters and working-condition parameters of the model.

Components	Values
Water head	H_u = 716 m H_l = 190 m $H_{\min}$ = 526 m H_s = 540 m $H_{\max}$ = 554 m
Suter transformation	$k_1 = 10$ $k_2 = 0.9$ $C_y = 0.2$ $C_h = 0.5$
Generator	J = 96.84 tm^2
Governor	T_{ID} = 1 s $T = 0.1$ s $k_0 = 7$ $T_{yB} = 0.05$ $T_y = 0.3$ s
Direct guide vane control	$k_c = 1/27$

Figure 10a shows the function between the ΔT and T_r of the two PSUs under three different water-head conditions. Under three different water-head conditions, the curves can be divided into three sections according to the status of the fluctuation:$\Delta T \in [0, 6\text{ s}]$,$\Delta T \in (6\text{ s}, 20\text{ s}]$ and $\Delta T \in (20\text{ s}, 50\text{ s}]$. Specifically, in the range of $\Delta T \in [0, 6\text{ s}]$, the T_r changes little under three different conditions and the interval time has little effect on it. In the range of $\Delta T \in (6\text{ s}, 20\text{ s}]$, the T_r curves have a severe fluctuation under all of the three different conditions. Moreover, with the water head decreasing, the fluctuation is more severe. In the range of $\Delta T \in (20\text{ s}, 50\text{ s}]$, under the conditions of 554 m and 540 m, the T_r is almost a constant with different ΔT. But under the condition of 526 m, the T_r increase with the increase of ΔT.

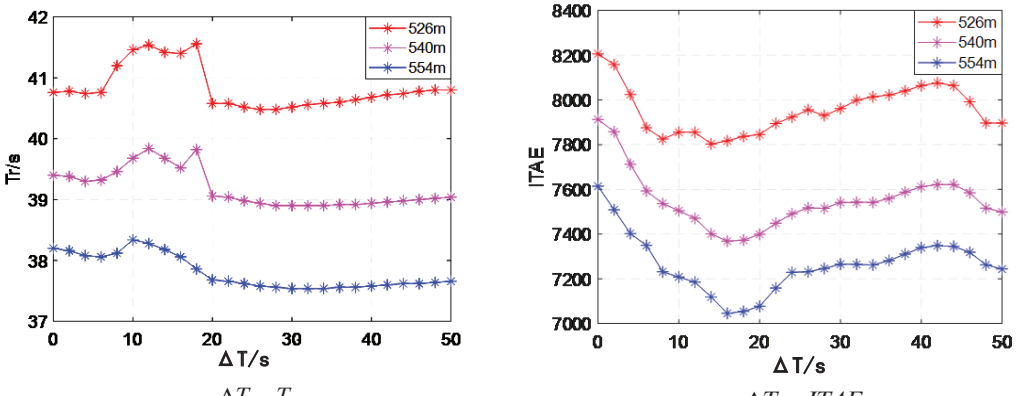

(a) $\Delta T \sim T_r$ (b) $\Delta T \sim ITAE$

Figure 10. Influence of interval time ΔT on T_r and ITAE of rotational speed.

Figure 10b shows the function between the ΔT and *ITAE* of the two PSUs under three different water-head conditions. The ITAE curves are similar under the conditions of 554 m and 540 m. The variation curves of ITAE showed a trend of decreasing firstly, then increasing, and finally decreasing again, and the variation law was relatively simple. However, under the 526 m conditions, the ITAE curve has a more complex fluctuation. Especially in the range of $\Delta T \in [0, 8\text{s}]$, the ITAE decreases with the increase of ΔT. Then in the range of $\Delta T \in (8\text{s}, 20\text{s}]$, the curve of ITAE fluctuates irregularly with the increase of ΔT. In the range of $\Delta T \in (20\text{s}, 50\text{s}]$, the ITAE curve is similar to the other two conditions, and the value of the ITAE increases firstly with the ΔT increases, then decreases again.

To sum up, under different conditions with different water-heads, during the progress of the hydraulic coupling PSUs successive start-up, with the increase of ΔT, the value of T_r and ITAE changes greatly. This is due to the fact that, when the ΔT different, the operation state of 1#PSU is completely different than when the 2#PSU is started, and the hydraulic environment and water shock wave in the diversion system must be very different. Therefore, with different ΔT, the values of T_r and ITAE show great changes. Especially under the conditions of H_min = 526 m, compared to other conditions, with different ΔT, the influence of the hydraulic disturbance between two PSUs is more complicated on the dynamic progress of successive start-ups.

3. Optimization Schemes

In this section, the multi-objective grey wolf optimizer algorithm (MOGWO) has been used to solve the successive start-up strategy of two hydraulic coupling PSUs under low-water-head extreme conditions. MOGWO, with the characteristics of simple principle, few parameters to adjust, fast convergence, and strong global search ability, has been widely used in solving multi-objective optimization problems.

3.1. Optimization Algorithm

The optimization process of MOGWO is shown as follows.

Step 1: Assigning suitable values to related parameters, including the number of optimization variables; the number of gray waves individuals, n; maximum iterations M, and the number of Pareto archives, and other basic parameters for multi-optimization, such as the grid inflation parameter, the number of grids per each dimension, leader selection pressure parameter, and extra repository member selection pressure.

Step 2: Initializing the variable to be optimized $X_i(k)$ (i = 1, 2, ... n), and k represents the number of iterations.

Step 3: Inputting X to the model of successive start-up, calculating the fitness function and position vectors of every individual, and judge whether the constraint conditions are satisfied. If the answer is yes, then it is ready for the next step; if not, then it is best to return to Step 1.

Step 4: Comparing the fitness function of each individual, determining the dominant relationship between individuals, saving the non-dominated individuals in the Pareto archive.

Step 5: Calculating the distance for each Pareto archive individual and choosing the α, β, and δ gray waves individuals; the α, β, and δ represent the best, second-best, and third-best solutions respectively, and they are the leaders of the herd that in the Pareto archive and others are named as w.

Step 6: Updating the position of the current w individuals with Equations (16)–(18)

$$\begin{cases} D_\alpha = \left| C_1 \cdot X_\alpha - X_{(k)} \right| \\ D_\beta = \left| C_2 \cdot X_\beta - X_{(k)} \right| \\ D_\delta = \left| C_3 \cdot X_\delta - X_{(k)} \right| \end{cases} \tag{16}$$

$$\begin{cases} X_1 = X_\alpha - A_1 \cdot D_\alpha \\ X_2 = X_\beta - A_2 \cdot D_\beta \\ X_3 = X_\delta - A_3 \cdot D_\delta \end{cases} \tag{17}$$

$$X_{(k+1)} = \frac{X_1 + X_2 + X_3}{3} \tag{18}$$

where both the A and C are coefficient vectors.

Step 7: Calculating the value of fitness, comparing it with the individuals in the Pareto archive of the $(k-1)th$ generation, and updating the Pareto archive according to the dominance relationship.

Step 8: Calculating the distance between each individual in the Pareto archive, and, if the number of non-dominated individuals is more than the archive size, removing some individuals, as many as necessary according to the archive size.

Step 9: Updating the best, second-, and third-best solution.

Step10: Determining whether the maximum iteration criteria are satisfied; if the answer is yes, it is best to return to Step 6, and if not, output the optimal Pareto solution is the next step.

The optimization process is shown in Figure 11.

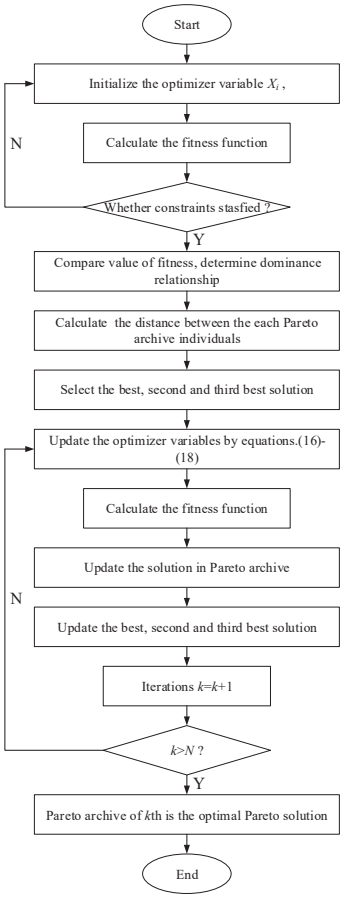

Figure 11. The optimization process for a successive start-up strategy.

3.2. Objective Function

Researchers pay more attention to the rapidity and stationarity of a unit when it starts up. Rapidity is quantitatively characterized by the rise time of the rotating speed, while stationarity is quantitatively characterized by the integral time absolute error (ITAE) of the rotating speed, a relatively comprehensive index. However, the rapidity and stability are irreconcilable, so it is impossible to get the best result for the two indices at the same time. In actual production, usually the aim is to achieve the optimal combination of these two performance indices. In this study, select the sum of the rise time of the rotating speed of two PSUs and the sum of the ITAE of two PSUs as the objective function. The two optimization objectives can be expressed as Equation (19).

$$\begin{cases} \min f_1 = T_{r1} + T_{r2} \\ \min f_2 = ITAE_1 + ITAE_2 \end{cases} \tag{19}$$

3.3. Optimizer Variables

During the process of start-up, the guide vane opening change process is shown in Figure 12. In the figure, θ represents the inclination angle of the guide vane opening ascending process line, and k_c represents the maximum velocity of guide vane opening change. The y_c represents the maximum relative opening of the guide vane during the start-up process. In this study, the k_c has been set as 1/27.

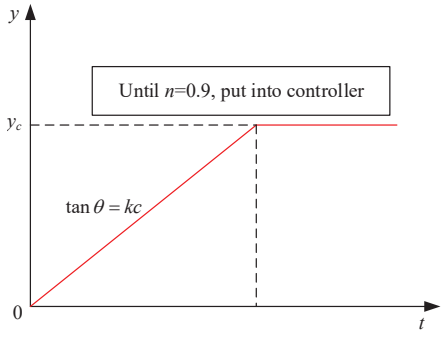

Figure 12. Schematic diagram of guide vane opening change process.

y_c and the controller parameters are selected as the optimization variables. In Section 2, interval time had great influence on the process of successive start-up and should be selected as an optimization variable. Moreover, due to the different operation statuses during successive start-ups, the two hydraulic coupling PSUs should own different control parameters, and the optimization variables in the two cases are shown as Equations (20) and (21), respectively.

$$X_1 = (K_p, K_i, K_d, y_c, \Delta T) \tag{20}$$

$$X_2 = (K_{p1}, K_{i1}, K_{d1}, \lambda_1, \mu_1, y_{c1}, \Delta T, K_{p2}, K_{i2}, K_{d2}, \lambda_2, \mu_2, y_{c2}) \tag{21}$$

On the right side of Equation (20), subscript 1 and 2 represent the 1# PSU and 2# PSU, respectively.

3.4. Constraint Conditions

In the actual production process, there are specific constraints on the relevant indicators of the start-up process. In this paper, three constraints are mentioned as follows.

(1) The upper and low boundaries of the optimization variables X

$$X \in [L, U] \tag{22}$$

where L and U represent the upper and lower boundaries, respectively. Specific values of the L and U are shown in Table 3.

Table 3. The boundaries of the optimization variables.

Variables	Boundaries	Values												
X_1	L_1	0.1	0.1	0.1	0.1	1	0.2	0						
	U_1	10	8	8	1	2	0.3	40						
X_2	L_2	0.1	0.1	0.1	0.1	1	0.2	0	0.1	0.1	0.1	0.1	1.0	0.2
	U_2	10	8	8	1	2	0.3	40	10	8	8	1	2.0	0.3

(2) Oscillation times of rotation speed

According to the requirements of the start-up transition process of the PSUs, the number of rotation speed oscillations shall not exceed two times.

(3) Limitation of water hammer pressure

The water hammer pressure of each link in the system shall not exceed the upper limit obtained by regulation guarantee calculation.

4. Numerical Calculation Experiment of Successive Start-Up under Low-Water-Head Extreme Conditions

In the real station, there are two main guide vane opening strategies for PSUs, one-stage starting and two-stage starting. The control methods used by these two methods are traditional PID control. However, under low-water-head extreme working conditions, the pumped storage unit can easily fall into the 'S' region during the process of start-up, and it's difficult for the PID controller to obtain an excellent control effect. The fractional-order PID (FOPID) has two more adjustable parameters than the traditional PID, so it has better control flexibility and can obtain a better adjustment effect. In this paper, two schemes are compared with others. Specifically, the controller and the parameters in the study on the successive start-up process are variable. PIDDP and FOPIDDP are researched respectively in this paper.

A pumped storage station in China has been selected as the reference system for this study, and the relevant parameters are the same as this real station. An accurate model of the speed regular system of two hydraulic coupling PSUs has been proposed, and a simulation study has performed in MATLAB 9.2. Two kinds of strategies for successive start-up under low conditions have been researched in this paper.

In this paper, set the number of gray wave individuals $n = 100$, and the maximum iterations $M = 300$. The results of the optimization of successive start-up strategies with two different controllers are as follows.

In this paper, the optimization result is a Pareto archive, which consists of a series of non-inferior solutions. Figure 13 shows the Pareto archive, and the value of the optimization variables in the Pareto archive are listed in Appendix A Tables A1 and A2. As shown in Figure 13, the Pareto archive under PID control is dominated by the Pareto archive under FOPID control. In other words, it is indicated that the FOPID controller obtains a better Pareto archive than the traditional PID controller.

In this paper, we use the method of relative objective proximity [28] to obtain the best solution under the two different controllers as shown in Figure 13. The value of these two solutions is shown in Table 4.

Inputting the best solution to the control system of the PSUs, we can obtain the dynamic processes of the performance indexes, including the rotating speed, flow, and actual working water-head curves during the process of successive start-up under low extreme water-head conditions, shown in Figures 14–16. The start-up process curves of the two PSUs, respectively, during the successive start-up process of the two schemes in the full-characteristic curves are shown in Figures 17 and 18.

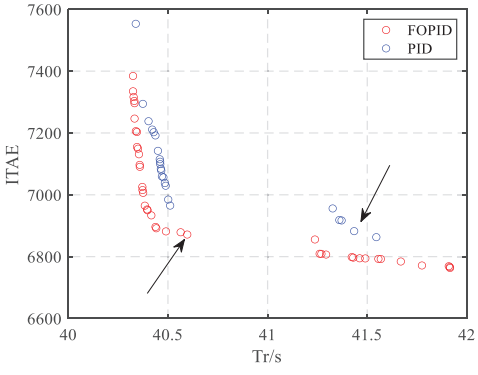

Figure 13. Comparison diagram of the Pareto archive of four schemes.

Table 4. Optimal solution of the best solution.

Schemes	K_{p1}	K_{i1}	K_{d1}	λ_1	μ_1	y_{c1}	ΔT	K_{p2}	K_{i2}	K_{d2}	λ_2	μ_2	y_{c2}
PIDDP	0.8220	4.7674	3.5252			0.2996	15.4059	0.5409	3.6460	1.7732			0.2903
FOPIDDP	1.137	1.694	5.452	0.300	1.066	0.298	28.45	1.273	1.999	5.484	0.149	1.066	0.299

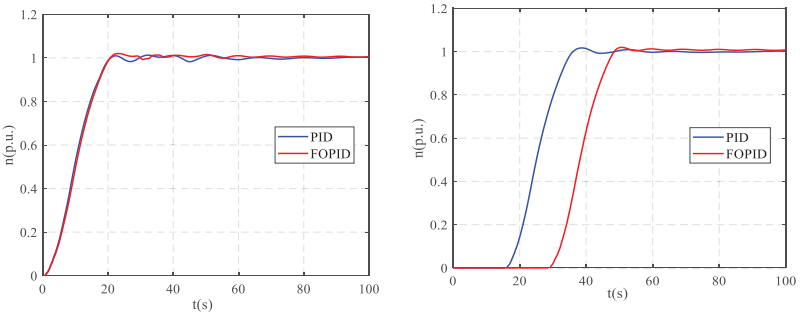

(**a**) 1#PSU (**b**) 2#PSU

Figure 14. The rotational speed dynamic curves of the two PSUs.

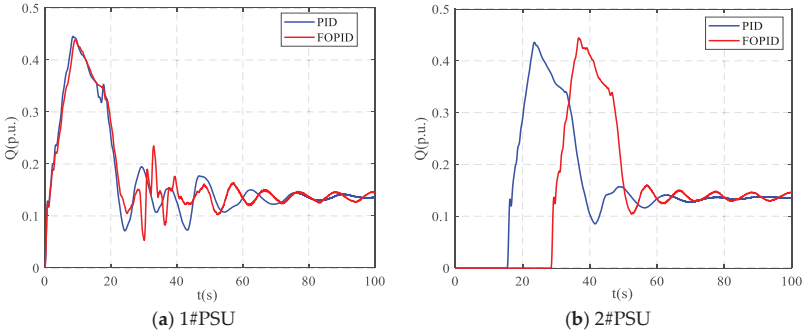

(**a**) 1#PSU (**b**) 2#PSU

Figure 15. The flow dynamic curves of the two PSUs.

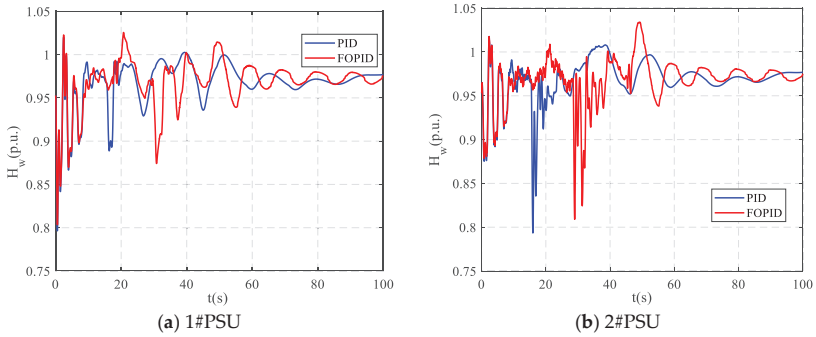

(**a**) 1#PSU (**b**) 2#PSU

Figure 16. The dynamic curves of the actual working water head of the two PSUs.

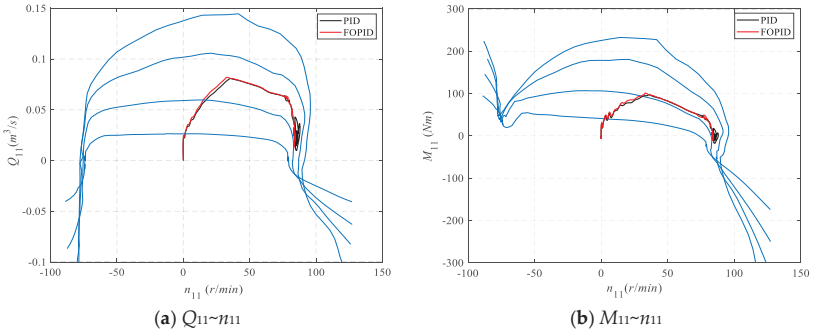

(**a**) Q_{11}~n_{11} (**b**) M_{11}~n_{11}

Figure 17. Start-up process curves in the full-characteristic curve of the 1# PSU.

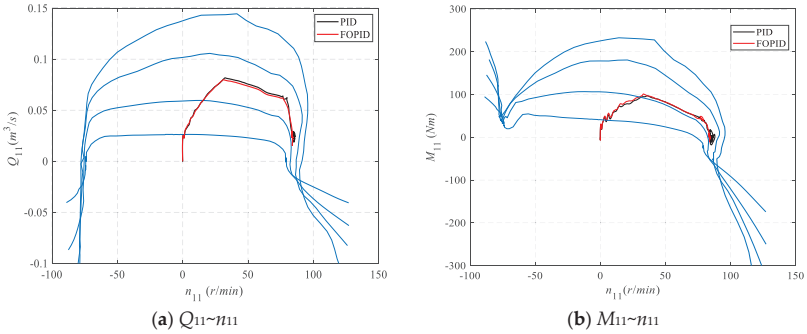

(**a**) Q_{11}~n_{11} (**b**) M_{11}~n_{11}

Figure 18. Start-up process curves in the full-characteristic curve of the 2# PSU.

The maximum and the rise time of the rotational speed were recorded, and the oscillation number of the rotational speed of the four schemes is shown in Table 5.

Table 5. The quantitative index of the rotational speed.

Schemes	1#PSU			2#PSU		
	Maximum (*p*.u.)	Rise Time (s)	Number of Oscillation	Maximum (*p*.u.)	Rise Time (s)	Number of Oscillation
PIDDP	1.02	20.74	2	1.017	20.64	1
FOPIDDP	1.009	20.66	1	1.019	19.99	0

Figure 14 shows the dynamic process of the rotational speed of the two PSUs, respectively, during the successive start-up process under low- water-head extreme conditions with two different controllers. It is easy to get that the rotational speed rise time is approximate for the two coupling PSUs under two different controllers; to be specific, the difference value is within 1 s. For the 1# PSU alone, the speed rise time has little difference under two different controllers. However, the overshoot of the rotational speed is smaller under the FOPID controller than under the PID. The dynamic process of the FOPID controller is much better with smaller oscillation, stability time, and steady-state error. For the 2# PSU alone, we can obtain that the rotational speed overshoot under the two controllers is greatly approximate. However, the dynamic curves of the rotational speed are more approximate under the FOPID, with the smallest number of oscillations. In conclusion, combined with Figure 14 and Table 5, it is obvious that the rotational speed indicators under the FOPID are better than under the traditional PID.

Figure 15 shows the dynamic process of the flow of the two PSUs, respectively, during the successive start-up process under low-water-head extreme conditions with two different controllers. In Figure 15a, for the 1# PSU alone, before the unit flow curve come to the first wave peak, the control of the PSUs is in the open-loop stage, so the flow dynamic process is roughly the same with two different controllers. When the simulation time $t = \Delta T$, with the 2# PSU start-up, due to the water interference in the diversion system, the flow curves of unit 1# all have obvious oscillations. After that, closed-loop adjustment is carried out under PID and FOPID control strategies, respectively. As shown in Figure 15a, the flow dynamic process curves of 1# PSU have an obvious under different controllers when $t \in [20s, 50s]$. Moreover, under the FOPID, the flow oscillation attenuation is faster. As shown in Figure 15b, the flow dynamic process of unit 2# is similar under two different controllers, and both can quickly decay to the steady-state.

Figure 16 shows the dynamic process of the actual working water head of the two PSUs, respectively, during the successive start-up process under low-water head extreme conditions with two different controllers. The value of the water head is relative to the H_s. Compared to the dynamic curves of the two PSUs, it is obvious that the start-up of 2# PSU could lead to a considerable oscillation in the process of the 1# PSU. At the same time, the hydraulic interference between the two PSUs will also cause a violent oscillation of the dynamic process curve of 2# PSU. Combining the actual working water-head dynamic curves of the two PSUs with different controllers, the dynamic process of the two PSUs are roughly similar in general, but the oscillation attenuation of the dynamic process curve under the FOPID is faster.

Figures 17 and 18 shows the start-up process curves in the full-characteristic curves of the two PSUs, respectively, during the successive start-up process under low-water-head conditions. For 1# PSU, as shown in Figure 17, the start-up process curves can avoid falling into the reverse 'S' region better under the FOPID. However, under the traditional PID, the start-up process curves fall into the reverse 'S' region, and both the flow characteristics and torque characteristics show reciprocating oscillations in this region. For 2# PSU, as shown in Figure 18, the start-up process curves can better avoid falling into the reverse 'S' region under the FOPID. However, under the traditional PID, only the flow characteristics can avoid falling into the reverse 'S' region, but torque characteristics also show reciprocating oscillations in this region. It can be summed up that, with the FOPID, the two PSUs can avoid falling into the reverse 'S' region better during the process of successive start-up under low-water-head extreme conditions.

5. Conclusions

The successive start-up strategy of two hydraulic coupling PSUs under low-water-head extreme conditions was studied in this paper. An accurate model of successive start-up was established. The influence of interval time on the dynamic characteristics of successive start-up was analyzed. A novel optimization scheme with FOPIDDP was proposed for successive start-up. For comparison, the optimization scheme PIDDP was

also tested. Moreover, MOGWO was adopted to solve the Pareto archive of the parameters of novel optimization schemes. All numerical simulation experiments were completed in MATLAB 9.2.

Several conclusions can be extracted from this study:

(1) The interval time ΔT could make a great influence on the successive start-up process; when ΔT is greater than a certain value, the instability of the PSUs will be intensified, especially for 1# PSU. Operating teams can refer to the research results of this paper to select the optimal interval time.
(2) The results show that the multi-objective optimization aiming at the speed rise time and ITAE value of the two units can effectively reduce the risk of falling into the anti-S instability zone when the units are successively started at low-water-head conditions.
(3) With muti-objective optimization, the Pareto archive provides a series of feasible solutions for decision-makers. Based on the result, the operating teams can select the optimal solution according to their actual demand and therefore can obtain the maximum benefit.
(4) The multi-objective optimization method with FOPID is feasible and conducive to avoiding the 'S' region during the process of successive start-up under-low-water head extreme conditions.

The results of this paper are helpful in solving the difficulty of regulating and controlling the hydraulic coupling PSUs under low-head conditions.

Author Contributions: Conceptualization, Y.L.; methodology, Y.L. and J.H.; software, Y.L.; validation, Y.L. and J.G.; formal analysis, Y.L.; investigation, Y.L. and Y.X.; resources, C.L.; data curation, Y.L.; writing—original draft preparation, Y.L.; writing—review and editing, Y.L.; visualization, Y.X.; supervision, C.L. All authors have read and agreed to the published version of the manuscript.

Funding: This work was supported by the National Natural Science Foundation of China (NSFC) (No.51809099, 51879111, 51679095) and the National Key Research and Development Program of China (2016YFC0401905).

Conflicts of Interest: The authors declare no conflict of interest.

Appendix A

Table A1. Pareto archive under PID controller.

Solutions	K_{p1}	K_{i1}	K_{d1}	y_{c1}	K_{p2}	K_{i2}	K_{d2}	y_{c2}	ΔT
1	1.1925	4.7705	3.8386	0.3000	1.0264	3.7686	1.7617	0.3000	24.8353
2	1.1841	4.8417	3.8247	0.3000	1.0211	3.7870	1.8279	0.3000	25.7208
3	0.8434	4.8025	3.3461	0.2991	0.5425	3.5893	1.7219	0.2956	15.2920
4	0.8220	4.7674	3.5252	0.2996	0.5409	3.6460	1.7732	0.2903	15.4059
5	0.8548	4.8194	3.3967	0.3000	0.5542	3.6370	1.8115	0.3000	15.4788
6	0.8144	4.6661	3.6072	0.3000	0.5509	3.5573	1.8191	0.2971	15.4504
7	0.8385	4.7589	3.3806	0.2990	0.5413	3.5597	1.7238	0.2946	15.4116
8	0.8146	4.7299	3.6102	0.3000	0.5489	3.6101	1.7905	0.2919	15.4256
9	0.8197	4.6696	3.6107	0.2998	0.5541	3.5570	1.8281	0.2969	15.5383
10	0.8203	4.6707	3.6111	0.3000	0.5522	3.5608	1.8247	0.2976	15.5976
11	0.8715	4.7503	3.6393	0.2999	0.5895	3.6629	1.7932	0.2901	15.5248
12	0.6285	4.7633	3.9859	0.2996	0.6314	3.9650	1.6867	0.2998	27.8300
13	0.8225	4.6906	3.6173	0.3000	0.5542	3.5862	1.8210	0.2959	15.7242
14	0.6425	4.7612	3.9762	0.2999	0.6399	3.9593	1.6977	0.2998	27.6187
15	1.0271	4.6495	3.5825	0.3000	0.6910	3.6774	1.7781	0.3000	15.4626
16	0.8545	4.8164	3.4118	0.3000	0.5541	3.6412	1.8111	0.2997	15.6067
17	1.2055	4.8233	3.8714	0.3000	0.9807	3.8226	1.9135	0.3000	25.5276
18	0.7513	4.8524	3.9405	0.3000	0.6625	3.9626	1.8100	0.3000	27.1635
19	0.5686	4.7506	3.9798	0.2984	0.6008	3.9461	1.6692	0.2993	27.8832
20	0.6550	4.7633	3.9743	0.2999	0.6573	3.9548	1.6987	0.2999	27.6223
21	0.8556	4.7457	3.6342	0.2996	0.5829	3.6513	1.7865	0.2899	15.2710
22	0.8477	4.7970	3.4457	0.3000	0.5569	3.6209	1.7398	0.2968	15.7298
23	0.8606	4.7962	3.3957	0.2999	0.5633	3.6284	1.8035	0.2999	15.4701
24	1.1936	4.7938	3.8537	0.3000	1.0299	3.7861	1.8083	0.3000	25.0752
25	0.6059	4.7542	3.9805	0.2986	0.6285	3.9491	1.6773	0.2994	27.8763
26	1.0301	4.9349	3.8476	0.3000	0.7399	3.9261	1.8736	0.3000	25.9410
27	1.1878	4.8585	3.8922	0.3000	0.9429	3.8568	1.9236	0.3000	25.6958
28	1.1430	4.9518	3.9508	0.3000	0.8703	3.9426	2.2738	0.3000	24.9287

Table A2. Pareto archive under FOPID controller.

Solutions	K_{p1}	K_{i1}	K_{d1}	λ_1	μ_1	y_{c1}	K_{p2}	K_{i2}	K_{d2}	λ_2	μ_2	y_{c2}	ΔT
1	1.179	1.673	5.567	0.296	1.077	0.298	1.262	1.997	5.421	0.146	1.053	0.296	28.58
2	1.178	1.673	5.563	0.296	1.076	0.298	1.262	1.988	5.420	0.146	1.053	0.296	28.57
3	1.136	1.680	5.504	0.292	1.077	0.298	1.268	1.985	5.470	0.146	1.065	0.299	28.58
4	1.173	1.687	5.524	0.297	1.082	0.297	1.293	2.000	5.480	0.144	1.062	0.300	28.52
5	1.070	1.662	5.459	0.298	1.072	0.297	1.281	1.955	5.343	0.149	1.054	0.295	28.53
6	1.075	1.665	5.472	0.297	1.072	0.297	1.277	1.964	5.351	0.148	1.055	0.296	28.57
7	1.075	1.666	5.472	0.297	1.072	0.297	1.278	1.964	5.355	0.148	1.056	0.296	28.58
8	1.139	1.700	5.423	0.300	1.059	0.298	1.270	2.000	5.500	0.150	1.061	0.300	28.25
9	1.138	1.694	5.453	0.300	1.066	0.298	1.274	2.000	5.486	0.149	1.067	0.299	28.47
10	1.133	1.692	5.472	0.300	1.067	0.298	1.272	1.998	5.476	0.149	1.066	0.299	28.45
11	1.137	1.694	5.452	0.300	1.066	0.298	1.273	1.999	5.484	0.149	1.066	0.299	28.45
12	1.139	1.694	5.460	0.300	1.067	0.298	1.274	2.000	5.486	0.149	1.068	0.299	28.50
13	1.139	1.700	5.425	0.300	1.059	0.298	1.270	2.000	5.500	0.150	1.061	0.300	28.26
14	1.143	1.674	5.574	0.296	1.076	0.298	1.277	1.989	5.435	0.148	1.074	0.299	28.56
15	1.130	1.670	5.545	0.296	1.076	0.298	1.273	1.983	5.434	0.148	1.071	0.297	28.58
16	1.107	1.678	5.492	0.292	1.077	0.298	1.263	1.967	5.396	0.147	1.060	0.292	28.58
17	1.134	1.670	5.551	0.296	1.076	0.298	1.275	1.983	5.428	0.148	1.071	0.297	28.56
18	1.132	1.672	5.549	0.295	1.076	0.298	1.274	1.982	5.422	0.148	1.071	0.297	28.55
19	1.141	1.676	5.569	0.296	1.076	0.298	1.275	1.986	5.436	0.148	1.074	0.299	28.58
20	1.141	1.673	5.569	0.296	1.076	0.298	1.277	1.987	5.433	0.148	1.073	0.299	28.56
21	1.056	1.651	5.476	0.290	1.067	0.299	1.277	1.972	5.335	0.150	1.080	0.300	28.35
22	1.156	1.686	5.581	0.296	1.077	0.299	1.280	1.994	5.446	0.149	1.075	0.300	28.52
23	1.152	1.683	5.575	0.296	1.076	0.298	1.279	1.990	5.444	0.149	1.074	0.300	28.50
24	1.058	1.654	5.477	0.290	1.067	0.299	1.279	1.973	5.342	0.150	1.080	0.300	28.37
25	1.129	1.671	5.537	0.295	1.076	0.298	1.272	1.982	5.425	0.149	1.069	0.297	28.60
26	1.143	1.674	5.574	0.296	1.076	0.298	1.277	1.989	5.435	0.148	1.074	0.299	28.56
27	1.130	1.670	5.545	0.296	1.076	0.298	1.273	1.983	5.434	0.148	1.071	0.297	28.58
28	1.141	1.677	5.566	0.295	1.076	0.299	1.275	1.986	5.437	0.148	1.073	0.299	28.56
29	1.110	1.678	5.497	0.292	1.077	0.298	1.263	1.966	5.393	0.147	1.062	0.292	28.59
30	1.107	1.678	5.492	0.292	1.077	0.298	1.263	1.967	5.396	0.147	1.060	0.292	28.58
31	1.134	1.670	5.551	0.296	1.076	0.298	1.275	1.983	5.428	0.148	1.071	0.297	28.56
32	1.132	1.672	5.549	0.295	1.076	0.298	1.274	1.982	5.422	0.148	1.071	0.297	28.55
33	1.141	1.676	5.569	0.296	1.076	0.298	1.275	1.986	5.436	0.148	1.074	0.299	28.58

References

1. Corizzo, R.; Ceci, M.; Fanaee-T, H.; Gama, J. Multi-aspect renewable energy forecasting. *Inf. Sci.* **2021**, *546*, 701–722. [CrossRef]
2. Dell, R.M.; Rand, D.A. Energy storage—A key technology for global energy sustainability. *J. Power Sources* **2001**, *100*, 2–17. [CrossRef]
3. Jiang, R.; Wang, J.; Guan, Y. Robust unit commitment with wind power and pumped storage hydro. *IEEE Trans. Power Syst.* **2011**, *27*, 800–810. [CrossRef]
4. Zhao, Z.; Yang, J.; Yang, W.; Hu, J.; Chen, M. A coordinated optimization framework for flexible operation of pumped storage hydropower system: Nonlinear modeling, strategy optimization and decision making. *Energy Convers. Manag.* **2019**, *194*, 75–93. [CrossRef]
5. Rehman, S.; Al-Hadhrami, L.M.; Alam, M.M.J.R.; Reviews, S.E. Pumped hydro energy storage system: A technological review. *Renew. Sustain. Energy Rev.* **2015**, *44*, 586–598. [CrossRef]
6. Mahmoud, M.; Ramadan, M.; Olabi, A.-G.; Pullen, K.; Naher, S. A review of mechanical energy storage systems combined with wind and solar applications. *Energy Convers. Manag.* **2020**, *210*, 112670. [CrossRef]
7. Lai, X.; Li, C.; Zhou, J.; Zhang, N. Multi-objective optimization of the closure law of guide vanes for pumped storage units. *Renew. Energy* **2019**, *139*, 302–312. [CrossRef]
8. Xu, Y.; Zheng, Y.; Du, Y.; Yang, W.; Peng, X.; Li, C. Adaptive condition predictive-fuzzy PID optimal control of start-up process for pumped storage unit at low head area. *Energy Convers. Manag.* **2018**, *177*, 592–604. [CrossRef]
9. Rezghi, A.; Riasi, A. The interaction effect of hydraulic transient conditions of two parallel pump-turbine units in a pumped-storage power plant with considering "S-shaped" instability region: Numerical simulation. *Renew. Energy* **2018**, *118*, 896–908. [CrossRef]
10. Hannett, L.N.; Feltes, J.W.; Fardanesh, B.; Crean, W. Modeling and control tuning of a hydro station with units sharing a common penstock section. *IEEE Trans. Power Syst.* **1999**, *14*, 1407–1414. [CrossRef]
11. Pan, W.; Zhu, Z.; Liu, T.; Liu, M.; Tian, W. Optimal control for speed governing system of on-grid adjustable-speed pumped storage unit aimed at transient performance improvement. *IEEE Access* **2021**, *9*, 40445–40457. [CrossRef]
12. Zhang, C.; Peng, T.; Li, C.; Fu, W.; Xia, X.; Xue, X. Multiobjective optimization of a fractional-order PID controller for pumped turbine governing system using an improved NSGA-III algorithm under multiworking conditions. *Complexity* **2019**, *2019*, 5826873. [CrossRef]
13. Xu, Y.; Zhou, J.; Xue, X.; Fu, W.; Zhu, W.; Li, C. An adaptively fast fuzzy fractional order PID control for pumped storage hydro unit using improved gravitational search algorithm. *Energy Convers. Manag.* **2016**, *111*, 67–78. [CrossRef]
14. Hou, J.; Li, C.; Guo, W.; Fu, W. Optimal successive start-up strategy of two hydraulic coupling pumped storage units based on multi-objective control. *Electr. Power Energy Syst.* **2019**, *111*, 398–410. [CrossRef]

15. Mirjalili, S.; Saremi, S.; Mirjalili, S.M.; Coelho, L.D.S. Multi-objective grey wolf optimizer: A novel algorithm for multi-criterion optimization. *Expert Syst. Appl.* **2016**, *47*, 106–119. [CrossRef]
16. Zhang, F.; Yang, C.; Zhou, X.; Gui, W. Fractional-order PID controller tuning using continuous state transition algorithm. *Neural Comput. Appl.* **2018**, *29*, 795–804. [CrossRef]
17. Zhou, J.; Chen, Y. Discussion on stochastic analysis of hydraulic vibration in pressurized water diversion and hydropower systems. *Water* **2018**, *10*, 353. [CrossRef]
18. Sim, W.-G.; Park, J.-H. Transient analysis for compressible fluid flow in transmission line by the method of characteristics. *KSME Int. J.* **1997**, *11*, 173–185. [CrossRef]
19. Yang, W.; Norrlund, P.; Bladh, J.; Yang, J.; Lundin, U. Hydraulic damping mechanism of low frequency oscillations in power systems: Quantitative analysis using a nonlinear model of hydropower plants. *Appl. Energy* **2018**, *212*, 1138–1152. [CrossRef]
20. Lai, X.; Li, C.; Guo, W.; Xu, Y.; Li, Y. Stability and dynamic characteristics of the nonlinear coupling system of hydropower station and power grid. *Commun. Nonlinear Sci. Numer. Simul.* **2019**, *79*, 104919. [CrossRef]
21. Li, C.; Mao, Y.; Yang, J.; Wang, Z.; Xu, Y. A nonlinear generalized predictive control for pumped storage unit. *Renew. Energy* **2017**, *114*, 945–959. [CrossRef]
22. Li, J.; Hu, Q.; Yu, J.; Li, Q. Study on S-shaped characteristic of Francis reversible unit by on-site test and CFD simulation. *Sci. China Technol. Sci.* **2013**, *56*, 2163–2169. [CrossRef]
23. Xu, B.; Chen, D.; Tolo, S.; Patelli, E.; Jiang, Y. Model validation and stochastic stability of a hydro-turbine governing system under hydraulic excitations. *Int. J. Electr. Power Energy Syst.* **2018**, *95*, 156–165. [CrossRef]
24. Zuo, Z.; Fan, H.; Liu, S.; Wu, Y. S-shaped characteristics on the performance curves of pump-turbines in turbine mode–A review. *Renew. Sustain. Energy Rev.* **2016**, *60*, 836–851. [CrossRef]
25. Zhao, Z.; Yang, J.; Yang, W. Study on the real-time accurate model of pumped storage unit based on equivalent circuit. *J. Hydraul. Eng.* **2019**, *50*, 475–487.
26. Yang, W.; Yang, J.; Guo, W.; Zeng, W.; Wang, C.; Saarinen, L.; Norrlund, P. A mathematical model and its application for hydro power units under different operating conditions. *Energies* **2015**, *8*, 10260–10275. [CrossRef]
27. Maiti, D.; Biswas, S.; Konar, A. Design of a fractional order PID controller using particle swarm optimization technique. *arXiv* **2008**, arXiv:0810.3776.
28. Song, H.J. A method based on objective adjacent scale for multi-objective decision-making and its application. *Math. Pract. Theory* **2004**, *5*, 30–36.

energies

MDPI

Article

Degradation Trend Prediction of Hydropower Units Based on a Comprehensive Deterioration Index and LSTM

Yunhe Wang [1], Zhihuai Xiao [1,*], Dong Liu [2,3], Jinbao Chen [1], Dong Liu [4] and Xiao Hu [5]

[1] School of Power and Mechanical Engineering, Wuhan University, Wuhan 430072, China
[2] College of Energy and Power Engineering, North China University of Water Resources and Electric Power, Zhengzhou 450045, China
[3] School of Civil and Hydraulic Engineering, Huazhong University of Science and Technology, Wuhan 430074, China
[4] China Yangtze Power Co., Ltd., Technical Center, Yichang 443000, China
[5] Department of Power Electronics Engineering, Hubei Water Resources Technical College, Wuhan 430200, China
* Correspondence: xiaozhihuai@126.com

Abstract: Deterioration trend prediction of hydropower units helps to detect abnormal conditions of hydropower units and can prevent early failures. The reliability and accuracy of the prediction results are crucial to ensure the safe operation of the units and promote the stable operation of the power system. In this paper, the long short-term neural network (LSTM) is introduced, a comprehensive deterioration index (CDI) trend prediction model based on the time–frequency domain is proposed, and the prediction accuracy of the situation trend of hydropower units is improved. Firstly, the time–domain health model (THM) is constructed with back-propagation neural network (BPNN) and condition parameters of active power, guide vane opening and blade opening and the time–domain indicators. Subsequently, a frequency-domain health model (FHM) is established based on ensemble empirical mode decomposition (EEMD), approximate entropy (ApEn), and k-means clustering algorithm. Later, the time–domain degradation index (TDI) is developed according to THM, the frequency-domain degradation index (FDI) is constructed according to FHM, and the CDI is calculated as a weighted sum by TDI and FDI. Finally, the prediction model of LSTM is proposed based on the CDI to achieve degradation trend prediction. In order to validate the effectiveness of the CDI and the accuracy of the prediction model, the vibration waveform dataset of a hydropower plant in China is taken as a case study and compared with four different prediction models. The results demonstrate that the proposed model outperforms other comparison models in terms of predicting accuracy and stability.

Keywords: hydropower units; degradation trend prediction; comprehensive deterioration index; long and short-term neural network; ensemble empirical mode decomposition; approximate entropy

Citation: Wang, Y.; Xiao, Z.; Liu, D.; Chen, J.; Liu, D.; Hu, X. Degradation Trend Prediction of Hydropower Units Based on a Comprehensive Deterioration Index and LSTM. *Energies* **2022**, *15*, 6273. https://doi.org/10.3390/en15176273

Academic Editor: Chirag Trivedi

Received: 31 July 2022
Accepted: 21 August 2022
Published: 28 August 2022

1. Introduction

Hydropower units, as the critical equipment for hydropower energy conversion, have always been a focus of attention in the power industry for their safety and stability [1–7]. Along with the continuous development of the unit to the large scale as well as the complex, the degree of integration is getting higher and higher, and the structure is also becoming more and more sophisticated [6]. With the increase in accumulated operation time, hydropower units are prone to abnormal vibration, equipment exhaustion, unit deterioration, and other occurrences [5]. As the deterioration degree increases, the equipment performance of the unit will decline gradually until equipment breakdown happens [7]. Not only will the safe and stable operation of hydropower units and power stations be affected, but this will also bring about economic losses such as the additional cost of maintenance. Consequently, in considering the safety and stability of the hydropower unit and the power

system, it is helpful to accurately predict the operating status trend of the hydropower unit to prevent early failure by detecting abnormal conditions of the hydropower unit. In this way, scientific and reliable maintenance plans and measures can be planned to optimize the comprehensive benefits of power plant operation. It is, therefore, of major significance to conduct research related to the condition trend prediction of hydropower units [1–7].

At this time, the research on health performance trend prediction of hydropower units is still at the initial stage, and the research experience of rotating machinery is summarized that the equipment quality degradation trend prediction is classified into three steps: (a) establishing a health state model; (b) constructing deterioration index (DI); and (c) achieving the trend prediction of the hydropower unit degradation [1]. The construction of a sensible equipment health state model, the proposal of DI that actually describe the operating state of the unit, and the adoption of an accurate predictive trend prediction model are the essential elements to realize the trend prediction of hydropower unit deterioration. In the existing domestic and international studies, the health model (HM) is constructed by analyzing the correlation between the stability parameters reflecting the operating condition of the unit and the working condition parameters. As abnormal vibration is one of the main causes of unit performance deterioration, the stabilization-related signals such as vibration and oscillation of the unit's shaft system can well describe the operating condition of the unit. Examples of stability parameters used to construct the HM in the current study are the original monitoring data, such as the original measured point values of frame vibration and shaft oscillation, sometimes domain indicator values, such as peak-to-peak and standard deviation (SD), and related working condition parameters, such as working head, active power, and guide vane opening, etc., which can be one-dimensional or multidimensional [1–16]. Shan et al. [1] used back-propagation (BPNN) in their study to establish a health state model with working condition parameters and horizontal vibration values of the Y-direction of the lower bracket. The relative error between the vibration health value and the measured vibration value was used as the DI. And the multi-objective particle swarm algorithm was used to optimize the parameters of the kernel extreme learning machine, and the optimized kernel extreme learning machine model was used to construct the prediction model. Fu et al. [2] applied modal decomposition to the turbine guide Y-direction oscillation monitoring data, aggregated and reconstructed the obtained modal components, and calculated the phase space matrix of each reconstructed modal component, as well as used support vector machines to predict each phase space matrix and summed the predicted values of each component to obtain the final predicted value of the oscillation degree and to achieve the deterioration prediction of the unit operating condition assessment. An et al. [7] developed an HM based on the radial basis function neural network (RBF) for the vibration peaks in the horizontal direction of the upper bracket of the unit and the working condition parameters and calculated the ratio of the health value to the measured value to obtain the unit degradation degree. This time series of the unit degradation degree is decomposed into several intrinsic mode functions (IMFs), and the complexity of the modal components is determined by calculating the approximate entropy (ApEn) of each modal component. When the ApEn is high, the RBF neural network is selected to predict the series. When the ApEn is small, a gray-system model is selected to predict the sequence, and the predictions of the decomposed components are summed to obtain the prediction results of the initial time series. In a similar way, An et al. [8] constructed an HM based on the horizontal vibration of the upper support and the water head and active power. The ratio of the true value to the healthy value under the current working condition parameters was used to evaluate the degree of unit deterioration for the current working condition. A gray-system model and RBF were used to construct the prediction model. Related research work [15,16] similarly developed HMs containing working head and active power for the prediction of the degradation trend of hydropower units.

After analysis of the above studies, it can be seen that: (1) The form of constructing the health status model of hydropower units in the existing studies is relatively easy, and most of the stability parameters for constructing the HM only consider the detection value of the

original single measurement point or a single time-domain index value, and such stability parameters cannot objectively reflect the operating status of the units comprehensively; (2) The form of constructing the DI is also relatively simple, which cannot authentically characterize the state change trend of hydropower units, and the large-scale historical data generated by the condition monitoring system is not effectively applied, and the reliability of its prediction results needs to be advanced [6]. Therefore, to address the shortcomings of constructing unit HM and DI in the current hydropower deterioration trend prediction, it is suggested that a comprehensive deterioration index (CDI) of hydropower units should be constructed with both the time-domain health model (THM) and frequency-domain health model (FHM), so as to comprehensively consider the change characteristics and trends of the operating state of hydropower units in the time-frequency domain to achieve the real-time prediction of hydropower unit deterioration degree. The research objective is to predict the deterioration level of hydropower units in real time.

State trend measurement is a time series prediction problem where the historical state index values are used to predict the future state index values for the purpose of predicting the future operating state of the unit. Whether a time series can predict future data based on historical data is dependent on the correlation between its future and historical data [17]. The time series reflecting the deterioration trend of the hydropower unit is between the unpredictable white noise time series and the fully predictable periodic signal time series, and therefore, it can be considered to be predictable to a reasonable degree. Due to the strong volatility and nonlinearity of the vibration signal, the calculated deterioration indicator series is strongly non-smooth and contains some noisiness, so it is a challenging topic to achieve an accurate prediction of the indicator series [5]. Experts and scholars have conducted relevant studies and proposed some prediction methods [1–19]. Qin et al. [17] established a long short-term memory neural network (LSTM) prediction model for wind speed prediction on the original wind speed series. Wang et al. [18] proposed a short-term wind speed prediction method based on ensemble empirical mode decomposition (EEMD) and an optimized BPNN. Lu et al. [3] proposed a state trend prediction model for hydropower units based on EEMD and genetic algorithm parameter seeking BPNN. Fu et al. [2] established a state trend prediction model for hydropower units based on aggregated EEMD and SVM theory, which can effectively predict the unit state. Yang et al. [19] proposed a prediction model combining wavelet transform and SVM to achieve short-term prediction of vibration signals. Due to the existence of background noise and electromagnetic interference, the state signals of hydropower units are often non-smooth, which can significantly affect the prediction results. Therefore, the signal needs to be pre-processed before building the prediction model [2]. Through the above literature analysis, the complexity and non-stationarity of the hydropower unit vibration signal lead to the inaccuracy of prediction, and the prediction accuracy of the deterioration trend of hydropower units needs to be enhanced further. LSTM has a unique memory and forgetting pattern, which can effectively deal with the long-term dependence of time series and effectively use the historical input information of time series to achieve an accurate prediction of the deterioration trend of hydropower units [17].

Through the above analysis, a trend prediction model for hydropower units based on CDI and LSTM is proposed in this paper. Firstly, a THM based on BPNN is constructed, and the Sparrow Search Algorithm (SSA) is used to optimize the parameters of BPNN; meanwhile, an FHM based on EEMD combined with approximate entropy and K-mean clustering is constructed; secondly, the time-domain deterioration index (TDI) and frequency-domain deterioration index (FDI) are calculated separately, in particular, the TDI is the variation of the real-time value relative to the health value, and the FDI is the Euclidean distance between the real-time feature vector and the health center vector. After a while, the CDI is obtained through weighted calculation, which can comprehensively and objectively reflect the operating trend and deterioration degree of the unit; a series of smooth modal components are obtained by modal decomposition of the CDI, and the LSTM-based prediction model is constructed for each modal component to make a

prediction, and the prediction results of each component are summed to obtain the final prediction result, which reflects the future operating status of the hydropower unit. In this paper, the validity of the CDI to characterize the operating status of hydropower units and the validity of the prediction model to reflect the deterioration trend of the units are examined by the actual operation cases of a hydropower plant in China.

2. Theoretical Background

2.1. SSA Algorithm and BPNN

An artificial neural network is a mathematical model established by simulating the structure of the human brain. BPNN is a feed-forward neural network with the forward transmission of signal and reverse transmission of error. Although it is widely used, there are disadvantages, such as the tendency to fall into local minima and slow convergence speed [20–23]. The setting of initial weights and thresholds of BPNN has a strong influence on the training effect of the network. In this paper, the initial values of BPNN weights and thresholds are optimized using the SSA, and the neural network is trained twice to achieve the global optimum.

Sparrow Search Algorithm (SSA) is a swarm intelligence algorithm proposed in 2020 based on the optimization of social features of a population. The algorithm simulates sparrow foraging and anti-predation behaviors, distinguishes individuals into finders, followers, and vigilantes, and accomplishes the acquisition of resources by continuously updating individual positions, each of which corresponds to a solution, thus obtaining the mathematically optimal solution. Compared with traditional algorithms, the sparrow search algorithm has a simpler structure, is easy to achieve, and has fewer control parameters and better local search capability [24]. If the number of individuals in the population is n, then the population consisting of all individuals can be expressed as shown in Equation (1).

$$X = [X_1, X_2, \cdots X_n]^T \tag{1}$$

where X_i represents an individual in the set $i = 1, 2, \cdots, n$.

The respective corresponding fitness function for each individual is shown in Equation (2).

$$F = [f(X_1), f(X_2), \cdots f(X_n)]^T \tag{2}$$

where $f(X_i)$ represents the fitness of each individual in the set $i = 1, 2, \cdots, n$.

Where the discoverer location is updated in the following way, as shown in Equation (3).

$$x_{i,j}^{t+1} = \begin{cases} x_{i,j}^t \cdot \exp\left(\frac{-i}{\alpha \times iter_{\max}}\right), & R_2 < ST \\ x_{i,j}^t + Q \cdot L, & R_2 \geq ST \end{cases} \tag{3}$$

where t represents the number of current iterations, $x_{i,j}^t$ represents the position of the ith individual in the tth generation in the jth dimension, α is a random number, $\alpha \in (0, 1)$, $iter_{\max}$ is the maximum number of iterations, R_2 represents the warning value, $R_2 \in [0, 1]$, ST represents the safety threshold, $ST \in [0.5, 1]$, Q is a random number obeying normal distribution, L is the all-1 matrix of $1 \times dim$, and the dim represents the dimensionality.

The position of the follower is updated as shown in Equation (4).

$$x_{i,j}^{t+1} = \begin{cases} Q \cdot \exp\left(\frac{x_{worst}^t - x_{i,j}^t}{i^2}\right), & i > \frac{n}{2} \\ x_p^{t+1} + \left|x_{i,j}^t - x_p^{t+1}\right| \cdot A^+ \cdot L, & i \leq \frac{n}{2} \end{cases} \tag{4}$$

where x_{worst}^t denotes the position of the worst adapted individual in the tth generation, and x_p^{t+1} denotes the position of the best adapted individual in the $t+1th$ generation. A denotes the matrix of $1 \times dim$, and each element is randomly preset to -1 or 1, $A^+ = A^T(AA^T)^{-1}$.

The vigilantes' positions are updated, as shown in Equation (5).

$$x_{i,j}^{t+1} = \begin{cases} x_{best}^{t} + \beta \cdot \left| x_{i,j}^{t} - x_{best}^{t} \right|, & f_i \neq f_g \\ x_{best}^{t} + k \cdot \left(\frac{\left| x_{i,j}^{t} - x_{best}^{t} \right|}{|f_i - f_w| + \varepsilon} \right), & f_i = f_g \end{cases} \tag{5}$$

where x_{best}^{t} indicates the global optimal position in the tth generation, β is the control step, following a normal distribution with a mean 0 and variance 1, $k \in [-1, 1]$, k is a random number, and ε is set as a constant to avoid the denominator being 0. f_i denotes the fitness value of the current individual; f_g and f_w denote the fitness values of the current global optimal and worst individuals, respectively.

2.2. Empirical Modal Decomposition and Approximate Entropy

2.2.1. Ensemble Empirical Mode Decomposition

Empirical mode decomposition (EMD), proposed by Huang et al. [25], is an effective method for adaptive analysis of nonlinear and non-smooth signals. The basic idea of EMD is to perform adaptive smoothing on the original signal and obtain a series of IMFs by decomposing it step by step. Ensemble empirical mode decomposition (EEMD) improves on the traditional EMD decomposition by adding Gaussian white noise to the original data several times to compose a new signal, and the uniform frequency distribution of Gaussian white noise effectively avoids the modal aliasing phenomenon that exists when using EMD for signal decomposition [26]. The EEMD decomposition steps are as Equations (6)–(8).

(1) Add the white noise $n_i(t)$ with a set noise level to the original signal $x_i(t)$ to form the new signal:

$$x_i(t) = x(t) + n_i(t) \tag{6}$$

where $n_i(t)$ denotes the ith additive white noise sequence, $x_i(t)$ denotes the additional noise signal of the ith trial, $i = 1, 2, \cdots, M$, M is the overall average number of times, which is the number of times white noise is added, and its value ranges from 100 to 300.

(2) To decompose the synthesized new signal by EMD, a series of IMFs components $c_{ij}(t)$, and a residual term $r_{ij}(t)$ are obtained:

$$x_i(t) = \sum_{j=1}^{J} c_{ij}(t) + r_{ij}(t) \tag{7}$$

The number of IMF components is m, which $c_{ij}(t)$ is the jth component of the decomposition after adding white noise for the ith time, J is the number of IMFs.

(3) Repeat steps (1) and (2) M times, and average the overall results, and the result is the IMF component of the original signal $x(t)$ obtained by EEMD decomposition:

$$c_j(t) = \frac{1}{M} \sum_{i=1}^{M} c_{ij}(t) \tag{8}$$

where $c_j(t)$ is the jth IMF of the EEMD decomposition, $i = 1, 2, \cdots, M$, $j = 1, 2, \cdots, J$. Through the EEMD algorithm, the signal is decomposed into a series of IMF components at different time scales, and the fluctuations of each IMF component are smoother compared to the original signal. The advantage of smoothly processing the nonlinear nonstationary indicator series by using EEMD decomposition to avoid the errors due to direct prediction could, in theoretical terms, lead to more accurate prediction results [27].

2.2.2. Approximate Entropy

ApEn characterizes the complexity of a sequence, and the higher the complexity of the sequence, the higher the approximate entropy value [28]. Approximate entropy is widely

used in biomedical signal detection [29] and mechanical equipment fault diagnosis [30], and it has corresponding applications in the field of financial system complexity measurement [31]. Approximate entropy is resistant to strong external interference, does not require a long data length, and can be applied to deterministic signals or noisy signals.

For the data sequence $\{x_1, x_2, \cdots, x_N\}$, its ApEn is calculated as follows [28].

(1) Form a set of $m-dimensional$ vectors of $\{x_i\}$ in a continuous order:

$$\boldsymbol{X}(i) = [x(i), x(i+1), \cdots x(i+m-1)] \tag{9}$$

where X_i represents an individual in the set, $i = 1, 2, \cdots, N-m+1$, N is the number of time series data points and m is the length of the window.

(2) Define the distance $d[\boldsymbol{X}(i), \boldsymbol{X}(j)]$ between $\boldsymbol{X}(i)$ and $\boldsymbol{X}(j)$ to be the one with the largest value of the difference between the two corresponding elements, as follows:

$$d[\boldsymbol{X}(i), \boldsymbol{X}(j)] = \max|x(i+k) - x(j+k)|,\ k \in (1, m-1) \tag{10}$$

where for each value of i, calculate the distance $d[\boldsymbol{X}(i), \boldsymbol{X}(j)]$ between $\boldsymbol{X}(i)$ and the remaining corresponding elements of $\boldsymbol{X}(j)$ $(j = 1, 2, \cdots, N-m+1, j \neq i)$.

(3) Iterate through each value, count the number of $d[\boldsymbol{X}(i), \boldsymbol{X}(j)] < r$ (r is the similarity tolerance, which is a pre-determined threshold, $r > 0$), and compare the value with the total number of vectors $N-m+1$, which denote as $C_i^m(r)$.

$$C_i^m(r) = \frac{1}{N-m+1}\text{num}\{d[\boldsymbol{X}(i), \boldsymbol{X}(j)] < r\} \tag{11}$$

where $i = 1, 2, \cdots, N-m+1$, $j = 1, 2, \cdots, N-m+1$, $j \neq i$.

(4) Firstly, perform the logarithmic operation on $C_i^m(r)$, and then find its average value for all i, denoted as $\Phi^m(r)$, as follows:

$$\Phi^m(r) = \frac{1}{N-m+1}\sum_{i=1}^{N-m+1}\ln C_i^m(r) \tag{12}$$

(5) Increase the number of dimensions to $m+1$ and repeat steps (1) to (4) to obtain $C_i^{m+1}(r)$ and $\Phi^{m+1}(r)$, as follows:

$$C_i^{m+1}(r) = \frac{1}{N-m}\text{num}\{d[\boldsymbol{X}(i), \boldsymbol{X}(j)] < r\} \tag{13}$$

$$\Phi^{m+1}(r) = \frac{1}{N-m}\sum_{i=1}^{N-m}\ln C_i^{m+1}(r) \tag{14}$$

(6) The ApEn of the sequence is calculated by the following equation:

$$\text{ApEn}(m, r) = \lim_{N\to\infty}[\Phi^m(r) - \Phi^{m+1}(r)] \tag{15}$$

In practical engineering applications, N is a finite value, at this time, the ApEn of the sequence can be calculated by the following equation:

$$\text{ApEn}(m, r, N) = \Phi^m(r) - \Phi^{m+1}(r) \tag{16}$$

where m is the pattern dimension, given before calculating the approximate entropy; r is the similarity tolerance.

It was shown that the value of $\text{ApEn}(m, r, N)$ is related to the values of m, r, and N [26]. When $m = 2$ and $r = (0.1 \sim 0.25)\sigma_x$ (σ_x is the SD of the original data series $\{x_i\}$), $\text{ApEn}(m, r, N)$ is almost independent of the data length N, as follows:

$$\text{ApEn}(m, r, N) \approx \text{ApEn}(m, r) \tag{17}$$

Therefore, in practical calculations, the sequence length is generally between 100–5000, the mode dimension $m = 2$, and the similarity tolerance $r = (0.1 \sim 0.25)\sigma_x$, which is chosen in this paper as $m = 2$, $r = 0.2\sigma_x$, σ_x is the SD of original data.

2.3. Long Short-Term Memory Neural Network

LSTM is developed on the foundation of a recurrent neural network (RNN) [32], which combines short-term memory and long-term memory through a special gate. The LSTM is based on the recurrent neural network (RNN) [32], which combines short-term memory and long-term memory with a special gate structure so that the network output has a strong correlation with current and historical inputs, solving the issue that the traditional recurrent neural network only has short-term memory, and can effectively use the time series history information to deal with the long-term correlation of time series.

The basic structure of LSTM is divided into three layers: input layer, hidden layer, and output layer. The hidden layer controls the information transmission by setting the threshold unit (gate structure), which gives it a unique memory pattern, and the structure of LSTM is shown in Figure 1.

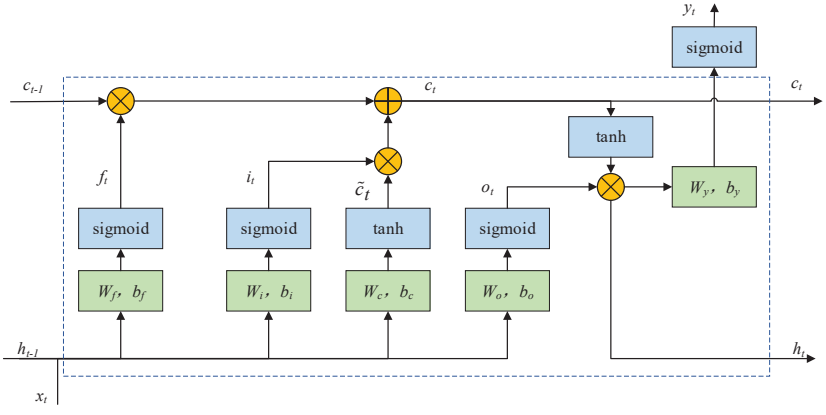

Figure 1. The structure of LSTM.

It can be seen that the LSTM hidden layer contains three main gate structures, namely: forgetting gate, input gate, and output gate. Where the forgetting gate is used to filter to retain the information of neuron c_{t-1} history state at moment $t-1$, the input gate determines the storage of new input information x_t of neuron at moment t, and the output gate is used to control the information delivery of the output value h_t of the hidden layer. According to Figure 1, the forward propagation algorithm of the LSTM can be derived as shown in Equations (18)–(24).

$$f_t = sig(W_f \cdot [h_{t-1} x_t] + b_f) \tag{18}$$

$$i_t = sig(W_i \cdot [h_{t-1} x_t] + b_i) \tag{19}$$

$$\widetilde{c}_t = \tanh(W_c \cdot [h_{t-1} x_t] + b_c) \tag{20}$$

$$c_t = f_t \cdot c_{t-1} + i_t \cdot \widetilde{c}_t \tag{21}$$

$$o_t = sig(W_o \cdot [h_{t-1} x_t] + b_o) \tag{22}$$

$$h_t = o_t \cdot \tanh(c_t) \tag{23}$$

$$y_t = sig(W_y \cdot h_t + b_y) \tag{24}$$

where Equation (18) represents the forgetting gate, Equations (19) and (20) represent the input gate, Equation (21) is the neuron state update expression, Equations (22) and (23) are the output gates, and Equation (24) is the calculation output of the neuron at moment t. x_t is the network input information at moment t, h_{t-1} is the network hidden layer state output value at moment $t-1$, $\widetilde{c}_t$ is the input gate candidate state value, c_{t-1} and c_t is the neuron state at different moments, sig is the $sigmoid$ activation function, W_f, W_i, W_c, W_o, W_y are the corresponding weight matrix, b_f, b_i, b_c, b_o, b_y are the corresponding threshold vectors, and y_t is the network prediction output at moment t.

After completing the forward propagation of the LSTM, it then enters the back-propagation process; that is, the LSTM is extended into a deep network in time order, and the weights and thresholds are updated iteratively using the back-propagation through time (BPTT) algorithm [33] and the chain rule until the optimal solution is obtained.

3. The Proposed Prediction Model Based on the CDI

3.1. Proposed Model

In this paper, in order to detect the failure signs of hydropower units in advance, realize fault warning, provide sufficient time margin for on-site maintenance and repair work, and thus improve the economic and social benefits of power stations, the EEMD-LSTM prediction model based on the CDI (CDI-EEMD-LSTM) in the time-frequency domain is proposed by making full use of the condition monitoring data of the industrialized information platform of hydropower units. The specific flow of the prediction model is shown in Figure 2, which includes four steps.

Step 1: The HMs of hydropower units are constructed, and this section is divided into two steps. The flowchart of Step 1 is shown in Figure 2.

(1) Constructing a THM of the unit based on SSA-BPNN, with the input being the operating parameters of the unit's historical health state and the output being the time-domain indicators of the unit's historical health state.

(2) Constructing an FHM based on EEMD-APEN and K-mean clustering algorithm, EEMD decomposition is performed on the vibration waveform numbers of the unit's historical health state to obtain the ApEn of each modal component, which constitutes a high-dimensional frequency-domain feature vector, and the health center vector of the hydropower unit is obtained by automatic clustering.

Step 2: The HMs and the health center vector are used to construct the CDI of the hydropower unit, which is divided into three steps. The flowchart of Step 2 is shown in Figure 3.

(1) Input the real-time operating parameters into the THM, obtain the health value under the current operating parameters, and calculate the relative error between the health value and the actual value as the TDI.

(2) Obtain the frequency-domain eigenvectors of the real-time waveform data of the unit vibration based on EEMD-ApEn, and calculate the Euclidean distance between the real-time frequency-domain eigenvectors and the health center vector as the FDI.

(3) Weight and sum the TDI and the FDI to construct the CDI in the time–frequency domain for hydropower units.

Step 3: The CDI-EEMD-LSTM prediction model is constructed.

To further improve the accuracy of trend prediction, EEMD is combined with LSTM. The EEMD of the CDI is performed first, the LSTM prediction model is constructed for each modal component obtained, and the fixed-length data is used as the input of the LSTM prediction model. With the superior accuracy of LSTM in time series prediction, each modal component is predicted, and eventually, the future state trend of the unit health index series is obtained by accumulation. The flowchart of Step 3 is shown in Figure 4.

Step 4: Evaluation and analysis of prediction results.

The prediction results of the CDI-EEMD-LSTM model were evaluated.

The process is shown in Figure 5.

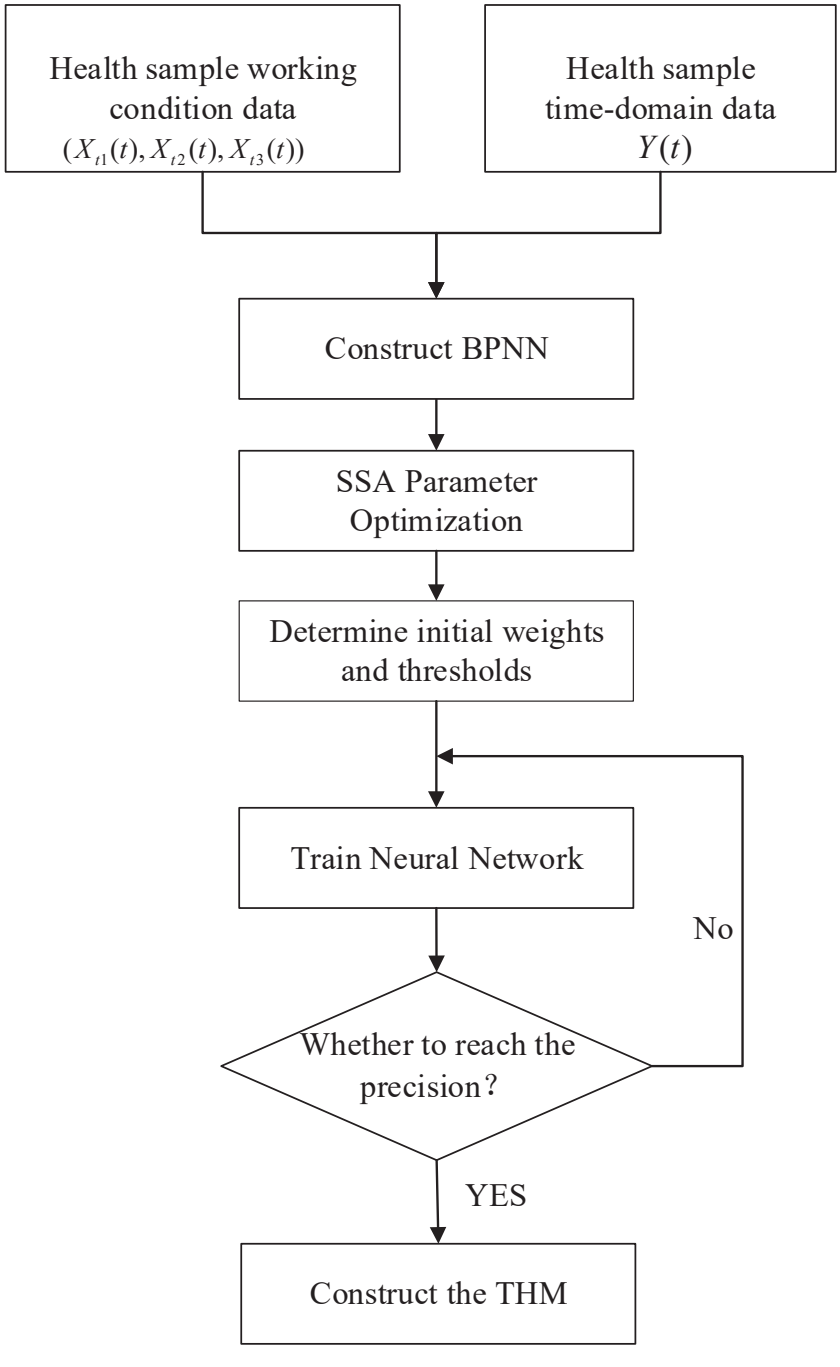

(**a**)

Figure 2. *Cont*.

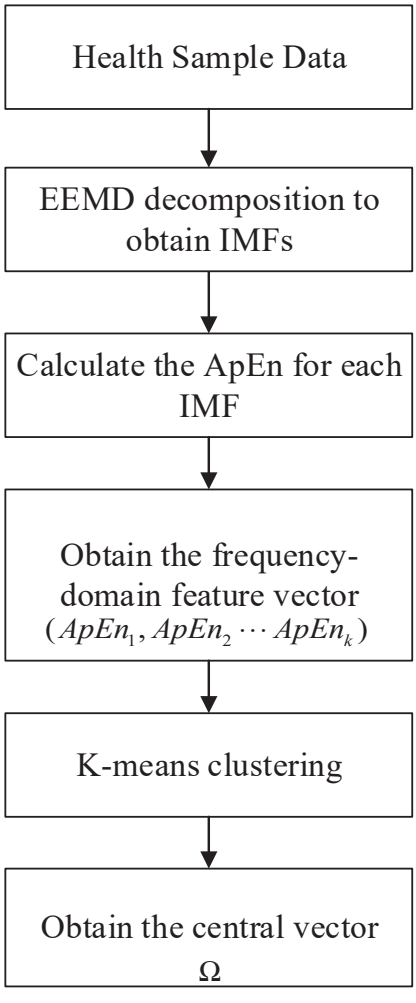

(**b**)

Figure 2. Flowchart of Step 1: (**a**) is the flowchart of constructing THM; (**b**) is the flowchart of constructing FHM.

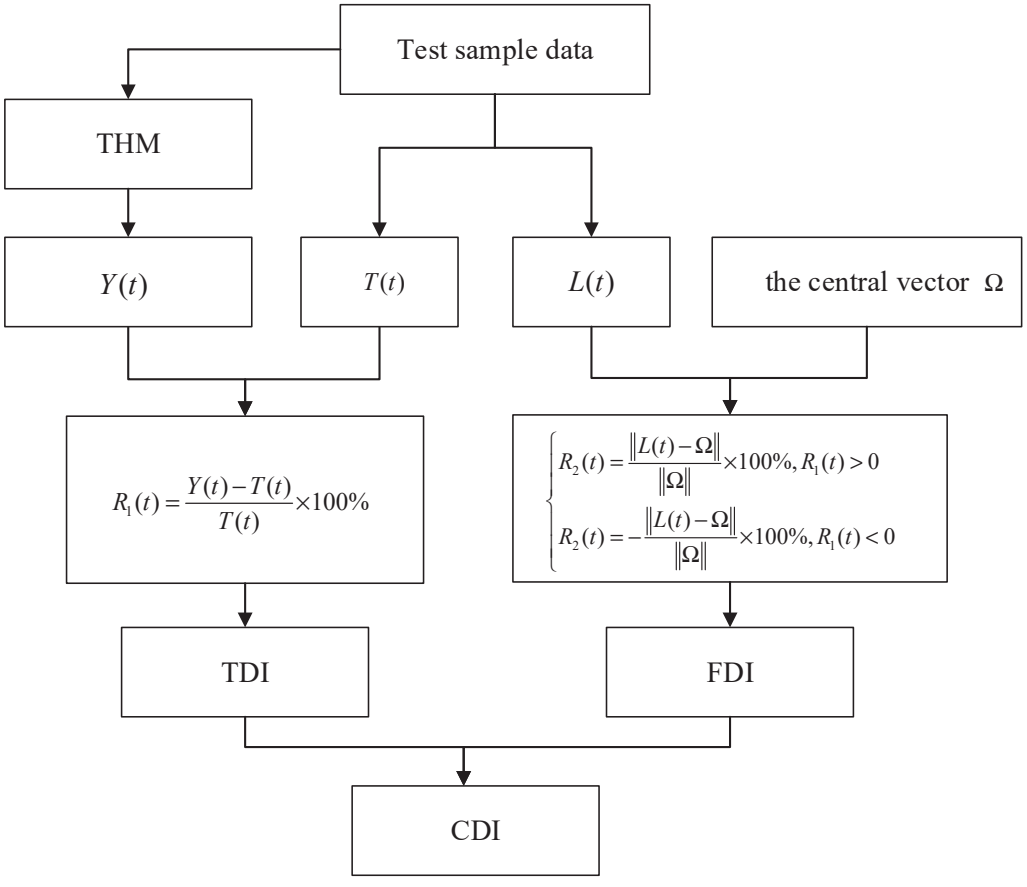

Figure 3. Flowchart of Step 2.

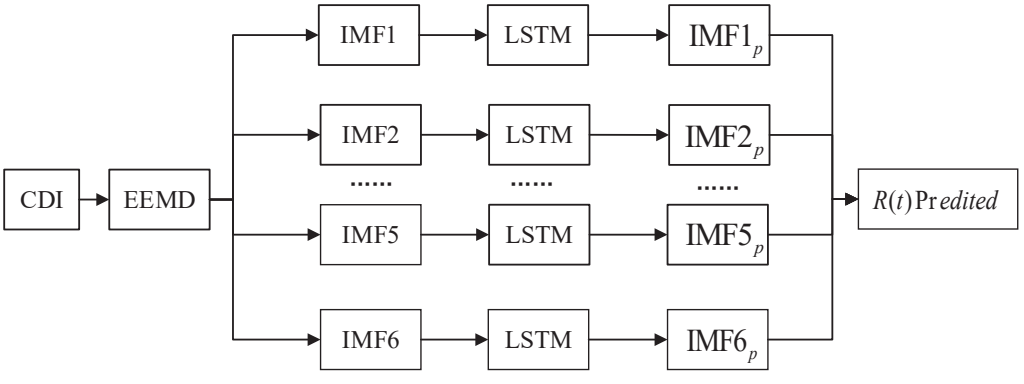

Figure 4. Flowchart of Step 3.

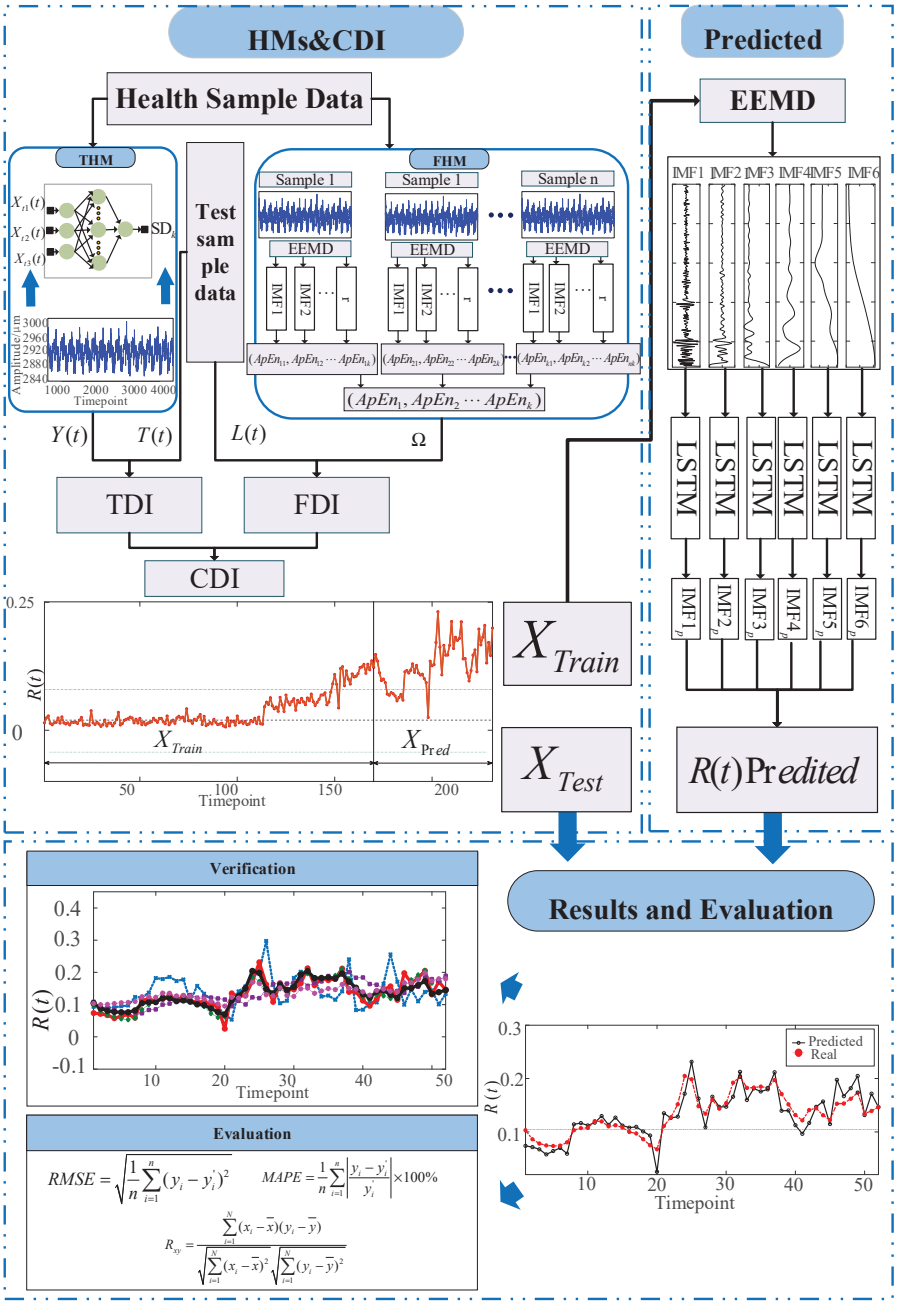

Figure 5. Trend prediction of hydropower unit health status based on CDI.

3.2. Evaluation Indicators

So as to evaluate the effectiveness of SSA-BPNN and CDI-EEMD-LSTM, this paper evaluated the prediction results using mean absolute percentage error (MAPE), root Mean

square error (RMSE), and correlation coefficient (CC). MAPE, RMSE, and CC are calculated as shown in Equations (25)–(27), respectively. The lower the RMSE and MAPE, the higher the accuracy of the model prediction. The CC is used to measure the strength of linear correlation between two variables, and a higher value indicates a higher correlation between the two, which also characterizes the more accurate prediction results.

$$MAPE = \frac{1}{n}\sum_{i=1}^{n}\left|\frac{y_i - y_i'}{y_i'}\right| \times 100\% \tag{25}$$

$$RMSE = \sqrt{\frac{1}{n}\sum_{i=1}^{n}(y_i - y_i')^2} \tag{26}$$

$$R_{xy} = \frac{\sum_{i=1}^{N}(x_i - \overline{x})(y_i - \overline{y})}{\sqrt{\sum_{i=1}^{N}(x_i - \overline{x})^2}\sqrt{\sum_{i=1}^{N}(y_i - \overline{y})^2}} \tag{27}$$

4. Experiment Results and Analysis

Vibration signals contain abundant state characteristics, so they can be employed in engineering applications to assess the health status of equipment [34–36]. The condition information of hydropower units is also embedded in the vibration signals, and the actual conditions of unit operation can be obtained by analysis of the vibration signals of hydropower units [37]. In order to validate its effectiveness and engineering application value, this paper uses actual measurement data of hydropower units for experimental analysis.

A hydroelectric power station unit No. 3 is used as the research object, which is a vertical shaft semi-parachute type. The water turbine type frame is ZZA315-LJ-800, the rated speed is 107.1 r/min, the rated power is 200 MW, the rated head is 47 m, and the generator model is SF200-56/11950. On 28 August 2015, during the start up of Unit No. 3, there were obvious abnormal noises in the upper frame, waterwheel chamber, worm shell and tail pipe, etc. The noise of each department was more intense when the unit was loaded with 200 MW, and there were also obvious vibration and abnormal noises in the cement foundation along the −X direction in the inlet hole of the tail pipe of the hydraulic turbine. On 30 August, it was found that the steel plate of the middle ring of the runner chamber of the No. 3 unit was dislodged, the middle ring and the lower ring had serious cracks, and the blade skirt was seriously damaged.

Through retrospective analysis, the technicians deduced that the lining of the runner chamber fell off between 28 August 2015 at 14:17:03 and 28 August 2015 at 14:37:12. It is caused by the defects in the construction of the runner room, coupled with poor operating conditions, resulting in the fatigue damage of the runner room, the emergence of cracks, and the increase in vibration of the steel structure parts of the runner room, which eventually leads to the combination bolt loosening and shearing, and the rotor blade rubs against the cracked steel plate in the middle ring of the rotor chamber causing the steel plate to be torn and fall off.

A total of 507 sets of data, including point value data and waveform data, were obtained from the power station condition monitoring system before and after the failure of unit No. 3, with a sampling interval of about 20 min. Each set of data contains X and Y pendulum waveforms of the upper guide bearing, X and Y pendulum waveforms of the thrust bearing, X and Y pendulum waveforms of the water guide bearing, and axial vibration A, B, and C waveforms. Each waveform contains 16 key phases, with a total of 4096 points, and the sampling frequency is 458 Hz. Before the failure, unit No. 3 was operating at 63% of guide vane opening, 20% of blade opening, and working head of 50 to 55 m, and the vibration waveform data of axial A direction at the working point near this condition was selected for prediction analysis and verification of unit deterioration trend. All numerical simulation experiments are completed in MATLAB 9.2.

4.1. Constructing the CDI in the Time-Frequency Domain for Hydropower Units

4.1.1. Constructing a Time-Frequency Domain Health Model

Step 1: Constructing a THM for the unit.

The sample data (active power, guide vane opening and blade opening) of the health condition of a hydropower plant hydropower unit No. 3 are used as input, and the SD of the unit's axial A-directional vibration waveform is used as output. Compared with other time-domain indicators, the waveform SD can objectively reflect the operating status of hydropower units, and can identify unit health or fault conditions or even multiple fault categories [38]. The mapping relationship between waveform SD $Y(t)$ and operating parameters $X(t)$ is constructed as Equation (28):

$$Y(t) = f_{SSA-BP}[X_{t1}(t), X_{t2}(t), X_{t3}(t)] \tag{28}$$

where $[X_{t1}(t), X_{t2}(t), X_{t3}(t)] \in X(t)$.

The SD of the axial A-directional vibration waveform $Y(t)$ and the corresponding operating conditions (active power $X_{t1}(t)$, guide vane opening $X_{t2}(t)$ and blade opening $X_{t3}(t)$), of 170 sets were selected when the unit was in the initial healthy state in the middle and early August. Moreover, 110 groups were randomly selected as the training set, 30 groups as the validation set, and 30 groups as the test set for the THM. The original values of the SD of the waveform of the axial A-direction vibration of the unit are shown in Figure 6, where the timepoint is the sample points in chronological order.

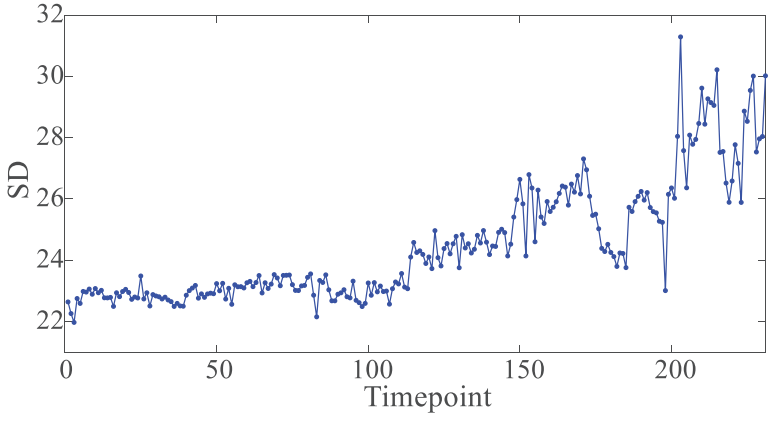

Figure 6. SD of the original axial A-directional vibration waveform.

When using SSA for the initial weights and initial thresholds of BPNN for the optimization search, to avoid over-learning and under-learning, both the initial weights a and thresholds b are set to [−30, 30], and MAPE is selected as the fitness function of SSA. The settings and modeling results of BPNN are shown in Table 1 and Figure 7.

Table 1. The parameters of BPNN.

Epochs	Training Function	Goal	Learning Rate
5000	traingda	$1e^{-7}$	0.1

From Table 1 and Figure 7, it is observed a good fit between the fitting output calculated by the THM and the real SD. The RMSE of the THM is 0.1806 and MAPE is 30.23%, which shows that the error values are low and the model is fitted with high precision. It can accurately reflect the relationship between the operating parameters and the time-domain

characteristics under the unit's health condition and provides a basis for constructing a TDI sequence for the unit.

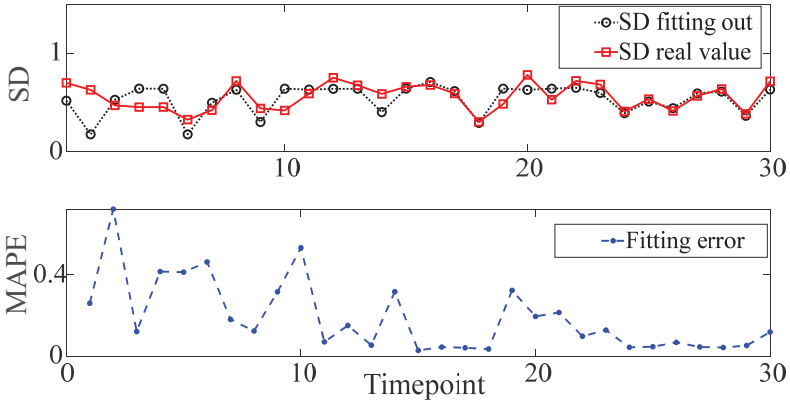

Figure 7. Fitting results and fitting errors of SSA-BP HM.

Step 2: Construct the FHM and a frequency-domain health center feature vector.

While time-domain features can characterize the unit deterioration condition to a certain degree, in practice, the frequency-domain features of the vibration signal can reflect more information about the unit status, and the nonlinearity and non-stability of the unit deterioration trend will also be reflected by the signal frequency-domain features. Therefore, it is necessary to consider the frequency-domain characteristics of the unit to construct the CDI.

In this paper, to construct an FHI based on EEMD decomposition with ApEn and K-mean clustering, the unit frequency-domain feature vectors are extracted based on EEMD-ApEn, and the central feature vector in the health state is obtained using K-mean clustering. The specific steps implemented in this paper are shown below.

(1) 170 sets of axial A-directional vibration waveform data corresponding to the THM are selected, and EEMD is performed for each set of waveform data with noise level $k = 0.2$, overall mean $M = 100$, and the number of decompositions is 6. The eigenmodal components $IMF1 \sim IMF6$ are obtained after decomposition.

(2) Calculate the ApEn of each modal component separately to obtain the frequency-domain feature vector L in the health state.

$$L = [ApEn1, ApEn2, \cdots, ApEn6] \tag{29}$$

(3) The feature vectors of the unit health samples are automatically clustered using the K-means method to obtain the cluster center Ω in the health condition, and the cluster center Ω is the health center vector of the FHM. This health center vector value characterizes the frequency-domain feature vector possessed by the unit during normal operation, so it can be used as the health vector to evaluate the unit deterioration from the frequency-domain perspective.

4.1.2. Constructing the Comprehensive Degradation Index

This section is divided into three steps.

Step 1: Obtain a sequence of TDI.

A sequence of TDI is constructed from the sample data of the unit in the process of developing from the healthy state to the fault state. A number of 230 sets of working parameters of the unit are selected in chronological order, and the working condition data during the development of the unit fault are input into Equation (28) to obtain the health value $Y(t)$ under the current corresponding working condition, and the relative error

between the actual value $T(t)$ and the health value $Y(t)$ is adopted as the TDI of the unit, and the mathematical expression is Equation (30).

$$R_1(t) = \frac{Y(t) - T(t)}{T(t)} \times 100\% \tag{30}$$

where $R_1(t)$ is the sequence of vibration signal time-domain deterioration indicators as shown in Figure 8, which represents the deviation degree and deviation direction of the time-domain characteristics of the unit relative to the normal value in the physical sense.

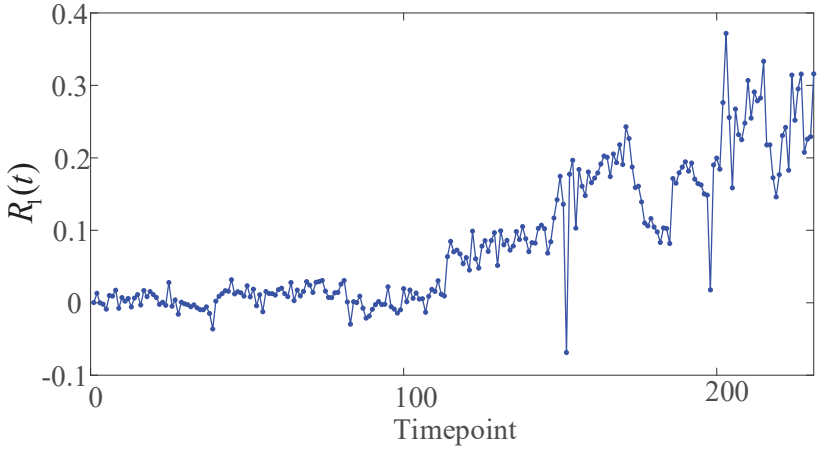

Figure 8. Unit time-domain degradation index sequence $R_1(t)$.

The actual values of SD of axial vibration waveforms are compared with the healthy values, as shown in Figure 9. From Figure 9, it can be observed that the difference between the actual value series and the healthy value series is not significant at the beginning of operation, and the unit is well in health at this time. With an increasing operating time of the unit, the gap between the actual value series and the healthy value series gradually increases, the operating performance of the unit gradually deteriorates, and the TDI deviates toward the trend of more than the healthy value and the deviation degree increases sharply.

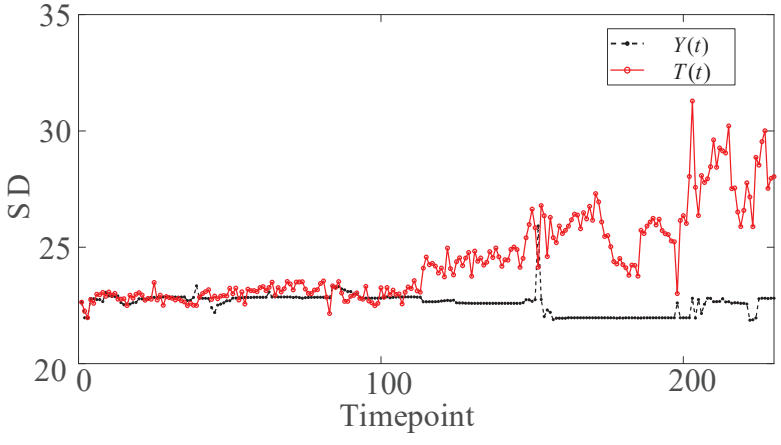

Figure 9. Comparison between $T(t)$ and $Y(t)$.

As shown in Figures 5 and 6, the TDI series has a strong non-stationary nature with fluctuating changes. The degree of deviation of the healthy value generally has an increasing trend, indicating that the condition of the unit gradually deteriorates with increasing operation time.

Step 2: Obtain a sequence of FDI.

The 230 sets of vibration waveform data corresponding to the CDI are selected, and the frequency-domain features of the unit are extracted based on EEMD-ApEn to obtain the frequency-domain feature vector collection $L(t)$, and the Euclidean distance between the $L(t)$ and the health center vector Ω is calculated to obtain the sequence of FDI $R_2(t)$. $R_2(t)$ is calculated as Equation (31).

$$\begin{cases} R_2(t) = \frac{\|L(t)-\Omega\|}{\|\Omega\|} \times 100\%, R_1(t) > 0 \\ R_2(t) = -\frac{\|L(t)-\Omega\|}{\|\Omega\|} \times 100\%, R_1(t) < 0 \end{cases} \tag{31}$$

where $R_2(t)$ is sequence of the FDI shown in Figure 10, which physically indicates the deviation of the unit frequency-domain characteristics relative to the normal value, and constant positive because of the Euclidean distance. $L(t)$ is the approximate entropy eigenvector of the actual measured vibration signal at time t. In order to ensure the homogeneity between the frequency-domain and time-domain degradation directions to avoid the phenomenon of mutual cancellation, $R_2(t)$ and $R_1(t)$ need to have the same sign, which means the TDI and FDI deviate from the normal value at the moment of the same time to maintain the same direction.

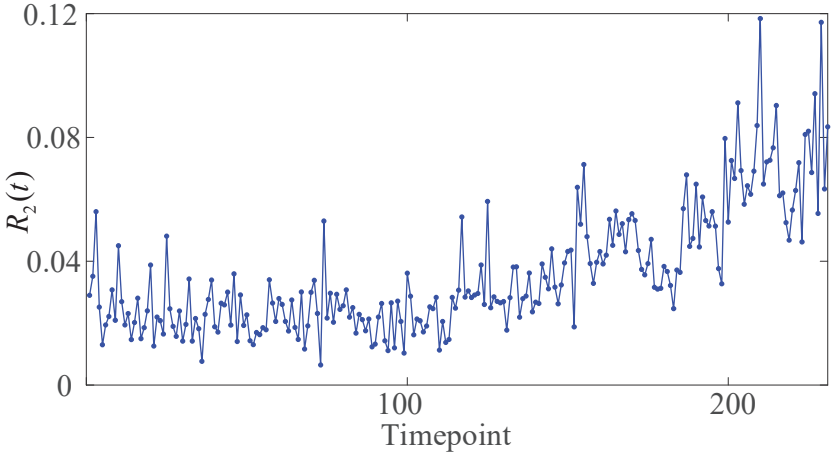

Figure 10. The sequence of FDI $R_2(t)$.

As shown in Figure 10, the $R_2(t)$ series has a strong non-smoothness and fluctuates with an overall increasing trend, which also indicates that the FDI can reflect the changing characteristics of the unit state gradually deviating from the healthy state with increasing operation time.

Step 3: Obtain the CDI in the time–frequency domain.

The TDI $R_1(t)$ and the FDI $R_2(t)$ are weighted and summed to obtain the time series of CDI in the time–frequency domain of hydropower units, as shown in Equation (32).

$$R(t) = \omega_1 \cdot R_1(t) + \omega_2 \cdot R_2(t) \tag{32}$$

where ω_1 and ω_2 are the weighting coefficients. To enhance the sensitivity of the degradation index to the abnormal data, the weights are taken as shown in Equations (33) and (34).

$$\omega_1 = \frac{|R_2(t)|}{|R_1(t)| + |R_2(t)|} \tag{33}$$

$$\omega_2 = \frac{|R_1(t)|}{|R_1(t)| + |R_2(t)|} \tag{34}$$

As seen in Figure 11, the $R(t)$ series indicates that the unit health deteriorates gradually with increasing operating time.

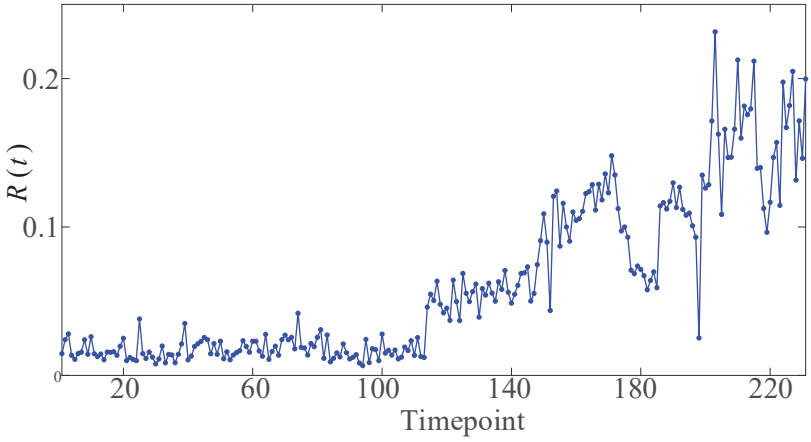

Figure 11. The sequence of CDI in the time–frequency domain of the unit $R(t)$.

4.2. Prediction Model of Unit Deterioration Trend Based on CDI-EEMD-LSTM

Based on the unit CDI obtained in Section 4.1, combined with the signal processing capability of EEMD and the time series prediction capability of LSTM, a forecasting investigation on the future trend of unit health status is carried out. To be consistent with engineering practice, the first 3/4 of the series in chronological order is used as the training set X_{Train} and the remaining part as the test set X_{Pred}. In the CDI-EEMD-LSTM, the CDI sequence can be decomposed into different frequency modal components by EEMD, and the fixed-length data in each modal component is used as the input of the LSTM, and the powerful nonlinear fitting ability of the LSTM is used to make single-step prediction for each modal component, and the prediction results of each modal component are accumulated to finally output the single-step prediction results of the CDI sequence. RMSE, MAPE, and similarity coefficient CC are employed as prediction effectiveness evaluation metrics, which are calculated as shown in Equations (25)–(27). The division of the training set and the prediction test set of the integrated degradation index is shown in Figure 12.

(1) Determining the input step length

The length of input data in LSTM affects the effect of prediction; too long input length will lead to information redundancy and affect the efficiency of the prediction model; too short will affect the accuracy of the prediction model. Firstly, the input length of the CDI prediction model is calculated by computing the autocorrelation coefficient of the index series. The autocorrelation of the CDI time series is shown in Figure 13, and the autocorrelation coefficient of each index is still above the 95% confidence level when the delay step is <10. In order to calculate the prediction effect of time series with different input step lengths within delay Step 10, RMSE, MAPE, and similarity coefficient R were used as evaluation indicators. The test was repeated 20 times, and the results are shown

in Table 2. When the input length is 8, the RMSE and MAPE metrics of the prediction results are the smallest, and the similarity coefficient CC is the largest, so the input length of the model is determined to be 8 and the prediction step is 1, that is, LSTM is an 8-input, 1-output network.

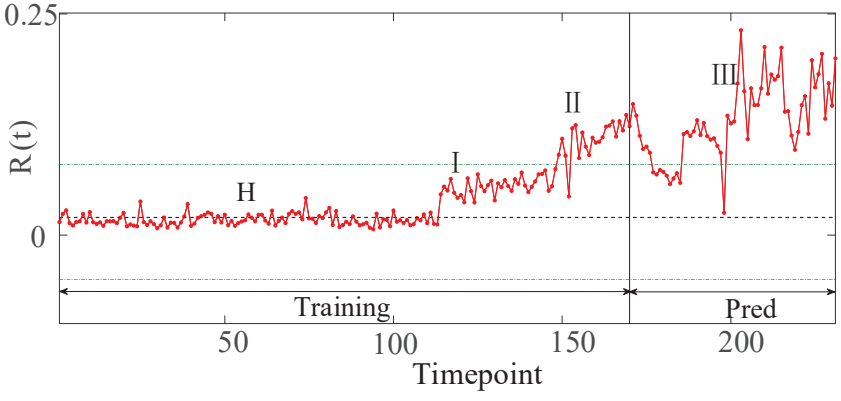

Figure 12. Division of training set and prediction test set of CDI.

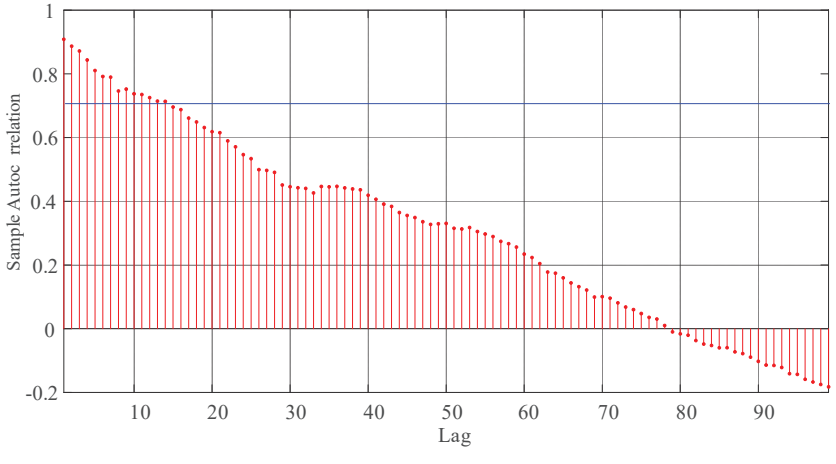

Figure 13. Sequential autocorrelation analysis of CDI.

Table 2. Evaluation of prediction effects with different input lengths.

Input Length	RMSE	MAPE/%	CC
2	0.0320	22.66	0.7563
4	0.0306	23.64	0.7404
6	0.0310	24.86	0.7360
8	0.0292	21.67	0.9030
10	0.0334	26.48	0.6754

(2) Signal decomposition

Firstly, a series of indicators h is decomposed by EEMD to obtain each modal component, as shown in Figure 14. In terms of the number of sets and decomposition noise intensity selection, with the increase of the number of sets, the effect of Gaussian white noise added in the EEMD process on the decomposition effect gradually decreases and

stabilizes, and different studies have shown that the effect of noise intensity on the result error is also relatively mild [39,40], so when using EEMD to process the time series of the degradation index, the number of sets is set to 100, and the auxiliary noise intensity is 0.2.

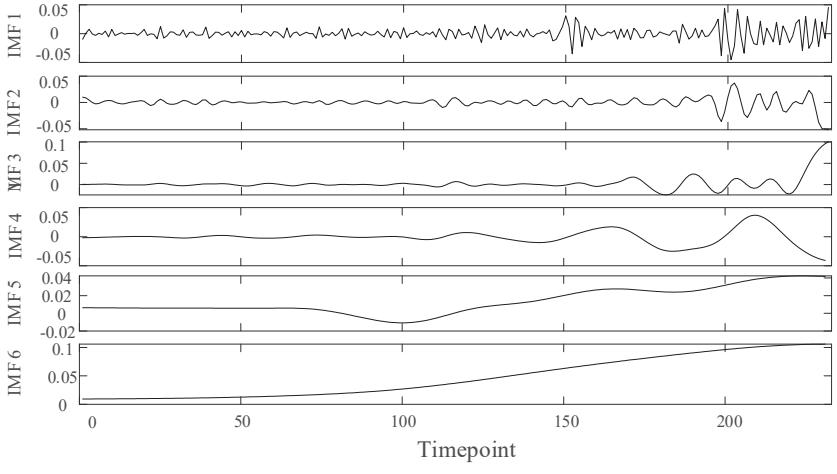

Figure 14. Modal components of the CDI.

(3) Analysis of prediction results

The prediction results of the proposed CDI-EEMD-LSTM are shown in Figure 15, and the evaluation indexes are shown in Table 3. Based on the signal processing capability of EEMD and the nonlinear fitting capability of LSTM, the prediction value of the model is almost consistent with the trend of the real value and can well reflect the fluctuation of the series $R(t)$. The RMSE is 0.019, the MAPE is 15.1%, and the CC is 0.903, which can accurately predict the changing trend of the unit health status.

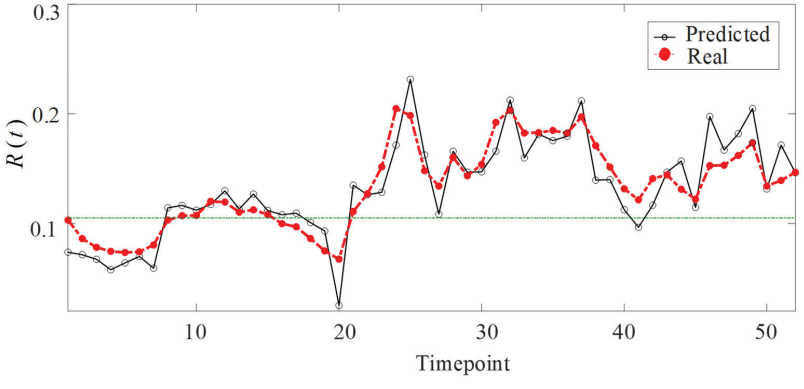

Figure 15. Prediction results of CDI-EEMD-LSTMNN.

Table 3. Index of prediction evaluation of CDI-EEMD-LSTM prediction model.

Prediction Model	MAPE/%	RMSE	CC
CDI-EEMD-LSTM	15.1	0.019	0.903

Figure 16 shows the prediction results of LSTM for each modal component of the CDI, and it can be seen that the prediction results of each component basically match the actual values. Further analysis of the prediction errors of each component shows that the smoother the modal component, the better the prediction outcome. Among the prediction results for all six modal components, the IMF1 component has the maximum prediction error and is the main source of deviation between the predicted and actual values of the index.

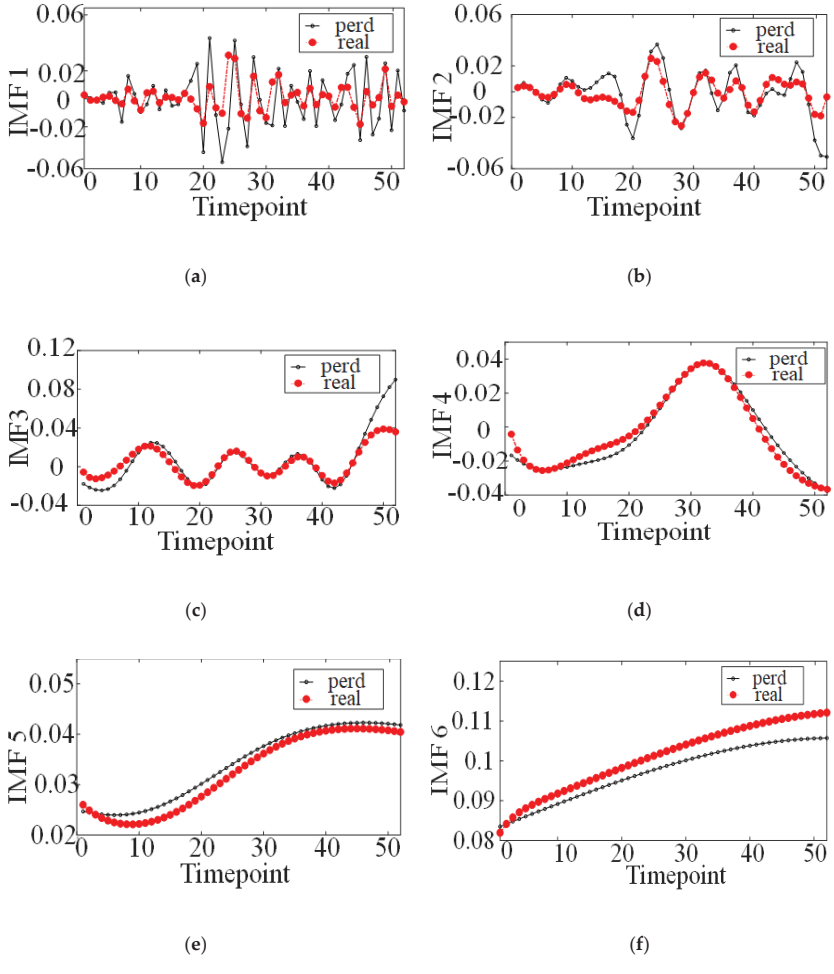

Figure 16. Prediction results of each modal component of the CDI. (**a**) is the prediction result of IFM1; (**b**) is the prediction result of IFM2; (**c**) is the prediction result of IFM3; (**d**) is the prediction result of IFM4; (**e**) is the prediction result of IFM5; (**f**) is the prediction result of IFM6.

4.3. Multi-Model Comparison Validation

4.3.1. Comparison of Indexes

The unit characteristics indexes can reflect the unit state changes, and it can be known from the literature [6] that the SD, peak-to-peak value, skewness, and kurtosis of the signal waveform increase constantly with time, reflecting the trend of unit deterioration in the same way as the CDI of the unit. The trends of the CDI proposed in this paper are consistent with the trends of the DI proposed in the literature [6]. In order to measure the sensitivity of the CDI proposed in this paper to reflect the state change of the unit, the indicator gradient

rate (IGR) of the indexes is applied. Calculate the IGR of each index, that is, the sharpness of changes, to measure the sensitivity of the indexes to the change of unit status. The four points of H, I, II, and III, where the change of indexes amplitude is obvious, are selected in Figure 17, and the indexes are known to be healthy at the point of H. The change of the indexes' amplitude at the point I, II, and III relative to the amplitude of the indexes at the point of H is calculated as the IGR of the indexes, separately. The calculation is shown in the following Equations (35)–(37).

$$k_1 = \left| \frac{r(\mathrm{I}) - r(H)}{r(H)} \right| \tag{35}$$

$$k_2 = \left| \frac{r(\mathrm{II}) - r(H)}{r(H)} \right| \tag{36}$$

$$k_3 = \left| \frac{r(\mathrm{III}) - r(H)}{r(H)} \right| \tag{37}$$

where $r(\mathrm{I})$, $r(\mathrm{II})$, and $r(\mathrm{III})$ are the amplitudes of signal SD, kurtosis, skewness, and peak-to-peak values at moments I, II, and III, respectively; k_1, k_2, and k_3 are the IGR of signal SD, kurtosis, skewness, and peak-to-peak values at moments I, II, and III.

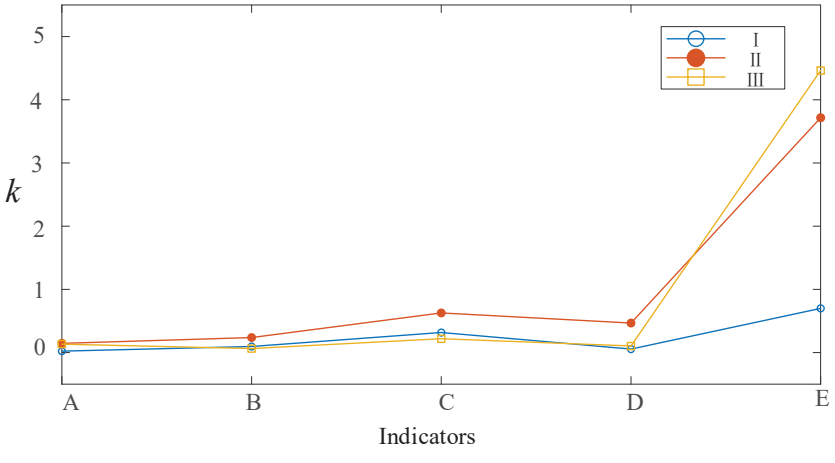

Figure 17. IGR of each index.

The IGR of each index is shown in Table 4 and Figure 17. In Table 4, where A, B, C, D, and E respectively represent the indicators: SD, kurtosis, skewness, peak-to-peak, and CDI. It can be seen that the IGR of the CDI is much better than the other indexes, which indicates that the index is more sensitive to the changes in the unit's operation status and can be more representative of the deterioration process from normal to failure than the traditional time and frequency-domain indexes.

Table 4. IGR of each indicator.

IGR	A	B	C	D	E
k_1	0.022	0.095	0.317	0.055	0.700
k_2	0.146	0.237	0.627	0.467	3.715
k_3	0.134	0.063	0.219	0.104	4.463

4.3.2. Comparison of Predicted Results

To further verify the advantages of the proposed model prediction model in predicting the trend of failure sign indicators of hydropower units, four control groups were designed to verify the accuracy of the prediction model, where the four control groups are EEMD-GA-BP (the first control group), original sequence-LSTM (the second control group), EMD-LSTM (the third control group), and EEMD-SVM (the fourth control group). The selection of these models is based on the basic model and similar model to the proposed model, and the first control group is proposed in the 42nd literature [41], and the fourth control group is proposed in the second literature [2]. The proposed model is compared with four control groups and the original sequence. In the control group experiments, the training set and test set divisions and all parameters of the LSTM network are kept the same as those of the experimental group, and in using EEMD-GA-BPNN for deterioration indicator prediction, the BPNN structure is a three-layer structure of input layer-hidden layer-output layer, and the initial weights of the neural network and the initial threshold value of the neural network are optimized by genetic algorithm. The final prediction results obtained for each comparison model and the experimental model after training are shown in Figure 18. The evaluation indexes of the 5 prediction models are compared, as shown in Table 5.

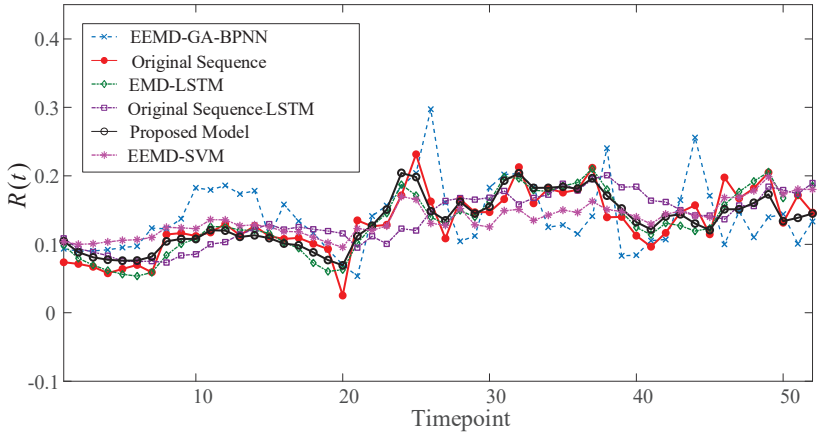

Figure 18. Comparison of prediction results of different prediction models.

Table 5. Evaluation indicators of prediction results of different forecasting models.

Predicted Models	RMSE	MAPE	CC
EEMD-GA-BPNN	0.313	0.047	0.576
EEMD-SVM	0.232	0.191	0.831
Original Sequence-LSTM	0.285	0.037	0.621
EMD-LSTM	0.152	0.021	0.884
Proposed model	0.151	0.019	0.903

It can be visually seen from Figure 18 that among the several prediction models compared, the constructed EEMD-LSTM model prediction results are more closely matched to the actual change trend of the deterioration indicators. In contrast, when the LSTM is used to predict the original indicator sequence directly, the non-smoothness of the sign indicators during the normal-to-fault evolution leads to a serious deviation of the prediction results from the actual changes of the indicators.

The prediction result of the EEMD-GA-BPNN model is similar to that of the EEMD-SVM model, but the prediction result of the LSTMNN model is better than that of the BPNN and SVM models. From Table 5, it is observed that EMD-LSTM and EEMD-LSTM

outperformed EEMD-GA-BP and EEMD-SVM in all evaluation metrics. In the EEMD-LSTM model compared with the EEMD-GA-BP model, the RMSE and MAPE decreased by 0.162 and 0.028, respectively, and the CC improved by 0.327, while compared with the EEMD-LSSVM model, the RMSE and MAPE decreased by 0.081 and 0.172, respectively, and the CC improved by 0.072. The superiority of the LSTM model in nonlinear fitting is demonstrated. It can be shown that the LSTM has an outstanding prediction effect and higher accuracy for time-series indicators during the unit state fading process compared with the traditional BPNN and SVM and has a great advantage in the self-learning of time series. It can thus be shown that the LSTM is feasible for the prediction model of the time series of deterioration indicators.

Meanwhile, according to each evaluation index in Table 5, it can be seen that EEMD-LSTM compared with the original sequence-LSTM model, RMSE and MAPE decreased by 0.134 and 0.018, respectively, and CC improved by 0.282, which greatly improved the prediction accuracy. Compared with the EMD-LSTM model, RMSE and MAPE were reduced by 0.001 and 0.002, respectively, and CC was improved by 0.019. It can be seen that the EEMD-LSTM model has the best evaluation indicators and the highest prediction accuracy. The EEMD-LSTM predicts the degraded indicators more effectively than the EMD-LSTM, indicating the advantage of EEMD over EMD in signal smoothness decomposition, which shows that decomposing the mutated signals into smoothed component signals and reducing the non-smoothness and non-linearity of the indicator sequences can enhance the accuracy of prediction.

In the case study of this paper, the default values given by the toolbox are used for most of the parameters of the LSTM model, which may lead to a slight increase in the evaluation metrics. Overall, the overall prediction performance of the proposed EEMD-LSTM model is better than several of the remaining comparative models and can be used to predict the deterioration trend of hydropower units.

5. Conclusions

In order to improve the measurement accuracy of non-stationary and non-linear state trends of hydropower units, a trend prediction model (EEMD-LSTM) based on CDI is proposed in this paper. A THM is established by considering the mapping relationship between operating parameters such as active power, guide vane opening and blade opening, and the time-domain indicators, and an FHM is constructed based on EEMD-ApEn and the K-mean clustering algorithm. Based on the above health models, TDI and FDI were constructed, respectively, and the CDI was formed by weighted fusion. The main conclusions of this paper are as follows:

1. Autocorrelation analysis was performed on the deteriorated indicator series to obtain the appropriate correlation length. Too long or too short correlation length of the indicator series can cause excessive prediction errors. The analysis showed that the prediction input step length of the deterioration indicator series could be 8 steps when using historical data for prediction.
2. The EEMD-LSTM model compared with the EEMD-GA-BPNN model, RMSE and MAPE decreased by 0.162 and 0.028, respectively, and CC enhanced by 0.327, while compared with the EEMD-SVM model, RMSE and MAPE decreased by 0.081 and 0.172, respectively, and CC enhanced by 0.072. It can be obtained that the LSTM is more effective in predicting the time-series indicators in the asymptotic process, which is outstanding relative to the traditional prediction model in terms of time series self-learning. Thus, it can be shown that LSTM is feasible for predicting the deterioration trend of hydropower units.
3. EEMD-LSTM compared with the original sequence-LSTM model, RMSE and MAPE were reduced by 0.134 and 0.018, respectively, and CC was improved by 0.282, and the prediction accuracy was greatly improved. Compared with the EMD-LSTM model, RMSE and MAPE are reduced by 0.001 and 0.002, respectively, and CC is improved by 0.019. The EEMD-LSTM model has the highest evaluation prediction

accuracy. EEMD-LSTM outperforms EMD-LSTM in predicting degraded indicators, which shows the advantage of EEMD over EMD in signal smoothness decomposition, thus showing that decomposing mutated signals into smooth component signals and reducing the non-smoothness and non-linearity of indicator sequences can enhance the prediction accuracy.

In the case study of this paper, most of the parameters of the LSTM model use the default values given by the toolbox, which may lead to a slight increase in the evaluation metrics. Overall, the overall prediction performance of the proposed EEMD-LSTM model is better than the remaining several comparative models and can be used to predict the deterioration trend of hydropower units.

Author Contributions: Conceptualization, Y.W.; methodology, Y.W. and D.L. (Dong Liu, liudongwhu@126.com); software, J.C.; validation, Y.W. and X.H.; formal analysis, D.L. (Dong Liu, lewistwhu@163.com); investigation, Y.W. and D.L. (Dong Liu, liudongwhu@126.com); resources, Z.X.; data curation, Y.W.; writing—original draft preparation, Y.W.; writing—review and editing, D.L. (Dong Liu, liudongwhu@126.com); visualization, Y.W. and Z.X.; supervision, Z.X. All authors have read and agreed to the published version of the manuscript.

Funding: This work was supported by the National Natural Science Foundation of China (NSFC) (No. 51979204) and China Postdoctoral Science Foundation (Grant No. 2020M682416).

Data Availability Statement: The data used to support the findings of this study are not available because it involves the parameters and full characteristic data of the actual hydropower station.

Conflicts of Interest: The authors declare no conflict of interest.

References

1. Shan, Y.; Liu, J.; Xu, Y.; Zhou, J. A combined multi-objective optimization model for degradation trend prediction of pumped storage unit. *Measurement* **2021**, *169*, 108373. [CrossRef]
2. Fu, W.; Zhou, J.; Zhang, Y.; Zhu, W.; Xue, X.; Xu, Y. A state tendency measurement for a hydro-turbine generating unit based on aggregated EEMD and SVR. *Meas. Sci. Technol.* **2015**, *26*, 125008. [CrossRef]
3. Hu, X.; Li, C.; Tang, G. A hybrid model for predicting the degradation trend of hydropower units based on deep learning. In Proceedings of the 2019 Prognostics and System Health Management Conference (PHM-Qingdao), Paris, France, 2–5 May 2019; pp. 1–5.
4. Liu, D.; Lai, X.; Xiao, Z.; Hu, X.; Zhang, P. Fault diagnosis of rotating machinery based on convolutional neural network and singular value decomposition. *Shock. Vib.* **2020**, *2020*, 1–13. [CrossRef]
5. Li, C.; Tang, G.; Xue, X.; Saeed, A.; Hu, X. Short-term wind speed interval prediction based on ensemble GRU model. *IEEE Trans. Sustain. Energy* **2019**, *11*, 1370–1380. [CrossRef]
6. Liu, D.; Lai, X.; Hu, X.; Xiao, Z. Research on online assessment method of condition deterioration of hydropower units based on vibration signal. *J. Water Resour.* **2021**, *52*, 461–473.
7. An, X.; Pan, L. Characteristic parameter degradation prediction of hydropower unit based on radial basis function surface and empirical mode decomposition. *J. Vib. Control* **2013**, *21*, 2200–2211. [CrossRef]
8. An, X.; Pan, L.; Yang, L. Condition parameter degradation assessment and prediction for hydropower units using Shepard surface and ITD. *Trans. Inst. Meas. Control* **2014**, *36*, 1074–1082. [CrossRef]
9. Guo, L.; Lei, Y.; Li, N.; Yan, T.; Li, N. Machinery health indicator construction based on convolutional neural networks considering trend burr. *Neurocomputing* **2018**, *292*, 142–150. [CrossRef]
10. Li, J.; Yao, X.; Wang, X.; Yu, Q.; Zhang, Y. Multiscale local features learning based on BP neural network for rolling bearing intelligent fault diagnosis. *Measurement* **2019**, *153*, 107419. [CrossRef]
11. Wu, J.; Hu, K.; Cheng, Y.; Zhu, H.; Shao, X.; Wang, Y. Data-driven remaining useful life prediction via multiple sensor signals and deep long short-term memory neural network. *ISA Trans.* **2019**, *97*, 241–250. [CrossRef]
12. Lu, S.; Li, Q.; Bai, L.; Wang, R. Performance predictions of ground source heat pump system based on random forest and back propagation neural network models. *Energy Convers. Manag.* **2019**, *197*, 111864. [CrossRef]
13. Zhang, X.; Jiang, Y.; Li, C.; Zhang, J. Health status assessment and prediction for pumped storage units using a novel health degradation index. *Mech. Syst. Signal Process.* **2022**, *171*, 108910. [CrossRef]
14. Liu, D.; Zeng, H.; Xiao, Z.; Peng, L.; Malik, O.P. Fault diagnosis of rotor using EMD thresholding-based de-noising combined with probabilistic neural network. *J. Vibroeng.* **2017**, *19*, 5920–5931.
15. Chen, P.; Deng, Y.; Zhang, X.; Ma, L.; Yan, Y.; Wu, Y.; Li, C. Degradation Trend Prediction of Pumped Storage Unit Based on MIC-LGBM and VMD-GRU Combined Model. *Energies* **2022**, *15*, 605. [CrossRef]

16. Tuerxun, W.; Chang, X.; Guo, H.Y.; Jin, Z.J.; Zhou, H.J. Fault diagnosis of wind turbines based on a support vector machine optimized by the sparrow search algorithm. *IEEE Access* **2021**, *9*, 69307–69315. [CrossRef]
17. Qin, Q.; Lai, X.; Zou, J. Direct Multistep Wind Speed Forecasting Using LSTM Neural Network Combining EEMD and Fuzzy Entropy. *Appl. Sci.* **2019**, *9*, 126. [CrossRef]
18. Wang, S.X.; Zhang, N.; Wu, L.; Wang, Y.M. Wind speed forecasting based on the hybrid ensemble empirical mode decomposition and GA-BP neural network method. *Renew. Energy* **2016**, *94*, 629–636. [CrossRef]
19. Zou, M.; Zhou, J.; Liu, Z.; Zhan, L. A hybrid model for hydroturbine generating unit trend analysis. In Proceedings of the Third International Conference on Natural Computation (ICNC 2007), Hainan, China, 24–27 August 2007; Volume 2, pp. 570–574.
20. Jin, T.; Cheng, Q.; Chen, H.; Wang, S.; Guo, J.; Chen, C. Fault diagnosis of rotating machines based on EEMD-MPE and GA-BP. *Int. J. Adv. Manuf. Technol.* **2021**, 1–12. [CrossRef]
21. Zichun, Y. The BP Artificial Neural Network Model on Expressway Construction Phase Risk. *Syst. Eng. Procedia* **2012**, *4*, 409–415.
22. Liu, H.; Mi, X.; Li, Y. Comparison of two new intelligent wind speed forecasting approaches based on wavelet packet decomposition, complete ensemble empirical mode decomposition with adaptive noise and artificial neural networks. *Energy Convers. Manag.* **2018**, *155*, 188–200. [CrossRef]
23. Zhou, K.B.; Zhang, J.Y.; Shan, Y.; Ge, M.-F.; Ge, Z.-Y.; Cao, G.-N. A hybrid multi-objective optimization model for vibration tendency prediction of hydropower generators. *Sensors* **2019**, *19*, 2055. [CrossRef] [PubMed]
24. Xue, J.; Shen, B. A novel swarm intelligence optimization approach, sparrow search algorithm. *Syst. Sci. Control Eng.* **2020**, *8*, 22–34. [CrossRef]
25. Huang, N.E.; Shen, Z.; Long, S.R.; Wu, M.C.; Shih, H.H.; Zheng, Q.; Yen, N.-C.; Tung, C.C.; Liu, H.H. The empirical mode decomposition and the Hilbert spectrum for nonlinear and non-stationary time series analysis. *Proc. R. Soc. A Math. Phys. Eng. Sci.* **1998**, *454*, 903–995. [CrossRef]
26. Ma, F.; Chen, X.; Du, J. Bearing Fault Diagnosis Based on Improved Hilbert-Huang Transform. In Proceedings of the 5th International Conference on Civil Engineering and Transportation, Guangzhou, China, 28–29 November 2015; pp. 551–555.
27. Huang, Y.; Yang, L.; Liu, S.; Wang, G. Multi-step wind speed forecasting based on ensemble empirical mode decomposition, long short term memory network and error correction strategy. *Energies* **2019**, *12*, 1822. [CrossRef]
28. Pincus, S.M. Approximate entropy as a measure of system complexity. *Proc. Natl. Acad. Sci. USA* **1991**, *88*, 2297–2301. [CrossRef]
29. Zhang, Z.A.; Zhou, Y.A.; Chen, Z.Y.B.; Tian, X.; Du, S.; Huang, R. Approximate entropy and support vector machines for electro-encephalogram signal classification. *Neural Regen. Res.* **2013**, *88*, 1844–1852.
30. Unal, M.; Onat, M.; Demetgul, M.; Kucuk, H. Fault diagnosis of rolling bearings using a genetic algorithm optimized neural network. *Measurement* **2014**, *58*, 187–196. [CrossRef]
31. Teng, Y.; Shang, P.; He, J. Multiscale fractional-order approximate entropy analysis of financial time series based on the cu-mulative distribution matrix. *Nonlinear Dyn.* **2019**, *97*, 1067–1085. [CrossRef]
32. Werbos, P.J. Backpropagation Through Time—What It Does And How To Do It. *Proc. IEEE* **1990**, *78*, 1550–1560. [CrossRef]
33. Singh, A.; Singh, L.P.; Singh, S.; Singh, H.; Chhuneja, N.K.; Singh, M. Evaluation and analysis of occupational ride comfort in rotary soil tillage operation. *Measurement* **2019**, *131*, 19–27. [CrossRef]
34. Rezaeianjouybari, B.; Shang, Y. Deep learning for prognostics and health management, State of the art, challenges, and opportunities. *Measurement* **2020**, *163*, 107929. [CrossRef]
35. Soualhi, M.; Nguyen, K.T.P.; Soualhi, A.; Medjaher, K.; Hemsasc, K.E. Health monitoring of bearing and gear faults by using a new health indicator extracted from current signals. *Measurement* **2019**, *141*, 37–51. [CrossRef]
36. Li, H.; Wang, Y.; Yang, X.P.; Jia, R.; Luo, X.Q. Vibration fault diagnosis for hydropower generating unit based on multiwavelet and PSO-RBF neural network. *J. Northwest A F Univ. Nat. Sci. Ed.* **2017**, *45*, 227–234.
37. Li, L.M.; Wang, Z.S. Method of redundant features eliminating based on k-means clustering. *Appl. Mech. Mater.* **2014**, *488*, 1023–1026. [CrossRef]
38. Lu, N.; Xiao, Z.; Malik, O.P. Feature extraction using adaptive multiwavelets and synthetic detection index for rotor fault diagnosis of rotating machinery. *Mech. Syst. Signal Process.* **2015**, *52*, 393–415. [CrossRef]
39. Wang, W.; Chen, Q.; Yan, D.; Geng, D. A novel comprehensive evaluation method of the draft tube pressure pulsation of Francis turbine based on EEMD and information entropy. *Mech. Syst. Signal Process.* **2019**, *116*, 772–786. [CrossRef]
40. Liu, D.; Xiao, Z.; Hu, X.; Zhang, C.; Malik, O. Feature extraction of rotor fault based on EEMD and curve code. *Measurement* **2019**, *135*, 712–724. [CrossRef]
41. Lu, D.; Xiao, Z.H.; Liu, D.; Hu, X.; Deng, T. EEMD-GA-BP-based state trend prediction of hydropower units. *China Rural Water Conserv. Hydropower* **2021**, 186–194. [CrossRef]

energies

MDPI

Article

A 1D-3D Coupling Model to Evaluate Hydropower Generation System Stability

Meng Zhang [1,2,3,†], Jinhai Feng [2,3,†], Ziwen Zhao [2,3], Wei Zhang [1,*], Junzhi Zhang [4] and Beibei Xu [2,4]

[1] State Grid Gansu Liujiaxia Hydropower Plant, Yongjing 731600, China
[2] Key Laboratory of Agricultural Soil and Water Engineering in Arid and Semiarid Areas, Ministry of Education, Northwest A&F University, Xianyang 712100, China
[3] Institute of Water Resources and Hydropower Research, Northwest A&F University, Xianyang 712100, China
[4] Northwest Engineering Corporation Limited, Xi'an 710000, China
* Correspondence: t1234567.zhang_wei1024@163.com; Tel.: +86-176-1290-2779
† These authors contribute equally to this paper.

Abstract: This paper proposes a novel 1D-3D approach for the stability characteristics of the hydropower generation system (HGS) in transition processes. First, a 1D-3D coupling model was established for the HGS in the load-reduction process. Second, a sensitivity analysis of the HGS's parameters to the rotation speed and discharge was conducted. Third, the pressure pulsation characteristics of the HGS with three typical guide vane openings were analyzed during the load-reduction process. The results show that with the closure of the guide vane, the discharge gradually decreases and it is sensitive to the change in hydraulic parameters. The rotation speed fluctuates at the early stage of the transition process and is easily affected by mechanical parameters. In addition, the pressure pulsation inside the Francis turbine is more intense under small openings than large openings, and the primary frequency of pressure pulsation under three opening degrees is the blade frequency. The 1D-3D coupling model successfully integrates the advantages of traditional methods and provides a reference for predicting system stability and exploring the stability mechanism.

Keywords: 1D–3D coupling model; transition stability; sensitivity analysis; pressure pulsation; hydro power

Citation: Zhang, M.; Feng, J.; Zhao, Z.; Zhang, W.; Zhang, J.; Xu, B. A 1D-3D Coupling Model to Evaluate Hydropower Generation System Stability. *Energies* **2022**, *15*, 7089. https://doi.org/10.3390/en15197089

Academic Editor: Helena M. Ramos

Received: 29 July 2022
Accepted: 16 September 2022
Published: 27 September 2022

1. Introduction

The hydropower generation system (HGS) is playing an increasingly important role in the world's energy applications [1,2]. The rapid growth of intermittent energy sources, such as wind power and photovoltaic, has changed the world's energy structure [3,4]. Therefore, as the proportion of hydropower units increases, the hydropower station is shifting from traditional power generation to peak load and frequency regulation. Due to the intermittent characteristics of wind power and photoelectric power, the requirements of real-time balance of electric energy in the power system cannot be satisfied. With rapid start–stop characteristics of changing load, the hydropower generation system has therefore become the best choice for complementary energy [5,6].

The HGS has received a lot of attention in recent years. There are some risks in the quality of the power grid due to the randomness and unpredictability of intermittent energy [7–9]. To keep the balance between active power and reactive power in the power grid, a higher requirement is put forward for the flexible operation of HGS. Moreover, the stability problem caused by the flexible operation and operation switching has also become a research hotspot. In the transition process of the HGS, the hydraulic–mechanical–electrical subsystem shows a cooperative variation relationship [10]. However, due to the difference in the response time to flow, the machinery, and electricity, the hysteresis appears in a cooperative variation relationship, causing energy fluctuations across the whole system [11]. In addition, the energy fluctuation of the HGS is particularly obvious when the operation

switching time is long. The excessive energy fluctuation behavior under the transition process (short time, large scale) not only affects the performance of hydropower but also undoubtedly reduces the service life of the HGS [12,13].

The stability of the HGS in the transition process is a hot issue in many fields, such as the design and operation of hydraulic machinery. It is divided into two kinds of research. First, based on the theory of computational fluid dynamics, the stability mechanism is revealed by observing the internal flow field behavior of the hydroturbine [14,15]. For example, Simon Pasche et al. investigated the birth and the growth of the synchronous pressure wave in Francis turbines, which brought deeper comprehension of the synchronous wave generation mechanism [16]. Zhou et al. used baffles in the draft tube to hinder the swirling flow emerging from a Francis turbine runner during part-load operation [17]. Zhou et al. found the pressure fluctuation in the vaneless zone. The finding is of great significance in terms of understanding the influence of the clearance flow on the load rejection process [18]. The unsteady behavior of the Francis turbine at several operating points was simulated by Ahmed Laouari [19]. The results showed that the strong pressure pulsation and torque oscillations occurred even at the best efficiency operating point. Various studies [20–24] also verified the feasibility of pressure pulsation and velocity distribution of an ultra-high head turbine in a hydropower station under rated and part-load operation. Second, the whole HGS model was established, and the stability law was investigated by combining mathematics and dynamics theory. Guo et al. investigated system stability considering the coupling effect of water potential energy in the surge tank and power grid [25]. Xu et al. established the Hamiltonian model of the HGS with a multi-hydroturbine, and the stability was simulated by introducing several kinds of disturbance [26]. Li identified the fast–slow behavior of the hydropower generation system, which caused the system energy fluctuation [27].

The method of 1D and 3D coupling modeling has been applied in many fields. David et al. discussed several different physical application models, based on the Newton-based method, and adopted the coupling strategy from the loosely coupled Gauss–Seidel and operator splitting methods to the tightly coupled method, achieving a breakthrough in the understanding of coupling problem progress [28]. Zhang et al. studied the performance of neutron and thermal-liquid coupling algorithms in transient problems. Three methods, including operator splitting semi-implicit (OSSI), Picard iteration (PI), and Jacobi-Free Newton–Krylov (JFNK), were used for comparison. The results show that the improved PI and JFNK coupling algorithm can achieve better computing performance in TINTE due to its better accuracy and stability [29]. Peng et al. used the OpenMC software coupled with the commercial computational fluid dynamics of ANSYS. The realization and parallel performance of the PI algorithm of grouped Gauss–Seidel type and grouped Jacobi type were studied. The results show that the adaptive load balancing algorithm can improve the computational efficiency of the block Jacobi algorithm and the performance of the Gauss–Seidel algorithm [30]. Cheng et al. simulated the whole process of water flow and reconnection for the pumped storage system, and showed that the two high-amplitude single pulses generated by the axial force and radial force of the flow channel during this process are destructive [31]. Liu et al. simulated the extreme case of simultaneous load shedding in a prototype pumped storage system. The results show that the maximum pressure is caused by strong static and dynamic interference (RSI), and the maximum pressure upstream of the runner exceeds the industry standard [32]. The application of the two aforementioned methods enriches the stability theories in transition processes. However, both methods have their limitations: (1) The systematic model can only idealize the dynamic process for a long time, which cannot be accurately solved due to the inability of fluid characteristics; (2) due to the complexity of the system, the internal properties cannot be used for calculation; (3) the transition process of the HGS involves collaborative changes in multiple subsystems, and the internal characteristic method cannot meet the requirements of collaborative changes for the subsystems of the HGS.

Motivated by the above analysis, the stability of the HGS was studied during the load-reduction process. Three innovations appear in this paper. First, the synergic model is innovatively introduced, which combines the advantages of system modeling and inner characteristic modeling. Second, the sensitivity of different subsystem parameters to the system output is determined during load-decreasing process. Third, the pressure pulsation inside the hydroturbine under three typical guide vane openings was obtained from a transient perspective.

This paper is organized as follows: Section 2 introduces the synergic system model. Section 3 presents the dynamic behavior and the pressure pulsation under different turbine locations. Section 4 provides the conclusions.

2. The Internal Characteristic Model of the Hydropower Generation System

Figure 1a is the sketch map of the HGS. Figure 1b is the inner flow field diagram of the turbine. Traditional systematic modeling was used to model each subsystem separately to study the characteristics of the HGS. The dynamic behavior of subsystems (generators, pressure pipe, penstock, Francis turbine generator, and tailrace tunnel) are easy to describe with ordinary differential equations (ODEs). However, as the energy transformation hub of the HGS, the complexity of the Francis turbine structure creates the turbulent characteristics of flow, which cannot be described using ODEs. Therefore, with systematic modeling, it is difficult to express the transient flow characteristics in the Francis turbine. Compared with systematical modeling, internal characteristic modeling focuses on the refined modeling of a single Francis turbine subsystem, as shown in Figure 1b. The application of the turbulence equation describes the characteristics of the fluid in a more detailed and accurate way, and reveals the unstable mechanism of the unit more intuitively. However, the main drawback or barrier to the internal characteristic modeling method is the reduction process of computing resources and data, which will remain difficult to resolve for the foreseeable future. Combining the advantages of the two approaches, Section 2 establishes the 1D-3D coupling model of the HGS.

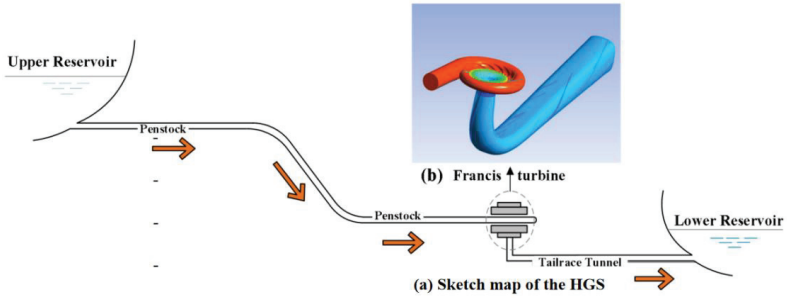

Figure 1. The sketch map of the hydropower generating system and internal characteristic Francis turbine model.

2.1. Hydroturbine Model

As the hub of the energy conversion of the HGS, the turbine converts kinetic energy of flow into mechanical energy. The classical hydroturbine model adopts the hydroturbine torque and flow as output, which is expressed as

$$\begin{cases} M_t = M_t(H, n, a) \\ Q = Q(H, n, a) \end{cases}, \tag{1}$$

where M_t is the active torque of hydroturbine, and Q is the flow of hydroturbine inlet. Both torque and flow are the function of the water head H of the turbine inlet, rotation speed n, and guide vane opening a.

Expand Equation (1) in an arbitrary operational state using Taylor theory. Therefore, the limitation increment of torque and flow are

$$\begin{array}{c} \Delta M_t = \frac{\partial M_t}{\partial a}\Delta a + \frac{\partial M_t}{\partial n}\Delta n + \frac{\partial M_t}{\partial H}\Delta H \\ \Delta Q = \frac{\partial Q}{\partial a}\Delta a + \frac{\partial Q}{\partial n}\Delta n + \frac{\partial Q}{\partial H}\Delta H \end{array} \tag{2}$$

The essence of Equation (2) means the variance of output (M_t and Q) equals the sum of the variance of input (a, n, and H) under their direction.

2.1.1. External Characteristic Method of the Turbine

In the external characteristic method, the full characteristic curve of the hydroturbine is regarded as the boundary condition for calculating the long transition process of the HGS. In this paper, the model of the Francis turbine came from a hydraulic machinery experiment platform in Norway [33].

From Equation (2), the partial derivative represents the direction differential. The differential form of Equation (2) is transformed as follows:

$$\begin{array}{c} \dot{M}_t = \frac{\partial M_t}{\partial a}\dot{a} + \frac{\partial M_t}{\partial n}\dot{n} + \frac{\partial M_t}{\partial H}\dot{H} \\ \dot{Q} = \frac{\partial Q}{\partial a}\dot{a} + \frac{\partial Q}{\partial n}\dot{n} + \frac{\partial Q}{\partial H}\dot{H} \end{array} \tag{3}$$

The calculation step for six coefficients ($\frac{\partial M_t}{\partial a}$, $\frac{\partial M_t}{\partial n}$, $\frac{\partial M_t}{\partial H}$, $\frac{\partial Q}{\partial a}$, $\frac{\partial Q}{\partial n}$ and $\frac{\partial Q}{\partial H}$) with partial derivative form are obtained in [34].

2.1.2. Pressure Pipe

In the actual design of a hydropower station, the assumption of the elasticity of the pipe wall causes a big error. Therefore, the pressure pipe model, which considers the elastic water hammer and pipe friction, is as follows [35]:

$$\dddot{q} + \frac{24}{T_r^2}\ddot{q} + \frac{96f}{T_r^3}\dot{q} = -\frac{3}{h_w T_r}\ddot{h} - \frac{12f}{h_w T_r^2}\dot{h} - \frac{24}{h_w T_r^3}h \tag{4}$$

By introducing the state variables (x_1, x_2, and x_3) into Equation (4), the pressure pipe model is expressed as

$$\begin{cases} \dot{x}_1 = x_2 + b_2 h \\ \dot{x}_2 = x_3 + b_1 h \\ \dot{x}_3 = -a_0 x_1 - a_1 x_2 + (b_0 - a_1 b_2)h \end{cases} \tag{5}$$

In addition,

$$q = x_1 \tag{6}$$

where $a_0 = \frac{96f}{T_r^3}$,$a_1 = \frac{24}{T_r^2}$,$b_0 = -\frac{24}{h_w T_r^3}$,$b_1 = -\frac{12f}{h_w T_r^2}$,$b_2 = -\frac{3}{h_w T_r}$; f is the frequency; h_w is the pipe characteristic coefficient; and T_r is the period of the water hammer.

Couple Equations (3), (5) and (6) and the dynamic equation of the water head is

$$\dot{h} = \frac{1}{e_{qh}}(-e_{qx}\dot{\omega} - e_{qy}\dot{y} + x_2 + b_2 h) \tag{7}$$

2.1.3. Generator

To study the dynamic characteristics of the generator during the load-reduction process, the second order model of the synchronous motor is adopted as follows [12]:

$$\begin{cases} \dot{\delta} = \omega_1 \omega \\ \dot{\omega} = \frac{1}{T_{ab}}(m_t - m_e - D\omega) \end{cases} \tag{8}$$

where δ is the angle of rotor; w is the angular speed; T_{ab} is the time constant value of unit inertia; and D is the damping coefficient. $\omega_1 = 2\pi f_0$, where f_0 is the power grid frequency of 50 HZ. Taking the influence of the rotation speed change on torque into generator damping, we obtain $m_e = p_e$, where m_e is the electromagnetic torque, and p_e is the electromagnetic power. Its equation is $P_e = \frac{E'_q V_s}{x'_{d\Sigma}} \sin\delta + \frac{V_s^2}{2} \frac{x'_{d\Sigma} - x_{q\Sigma}}{x'_{d\Sigma}\ x_{q\Sigma}} \sin 2\delta$, where E'_q is the transient voltage of q axis; V_s is the infinite bus voltage; $x'_{d\Sigma}$ is the transient reactance of d axis; and $x_{q\Sigma}$ is the synchronous reactance.

2.2. Internal Characteristic Model of the Turbine

Figure 2 shows the inner characteristic model of the Francis turbine, including the volute, the guide vane, the hydroturbine runner, and the draft pipe. The diameter of the hydraulic turbine runner D_s = 0.394 m, the blade number z = 30, the fixed guide blade number z_c = 30, the active guide blade number z_0 = 28, the rated flow Q = 0.2 m^3/s, the rated water head H = 11.94 m, the rated speed n = 325 r/min, the rotation frequency f = 5.42 Hz, and the blade passing frequency f_1 = 108.33 Hz.

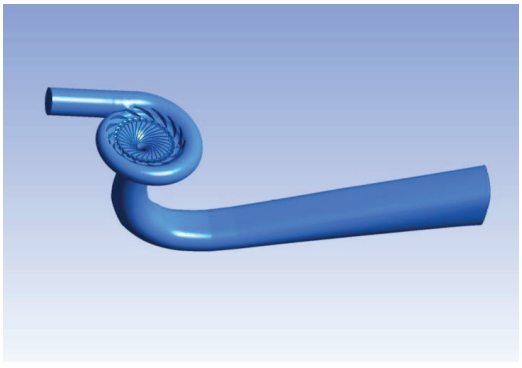

Figure 2. Calculation model of the Francis turbine.

2.2.1. Meshing

Figure 3 shows the Mesh of computational domain about the model of Francis turbine, including volute, runner and draft tube. The total number of mesh points for the rotor blade and water tube was 12,960,875. When the rated operating point was not constant, the results of the Y+ value for all walls were averaged after the two rotations of the intermediate wheel when time t was 0.34 s. The results are shown in Table 1. The Y+ value refers to the dimensionless distance from the centroid of the first layer to the wall surface. According to the mesh-independent verification in the literature [33,36], the mesh met the calculation requirements.

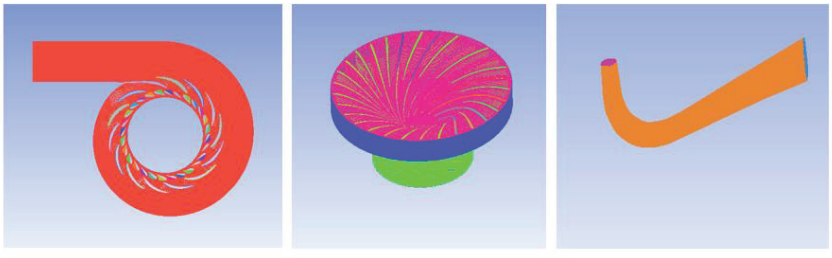

(a) volute (b) runner (c) draft tube

Figure 3. Mesh of computational domain.

Table 1. Meshing and *Y*+ values.

		Ref [33]	Ref [36]	This Paper
Y+	Number of meshing/10^6	12.03	14.59	12.96
	Volute		65	69.80
	Fixed guide vane	65	22.8	65
	Y+ active guide vane	11	17.2	11
	Runner	11	6.1	9
	draft tube	40		38.20

From Table 1, *Y*+ refers to the dimensionless distance from the center of mass of the first layer mesh to the wall surface, which is related to the velocity, viscosity, shear stress, etc. It is used to represent the fineness of the mesh. The smaller *Y*+, the more precise the solution of the flow in transition processes. According to the mesh-independent verification in the literature [33,36], the meshing met the computational requirements.

2.2.2. Turbulence Model

The *k-w* turbulence model was selected in the internal characteristic method. The wall surface was set as a no-slippage wall surface. The inlet boundary condition was set as the flow inlet, and the outlet boundary condition was set as free flow. The calculation precision was set as 10^{-4}. The average static pressure was 114.98 kpa. When the rotor was fixed, the rotor interface was set as the frozen rotor. The transient freeze action interface was set to transient rotor-stator type. The time step of the unsteady flow calculation was the time (0.000567 s) for the rotation of 4° of the rotor. The sampling time was 10 cycles, and the runner rotated 360° per cycle. Data from the last two cycles were selected for a pressure pulsation characteristics analysis.

2.2.3. Monitoring Points

To obtain the information of the internal pressure pulsation of the Francis turbine during the transition process, several monitoring points were set up inside the volute, the inlet of the runner, and inside the draft pipe, as shown in Figure 4. Inside the volute, four monitoring points were set from the inlet to the nose, denoted as G1 to G4, as shown in Figure 4a. At the entrance of the runner, three monitoring points were evenly arranged along with the height, namely, P1, P2, and P3, as shown in Figure 4b. Five monitoring points, Q1 to Q5, were set up inside the draft pipe from the inlet to the outlet, as shown in Figure 4c.

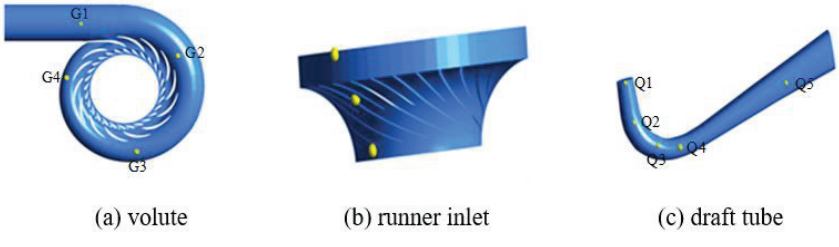

Figure 4. Location of monitoring points in the Francis turbine.

3. Stability Analysis of the HGS and Turbine

The transition stability of the HGS generally includes the system stability and flow stability. The systematical model allows for observation for long time scales. Moreover, the application of the parameter sensitivity analysis method in the systematical model

can provide a meaningful direction for enhancing system stability during the operation switching process. Compared with the systematic model, the internal characteristic method focuses on the Francis turbine. The characteristics of kinetic flow, the distribution of sound noise, and the dynamic and static interference between machinery and flow can be better described. Therefore, combining the advantages of the two methods, coupled modeling was carried out to study the system stability and the flow stability in the Francis turbine during the load-reduction process.

The systematical model was simulated to obtain the system characteristics, including parameter responses and parameter sensitivity. The values with typical GVOs under the load-reduction process were extracted as the boundary condition of the following internal characteristic model. The pressure pulsation under the different location of the hydroturbine was obtained.

3.1. HGS Dynamic Response during the Load-Reduction Process

Hydropower units close the guide vane to reduce its power output to balance the decline in the power load. Due to the structure of the unit, the system behavior and internal flow characteristics of the unit differ greatly under different GVOs. Therefore, three typical GVOs (3.91° small opening, 9.84° rated opening, and 12.43° large opening) under the load-reduction process were selected to study the HGS system behavior and the transient pressure behavior of the turbine. Please note that the value of system responses are represented in relative deviation form (discharge q, rotation speed w, and GVO y), which take values (Q = 0.2 m^3/s, n = 325 r/min, a = 9.84°) under rated operation as reference.

Figure 5 is the parameter response (discharge q, rotation speed w, and GVO y) of the HGS during the load-reduction process. The rotation speed (w) and discharge (q) appeared to fluctuate when the guide vane closes from 0.3 (12.43°) to −0.7 (3.91°) according to a linear law for 50 s. Specifically, the discharge (q) decreased from 0.3 to −0.4, and the maximum value 0.09 (354.25 r/min) of rotation speed (w) appeared at t = 1.8 s. In addition, values (discharge q, rotation speed w, and GVO y) at three typical guide vane openings are shown in Table 2.

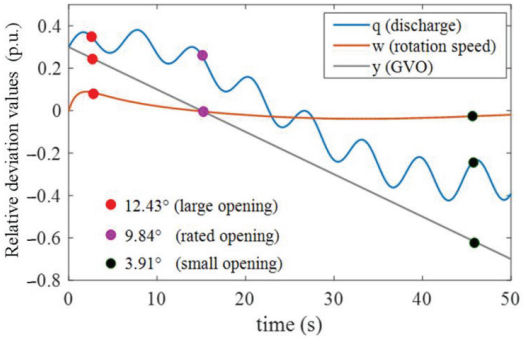

Figure 5. Responses of the HGS during load-reduction process.

Table 2. HGS values under typical guide vane openings.

Guide Vane Opening (GVO)	Timing Point (s)	Discharge (m^3/s)	Rotation Speed (r/min)
12.43° (large opening)	2.7	0.2686	352.95
9.84° (rated opening)	15	0.2526	0
3.91° (small opening)	45	−0.1535	316.55

Sensitivity Analysis under Three Typical GVOs

Sensitivity analysis is a useful method by which dynamic systems can be described by ordinary differential equations. It can measure the influence of different input parameters to a single variable output [37–39]. Herein, it was used to identify the structure and parameters of a dynamic model and obtain the contribution to system variables. A fast method by Simeone Marino was introduced [40], and the six parameters (*D*, *xd*, *xq*, *hw*, *Tab*, and *Tr*) were simulated to measure the contribution to the discharge and rotation speed. In addition, parameter sensitivity under three typical GVOs were explored. The sensitivity indexes are shown in Figure 6.

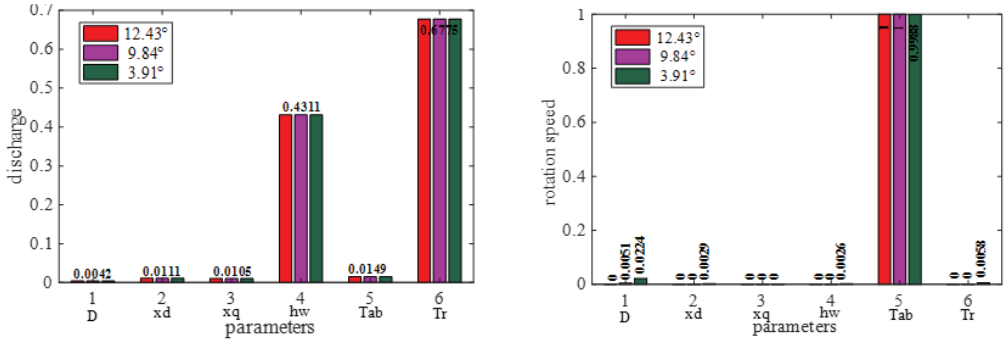

(a) discharge sensitivity (b) rotation speed sensitivity

Figure 6. Parameter sensitivity under three typical GVOs (12.43°, 9.84°, and 3.91°).

Figure 6 shows the sensitivity index of six parameters (*D*, *xd*, *xq*, *hw*, *Tab*, and *Tr*) under three typical GVOs (12.43°, 9.84°, and 3.91°) during the load-reduction process. A notable feature of discharge (Figure 6a) was that the sensitivity indexes were equal whereas the rotation speed exhibited little difference under different GVOs. In addition, parameters *hw* and *Tr* deduced the significant influence while the parameters *D*, *xd*, *xq*, *hw*, *Tab*, and *Tr* did not affect discharge. For rotation speed, the sensitivity value of the *Tab* parameter nearly reached 1.

The character parameters played a significant role in the corresponding subsystem. In particular, during the decreasing load process, hydraulic parameters (*hw* and *Tr*) made a great contribution to the discharge output, whereas the rotation speed was more sensitive to the unit inertial time constant (*Tab*). The electrical parameters (*xd* and *xq*) had little influence on the flow and rotation speed.

In the next part, the related values under three typical GVOs are used as operation input to study the flow character of the Francis turbine, respectively. Then, the transient inner pressure pulsation is obtained.

3.2. Analysis of Pressure Pulsation

The characteristics of the pressure pulsation inside the turbine during the load-reduction transition process are analyzed in this section based on the results of external characteristics. Sections 3.2.1–3.2.3 describe the pressure pulsation characteristics of the draft pipe, runner inlet, and volute inlet of the turbine, respectively. In addition, to facilitate a more intuitive analysis of the pressure pulsation information, the pressure pulsation coefficient was defined, and its calculation formula is as follows:

$$C_p = \frac{p_i - P_{ave}}{P_{ave}} \tag{9}$$

where C_p is the pressure pulsation coefficient; p_i is the static pressure value; and P_{ave} is the average value of static pressures.

3.2.1. Draft Tube

Figure 7 shows the spectral characteristics in the draft tube under the three guide vane openings. It can be seen from Figure 7 that the main frequency of the pressure pulsation in the draft tube of the large opening condition and the rated opening condition is the low frequency pulsation (2.71 Hz), which is 0.5 times that of the frequency conversion (f_r = 5.42), and the pressure pulsation frequency in the draft tube of the small opening condition is mainly for low frequency pulsation (5.42 Hz) and leaf frequency (162.6 Hz). With the closure of the guide vane, the pressure pulsation amplitude in the draft tube gradually decreased. The maximum pressure pulsation amplitude was 0.0036 under the large opening condition, which is 80 times the maximum amplitude of the pressure pulsation under the small opening condition. Under the rated opening condition, the maximum pressure pulsation amplitude appeared in the draft pipe elbow. Because the flow direction was abrupt and the flow rate was large when the fluid flows through the draft pipe elbow, the unevenness of the internal flow was intensified, the water flow was disordered. For the large opening condition and small opening conditions, the pressure pulsation amplitude at the inlet of the draft tube was the largest. The reason for this is that when the working condition deviates from the optimal condition, the inlet water flow of the runner obviously deviates from the normal outlet, resulting in a ring volume, which causes a large draft tube vortex.

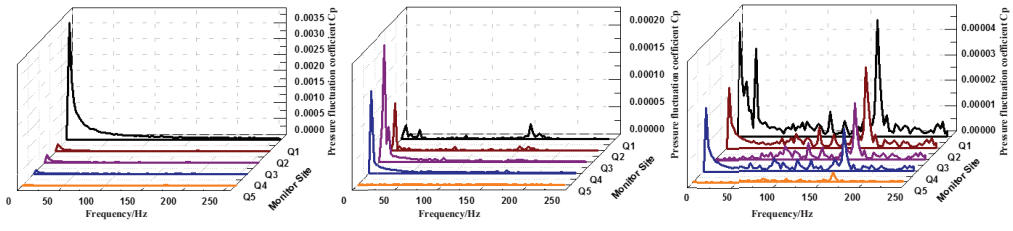

(**a**) Large opening condition (**b**) Rated condition (**c**) Small opening condition

Figure 7. Outlet pressure pulsation frequency domain diagram.

3.2.2. Runner Inlet

The spectral characteristics of each monitoring point at the inlet of the runner under the three vane opening degrees are shown in Figure 8. The pressure pulsation frequency at the inlet of the runner was mainly low frequency pulsation (5.42 Hz) and leaf frequency (162.6 Hz). The low frequency pulsation amplitude gradually increased from the upper crown to the lower ring direction, and the effect closer to the lower ring leaf frequency was more significant, mainly because the direction of the flow changed from the radial direction to the axial direction at the inlet of the runner and the angle near the lower ring. The change was closer and at a right angle, and the water flow was more disordered. As the guide vane opening decreased, the influence of the leaf frequency first decreased and then increased, indicating that the influence of the vortex in the draft tube gradually decreased.

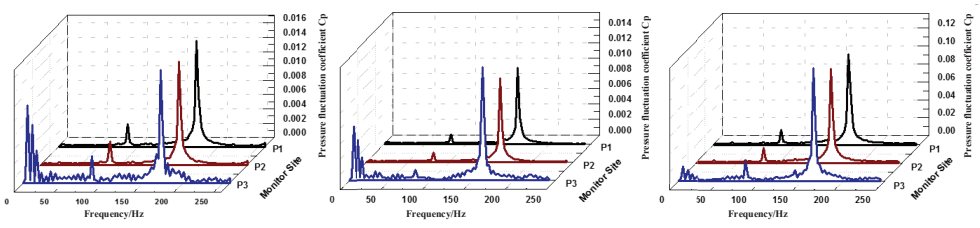

(**a**) Large opening condition (**b**) Rated condition (**c**) Small opening condition

Figure 8. Runner pressure pulsation frequency domain diagram.

3.2.3. Volute

Figure 9 shows the spectral characteristics of each monitoring point in the volute under three guide vane openings. Under the three GVOs, the main frequency was abundant, which mainly presented as low frequency pulsation, 0.5 multiple blade frequency pulsation, and blade frequency pulsation. Therein, the low frequency pulsation amplitude was smaller with the opening of the guide vane. The working condition was obviously reduced, and the low-frequency pulsation amplitude of the small opening condition was almost zero. This is because the low-frequency pulsation generated in the draft tube was large and propagated upstream to the volute, which caused the volute to be significantly affected by the low-frequency pulsation. In the small opening condition, the low frequency pulsation generated in the draft tube was small, the amplitude of the low frequency pulsation in the volute was significantly reduced, and the main frequency of the pressure pulsation at the G4 point near the nose was the leaf frequency, which was due to the nasal end distance. The runner was closer and more susceptible to the rotation of the runner blades. With the decrease in the opening degree of the guide vane, the 0.5-fold leaf frequency and the leaf frequency pulsation in the volute first decreased and then increased, mainly because the large opening degree condition and the small opening degree condition deviated from the optimal working condition. The resulting pressure pulsation and the instability of the runner also increased. The pressure pulsation caused by the rotation of the runner blade propagated upstream and the influence on the volute was also increased. Under rated opening conditions, the flow behavior was relatively stable, which was favorable for the pressure pulsation component caused by the rotation of the runner to propagate upstream, and the volute was affected by the rotation of the runner blade.

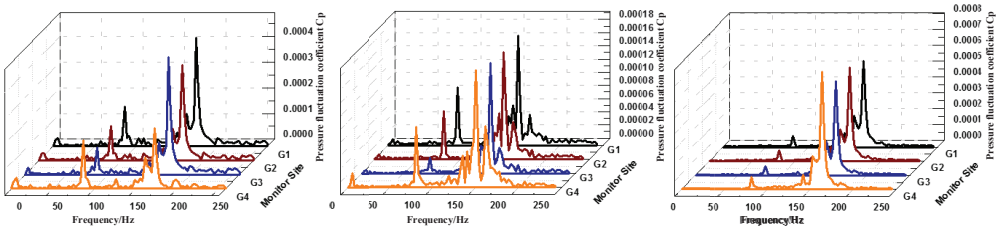

(**a**) Large opening condition (**b**) Rated condition (**c**) Small opening condition

Figure 9. Volute pressure pulsation frequency domain diagram.

3.3. Distribution of Pressure Pulsation

The advantage of the 3D method lies in the visualization of the internal flow state, including the streamline pressure field distribution and energy field. The visualization of the internal flow state was helpful to directly reveal the mechanism of unstable operation

in the transition process of the Francis turbine. This was then used to improve the efficiency design of the runner. Therefore, based on the comparison of the pressure pulsation in different locations of the turbine in Section 3.2, the pressure field was visualized to explore the distribution propagation law of pressure pulsation under the load reduction process, as shown in Figure 10.

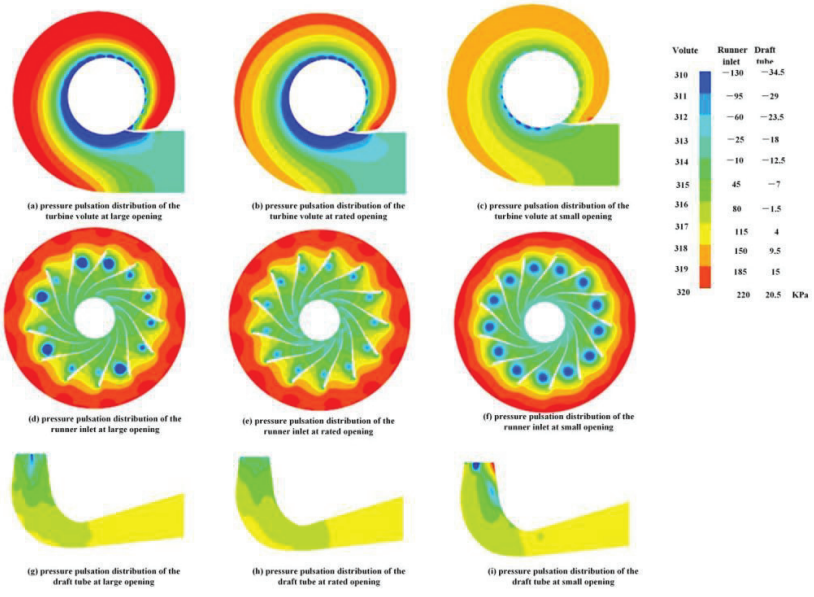

Figure 10. Pressure pulsation distribution in the volute, runner, and draft tube under three GVOs.

Figure 10 shows the pressure pulsation distribution of the turbine volute, the runner inlet, and the draft tube from top to bottom. The static pressure in the volute increased with the increase in the load. The static pressure in the volute section decreased gradually along the radial direction from the volute wall to the volute outlet, and a minimum value appeared in the initial spiral section. The reason for this phenomenon is that, under nonoptimal GVOs, the flow stability in the volute was relatively poor, leading to obvious changes in the static pressure distribution under 3.91°. For the runner, there was an obvious negative pressure zone on the suction side of the leading edge at 12.43° and 3.91°. This is because the guide vanes at 12.43° and 3.91° were far from the optimal working condition. The outlet velocity of the guide vane produced a circumferential velocity component, and the water flow at the runner and the impeller underwent cavitation erosion, forming a negative pressure area. When moving to the rated operating point, the circumferential velocity component decreased, the water loss stability was improved, and the negative pressure area disappeared. Compared to that at 3.91°, the distribution of the low-pressure zone at 12.43° was not uniform. In the process of load reduction, the negative pressure area of the draft tube decreased and then increased. Under the nonoptimal GVOs, the outlet velocity of the turbine runner produced a circumferential velocity component, which led to flow disorder in the straight cone section and elbow section of the draft tube, forming a large negative pressure area.

4. Conclusions

This paper explores the dynamic character of a HGS and pressure pulsation in the full flow path of a Francis turbine during the load decreasing process. A 1D-3D coupling model for a HGS was established. Through the results, the following conclusions were obtained.

(1) The systematical model shows the dynamical response of the HGS during the load-reduction process. The discharge gradually decreased with the closure of the guide vane, and the rotation speed reached a maximum value at the initial stage of the guide vane action; then, it converged to 0.

(2) The sensitivity analysis indicated the coupling relationship among subsystems based on the systematical model. Hydraulic parameters (*hw* and *Tr*) had significant effects on the discharge output. The rotation speed output was mainly influenced by the machinery parameter (*Tab*). The findings are useful for understanding the effects of parameters on system stability when different subsystems are running together.

(3) The amplitude of pressure pulsation was the largest under a small opening (3.91°), and the smallest under a large opening (12.43°). The main pressure pulsation frequency of the Francis turbine was the blade frequency under different GVOs. In off-design conditions (12.43°and 3.91°), the flow at the inlet of the runner obviously deviated from the normal outlet, resulting in extremely unstable pressure pulsation at the draft tube inlet.

(4) The 3D pressure pulsation distribution showed that the negative pressure zone obviously diffused along the inner boundary of the volute, the leading edge of the runner, and the straight cone section of the draft tube, as the GVOs were far from the rated opening (9.84°). Therefore, the flow stability suffered. Correspondingly, the system parameters under off-design conditions fluctuated sharply, which further caused the mechanical vibration and power signal fluctuation. These findings provide mechanism support for the instability phenomenon in the transition process.

Author Contributions: Conceptualization, B.X.; Data curation, M.Z.; Formal analysis, M.Z. and J.F.; Funding acquisition, B.X.; Investigation, J.Z.; Methodology, J.F. and Z.Z.; Resources, J.F.; Software, Z.Z. and J.Z.; Supervision, W.Z.; Validation, Z.Z.; Writing—original draft, Z.Z.; Writing—review & editing, W.Z. All authors have read and agreed to the published version of the manuscript.

Funding: This work was supported by the scientific research foundation of National Natural Science 595 Foundation of China—Outstanding Youth Foundation (51622906) and National Natural Science 596 Foundation of China (51479173).

Conflicts of Interest: The authors declare no conflict of interest.

References

1. Decaix, J.; Alligne, S.; Müller, A.; Nicolet, C.; Münch, C.; Avellan, F. Identification of 1-D cavitation model parameters by means of computational fluid dynamics. *J. Hydraul. Res.* **2021**, *60*, 271–282. [CrossRef]
2. Zhang, H.; Pang, W.; Chen, D.; Tian, Y.; Patelli, E.; Li, C.; Zhou, J. Transient stability of a hydro-turbine governing system with different tailrace tunnels. *J. Hydraul. Res.* **2020**, *58*, 60–69. [CrossRef]
3. Müller, A.; Favrel, A.; Landry, C.; Avellan, F. Fluid–structure interaction mechanisms leading to dangerous power swings in Francis turbines at full load. *J. Fluids Struct.* **2021**, *35*, 102293. [CrossRef]
4. Camal, S.; Teng, F.; Michiorri, A. Scenario generation of aggregated Wind, Photovoltaics and small Hydro production for power systems applications. *Appl. Energy* **2019**, *242*, 1396–1406. [CrossRef]
5. Favrel, A.; Junior, J.G.P.; Müller, A.; Landry, C.; Yamamoto, K.; Avellan, F. Swirl number based transposition of flow-induced mechanical stresses from reduced scale to full-size Francis turbine runners. *J. Fluids Struct.* **2020**, *94*, 102956. [CrossRef]
6. Luis, I.L.; Fernando, I.; Hernan, D.B. Power dispatch assessment of a wind farm and a hydropower plant: A case study in Argentina. *Energy Convers. Manag.* **2019**, *180*, 391–400.
7. Guillermo, M.L.; Jose, I.S.; Jose, A. Eigen analysis of wind-hydro joint frequency regulation in an isolated power system. *Int. J. Electr. Power Energy Syst.* **2018**, *103*, 511–524.
8. Jiang, R.; Wang, J.; Guan, Y. Robust unit commitment with wind power and pumped storage hydro. *IEEE Trans. Power Syst.* **2012**, *27*, 800–810. [CrossRef]
9. Serban, I.; Marinescu, C. Aggregate load-frequency control of a wind-hydro autonomous microgrid. *Renew. Energy* **2011**, *36*, 3345–3354. [CrossRef]
10. Yang, W.; Per, N.; Chung, C. Eigen-analysis of hydraulic-mechanical-electrical coupling mechanism for small signal stability of hydropower plant. *Renew. Energy* **2018**, *115*, 1014–1025. [CrossRef]
11. Zhang, H.; Chen, D.; Wu, C. Dynamics analysis of the fast-slow hydro-turbine governing system with different time-scale coupling. *Commut. Nonlinear Sci. Numer. Simul.* **2018**, *54*, 136–147. [CrossRef]
12. Zhang, H.; Chen, D.; Xu, B. Nonlinear modeling and dynamic analysis of hydro-turbine governing system in the process of loadrejection transient. *Energy Convers. Manag.* **2015**, *90*, 128–137. [CrossRef]

13. Chirag, T. Transient Pressure Measurements on a high head model francis turbine uring emergency shutdown, total load rejection, and runaway. *J. Fluids Eng.-Trans. ASME* **2014**, *136*, 121107.
14. Chirag, T.; Bhupendra, G.; Cervantes, M. Effect of transients on Francis turbine runner life: A review. *J. Hydraul. Res.* **2013**, *51*, 121–132.
15. Hyen-Jun, C.; Asid, Z.; Hyoung-Woon, R. CFD validation of performance improvement of a 500 kW Francis turbine. *Renew. Energy* **2013**, *54*, 111–123.
16. Pasche, S.; Gallaire, F.; Avellan, F. Origin of the synchronous pressure fluctuations in the draft tube of Francis turbines operating at part load conditions. *J. Fluids Struct.* **2019**, *86*, 13–33. [CrossRef]
17. Zhou, X.; Wu, H.; Shi, C. Numerical and experimental investigation of the effect of baffles on flow instabilities in a Francis turbine draft tube under partial load conditions. *Adv. Mech. Eng.* **2019**, *11*, 1687814018824468. [CrossRef]
18. Zhou, D.; Chen, H.; Zhang, J.; Jiang, S.; Gui, J. Numerical study on flow characteristics in a francis turbine during load rejection. *Energies* **2019**, *12*, 716. [CrossRef]
19. Laouari, A.; Ghenaiet, A. Predicting unsteady behavior of a small francis turbine at several operating points. *Renew. Energy* **2019**, *133*, 712–724. [CrossRef]
20. Farvel, A.; Muller, A.; Landry, C. Study of the vortex-induced pressure excitation source in a Francis turbine draft tube by particle image velocimetry. *Exp. Fluids* **2015**, *56*, 215.
21. Zhang, R.; Wu, J. Characteristics and control of the draft-tube flow in part-load Francis turbine. *J. Fluids Eng.-Trans. ASME* **2009**, *131*, 021101. [CrossRef]
22. Christian, L.; Arthur, F.; Andres, M. Local wave speed and bulk flow viscosity in Francis turbines at part load operation. *J. Hydraul. Res.* **2016**, *54*, 185–196.
23. Chen, T.; Zheng, X.; Ning, Y. Influence of upstream disturbance on the draft-tube flow of Francis turbine under part-load conditions. *J. Hydrodyn.* **2018**, *30*, 131–139. [CrossRef]
24. Simon, P.; Francois, A.; Francios, G. Optimal control of part load vortex rope in Francis turbines. *J. Fluids Eng.-Trans. ASME* **2019**, *141*, 081203.
25. Guo, W.; Peng, Z. Hydropower system operation stability considering the coupling effect of water potential energy in surge tank and power grid. *Renew. Energy* **2019**, *134*, 846–861. [CrossRef]
26. Xu, B.; Wang, F.; Chen, D.; Zhang, H. Hamiltonian modeling of multi-hydro-turbine governing systems with sharing common penstock and dynamic analyses under shock load. *Energy Convers. Manag.* **2016**, *108*, 478–487. [CrossRef]
27. Li, H.; Chen, D.; Gao, X. Fast-slow dynamics of a hydropower generation system with multi-time scales. *Mech. Syst. Signal Processing* **2018**, *110*, 458–468. [CrossRef]
28. David, E.; Lois, C.; Carol, W.; Gropp, W.; Myra, E.; Pernice, M.; Bell, J.; Brown, J.; Clo, A.; Connors, J.; et al. Multiphysics simulations: Challenges and opportunities. *Int. J. High Perform. Comput. Appl.* **2013**, *27*, 4–83. Available online: http://hpc.sagepub.com/content/27/1/4 (accessed on 6 September 2022).
29. Zhang, H.; Guo, J.; Lu, J.; Li, F.; Xu, Y.; Downar, T.J. An Assessment of Coupling Algorithms in HTR Simulator TINTE. *Nucl. Sci. Eng.* **2018**, *190*, 287–309. [CrossRef]
30. Zhang, Q.; Peng, T.; Zhang, G.; Liu, J.; Guo, X.; Gong, C.; Yang, B.; Fan, X. An Efficient Scheme for Coupling OpenMC and FLUENT with Adaptive Load Balancing. *Sci. Technol. Nucl. Install.* **2021**, *2021*, 5549602. [CrossRef]
31. Zhang, X.; Cheng, Y.; Yang, Z.; Chen, Q.; Liu, D. Water column separation in pump-turbine after load rejection: 1D-3D coupled simulation of a model pumped-storage system. *Renew. Energy* **2021**, *163*, 685–697. [CrossRef]
32. Liu, L.; Zhang, X.; Yang, Z.; Liu, K.; Cheng, Y. Evaluating the pressure fluctuations during load rejection of two pump-turbines in a prototype pumped-storage system by using 1D-3D coupled simulation. *Renew. Energy* **2021**, *171*, 1276–1289. [CrossRef]
33. Trivedi, C.; Cervantes, M. Experimental and numerical studies for a high head Francis turbine at several operating points. *J. Fluids Eng.-Trans. ASME* **2013**, *135*, 111102. [CrossRef]
34. Zeng, W.; Yang, J. Instability of pumped storage stations at no-load operation based on a parameter-varying model. *Renew. Energy* **2016**, *90*, 420–429. [CrossRef]
35. Chen, D.; Ding, C.; Do, C.; Ma, X.; Zhao, H.; Wang, Y. Nonlinear dynamic analysis for a Francis hydro-turbine governing system and its control. *J. Frankl. Inst.-Eng. Appl. Math.* **2014**, *351*, 4596–4618. [CrossRef]
36. Jost, D.; Skerlavaj, A.; Morgut, M. Numerical simulation of flow in a high head Francis turbine with prediction of efficiency, rotor stator interaction and vortex structures in the draft tube. *J. Phys.* **2015**, *579*, 203–217.
37. Saltelli, A.; Tarantola, S. A quantitative model-independent method for global sensitivity analysis of model output. *Technometrics* **1999**, *41*, 19–56. [CrossRef]
38. Hal, C. Sensitivity analysis of transient population dynamics. *Ecol. Lett.* **2007**, *10*, 1–15.
39. Berta, S.; Jesus, F.; Joaquin, M. Sensitivity analysis to assess the influence of the inertial properties of railway vehicle bodies on the vehicle's dynamic behaviour. *Veh. Syst. Dyn.* **2013**, *51*, 51–279.
40. Simeone, M.; Ian, H.; Christian, R. A methodology for performing global uncertainty and sensitivity analysis in systems biology. *J. Theor. Biol.* **2008**, *254*, 178–196.

MDPI
St. Alban-Anlage 66
4052 Basel
Switzerland
Tel. +41 61 683 77 34
Fax +41 61 302 89 18
www.mdpi.com

Energies Editorial Office
E-mail: energies@mdpi.com
www.mdpi.com/journal/energies

MDPI
St. Alban-Anlage 66
4052 Basel
Switzerland

Tel: +41 61 683 77 34

www.mdpi.com

ISBN 978-3-0365-5838-7